PETROLOGICAL CONSTRAINTS ON THE ORIGIN OF ENCLAVES FROM KASATOCHI VOLCANO, ALEUTIAN ISLANDS, ALASKA

By

Adrienne Kentner

RECOMMENDED:

Dr. Pavel Izbekov

Dr. Mary Keskinen

Dr. Elisabeth Nadin, Advisory Committee Chair

Dr. Paul McCarthy, Chair,
Department of Geology and Geophysics

APPROVED:

Dr. Paul Layer
Dean, College of Natural Science and Mathematics

Dr. John Eichelberger
Dean of the Graduate School

11/26/13
Date

PETROLOGICAL CONSTRAINTS ON THE ORIGIN OF ENCLAVES FROM KASATOCHI VOLCANO, ALEUTIAN ISLANDS, ALASKA

A

THESIS

Presented to the Faculty

of the University of Alaska Fairbanks

in Partial Fulfillment of the Requirements

for the Degree of

MASTER OF SCIENCE

By

Adrienne Kentner, B.S.

Fairbanks, Alaska

December 2013

Abstract

Products of the 2008 eruption of Kasatochi volcano in the Aleutian Islands, Alaska, include mafic and ultramafic crystalline intrusive rocks. I analyzed 42 such samples that were collected from Kasatochi in 2012. The mafic enclaves are hornblende gabbros that are texturally and compositionally layered and are composed of plagioclase (An_{91-93}), pargasitic hornblende, clinopyroxene, and accessory magnetite. The ultramafic samples include variable amounts of clinopyroxene and olivine with interstitial pargasitic hornblende and accessory spinel. Modal mineral abundances in the ultramafic enclaves were used to classify the samples as wehrlite, olivine-clinopyroxenite, and clinopyroxenite. Compositions of interstitial hornblende in the pyroxenite samples are the same as those for the gabbro, implying that the ultramafic enclaves resided within the same magma as the cumulate gabbro long enough to begin re-equilibration. The results of both whole-rock X-ray fluorescence and mineral electron microprobe analyses of the pyroxenite and peridotite samples indicate a non-mantle source: clinopyroxene Cr# is less than 25, Ni-in-olivine is less than 1600 ppm, and spinel is Cr# is less than 50. The presence of disequilibrium textures, such as resorption in clinopyroxene, intimate a prolonged residence time in the host magma. Bulk and mineral compositions for representative mafic and ultramafic samples show that the two sample suites are chemically unrelated and therefore have different igneous origins. The mafic samples display textures and compositions that reflect a cumulate origin related to magma stored below Kasatochi, both of which were brought to the surface during the 2008 eruption. I also interpret the ultramafic enclaves as cumulates, but from a separate, unrelated magmatic source. The ultramafic and mafic enclaves from Kasatochi share mineralogical and compositional similarities with inclusions from neighboring Adak Island, suggesting that similar igneous processes occur at both volcanic centers.

Table of Contents

List of Figures

Page

List of Tables

Page

List of Appendices

List of Supplemental Files

Acknowledgements

Many contributed to this small, fascinating, project, all out of their love for science and the kindness in their hearts. First, I would like to thank Elisabeth Nadin for taking me as a graduate student and leading me through this research; none of this would be possible without you. Thank you for taking me out in the field and financially supporting lab analyses. Pavel Izbekov, my committee member and petrology mentor, made the trip to Kasatochi possible using his frequent flier miles to pay for my flight to Adak. Travelling to the Aleutians was the highlight of my degree; thank you for making it happen. The U.S. Fish and Wildlife Service also made the trip to Kasatochi possible by providing me with a berth aboard the R/V Tiglax. Thank you to the R/V Tiglax biology crew for teaching me about the wildlife and to the ship's crew for charting the course and feeding us like royalty. Chris Nye and Willie Scott helped teach me about the geology and collect samples on Kasatochi. Thank you, Chris for helping me make sense of the enclaves and for sharing your samples before I went out to collect my own. I owe a huge debt of gratitude to Ken, Karen, Maciej, and Owen for helping me navigate the machines in the Advanced Instrumentation Laboratory and to Jessica and Rebekah for sacrificing their time to help me make thin sections and prepare samples. I cannot forget to thank Rainer: always around to help with a problem, whether I needed help identifying a mineral in thin section, re-calculating mineral formulas, or coming up with examples for students. Mary, being your TA was a joy. Thank you so much for our weekly chats and thoughtful thesis edits. For moral support, I thank my cabin-mate, fellow graduate students, and my friends in the Fairbanks climbing community. I could always find someone to share refreshments, happiness, and adventures with during the splendid, freezing, dark Fairbanks winters. Finally, I thank my Mom and Dad for always believing in me, supporting my crazy ideas, and never losing faith in my dreams. I love you with all my heart.

1. Introduction

Kasatochi volcano is a 3-km-wide island stratovolcano located in the central Aleutian Arc (Fig. 1). On August 7–8, 2008, Kasatochi violently erupted in a series of explosions with a volcanic explosivity index (VEI) of 3–4 that released the most SO_2 into the atmosphere since the 1991 eruptions of Pinatubo in the Philippines and Cerro Hudson in Chile (Kristiansen et al., 2010). There was only a two-week period of seismic unrest on the island before it erupted. Prior to the eruption, Kasatochi was primarily a site of biological studies of seabirds and marine mammals by the U.S. Fish and Wildlife Service (USFWS) and no historical eruptions were attributed to the volcano. Kasatochi is scientifically notable to arctic biologists studying bird repopulation, and to geologists because of the eruption's seismic intensity, short duration, and the large volume of SO_2 released.

Geologists mapping the island after August 8, 2008, discovered mafic enclaves along the shoreline and within the pyroclastic units deposited during the 2008 eruption. I visited the island in 2012 and discovered that ultramafic enclaves are also present at Kasatochi (Kentner et al., 2012). The term "enclave" is used herein to describe intrusive rocks that are included within and distinct from erupted lavas, without implying a petrologic origin (as with the terms xenolith and autolith). This paper constitutes the first report of ultramafic enclaves from the volcano, and the first in-depth description of the enclave suite, with insight into the sub-arc magma system composition and structure. Included are the results from modal abundance and textural analyses for the samples collected in 2012, as well as whole-rock wavelength-dispersive X-Ray fluorescence (WD-XRF) analyses of major and trace elements in 14 samples, and in-situ Electron Probe Microanalysis (EPMA) of major element oxides in plagioclase, amphibole, clinopyroxene, olivine, and spinel.

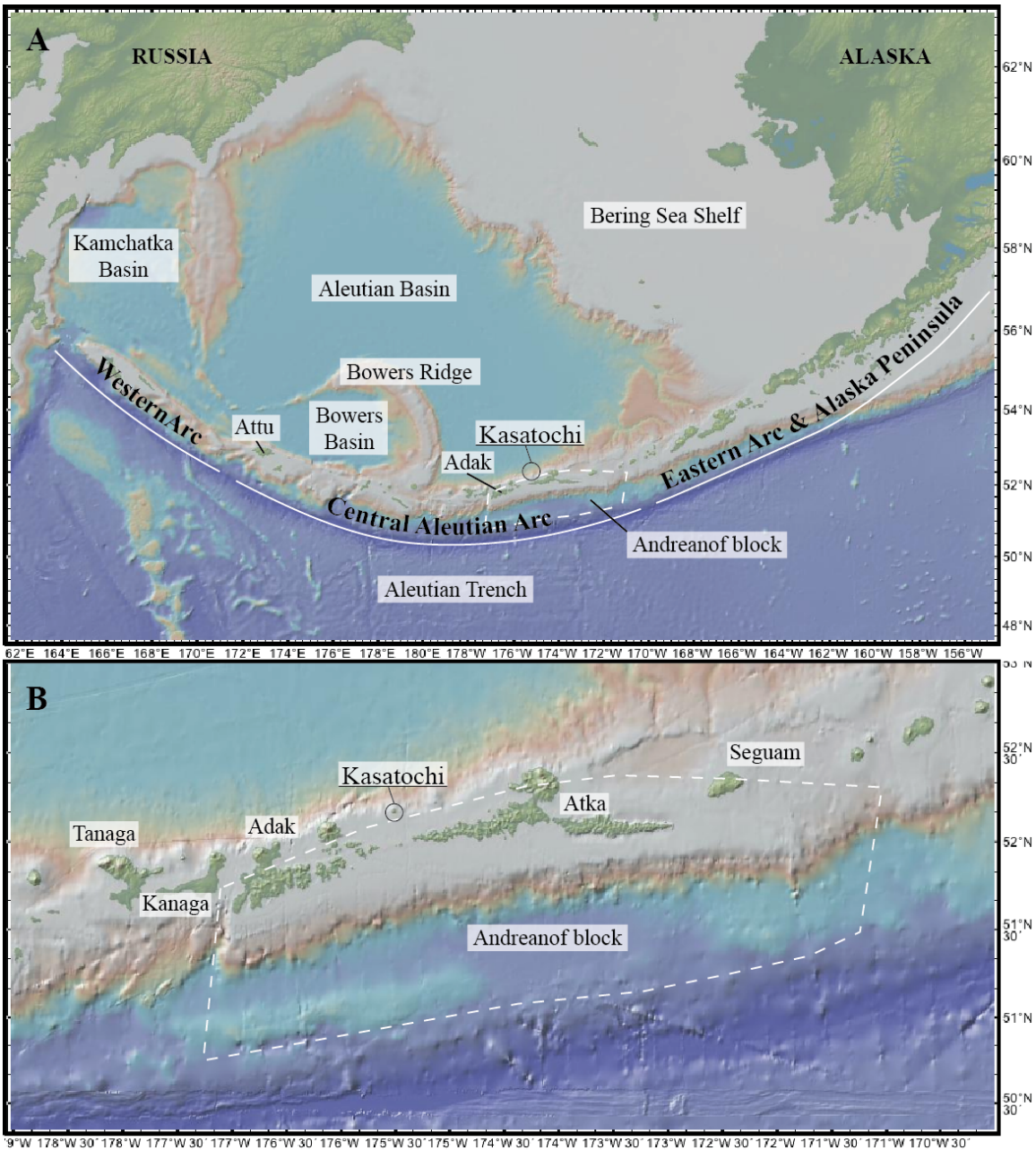

Figure 1. Location Map of Kasatochi Island
(A) Bathymetric map showing the components and major geographical features of the Aleutian Arc. (B) Close-up of the Central Aleutian Arc showing the Andreanof Block and the location of Kasatochi. The Andreanof Block is one of five tectonic blocks described for the central Aleutian arc. Bathymetric base map is from http://www.geomapapp.org and the Global Multi-Resolution Topography (GMRT) Synthesis (Ryan et al., 2009). Arc segmentation is based on Geist and others (1988) and Kay and others (1982).

2. Geologic Setting

Kasatochi Island is located in the center of the Aleutian Island arc, which spans ~2200 km across the northern Pacific between the Alaska and Kamchatka Peninsulas and comprises 27 historically active volcanoes (Kelemen et al., 2003; Jicha et al., 2006; Holbrook et al., 1999; Lizarralde et al., 2002; Shillington et al., 2004). Based on geophysical surveys, the Aleutian arc is 160–225 km wide and 25–35 km thick (Holbrook et al., 1999; Lizarralde et al., 2002). Compositional diversity in the arc stems from its geology, which includes continental arc volcanism along the Alaskan Peninsula, intra-oceanic subduction in the central arc, and strike-slip faulting without volcanism in the west (e.g., Fliedner and Klemperer, 2000; Kay and Kay, 1994). These changes in the style of subduction and geographic features such as fractures caused by rotation along the subduction zone are used to outline different segments of the Aleutian arc (Fig. 1; Geist et al., 1988). The most widely agreed-upon segments are the Alaskan Peninsula, the central Aleutians, and the western Aleutian arc (Fig. 1A). The central arc is further divided into five segments, including the Andreanof block where Kasatochi is located (Fig. 1B).

Subduction zones, including the Aleutian subduction zone, are the most notable locations of crustal creation and recycling (e.g., DeBari et al., 1987; Kelemen et al., 2003). These zones where oceanic crust is subducted underneath another plate form chains of volcanoes by partial melting of pre-existing crust and mantle. However, the interactions between the subducted slab and mantle that generate melt are only marginally understood due to the challenges of observing the processes firsthand. The generation of new crust in subduction zones can be studied by looking at accreted volcanic arcs (e.g., the Talkeetna arc in Alaska and the Kohistan arc in Pakistan) or by comparing enclaves included in subduction zone magmas to their host lava (e.g., Conrad and Kay, 1984; Debari et al., 1987).

The composition of magma that forms at a subduction zone is largely dependent on the age and relative density of the subducting plate, the amount of sediment input from

the accretionary wedge, and the composition of the overriding plate (Stern, 2002). Intra-oceanic arcs (IOA), such as the Central Aleutian Arc, are ideal locations for studying the creation of magma at subduction zones. In an IOA, two plates of juvenile oceanic crust interact, with one subducting underneath the other, the type locality being the Mariana Island Arc (e.g., Hawkins et al., 1984; Arculus, 1994; Stern, 2002; Takahashi et al., 2006). IOAs are less likely to have high sediment or continental crust involvement that would influence the resulting magma chemistry and make it difficult to determine the role of either mantle or crust in the creation of melt (e.g., Stern, 2002).

The Aleutian arc is an IOA and its volcanoes produce both calc-alkaline and tholeiitic lavas, with lavas from larger volcanic centers being predominantly tholeiitic and smaller centers calc-alkaline (e.g., Kay and Kay, 1994; Fournelle et al., 1994). The most common lava type produced by Aleutian volcanoes is basalt (e.g., Kelemen et al., 2003). The primary basalt type erupted from Aleutian arc volcanoes is high-Al with high FeO/MgO ratios, low MgO (<5 wt.%) and low Ni and Cr content (Kay and Kay, 1994). In comparison, the basaltic andesite and andesite erupted at Kasatochi in 2008 are tholeiitic to calc-alkaline with low MgO (<5 wt.%), and the mafic enclaves are tholeiitic with 5–15 wt.% MgO (Neill, 2013).

Aleutian magmas are quite diverse and include basalts enriched in light rare earth elements (LREEs) and depleted in heavy rare earth elements (HREEs), picrites, and adakites, which are primitive (low Mg#) andesites enriched in LREEs, depleted in HREEs, and with very high Sr/Y (e.g., Jicha et al., 2004; Kay and Kay, 1994; Yogodzinski and Kelemen, 2007). Research covering the compositional variation in arc lavas is plentiful (e.g., Kay and Kay, 1994; Kelemen et al., 2003; Yogodzinski and Kelemen, 1998). Studies of Aleutian inclusions, in contrast, are rare because they are more scarce and difficult to find. The bulk of published data on Aleutian inclusions is therefore from three volcanic centers on two different islands that neighbor Kasatochi to the west (Fig. 1): Kanaga, Moffett (Adak island), and Adagdak (Adak island) (Conrad et al., 1983; Conrad and Kay, 1984; DeBari et al., 1987; Yogodzinski and Kelemen, 2007; Pope, 1983).

The Adak and Kanaga inclusions are defined texturally as either cumulate inclusions (related to the host lava) or composite xenoliths that are interpreted as fragments of unrelated wall rock (Conrad et al., 1983; Conrad and Kay, 1984). The cumulate inclusions described are clinopyroxenite, olivine clinopyroxenite, wehrlite, dunite, strained hornblendite, two-pyroxene gabbro, and hornblende gabbro (Conrad et al., 1983; Conrad and Kay, 1984; DeBari et al., 1987). The hornblende gabbro described by Conrad and others (1983) is the most abundant type of cumulate inclusion from Adak and Kanaga. Texturally, Adak and Kanaga cumulates are adcumulate to mesocumulate, have grain sizes up to pegmatite, and display primary igneous layering and alignment of euhedral hornblende (Conrad et al, 1983; DeBari et al., 1987). They contain magnetite, An_{91-96} plagioclase, pargasitic hornblende and no orthopyroxene. Ultramafic inclusions from Adak and Kanaga are both mantle-derived and cumulate (DeBari et al., 1987). The mantle-derived xenoliths contain minor pargasite that formed under different conditions than those at which the rocks initially crystallized (DeBari et al., 1987). Olivine from the ultramafic samples is Fo_{84-92} and contains 0.15–0.49 wt.% NiO.

3. Methods

3.1 Sample Collection

In June of 2012, I joined the U.S. Fish and Wildlife Service aboard the R/V Tiglax for two days of sampling at Kasatochi Volcano. During the two days on land, I collected 42 samples of mafic and ultramafic intrusive rocks (Supplemental File 1). All samples were collected from talus deposits in two localities on the coastline of Kasatochi (Fig. 2). Samples (KS-12-) 01–18 were collected on June 18, 2012, at 600668 E, 5781123 N (UTM zone 1N; Fig. 2A and 2B) and samples (KS-12-) 20–42 were collected on June 19, 2012, at 601242 E, 5782216 N (UTM zone 1N; Fig. 2A and 2C). Mafic samples are found within Unit 3 of the 2008 eruption (Fig. 3; Waythomas et al., 2010), but the ultramafic samples were never found included in lava or pyroclastic flows. Although the mafic samples were present in cliffs of Unit 3, only three samples >2 cm across were found within the Unit 3 deposits (Fig. 3B), and they were all firmly cemented into the cliff wall. Samples were therefore collected at the bases of beach cliffs where the rapid dissection of the 2008 deposits (Scott et al., 2010) is eroding out and concentrating an abundance of small cobble- to large boulder- scale mafic enclaves along the shoreline. In contrast, the ultramafic samples were only found as 15–25 cm-scale cobbles along the beach and have not been found within the 2008 deposits. However, Kasatochi is a small island, so it can be stated with certainty that all the enclaves included in this study came from Kasatochi, even if their relationship to the 2008 eruption is only marginally verifiable. Mafic enclaves were chosen to represent the most common textures, including fine-, medium-, and coarse-grained varieties. These include mafic samples with prominent modal layering, mineral alignment, and cryptocrystalline interstitial glass. All of the relatively few ultramafic samples found were collected for examination.

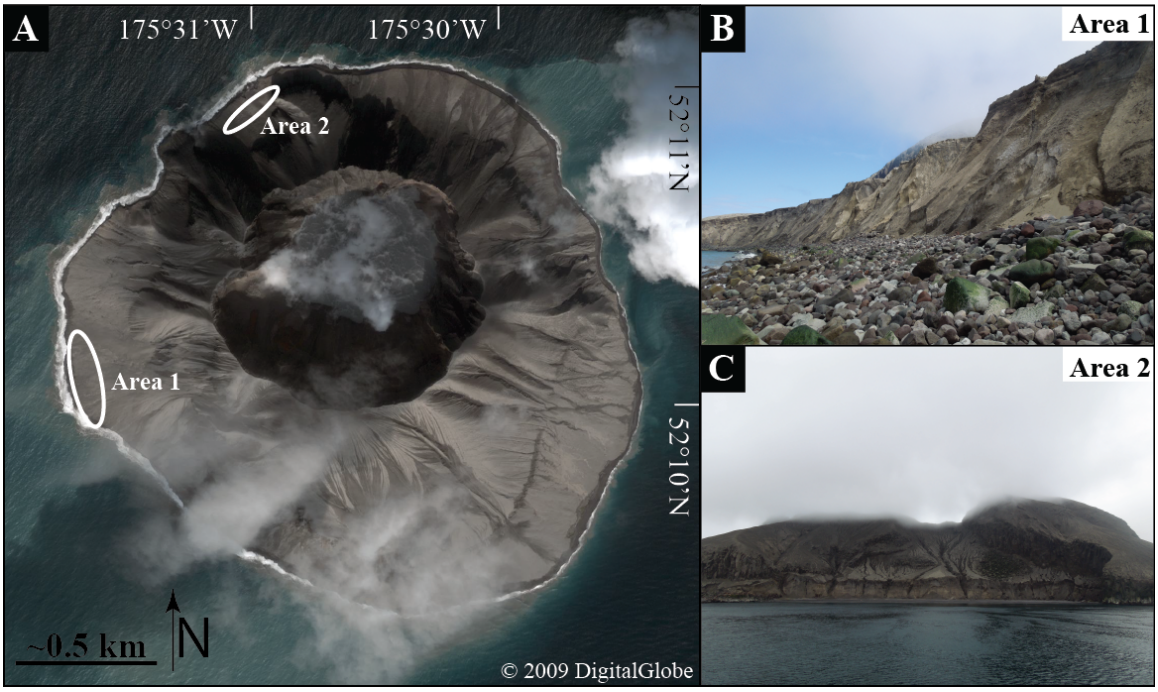

Figure 2. Sample Location Map
(A) Aerial image of Kasatochi taken in 2009 denoting both sample areas. (B) Photo of Area 1, taken from the beach, showing the cliff base from which the samples were gathered. (C) Photo of Area 2, taken from the R/V Tiglax, showing the cliff base from which the samples were collected (right-hand side of the beach shown in the photo). Mafic and ultramafic rock types were found in both areas.

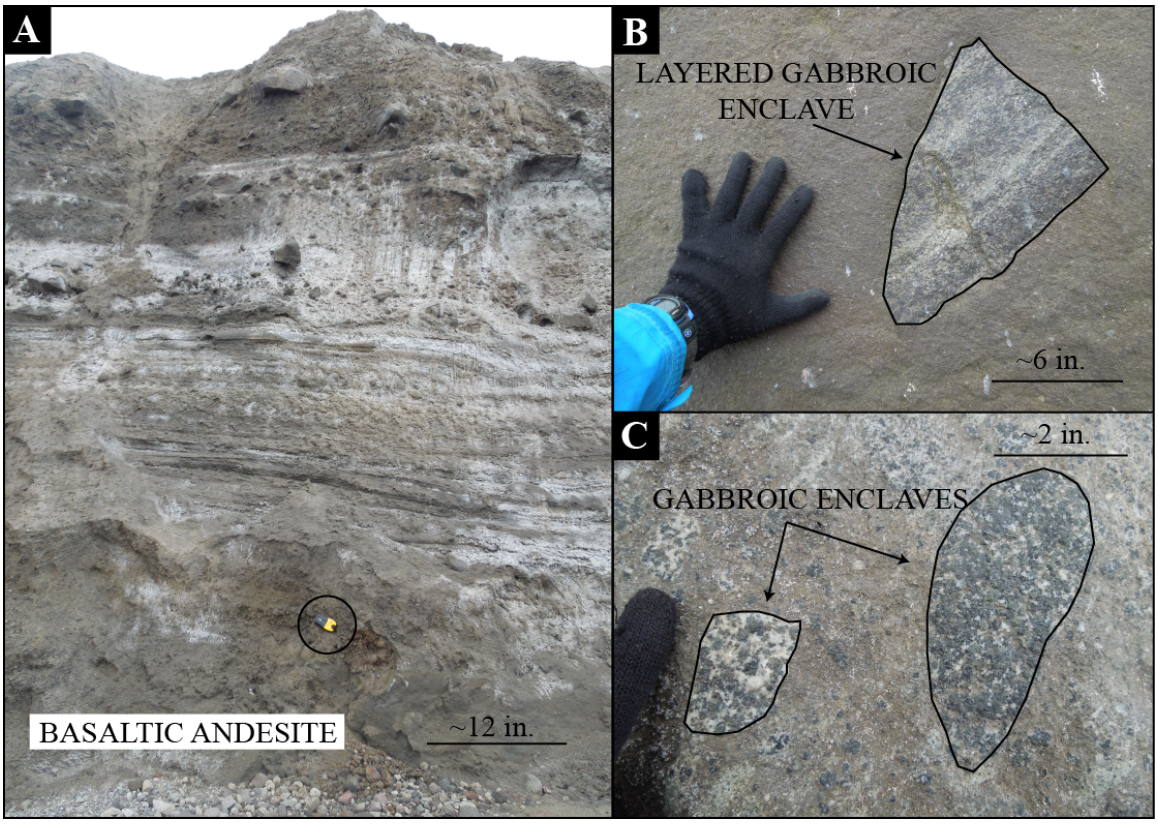

Figure 3. Unit 3 with Mafic Enclaves
(A) Photo of the cliff face near Area 1 showing 2008 pyroclastic flows. The dark layer at the bottom of the photo is basaltic andesite, but no mafic inclusions were found at the location pictured (yellow Garmin eTrex Vista handheld GPS for scale). (B) Close-up photo of a layered mafic enclave included in basaltic andesite in cliff face within Area 1 (my hand for scale). (C) Close-up photo of non-layered isotropic mafic enclaves in basaltic andesite in cliff face within Area 1 (my finger for scale).

3.2 Bulk Chemistry: Sample Preparation

I selected fifteen mafic and ultramafic enclaves for whole-rock WD-XRF analysis (Table 1). Enclaves from Kasatochi are very friable and crushing requires only a brass plate and rock hammer, eliminating contamination typically introduced by using a rock crusher.

All samples were reduced to a <150μm particle size powder using a ceramic puck and shatterbox. Powdering took seven minutes for mafic enclaves and up to 30 minutes for ultramafic rocks. All lab surfaces, including puck and shatterbox, were cleaned using compressed air and wiped down between samples. Moisture was removed from the samples by heating them in an oven at ~500°C for 24 hours immediately prior to melting.

A 1.5g split from the dry powders was mixed with 1g of $LiNO_3$ oxidizer and 8.5g of Li-tetraborate flux. The oxidizer is completely consumed during melting and all iron is converted to Fe^{3+}. The sample powder, oxidizer, and flux are measured into a platinum crucible used in a Claisse fluxer. The fluxer rotates the crucible, increasing rotation speed with increasing temperature, to ensure sample homogenization. The molten sample is then poured into a flat, polished platinum mold and allowed to cool into a 42mm glass disc. Cracked samples were either re-melted or were glued with epoxy for use as duplicates in error analysis (see section 4.3). Ultrapure flux was melted and cooled between samples to remove any residual sample left in the crucible or mold. The glass discs produced a flat and smooth analytical surface, but the epoxied samples required polishing prior to measurement.

Table 1. List of Samples and Analytical Methods
W=whole-rock composition by WD-XRF analysis, A=amphibole composition by EPMA, P=plagioclase composition by EPMA, C=clinopyroxene composition by EPMA, O=olivine composition by EPMA, S=spinel composition by EPMA

Sample Number	Rock Type	W	A	P	C	O	S
KS-12-04	MAFIC	Y	Y	Y			
KS-12-06	MAFIC	Y					
KS-12-11	ULTRAMAFIC	Y	Y		Y	Y	
KS-12-12	ULTRAMAFIC	Y					
KS-12-13	ULTRAMAFIC	Y	Y	Y	Y		
KS-12-19	ANORTHOSITE	Y					
KS-12-21	MAFIC	Y					
KS-12-22	ULTRAMAFIC	Y	Y		Y		Y
KS-12-24	MAFIC	Y					
KS-12-31	MAFIC	Y	Y	Y			
KS-12-33	ULTRAMAFIC	Y			Y	Y	Y
KS-12-34	MAFIC	Y					
KS-12-39	ULTRAMAFIC	Y					
KS-12-42	ULTRAMAFIC	Y					

3.3 Bulk Chemistry by WD-XRF

Bulk compositions were measured at UAF's Advanced Instrumentation Laboratory (AIL) using a PanAlytical Axios four-kilowatt WD-XRF spectrometer. I developed a routine for analyzing major and trace element analytes in fused glass discs prepared using Li-tetraborate flux in the Claisse fluxer. Major element channels include SiO_2, Al_2O_3, TiO_2, Fe_2O_3, MnO, CaO, MgO, K_2O, Na_2O, P_2O_5. Trace element channels include Ba, Ni, Cr, Zr, Cu, Zn, Y, Rb, and Sr. Peaks and backgrounds were measured for each analyte (Potts, 1987). Unlike in previous routines, peak overlaps in trace elements, especially problematic for Ba, are corrected for in the new routine. Error analysis (section 3.4) suggests that the fused discs are exceptionally well suited for major element analysis, but that the errors for trace elements are perhaps too large and that other methods should be used.

3.4 Bulk Chemistry: Error Analysis

Error is introduced into an analysis by three distinct factors: 1) error in the ability of the machine to collect and count a measured X-ray intensity (count rate), referred to as counting statistical error or CSE (measured by PanAlytical software); 2) accuracy in calibrating the routine; and 3) sample contamination, bias, and resulting inhomogeneity (Śliwiński, 2012). The PanAlytical software uses internal algorithms to address CSE, but replicate analyses of a certified reference material (CRM) as well as a representative sample from the Kasatochi enclaves (KS-12-04) are used for the final two errors (Table 2A, B).

The CRM, BHVO-1, a basalt from Hawaii, was measured six times and compared to the accepted published value (available on the GEOREM website) to assess the precision and accuracy of the machine. All major elements had a 1σ of < 0.5 wt.%. Except for TiO_2, MnO, and Na_2O (which were within 10 wt.% of the reference value), all major elements were within 1% of the published standard values (Table 2A). Trace element values all fall within 10% of the published values, except V, which has a slightly larger error of 9%. Standard deviations (1σ) were <10 ppm for all trace elements (Table 2A).

Error caused by sampling bias and contamination was estimated by analyzing two discs, -a and -b of KS-12-04 (a coarse-grained mafic enclave) three times each (Table 2B). Major elements were measured to a 1σ <0.2 for the same sample, and 1σ <0.4 between samples. Errors in trace element analyses were as low as a 1σ <5 for all but V in a single sample disc. Inter-sample comparisons yielded higher errors in trace element data, however, suggesting possible contamination during the sample preparation process. However, the sampling error is still low, and when the CRM is considered alongside the low values for V, error due to measurement is likely. Measured values of Ba fall below the lower limit of detection (LLD) for the program, therefore no error analysis is included for Ba. In samples that contain Ba, results for Ba should be used with caution because the analytical uncertainty increases as detection limit is approached (Potts, 1987).

Table 2A. WD-XRF Error analysis (CRM)
Analytical and machine accuracy were measured by repeated analysis of the published standard BHVO-1, which is basalt with a composition similar to the mafic samples in this study. Standard deviation measures the precision of the instrument and the relative difference ((average – published) / published) measures the accuracy of the instrument and our analytical and preparation methods.

Major elements (wt. % oxide)							**Avg.**	***1-σ***	**Published**	**Relative Difference**
	1	2	3	4	5	6				
SiO_2	49.54	49.63	49.41	49.37	49.57	49.60	49.52	*0.11*	**49.94**	-0.84
Al_2O_3	13.68	13.69	13.72	13.73	13.72	13.75	13.72	*0.02*	**13.8**	-0.61
TiO_2	2.78	2.78	2.77	2.77	2.78	2.78	2.77	*0.00*	**2.71**	2.39
Fe_2O_3	12.30	12.30	12.29	12.27	12.29	12.33	12.30	*0.02*	**12.23**	0.54
MnO	0.169	0.170	0.170	0.170	0.170	0.171	0.17	*0.00*	**0.168**	1.19
CaO	11.52	11.50	11.49	11.49	11.49	11.50	11.50	*0.01*	**11.4**	0.86
MgO	7.18	7.20	7.17	7.18	7.18	7.21	7.19	*0.02*	**7.23**	-0.59
K_2O	0.52	0.52	0.52	0.52	0.52	0.52	0.52	*0.00*	**0.52**	0.54
Na_2O	2.11	2.12	2.11	2.12	2.10	2.10	2.11	*0.01*	**2.26**	-6.72
P_2O_5	0.270	0.271	0.270	0.271	0.270	0.271	0.27	*0.00*	**0.273**	-0.92
Total	100.0	100.2	99.9	99.9	100.1	100.2	100.1		**100.53**	-0.47
Trace elements										
Ni	120	119	123	130		124	123	*4.43*	**121**	1.92
Cr	271	270	264	276		271	271	*4.33*	**289**	-6.37
V	287	286	300	296		275	289	*9.84*	**317**	-8.94
Zr	173	176	173	174		178	175	*2.22*	**179**	-2.31
Cu	139	143	141	138		145	141	*2.83*	**136**	3.85
Zn	107	102	108	99		103	104	*3.90*	**105**	-1.29
Y	22	28	29	23		30	26	*3.64*	**27.6**	-5.23
Rb	12	10	10	12		12	11	*1.15*	**11**	2.80
Sr	392	388	394	390		390	391	*2.14*	**403**	-3.05

Table 2B. WD-XRD Error Analysis (Enclave Sample)
Two glass discs of mafic enclave KS-12-04 (-a and -b) were used to measure sampling error and machine precision.

Sample	a1	a2	a3	b1	b2	b3		
Major elements (wt. % oxide)							**Avg.**	***1-σ***
SiO_2	41.24	40.96	41.04	40.72	40.70	40.57	40.87	*0.25*
Al_2O_3	23.47	23.39	23.39	23.20	23.16	23.17	23.30	*0.13*
TiO_2	1.02	1.01	1.02	0.98	0.98	0.98	1.00	*0.02*
Fe_2O_3	11.84	11.86	11.83	11.30	11.29	11.28	11.57	*0.30*
MnO	0.11	0.11	0.11	0.11	0.11	0.11	0.11	*0.00*
CaO	15.31	15.32	15.28	15.19	15.18	15.22	15.25	*0.06*
MgO	6.25	6.25	6.20	6.11	6.09	6.09	6.17	*0.08*
K_2O	0.11	0.11	0.11	0.11	0.11	0.11	0.11	*0.00*
Na_2O	1.05	1.05	1.06	1.07	1.06	1.06	1.06	*0.01*
P_2O_5	0.07	0.07	0.07	0.06	0.06	0.06	0.07	*0.01*
Total	100.47	100.12	100.11	98.84	98.73	98.64	99.48	*0.83*
Trace elements (ppm)								
Ni	26	26	23	24	28	28	26	*2*
Cr	14	13	16	13	15	14	14	*1*
V	493	484	483	463	467	464	476	*13*
Zr	22	22	23	22	24	24	23	*1*
Cu	272	268	269	263	265	266	267	*3*
Zn	67	68	66	57	60	59	63	*5*
Y	13	14	12	15	13	14	13	*1*
Ba	<DL	<DL	<DL	<DL	<DL	29	29	
Rb	4	3	3	4	2	1	3	*1*
Sr	479	476	472	477	479	478	477	*3*

3.5 Mineral Composition and Petrography: Sample Preparation

Thirty-three of the 44 samples collected in 2012 were prepared as polished thin sections for EPMA of mineral compositions. Ten of the samples were cut into slabs and polished for examination of macroscopic texture and modal layering (Appendix 1). Samples range in friability from low to high and most required epoxy impregnation prior to thin-section preparation (methods described by Jana, 2006). Petropoxy 154 was selected to use in impregnation because of its relatively low viscosity. I cured the glue overnight (roughly 12 hours) at ~75°C in an oven under intermittent vacuum. The vacuum was removed several times in order to allow bubbles to escape from the glue. Billets were then polished, cleaned, and re-heated for 12 hours to remove excess water. I also used Petropoxy 154 to adhere billets to glass slides. See Appendix 2 for a detailed description of thin-section preparation.

3.6 Petrographic Analysis

All samples were examined under reflected and transmitted light with a petrographic microscope for information on texture, modal abundances, mineral relationships, and amount of glass present. I counted the type of mineral at 1000 points per slide using an automated point counter for the 15 samples that were selected for WD-XRF analysis (Supplemental File 1).

3.7 Mineral Composition by EPMA

I measured major and minor element oxide concentrations in individual mineral phases by wavelength-dispersive (WDS) X-ray spectrometry using UAF AIL's 4-spectrometer Cameca SX-50 electron microprobe. Mineral phase targets were located in thin section and by energy dispersive spectrometry (EDS) using the EDAX EDS detector on the Cameca SX-50 electron microprobe. Mineral phases analyzed include plagioclase, amphibole, olivine, pyroxene, and spinel. Elemental and oxide concentrations were converted from raw intensities using a ZAF intensity correction. I used a 15 keV, 50 nA, 1–3 μm diameter focused beam for all analyses. I chose to use a high amperage beam to increase counts of elements present in trace amounts. Na was analyzed first in order to reduce the effect of volatilization, and I applied a Time-Dependent Intensity correction to the Na-intensities (Donovan and Tingle, 1996; Nielsen and Sigurdsson, 1981). Counting times and standards were chosen according to abundance of each elemental analyte present in the mineral measured. Standard compositions are compared to published standards values (Jarosewich et al., 1980). Typical analytical error is based on calculations by the PC-based program used with the Cameca SX-50, Probe for Windows (Advanced Microbeam Co.). Additional error analysis included measurement of multiple CRMs compared to published data, and measurement of a working standard before, after, and throughout an analysis of a particular mineral (Table 3). Two backgrounds were measured for each analyte. I re-calculated mineral structural formulae based on stoichiometry using the methods of Deer et al. (1992) for plagioclase and olivine, Leake et al. (1997) for amphiboles, Morimoto (1988) for pyroxene, and Stormer (1983) and Carmichael (1967) for spinel.

Table 3. EPMA Error Analysis by Mineral
Reference materials were used as standards for all minerals analyzed. n= number of analyses.

Amphibole							
Element	**Standard**		**Working Standard/ Unknown**		**Published Values**	**Relative Difference (standard)**	**Relative Difference (working standard)**
n=	3	*1-σ*	6	*1-σ*			
Si	18.75	*0.02*	19.15	*0.21*	18.87	-0.63	1.47
Al	7.96	*0.04*	8.04	*0.07*	7.89	0.96	1.90
Ca	7.27	*0.04*	8.10	*0.05*	7.36	-1.21	10.02
Mg	7.87	*0.03*	8.89	*0.08*	7.72	1.90	15.11
Fe	8.44	*0.09*	9.02	*0.24*	8.45	-0.07	6.72
K	1.93	*0.01*	0.19	*0.01*	1.70	13.18	-89.10
Na	2.23	*0.03*	1.82	*0.02*	1.93	15.45	-5.54
Ti	2.94	*0.16*	0.79	*0.09*	2.83	3.75	-72.23
Mn	0.09	*0.02*	0.12	*0.04*	0.07	24.76	71.19
Cl	0.02	*0.01*	0.02	*0.00*	0.00	-	-
O	42.10	*0.07*	41.86	*0.25*	43.14	-2.41	-2.97
H	-	-	-	-	0.11	-	-
Total	99.59	*0.16*	97.98	*0.58*	100.06	-0.47	-2.08

Spinel (chromite 206)							
Oxide	**Standard**	**1-σ**	**Working Standard/ Unknown**	**1-σ**	**Published Values**	**Relative Difference (standard)**	**Relative Difference (working standard)**
n=	7		10				
MnO	0.14	0.05	0.13	0.03	0.23	-37.76	-44.65
FeO	13.15	0.14	12.97	0.18	13.04	0.82	-0.52
MgO	16.45	0.07	16.42	0.15	15.20	8.24	8.04
Al_2O_3	10.14	0.06	10.13	0.07	9.92	2.22	2.12
TiO_2	0.14	0.05	0.10	0.05	0.12	16.31	-15.93
Cr_2O_3	59.88	0.46	59.52	0.42	60.50	-1.03	-1.62
SiO_2	0.00	-	0.07	0.04	0.05	-92.00	37.00
Total	99.90	0.51	99.31	0.59	99.06	0.85	0.25

Table 3. (cont.)

Spinel (chromite 421)							
Oxide	**Standard**	**1-σ**	**Working Standard/ Unknown**	**1-σ**	**Published Values**	**Relative Difference (standard)**	**Relative Difference (working standard)**
n=	7		12				
MnO	0.20	0.04	0.17	0.03	0.18	11.51	-3.61
FeO	36.64	0.48	36.37	0.82	37.31	-1.80	-2.53
MgO	8.53	0.16	8.71	0.40	8.11	5.13	7.38
Al_2O_3	13.69	0.19	13.91	0.35	12.77	7.19	8.94
TiO_2	0.81	0.09	0.76	0.07	0.82	-1.08	-6.89
Cr_2O_3	38.44	0.48	38.23	0.63	38.74	-0.79	-1.32
SiO_2	-	-	-	-	n.d.	-	-
Total	98.30	0.45	98.15	0.58	97.93	0.38	0.22

Plagioclase (An-202)							
Oxide	**Standard**		**Working Standard/ Unknown**		**Published Values**	**Relative Difference (standard)**	**Relative Difference (working standard)**
n=	7	*1-σ*		*1-σ*			
SiO_2	43.90	*0.12*	44.00	*0.16*	44.00	-0.22	-0.01
Al_2O_3	36.02	*0.11*	36.04	*0.17*	36.03	-0.04	0.03
FeO	0.50	*0.02*	0.49	*0.03*	0.62	-19.70	-20.82
CaO	19.09	*0.04*	19.07	*0.10*	19.09	0.01	-0.10
Na_2O	0.54	*0.01*	0.54	*0.01*	0.53	1.89	2.01
K_2O	0.03	*0.01*	0.03	*0.01*	0.03	-7.14	6.67
Total	100.08	*0.16*	100.17	*0.32*	100.30	-0.22	-0.13
An-content					0.97		

Table 3. (cont.)

Clinopyroxene (Augite 204)							
Oxide	**Standard**	**1-σ**	**Working Standard/ Unknown**	**1-σ**	**Published Values**	**Relative Difference (standard)**	**Relative Difference (working standard)**
n=	4			9			
Na_2O	1.92	*0.03*	1.26	*0.03*	1.27	51.11	-0.59
MgO	16.56	*0.13*	16.45	*0.14*	16.65	-0.52	-1.23
Al_2O_3	8.47	*0.06*	8.84	*0.08*	8.73	-3.01	1.31
SiO_2	46.56	*0.25*	49.91	*0.23*	50.73	-8.22	-1.61
CaO	15.70	*0.06*	15.42	*0.09*	15.82	-0.77	-2.52
TiO_2	0.83	*0.01*	0.94	*0.01*	0.74	12.15	26.40
FeO	7.00	*0.06*	6.61	*0.23*	6.32	10.75	4.56
MnO	0.15	*0.01*	0.14	*0.02*	0.13	18.36	8.35
Cr_2O_3	0.12	*0.02*	0.15	*0.06*	n.d.	-	-
Total	97.31		99.72		100.39		

Olivine (USNM 2566)							
Oxide	**Standard**		**Working Standard/ Unknown**		**Published Values**	**Relative Difference (standard)**	**Relative Difference (working standard)**
n=	7	*1-σ*	6	*1-σ*			
SiO_2	41.05	*0.18*	41.12	*0.17*	40.81	0.59	0.76
MgO	49.11	*0.17*	49.18	*0.32*	49.42	-0.62	-0.49
FeO	9.85	*0.06*	9.76	*0.29*	9.55	3.15	2.15
MnO	0.13	*0.02*	0.14	*0.02*	0.14	-10.61	1.31
CaO	0.12	*0.01*	0.12	*0.01*	0.05	139.14	146.67
Cr_2O_3	0.03	*0.02*	0.03	*0.02*	n.a.	-	-
NiO	0.37	*0.04*	0.39	*0.04*	0.37	0.08	5.95
Total	100.66		100.73		100.34		

4. Results

4.1 Petrography

I analyzed 42 hand samples collected from Kasatochi. The collection was separated into a mafic sample suite of 31 rocks and an ultramafic suite of 11 rocks. I cut and polished slabs of 11 rock samples chosen as representative of the entire suite and also based on atypical layering (Appendix 1). I used the rock slabs to estimate relative mineral abundance for very coarse-grained samples whose grains are too large for thin-section mounting and to get a better viewing surface to describe representative and unusual textures of the rocks. I prepared thin sections for 21 of the 31 mafic samples that best represent the entire rock suite and for all 11 ultramafic enclaves (Appendix 2).

4.2 Mafic Suite Textures

The mafic enclaves include up to 20% pore space with a higher percentage of pore space in coarser-grained rocks, which makes the most coarse-grained samples the most friable. Cryptocrystalline "glass" is found as unevenly distributed, interstitial blebs in >25% of the mafic hand samples (Fig. 4A). Visible in both hand sample and thin-section are euhedral plagioclase and amphibole that grew into glass-filled and void intergranular spaces (Fig. 4B & C).

Grain size in the mafic samples varies from ~1 μm to >11 cm. Layering is defined by both variation in grain size (Fig. 5A) and in the modal abundance of plagioclase or hornblende (Fig. 5B). In hand sample, amphibole and plagioclase are readily identifiable mineral phases. Acicular amphiboles, >1.5 cm in length, are found in radiating clusters with a moderate directional alignment (Fig. 5A). Elongate amphiboles (not necessarily acicular) grow sub-perpendicular to layer boundaries (Fig. 5B). Although layered samples are the most striking, fine- to coarse-grained unlayered samples are the most common (Fig. 5C). Fine-grained samples are equigranular and unaligned, with mostly

subhedral to euhedral amphibole, clinopyroxene, and plagioclase. Likewise, the coarse-grained samples are equigranular, but amphibole grains are elongate in one direction, defining a lineation (Fig. 5D).

In thin section, the mafic samples also include magnetite and clinopyroxene (Fig. 6). Plagioclase constitutes >50 vol.% of the total rock and is unzoned with occasionally has fine-sieve texture (Fig. 6A). Magnetite is small, and may also occur as interstitial anhedral grains. In hand sample, all dark phases in the mafic samples may be mistakenly attributed to amphibole, but thin sections reveal that clinopyroxene is common and occurs as euhedral to anhedral phenocrysts (Fig. 6B–F). Some clinopyroxene crystals display fine exsolution lamellae (Fig. 6B), and others have cyclic and sector zoning (Fig. 6E). The amphibole in thin section is brown, while the clinopyroxene is green-blue and weakly pleochroic (Fig. 6C). Amphibole occurs as euhedral primary crystals and also as interstitial crystals between clinopyroxene and plagioclase (Fig. 6D). Where clinopyroxene and amphibole are in contact, clinopyroxene has a smooth but not straight crystal edge (Fig. 6D). Hornblende is commonly ~20 vol.% of the mafic samples' mineralogy, and is usually poikilitic, with plagioclase, clinopyroxene, and magnetite inclusions visible in both hand sample and thin-section (Fig. 6F). The interstitial glass includes plagioclase, pyroxene, and Fe-Ti oxide microlites that are not visible in thin section, but can be seen using Backscattered Electron imagery (BSE) (Fig. 4B & C).

I point counted minerals in thin section to determine rock names for both the mafic and ultramafic samples (Table 4). I chose eight representative samples, seven of which I also used for whole-rock compositional analysis (see Section 4.4). Based on point counts, the mafic enclaves are (clinopyroxene) hornblende-gabbros that include up to 50% plagioclase, 5–20% hornblende, and >10% clinopyroxene (Fig. 7A, Table 4). All but one sample plot as clinopyroxene-hornblende gabbros, based on the presence of >10% clinopyroxene in the samples (Fig. 7A). Although clinopyroxene is important, I will refer to samples as hornblende gabbro because of the overwhelming amount of amphibole.

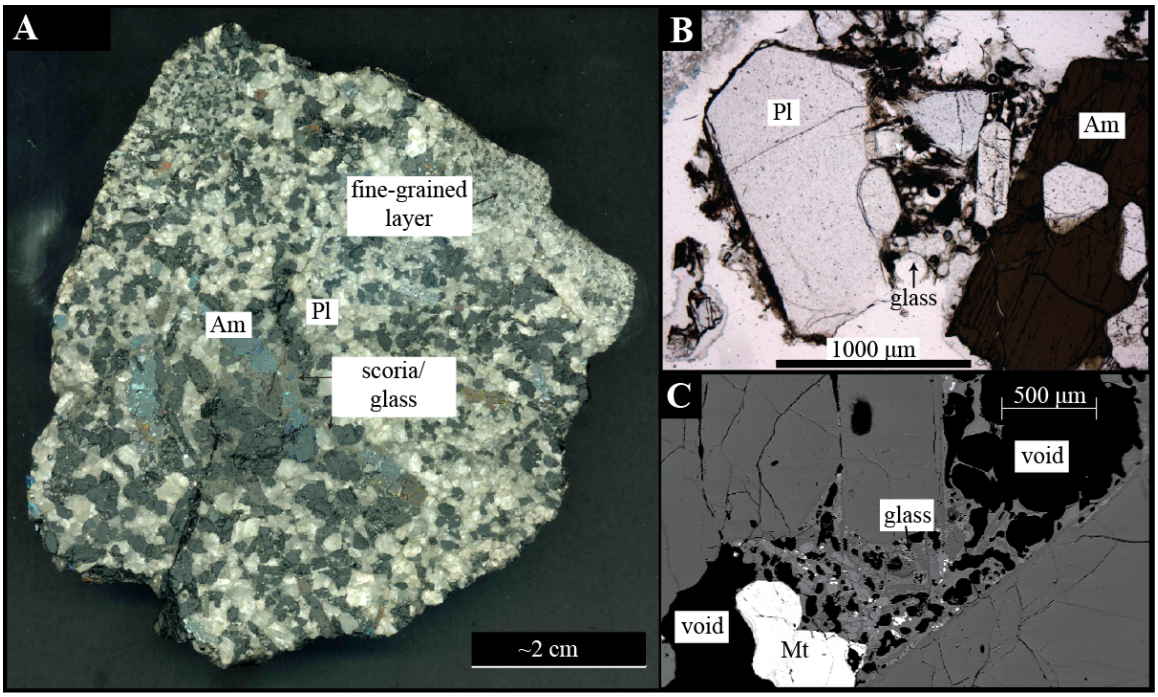

Figure 4. Interstitial Glass in Mafic Enclaves
(A) This scanned gabbro slab contains a cluster of 1–2 cm long hornblende (Am) and dark gray vesicular glass (scoria) in a matrix of equigranular plagioclase, amphibole, and clinopyroxene. (B) In thin section, the glass is opaque to dark brown with mostly intact bubble walls. Euhedral plagioclase and amphibole are preserved in the glass and in pore-spaces (colorless) around the glass. (C) In BSE, the glass contains distinct crystals, shown here by the different shades of gray in the glass in the center of the image. These crystals are too small to see in thin section, but are identifiable using EDS measurements. As in the thin section photomicrograph, bubble walls are mostly intact. Am = hornblende, Pl = plagioclase, and Mt = magnetite.

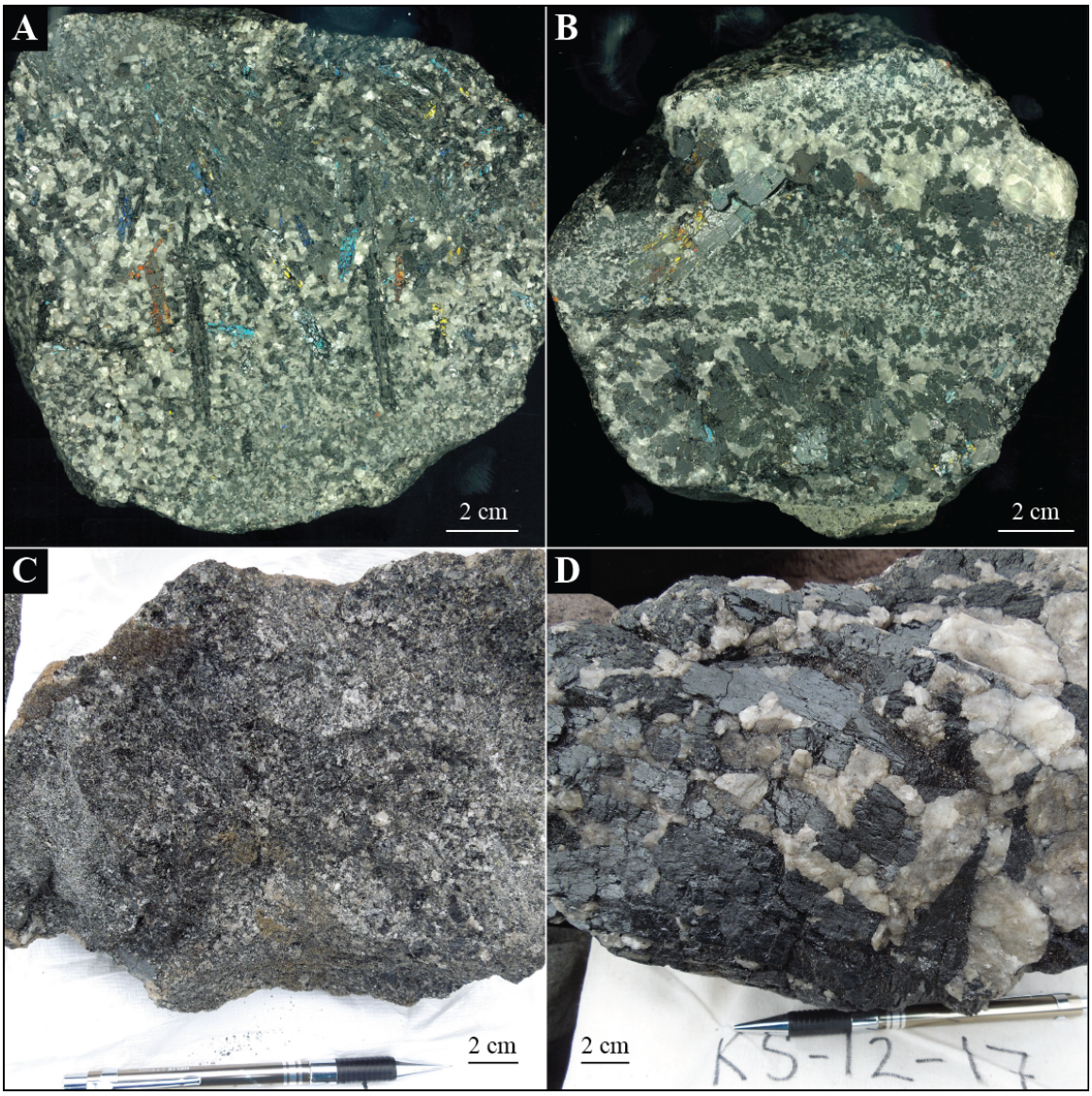

Figure 5. Mafic Suite Hand Samples
The images above are scanned slabs (A and B) and field images (C and D) of representative textures in the mafic enclaves: (A) Medium-grained mafic enclave with acicular radiating hornblende, (B) layered, fine- to coarse-grained mafic enclave, (C) fine-grained isotropic mafic enclave, and (D) pegmatitic mafic enclave.

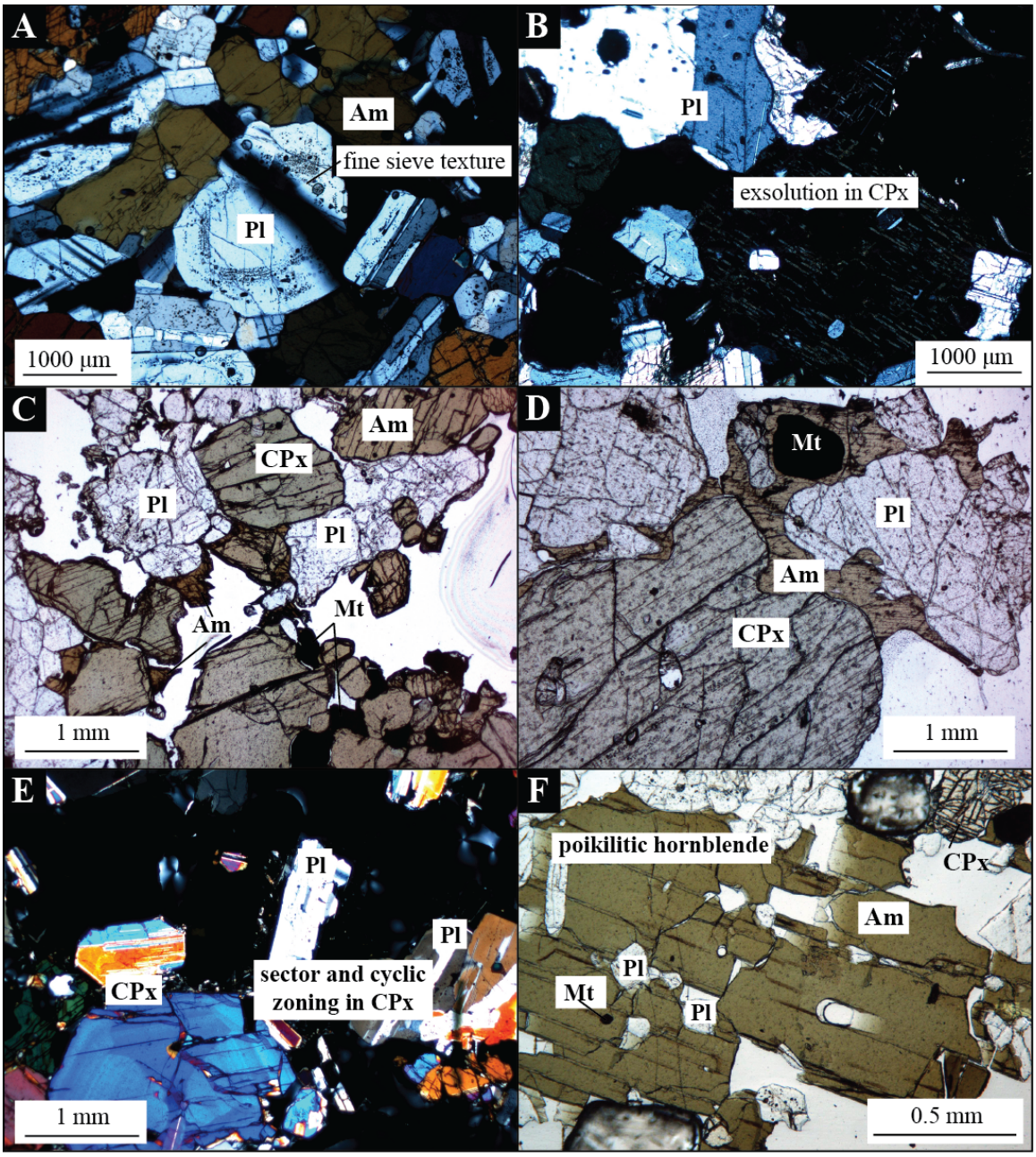

Figure 6. Mafic Suite Thin Section Photomicrographs
(A) Finely-sieved plagioclase surrounded by plagioclase and amphibole (XPL); (B) exsolved clinopyroxene and anhedral plagioclase (XPL); (C) equigranular texture with primary amphibole, clinopyroxene, and plagioclase, and secondary, interstitial magnetite and amphibole (PPL); (D) anhedral clinopyroxene and plagioclase with interstitial amphibole (PPL); (E) cyclic and sector zoned clinopyroxene in equigranular gabbro (XPL); (F) poikilitic amphibole with plagioclase and magnetite inclusions (PPL). Abbreviations: Pl = plagioclase, Am = amphibole, CPx = clinopyroxene, Mt = magnetite, XPL = cross polarized transmitted light photomicrograph, and PPL = plane polarized transmitted light photomicrograph

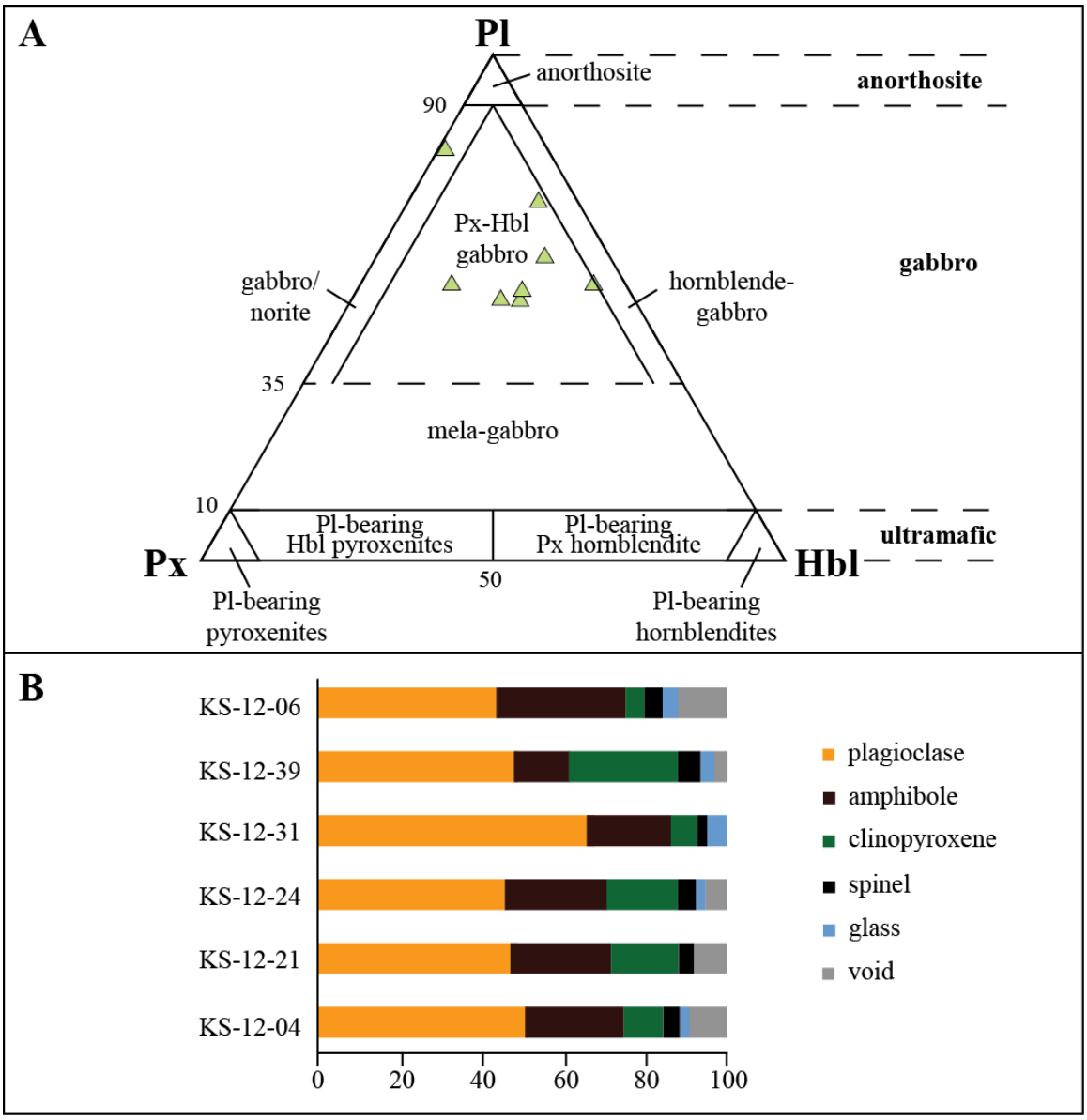

Figure 7. Mineral Modes for Mafic Enclaves
(A) Gabbroic samples are classified using the Streckeisen (1974) plagioclase-pyroxene-hornblende ternary diagram. According to this classification scheme, seven of eight mafic enclaves are clinopyroxene-hornblende gabbro and one is a gabbro. (B) Modal analyses for the gabbroic enclaves show that amphibole constitutes much less than half of the mineral makeup at only 5–20%. Plagioclase, on the other hand, accounts for >50% of the mineralogy. Abbreviations: See Fig. 6, Px = orthopyroxene + clinopyroxene

Table 4. Modal Analyses
I counted 1000 points per sample to estimate modal mineral percentages in 11 samples. Abbreviations: See Fig. 6, Sp = spinel (ultramafic) / magnetite (mafic), Gl = glass. Rock types are from the ternary diagrams shown in Figs. 7 and 10. Units are expressed in terms of volume percent (sum to 100%)

Sample	**KS-12-04b[c]**	**KS-12-11**	**KS-12-13**	**KS-12-21**	**KS-12-22**	**KS-12-24**
Rock Type	**gabbro**	**olivine - clinopyroxenite**	**clinopyroxenite**	**gabbro**	**wehrlite**	**gabbro**
Pl	51	0	0	47	0	46
Am	24	11	14	25	2	25
CPx	10	47	74	17	33	17
Ol	0	39	1	0	64	0
Sp	4	0	0	4	2	5
Gl	2	0	0	0	0	2
Void	9	3	12	8	1	5

Sample	**KS-12-31**	**KS-12-33**	**KS-12-34**	**KS-12-39**	**KS-12-06**
Rock Type	**gabbro**	**olivine - clinopyroxenite**	**wehrlite**	**gabbro**	**gabbro**
Pl	66	0	0	48	44
Am	21	0	2	14	32
CPx	7	72	15	27	5
Ol	0	27	69	0	0
Sp	2	0	1	6	4
Gl	5	0	0	3	4
Void	0	1	13	3	12

4.3 Ultramafic Suite Textures and Names

The ultramafic enclaves are medium-grained, granular, and moderately friable. They lack an outer rim of host material (Fig. 8A, B, and D). Hand samples are black, dark green, and light green based on proportions of light green olivine and dark green clinopyroxene (Fig. 8). The samples that appear black are actually green, and have layering that is only visible on a cut surface (Fig. 8A and B). This layering is made of varying ratios of pyroxene to olivine (Fig. 8B). The grain size among layers is uniform, and the minerals in both layered and non-layered samples are euhedral to subhedral.

The ultramafic enclaves are composed mainly of olivine and clinopyroxene, with minor spinel, secondary amphibole, and rare plagioclase. All pyroxene in the samples is clinopyroxene, which occurs as subhedral to anhedral grains with spinel inclusions (Fig. 9A–C). Olivine grains are rounded, granular, and do not show signs of strain in thin section (Fig. 9B). Clinopyroxene only rarely displays very fine exsolution lamellae or sector zoning (Fig. 9D). Cyclic zoning is not present in either clinopyroxene or olivine. Spinel is an accessory phase in both olivine and clinopyroxene grains (Fig. 9E). No exsolution is seen in spinel under reflected light microscopy (Fig. 9F). Amphibole is present in clinopyroxene-rich samples and is restricted to interstices between clinopyroxene and olivine (Fig. 9A, C, & E). Plagioclase is present only as a rare accessory phase in clinopyroxene-rich enclaves.

I assigned names to the ultramafic enclaves by plotting percentage of mineral present on the olivine-orthopyroxene-clinopyroxene ternary diagram of Streckeisen (1974) (Table 4, Fig. 10). I chose this ternary diagram rather than the olivine-pyroxene-hornblende ternary because in my samples, amphibole is present only as a secondary phase. The ultramafic samples include two rock type groups: peridotite and pyroxenite (Figure 10A). The peridotite samples are wehrlites, with 50–90% olivine and <50% clinopyroxene (Fig. 10A). The pyroxenite samples are olivine-clinopyroxenites with 50–90% clinopyroxene and <50% olivine, and clinopyroxenites with >90% clinopyroxene.

The abundances of clinopyroxene and olivine in the ultramafic samples fall along a continuum from wehrlite to clinopyroxenite (Figure 10A).

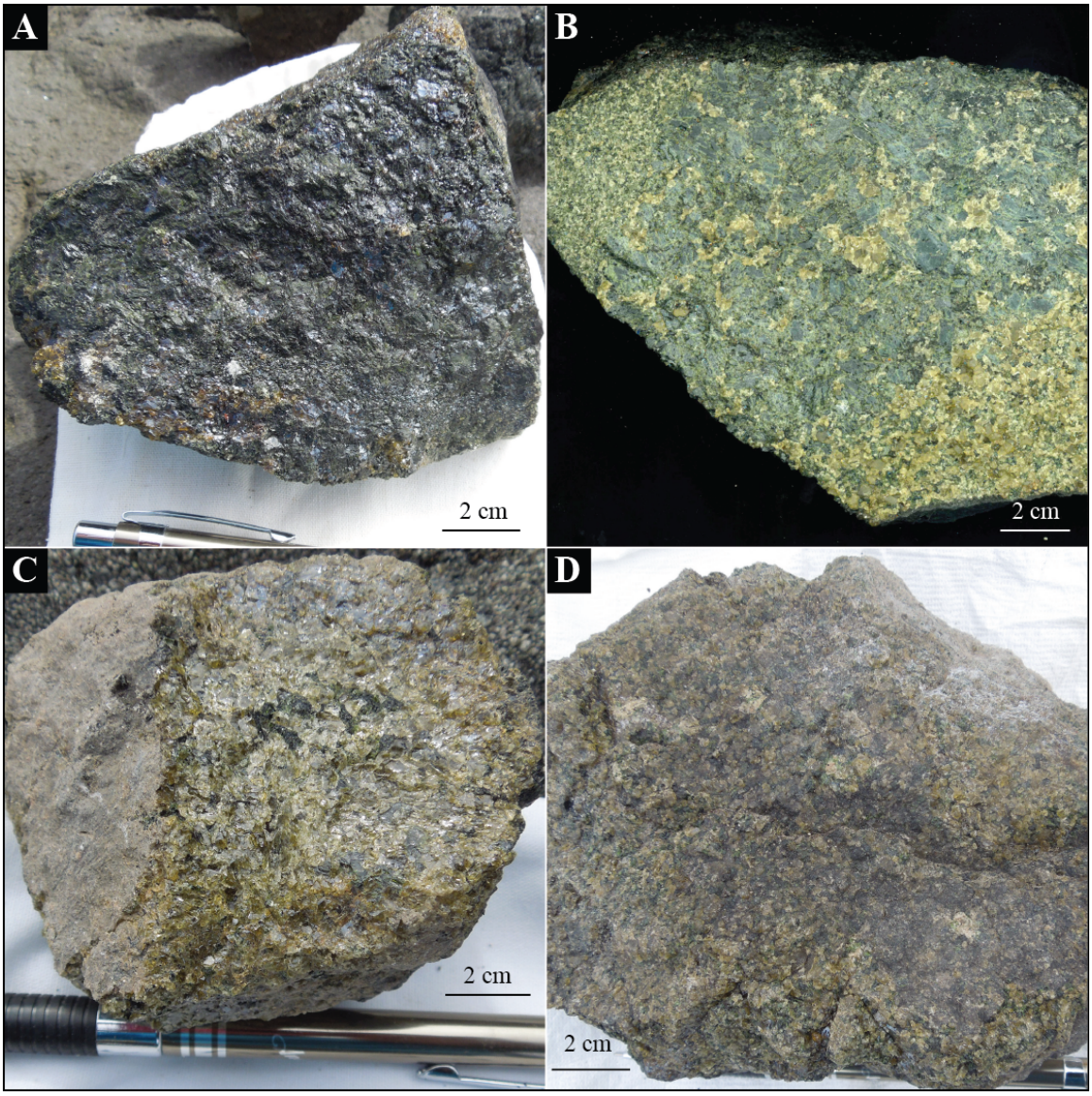

Figure 8. Ultramafic Suite Hand Samples
These photos show the range in textures and compositions of Kasatochi ultramafic enclaves. (A) Hand sample of coarse-grained clinopyroxenite is the same as pictured in (B) as a scan of a polished slab. (B) Shows modal layering of clinopyroxenite (dark green) and olivine-clinopyroxenite (lighter, pistachio green). (C) Medium grained, isotropic, granular peridotite; and (D) medium grained peridotite with a darker weathered surface.

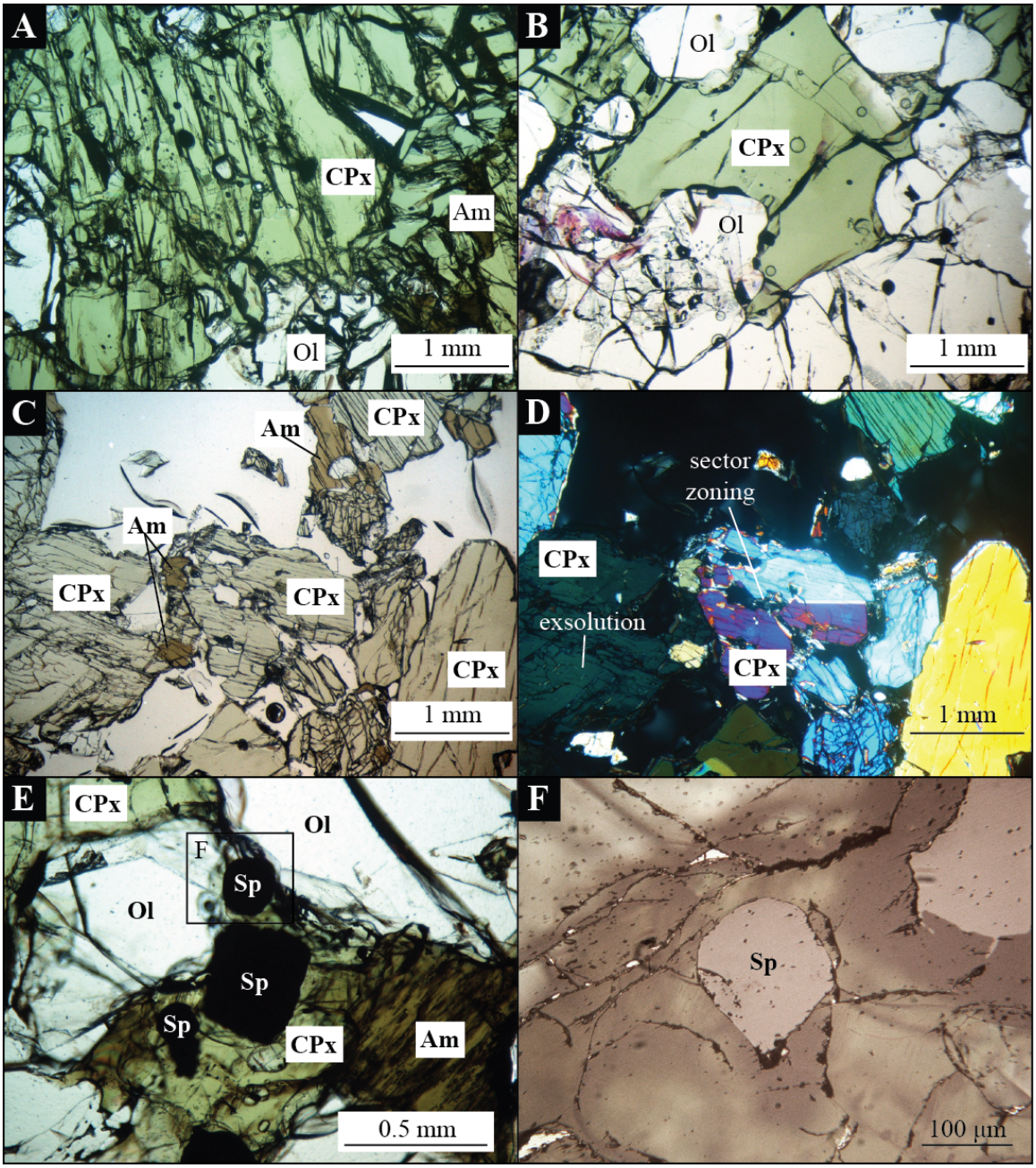

Figure 9. Ultramafic Suite Thin Section Photomicrographs
(A) Clinopyroxene and interstitial amphibole in wehrlite(PPL); (B) olivine clinopyroxenite with anhedral clinopyroxene surrounded by euhedral, rounded olivine (PPL); (C) clinopyroxenite composed of subhedral clinopyroxene with minor olivine and interstitial amphibole (PPL); (D) the clinopyroxene in this olivine clinopyroxenite is both sector zoned and finely exsolved (XPL); (E) olivine clinopyroxenite with spinel in clinopyroxene (PPL); (F) close-up of spinel in (E) that has moderate reflectivity and does not show any evidence of exsolution (RL). Abbreviations as in Fig. 6 and Table 4; RL = reflected light.

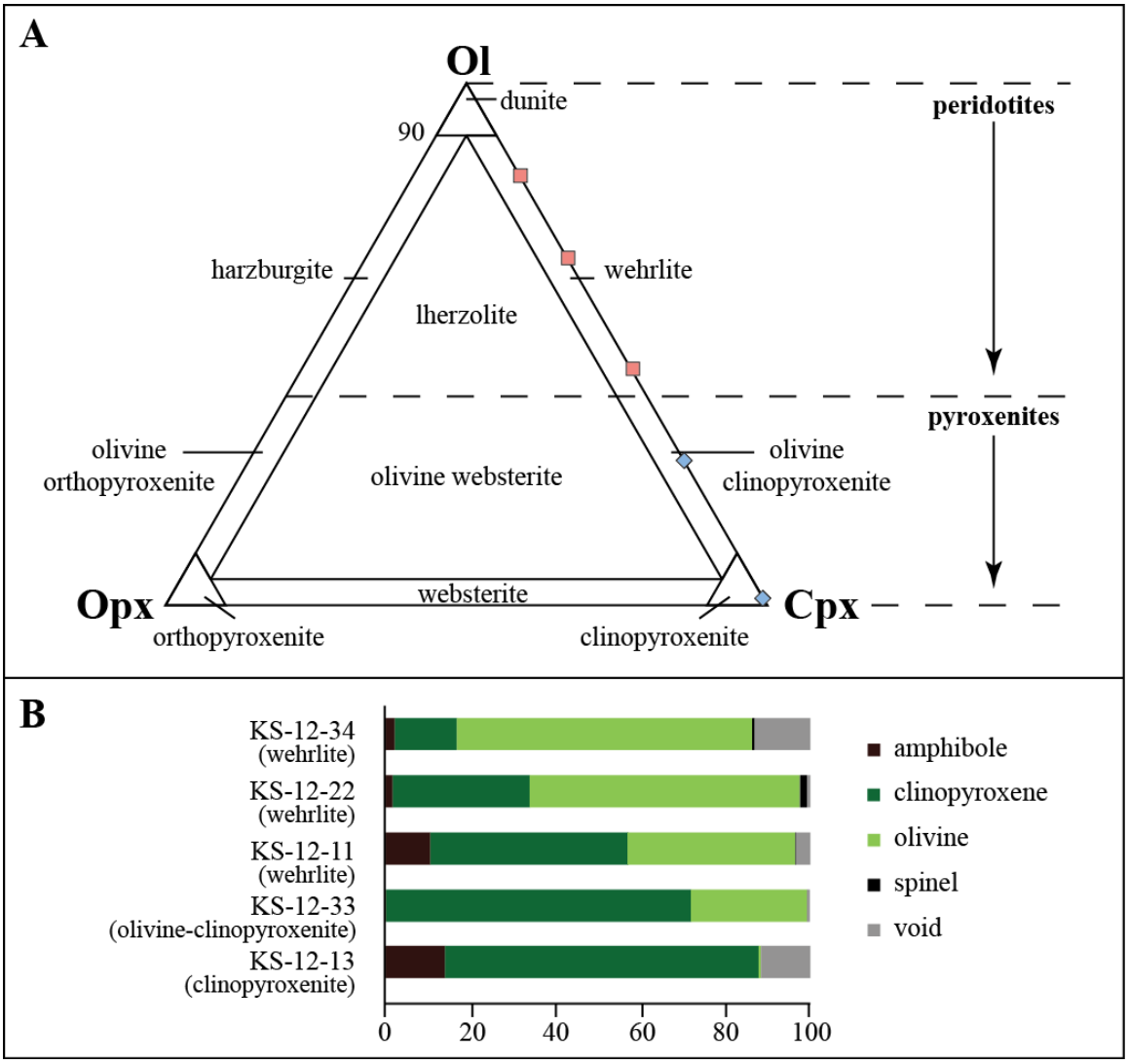

Figure 10. Mineral Modes for Ultramafic Enclaves
(A) The olivine-orthopyroxene-clinopyroxene ternary is the most commonly used ternary to describe ultramafic igneous rocks (Streckeisen, 1974). For the five samples measured, three are wehrlite, having <10% orthopyroxene and olivine > clinopyroxene, and two are clinopyroxenites (one olivine clinopyroxenite) having <10% orthopyroxene and clinopyroxene > olivine. (B) Results for mineral modal analyses for pyroxenite and peridotite. Ol = olivine, Opx = orthopyroxene, Cpx = clinopyroxene

4.4 Whole-Rock Composition

I used WD-XRF to measure major- and trace- element compositions in fused glass discs of six gabbros, four pyroxenites, three peridotites, and one anorthosite, as described in section 3.3. All results are shown in Table 5 and Supplementary File 1, with major elements reported as weight percent oxides (wt.%) and trace elements as parts per million (ppm). I used a routine set up with the help of M. Sliwinski in the advanced XRF class offered at UAF in spring 2013.

4.5 Whole-Rock Compositions of Gabbroic Enclaves

Major elements of the gabbroic enclaves are fairly uniform, and have silica contents that range from 40.49–42.62 wt. % SiO_2 (Fig. 11). Fe_2O_3 content is 11–13 wt.% and MgO is 6–9 wt.%, yielding an FeO_t/MgO total of 1.25–2.0 that places these samples in the tholeiitic field (Fig. 12A; Gast, 1968). Despite low values of K_2O (0.11–0.14 wt.%), the gabbroic enclaves are medium-K (Fig. 12B). Other major element concentrations include 11–23 wt.% Al_2O_3, 14.5–15.5 wt.% CaO, and 0.9–1.1 wt.% TiO_2 (Fig.11, Table 5). Trace element measurements include Ni and Cr (ppm), which are compatible elements that are concentrated in rocks that form during early stages of magma crystallization (Gast, 1968). Their concentrations in the gabbro samples are generally low, with <50ppm Cr and Ni (Table 5, Fig. 13A). Sample KS-12-31 has higher Ni (260ppm Ni) and sample KS-12-24 has higher Cr (111 ppm Cr) than the rest of the samples. All mafic enclave samples have 398–500 ppm Sr, with the exception of KS-12-31, which has 899 ppm Sr (Fig. 13B).

4.6 Whole-Rock Compositions of Ultramafic Enclaves

As discussed in section 4.3, I distinguished two groups of ultramafic enclaves on the basis of modal mineralogy: peridotite (wehrlite) and pyroxenite (clinopyroxenite and olivine-clinopyroxenite). The major and trace element compositions of these two groups also form two distinct groups (Table 5, Fig. 11).

The silica content of the pyroxenites is 45–51 wt.% (Table 5). Other notable major elements in the pyroxenite samples include 2–6 wt.% Al_2O_3, 7–9 wt.% Fe_2O_3, 14–22 wt.% CaO, 16–28 wt.% MgO, and <1 wt.% TiO_2 (Table 5). Ca and Mg contents of the pyroxenites co-vary with changes in modal percentage of clinopyroxene and olivine: in samples with more olivine, there are higher MgO values, whereas samples with more clinopyroxene have more CaO. The FeO_t/MgO of <0.5 and SiO_2 >45 wt.% indicates that these samples are calc-alkaline (Fig. 12A). In addition, they are low-K with <0.5 wt.% K_2O (Fig. 12B). Trace element compositions also reflect the variation in mineral abundance. For example, both Ni and Cr are higher in the olivine-clinopyroxenite samples than in the clinopyroxenite (Table 5, Fig. 13A), with 1120–2511 ppm Cr and 150–500 ppm Ni.

In contrast, the silica content of the wehrlites is significantly lower than that of the pyroxenites, at 40–42 wt.% SiO_2. All major element oxides in the wehrlite samples are within 2 wt.% of one another and are distinct from the pyroxenites (Fig. 11). Aluminum is lower in the wehrlites than in the pyroxenites, at ~1.5 wt.% Al_2O_3, as is CaO at 2–4 wt.%. Iron and magnesium are considerably higher in the wehrlites at ~15 wt.% Fe_2O_3 and ~40 wt.% MgO (Fig. 11). TiO_2 is the same, at <1 wt.% for both sample types. Like the pyroxenite samples, FeO_t/MgO is <0.5, but because the wehrlites are ~40 wt.% SiO_2, they plot within the tholeiitic rather than the calc-alkaline compositional field (Fig. 12A). Alkalis (Na_2O and K_2O) are <1 wt. % (Table 5) and the samples are medium-K because of their low SiO_2 composition (Fig. 12B). Trace element compositions include Cr, which at 2076 and 2166 ppm for the two wehrlite samples overlaps the field for the pyroxenites, and Ni, which is significantly higher at 923 and 976 ppm (Fig. 13A).

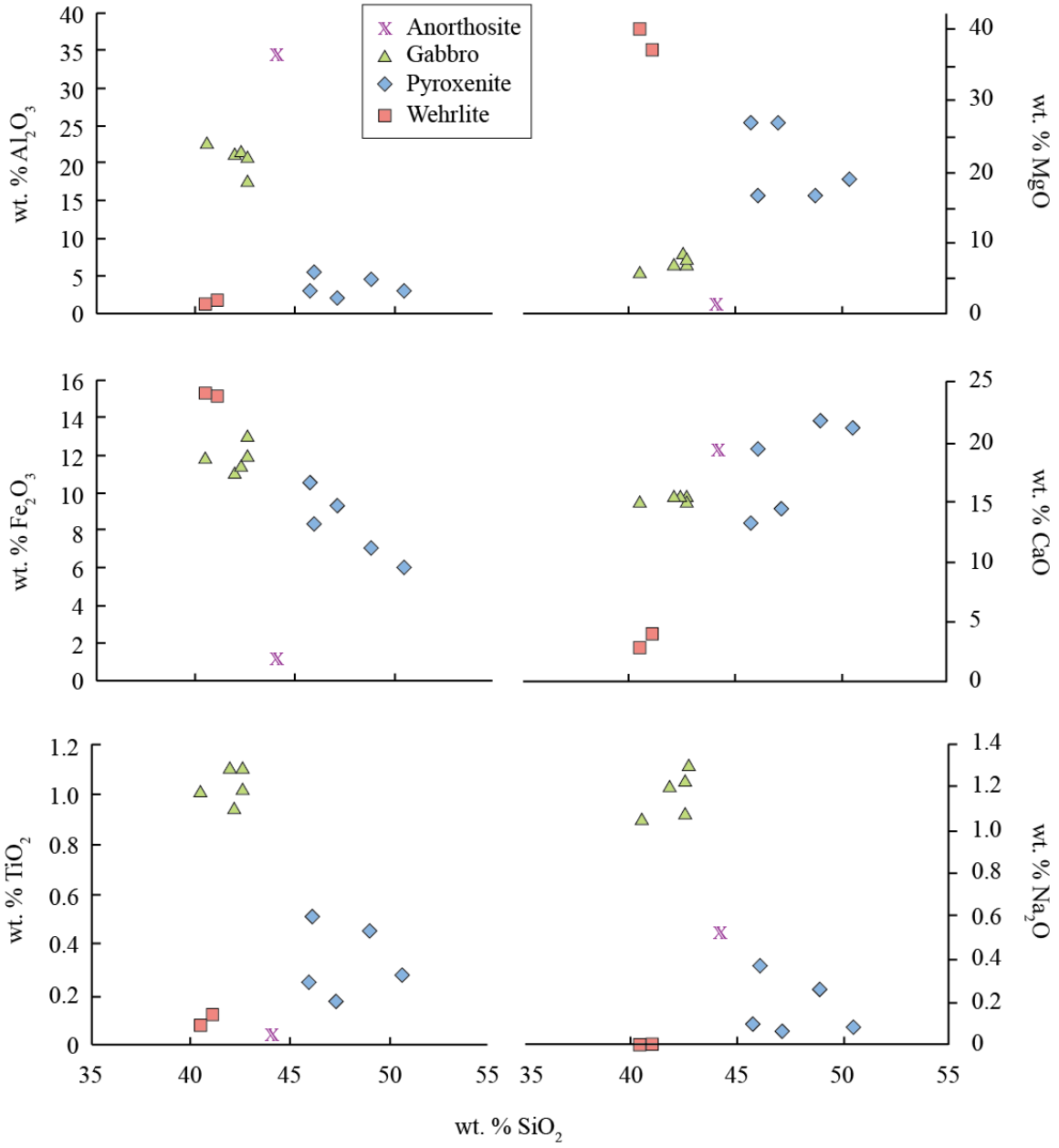

Figure 11. Harker Diagrams
Major element Harker diagrams for whole-rock compositions of Kasatochi enclaves. Mineral modes in wehrlite and pyroxenite (clinopyroxenite and olivine-clinopyroxenite) appear continuous (Fig. 10), but they have a compositional gap of 5–10 wt.% SiO_2. Gabbroic enclaves are within the same compositional range for wt.% SiO_2 as the pyroxenites, but do not overlap in other major elements. Wehrlite, pyroxenite, gabbro, and the anorthosite form distinct compositional groups.

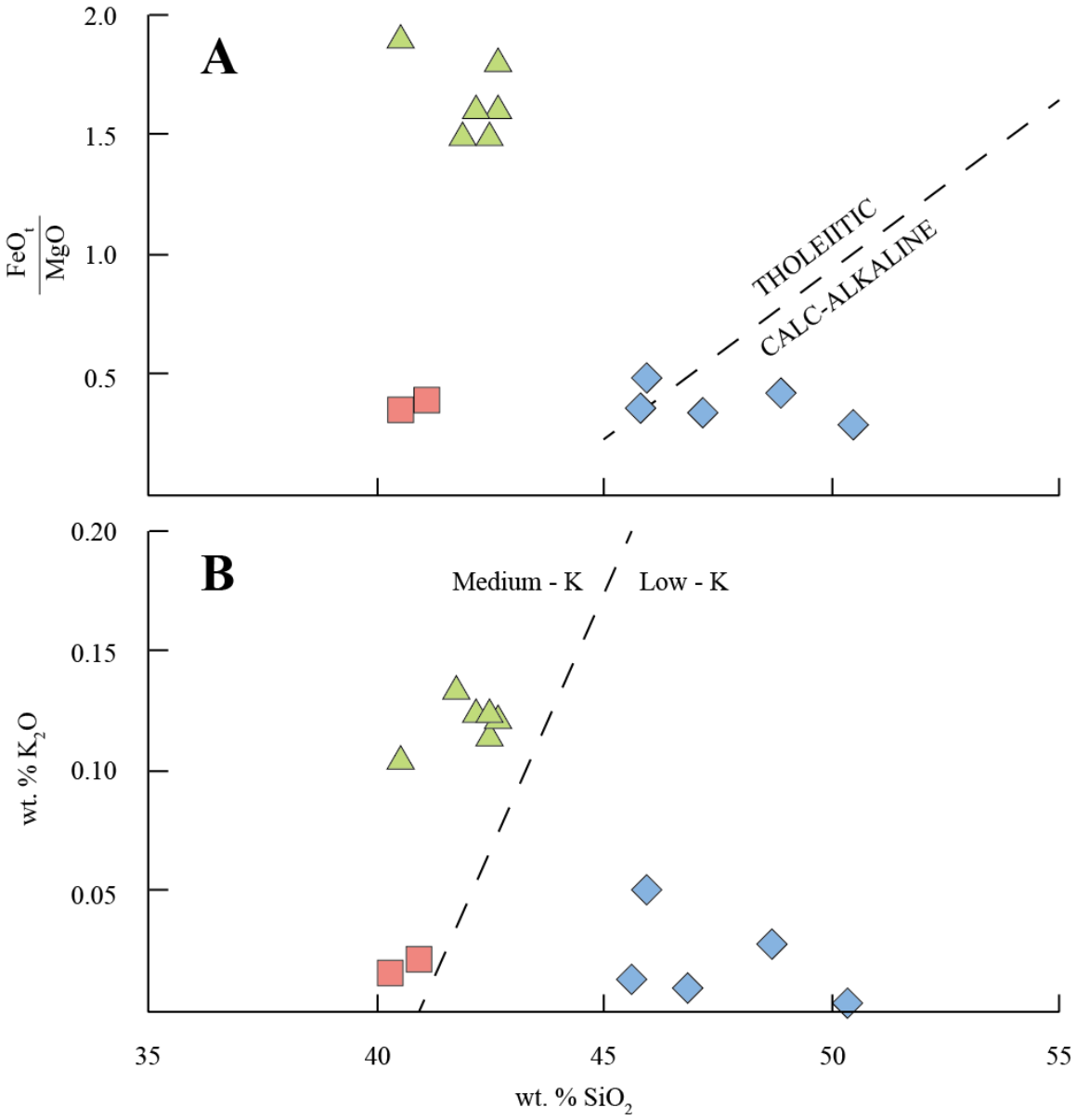

Figure 12. Whole-Rock Discrimination Diagrams
(A) Gabbros (green triangles) and wehrlites (red squares) plot in the tholeiitic field, whilc pyroxenites (blue diamonds) are calc-alkaline (fields from Gast, 1968). (B) The gabbro and wehrlite enclaves plot as "medium-K" rocks, whereas the clinopyroxenites plot as "low-K".

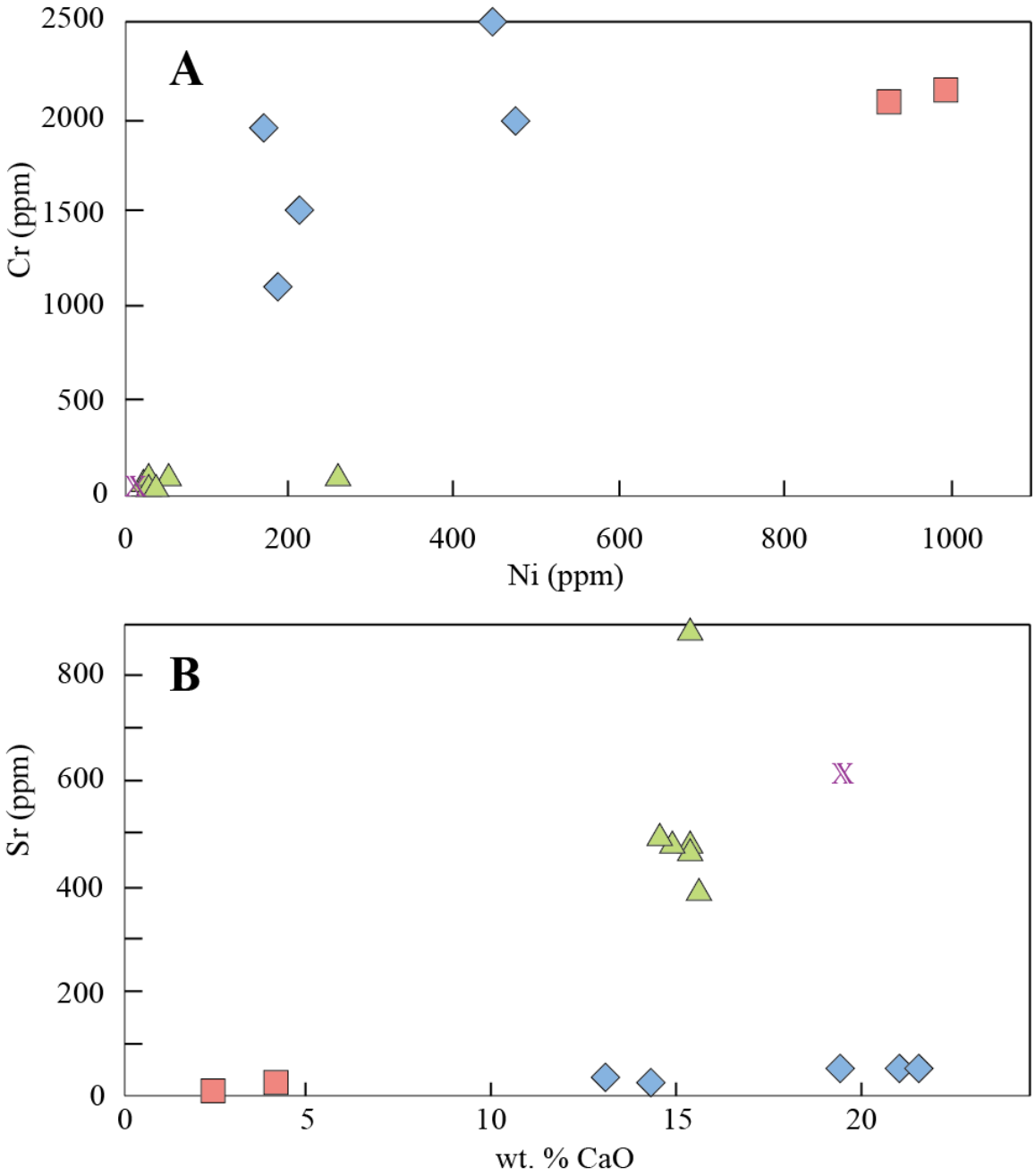

Figure 13. Whole-Rock Trace Element Compositions
(A) Cr is higher in the clinopyroxenites and wehrlites than in the gabbros, which have << 500 ppm Cr. Ni is highest in the wehrlites at ~1000 ppm, but is also higher than in the clinopyroxenite than in the gabbro, which is lower than ~250 ppm Ni. (B) Higher Sr in gabbro reflects the abundance of plagioclase relative to clinopyroxene. The overlap of wt.% CaO between gabbro and clinopyroxenite also reflects the presence of Ca-rich plagioclase in the gabbro, and of Ca-rich clinopyroxene in the clinopyroxenites (Green, 1980). Symbols are the same as in Fig. 11.

Table 5. Whole-Rock Compositions
Results from XRF analyses of fused glass discs for 14 ultramafic and mafic enclaves from Kasatochi and the standard BHVO-1 used as a working standard. <DL = below detection limit; *olivine clinopyroxenite; CRM = certified reference material

Sample	KS-12-04b[c]	KS-12-11	KS-12-12	KS-12-13	KS-12-19
Rock Type	gabbro	*pyroxenite	*pyroxenite	clinopyroxenite	anorthosite
Major elements (wt. % oxide)					
SiO_2	40.49	45.80	48.90	46.01	44.14
Al_2O_3	22.98	2.82	4.73	5.62	34.59
TiO_2	1.02	0.26	0.45	0.51	0.05
Fe_2O_3	11.89	10.53	7.08	8.30	1.03
MnO	0.11	0.17	0.13	0.14	0.01
CaO	15.37	13.27	21.50	19.41	19.34
MgO	6.18	27.32	16.35	16.79	1.11
K_2O	0.11	0.02	0.03	0.05	0.02
Na_2O	1.05	0.09	0.25	0.37	0.51
P_2O_5	0.01	0.01	0.00	0.01	0.01
Total	99.21	100.28	99.42	97.21	100.82
Trace elements (ppm)					
Ni	27	477	173	190	8
Cr	14	1996	1947	1120	7
V	491	140	250	270	19
Zr	21	6	11	12	15
Cu	243	13	29	37	14
Zn	58	50	29	34	6
Y	12	1	5	6	8
Ba	42	<DL	<DL	<DL	32
Rb	<DL	<DL	2	1	2
Sr	479	30	43	60	619

Table 5. (cont.)

Sample	KS-12-21	KS-12-22	KS-12-24	KS-12-31	KS-12-33
Rock Type	**gabbro**	**wehrlite**	**gabbro**	**gabbro**	***pyroxenite**
Major elements (wt. % oxide)					
SiO_2	42.62	40.48	42.52	41.99	47.15
Al_2O_3	21.01	1.32	17.80	21.49	2.10
TiO_2	1.04	0.09	1.11	1.11	0.18
Fe_2O_3	12.12	15.23	13.24	11.06	9.10
MnO	0.18	0.23	0.19	0.13	0.16
CaO	14.91	2.57	15.50	15.29	14.38
MgO	7.45	40.20	8.69	7.28	27.22
K_2O	0.12	0.02	0.12	0.14	0.01
Na_2O	1.24	<DL	1.10	1.21	0.06
P_2O_5	0.01	0.01	0.02	0.01	0.01
Total	100.69	100.14	100.26	99.70	100.34
Trace elements (ppm)					
Ni	36	997	55	260	453
Cr	43	2166	111	55	2511
V	428	58	497	374	109
Zr	29	3	25	53	8
Cu	29	16	78	326	19
Zn	74	82	73	104	44
Y	19	<DL	18	25	8
Ba	37	<DL	43	<DL	<DL
Rb	1	1	2	1	<DL
Sr	476	16	398	899	27

Table 5. (cont.)

Sample	KS-12-34	KS-12-39	KS-12-42	KS-12-06	BHVO-1
Rock Type	**wehrlite**	**gabbro**	***pyroxenite**	**gabbro**	**CRM**
Major elements (wt. % oxide)					
SiO_2	41.07	42.24	50.53	42.61	49.45
Al_2O_3	1.67	21.52	2.97	20.75	13.70
TiO_2	0.12	0.95	0.27	1.03	2.77
Fe_2O_3	15.12	11.39	6.03	12.96	12.26
MnO	0.23	0.16	0.11	0.19	0.17
CaO	4.12	15.27	20.96	14.69	11.46
MgO	37.92	7.09	19.49	7.20	7.14
K_2O	0.02	0.13	0.00	0.12	0.52
Na_2O	0.02	1.18	0.09	1.32	2.09
P_2O_5	0.01	0.02	0.01	0.02	0.27
Total	100.30	99.95	100.45	100.89	99.83
Trace elements (ppm)					
Ni	923	42	216	40	127
Cr	2076	50	1516	48	267
V	67	369	163	430	357
Zr	5	28	11	33	182
Cu	31	52	15	31	141
Zn	82	65	28	82	101
Y	<DL	18	2	24	28
Ba	<DL	41	<DL	44	142
Rb	2	1	1	2	12
Sr	22	477	37	499	406

4.7 Mineral Analyses

All mineral analyses were done by EPMA, as described in Section 3.7. I analyzed the following by WDS: five amphiboles from two gabbros and three ultramafic samples, three plagioclases from two gabbros and one ultramafic sample, four clinopyroxenes (ultramafic), two olivines (ultramafic), and two oxides (ultramafic). I also analyzed interstitial glass in one gabbro using EDS. All the mineral analyses are available in Supplementary File 1. Mineral recalculations referred to in Section 4.7 are available in Supplementary File 2.

4.7.1 Glass in Gabbroic Enclaves

Crystals within the glass of gabbroic sample KS-12-07 are only visible in BSE (Fig. 4). This image was combined with electron dispersive spectrometry (EDS) to identify crystal compositions (Fig. 4), which are clinopyroxene, plagioclase, and an Fe-Ti oxide (ilmenite). In addition to these three minerals is a small amount of basaltic glass also identified using EDS.

4.7.2 Plagioclase

Ca-rich plagioclase feldspar occurs in all samples except for the wehrlites (Table 6). The 18 crystals analyzed have compositions of $An_{91–96}$. An-content in plagioclase from the clinopyroxenite sample is slightly higher (An_{95}) than for the gabbroic enclaves ($An_{91–93}$). There is little to no variation in An-content between cores and rims in any of the crystals probed (Table 6; Fig. 14), suggesting an absence of zoning, which is supported by thin section analysis (Fig. 6). The core and rim values are not compositionally discrete and have a roughly 1:1 relationship, within error (Fig. 14). Finely sieved plagioclase was not analyzed. The scatter in An-content can be attributed to analytical error (~6 % relative difference between analyzed and published standard values). Measured values for K and Na are low: <0.5 wt.% Na_2O and only 0.1–0.2 wt.% K_2O in plagioclase from any samples (Table 6).

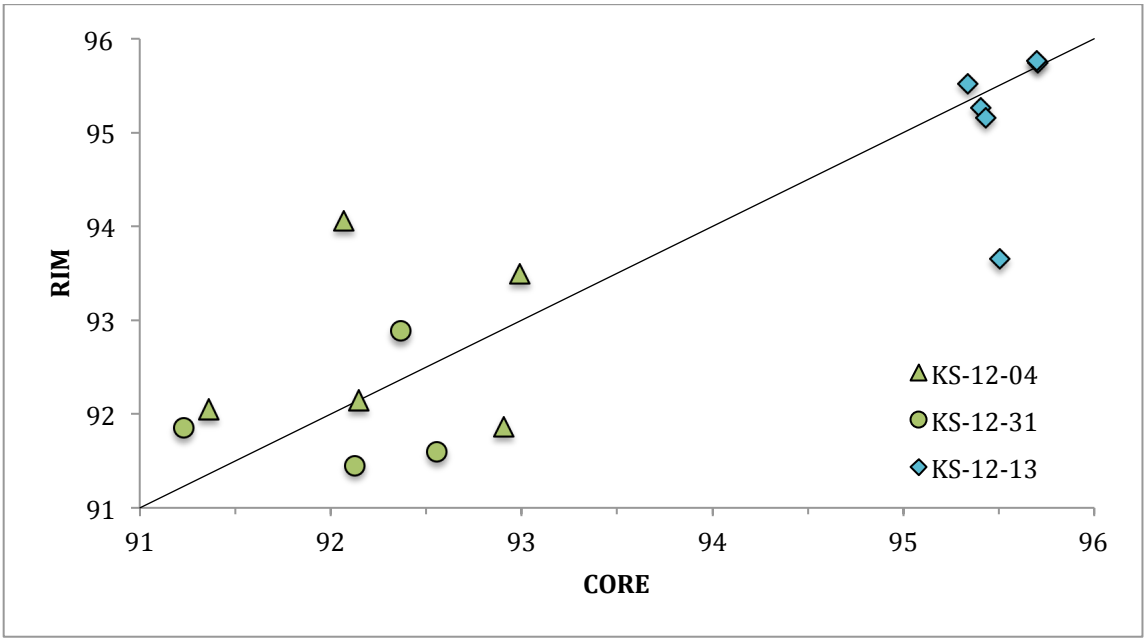

Figure 14. An-Content of Rims and Cores of Plagioclase
Anorthite composition of rim vs. core of multiple plagioclase crystals: KS-12-04 and KS-12-31 are gabbro, and KS-21-12-13 is clinopyroxenite. There is a roughly 1:1 correlation (within error) between An-content of cores and rims in plagioclase from either rock type. Plagioclase crystals in clinopyroxenite all have a higher in An-content than gabbros (An > 95).

Table 6. Plagioclase EPMA Results
Error reported to 1-σ. n-value = number of points analyzed per grain. An = 100 * Ca/(Ca+Na+K)

Sample	**KS-12-13**		**KS-12-13**		**KS-12-13**		**KS-12-13**		**KS-12-13**	
Rock Type	Clinopyroxenite		Clinopyroxenite		Clinopyroxenite		Clinopyroxenite		Clinopyroxenite	
grain	PL1		PL1		PL2		PL2		PL3	
location	core		rim		core		rim		core	
n=	5	*1-σ*	4	*1-σ*	4	*1-σ*	4	*1-σ*	4	*1-σ*
SiO_2	43.56	*0.09*	43.58	*0.07*	43.42	*0.21*	44.22	*0.18*	43.65	*0.08*
Al_2O_3	35.93	*0.13*	35.98	*0.19*	35.65	*0.23*	35.46	*0.11*	35.82	*0.05*
FeO	0.42	*0.02*	0.40	*0.03*	0.40	*0.01*	0.47	*0.01*	0.43	*0.02*
CaO	19.04	*0.08*	19.07	*0.08*	19.03	*0.08*	18.63	*0.11*	19.01	*0.01*
Na_2O	0.46	*0.01*	0.46	*0.01*	0.49	*0.01*	0.69	*0.06*	0.50	*0.01*
K_2O	0.02	*0.00*	0.01	*0.01*	0.01	*0.00*	0.01	*0.00*	0.01	*0.00*
Total	99.42		99.51		98.99		99.48		99.42	
An	95.7		95.7		95.5		93.7		95.4	

Sample	**KS-12-13**		**KS-12-13**		**KS-12-13**		**KS-12-13**		**KS-12-13**	
Rock Type	Clinopyroxenite		Clinopyroxenite		Clinopyroxenite		Clinopyroxenite		Clinopyroxenite	
grain	PL3		PL4		PL4		PL5		PL5	
location	rim		core		rim		core		rim	
n=	4	*1-σ*	4	*1-σ*	3	*1-σ*	4	*1-σ*	2	*1-σ*
SiO_2	43.57	*0.25*	43.53	*0.01*	43.42	*0.02*	43.83	*0.08*	43.72	*0.01*
Al_2O_3	35.79	*0.16*	35.75	*0.03*	35.69	*0.02*	35.91	*0.03*	35.92	*0.01*
FeO	0.41	*0.01*	0.41	*0.01*	0.39	*0.01*	0.42	*0.02*	0.41	*0.01*
CaO	18.92	*0.03*	19.12	*0.02*	18.88	*0.06*	18.90	*0.07*	18.96	*0.00*
Na_2O	0.51	*0.01*	0.50	*0.02*	0.52	*0.01*	0.50	*0.01*	0.48	*0.00*
K_2O	0.01	*0.00*	0.01	*0.00*	0.02	*0.00*	0.01	*0.00*	0.02	*0.01*
Total	99.21		99.31		98.92		99.58		99.50	
An	95.3		95.4		95.2		95.3		95.5	

Table 6. (cont.)

Sample	**KS-12-13**		**KS-12-13**		**KS-12-13**		**KS-12-13**		**KS-12-31**	
Rock Type	Clinopyroxenite		Clinopyroxenite		Clinopyroxenite		Clinopyroxenite		Gabbro	
grain	PL6		PL6		PL7		PL7		PL1	
location	core		rim		core		rim		core	
n=	4	*1-σ*	2	*1-σ*	5	*1-σ*	3	*1-σ*	3	*1-σ*
SiO_2	43.48	*0.08*	49.03	*0.72*	43.59	*0.05*	43.72	*0.07*	44.84	*0.18*
Al_2O_3	35.66	*0.07*	30.94	*0.00*	35.97	*0.03*	36.17	*0.07*	35.51	*0.20*
FeO	0.39	*0.01*	0.66	*0.03*	0.40	*0.01*	0.41	*0.00*	0.56	*0.02*
CaO	19.02	*0.03*	14.43	*0.27*	19.10	*0.02*	19.07	*0.05*	18.52	*0.18*
Na_2O	0.49	*0.01*	3.06	*0.07*	0.47	*0.01*	0.46	*0.01*	0.90	*0.12*
K_2O	0.01	*0.01*	0.11	*0.01*	0.01	*0.00*	0.01	*0.00*	0.03	*0.00*
Total	99.05		98.23		99.53		99.85		100.33	
An	95.5		71.8		95.7		95.8		91.8	

Sample	**KS-12-31**		**KS-12-31**		**KS-12-31**		**KS-12-31**		**KS-12-31**	
Rock Type	Gabbro		Gabbro		Gabbro		Gabbro		Gabbro	
grain	PL1		PL2		PL2		PL3		PL3	
location	core		core		rim		core		rim	
n=	3	*1-σ*	3	*1-σ*	3	*1-σ*	4	*1-σ*	4	*1-σ*
SiO_2	44.84	*0.18*	44.59	*0.20*	44.53	*0.19*	44.87	*0.15*	44.65	*0.12*
Al_2O_3	35.51	*0.20*	35.62	*0.13*	35.20	*0.17*	35.69	*0.03*	35.65	*0.13*
FeO	0.56	*0.02*	0.51	*0.01*	0.54	*0.01*	0.50	*0.01*	0.47	*0.02*
CaO	18.52	*0.18*	18.69	*0.02*	18.39	*0.06*	18.66	*0.08*	18.70	*0.06*
Na_2O	0.90	*0.12*	0.82	*0.02*	0.92	*0.07*	0.84	*0.01*	0.78	*0.02*
K_2O	0.03	*0.00*	0.01	*0.01*	0.03	*0.00*	0.01	*0.00*	0.01	*0.00*
Total	100.33		100.23		99.60		100.57		100.27	
An	91.8		92.6		91.6		92.4		92.9	

Table 6. (cont.)

Sample	**KS-12-31**		**KS-12-31**		**KS-12-31**		**KS-12-31**		**KS-12-31**	
Rock Type	Gabbro		Gabbro		Gabbro		Gabbro		Gabbro	
grain	PL4		PL4		PL5		PL5		PL6	
location	core		rim		core		rim		core	
n=	4	*1-σ*	4	*1-σ*	4	*1-σ*	2	*1-σ*	3	*1-σ*
SiO_2	44.86	*0.22*	44.79	*0.30*	44.77	*0.06*	44.78	*0.01*	44.41	*0.13*
Al_2O_3	35.36	*0.17*	35.48	*0.17*	35.69	*0.10*	35.35	*0.05*	35.37	*0.19*
FeO	0.51	*0.01*	0.52	*0.02*	0.53	*0.02*	0.65	*0.03*	0.53	*0.01*
CaO	18.46	*0.05*	18.48	*0.12*	18.52	*0.01*	18.44	*0.11*	18.61	*0.06*
Na_2O	0.97	*0.02*	0.89	*0.05*	0.86	*0.01*	0.95	*0.02*	0.81	*0.01*
K_2O	0.02	*0.01*	0.02	*0.01*	0.02	*0.00*	0.01	*0.00*	0.01	*0.00*
Total	100.18		100.18		100.40		100.18		99.74	
An	91.2		91.8		92.1		91.4		92.6	

Sample	**KS-12-31**		**KS-12-04**		**KS-12-04**		**KS-12-04**		**KS-12-04**	
Rock Type	Gabbro		Gabbro		Gabbro		Gabbro		Gabbro	
grain	PL6		PL1		PL1		PL2		PL2	
location	rim		core		rim		core		rim	
n=	3	*1-σ*	4	*1-σ*	4	*1-σ*	4	*1-σ*	4	*1-σ*
SiO_2	45.34	*0.31*	44.42	*0.27*	44.76	*0.21*	44.64	*0.10*	44.67	*0.07*
Al_2O_3	35.27	*0.28*	35.54	*0.20*	35.37	*0.26*	35.51	*0.09*	35.31	*0.09*
FeO	0.55	*0.01*	0.54	*0.02*	0.53	*0.01*	0.55	*0.01*	0.53	*0.01*
CaO	18.25	*0.24*	18.58	*0.08*	18.36	*0.25*	18.56	*0.04*	18.51	*0.06*
Na_2O	1.05	*0.13*	0.77	*0.04*	0.88	*0.11*	0.86	*0.01*	0.86	*0.02*
K_2O	0.02	*0.01*	0.02	*0.00*	0.02	*0.01*	0.02	*0.00*	0.02	*0.00*
Total	100.48		99.86		99.93		100.14		99.91	
An	90.4		92.9		91.9		92.2		92.2	

Table 6. (cont.)

Sample	**KS-12-04**		**KS-12-04**		**KS-12-04**	
Rock Type	Gabbro		Gabbro		Gabbro	
grain	PL3		PL3		PL4	
location	core		rim		core	
n=	3	*1-σ*	3	*1-σ*	4	*1-σ*
SiO_2	44.62	*0.09*	44.79	*0.24*	44.87	*0.06*
Al_2O_3	35.21	*0.07*	35.43	*0.18*	35.52	*0.06*
FeO	0.54	*0.02*	0.55	*0.02*	0.56	*0.01*
CaO	18.28	*0.03*	18.49	*0.11*	18.55	*0.03*
Na_2O	0.94	*0.02*	0.87	*0.04*	0.87	*0.02*
K_2O	0.03	*0.00*	0.02	*0.00*	0.02	*0.00*
Total	99.61		100.14		100.38	
An	91.4		92.1		92.1	

Sample	**KS-12-04**		**KS-12-04**		**KS-12-04**	
Rock Type	Gabbro		Gabbro		Gabbro	
grain	PL4		PL5		PL5	
location	rim		core		rim	
n=	4	*1-σ*	4	*1-σ*	5	*1-σ*
SiO_2	44.32	*0.09*	44.30	*0.17*	44.31	*0.10*
Al_2O_3	35.86	*0.06*	35.47	*0.12*	35.57	*0.03*
FeO	0.53	*0.00*	0.51	*0.01*	0.49	*0.01*
CaO	18.84	*0.05*	18.59	*0.08*	18.73	*0.02*
Na_2O	0.65	*0.02*	0.77	*0.04*	0.71	*0.01*
K_2O	0.02	*0.01*	0.01	*0.00*	0.02	*0.00*
Total	100.22		99.65		99.84	
An	94.1		93.0		93.5	

4.7.3 Amphibole

Amphiboles from two gabbroic enclaves, two pyroxenites, and a wehrlite are compositionally quite similar to one another (Table 7), all falling into the category of calcic amphiboles commonly known as hornblende (Leake et al., 1997). The pargasitic variety of hornblende is defined by $Ca > 1.50$, $(Na + K)_A > 0.5$, $0.5 < Na < 1.50$, and $Fe^{3+} < {}^{iv}Al$ (Fig. 15). I recalculated amphibole compositions based on 13 cations per formula unit (pfu) and 23 oxygen atoms pfu (Supplemental File 2) based on the methods of Leake and others (1997). A plot of the number of Si ions pfu vs. Mg# (Mg/ (Mg+Fe) indicates that all 25 analyzed amphiboles are pargasite, and they cluster in the high-Mg# end of the field. I recalculated the amphibole compositions in terms of Fe, based on EPMA analyses, and found that the ultramafic samples in general crystallized amphibole at a lower oxidation state than the mafic enclaves did, with the exception of one wehrlite sample (Fig. 16).

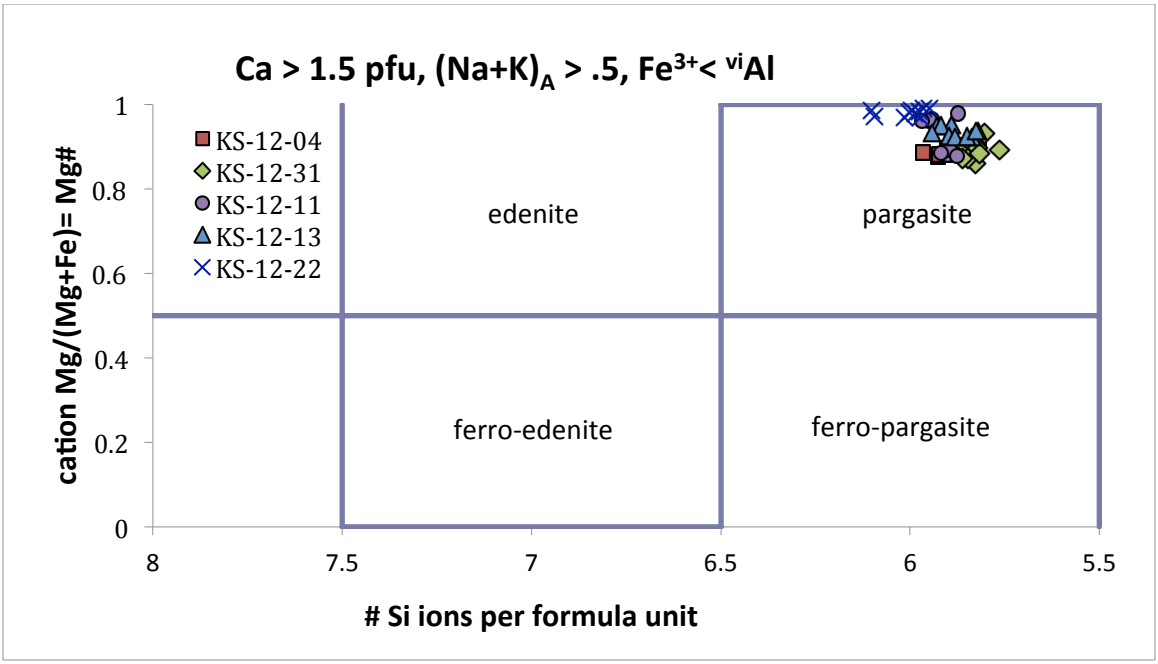

Figure 15. Amphibole Classification Diagram
All amphiboles, from both mafic and ultramafic samples, are calcic, pargasitic hornblendes based on calculated compositions (classification scheme of Leake et al. (1997), with Ca > 1.5 pfu, $(Na + K)_A > 0.5$, and $Fe^{3+} > {}^{iv}Al$). Samples are: KS-12-04 = gabbro; KS-12-31 = gabbro; KS-12-11 = olivine clinopyroxenite; KS-12-13 = clinopyroxenite; and KS-12-22 = wehrlite

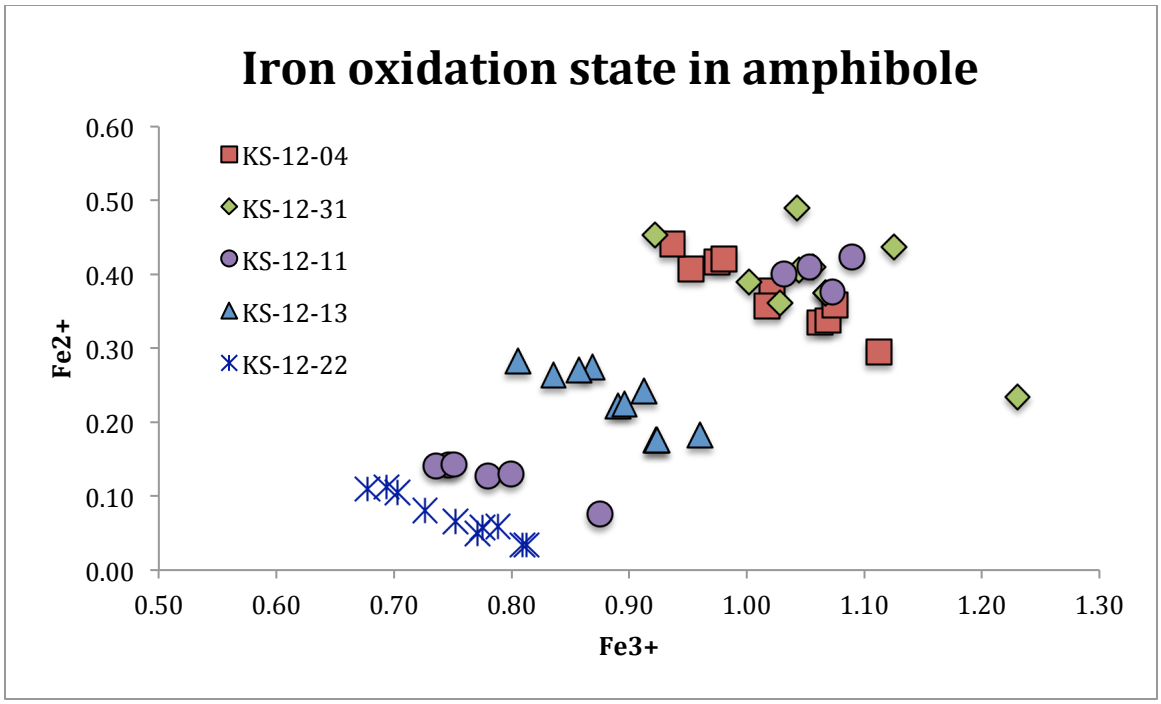

Figure 16. Iron Oxidation State in Amphibole
Recalculated Fe^{3+} and Fe^{2+} for amphiboles—based on stoichiometry and using methods of Leake et al. (1997)—is higher for gabbros than for the ultramafic samples, except for one werhrlite sample, which overlaps with the gabbros. Samples are: KS-12-04 = gabbro; KS-12-31 = gabbro; KS-12-11 = olivine clinopyroxenite; KS-12-13 = clinopyroxenite; and KS-12-22 = wehrlite

Table 7. Amphibole EPMA Results
Error reported to 1-σ. n-value = number of points analyzed per grain. Names based on the classification scheme of Leake and others (1997). OL-CPX = olivine clinopyroxenite

Sample	**KS-12-04**		**KS-12-04**		**KS-12-04**		**KS-12-04**	
Rock Type	Gabbro		Gabbro		Gabbro		Gabbro	
grain	am1	core	am1	rim	am2	core	am2	rim
n=	7	*1-σ*	3	*1-σ*	6	*1-σ*	5	*1-σ*
SiO_2	41.81	*0.69*	40.75	*0.13*	41.46	*0.92*	41.32	*0.39*
Al_2O_3	13.61	*0.57*	14.13	*0.12*	14.09	*0.55*	13.89	*0.42*
CaO	11.91	*0.09*	11.97	*0.11*	11.90	*0.09*	11.91	*0.07*
MgO	14.86	*0.38*	14.80	*0.08*	14.55	*0.71*	14.92	*0.18*
FeO	11.40	*0.49*	11.68	*0.36*	11.53	*0.40*	11.81	*0.36*
K_2O	0.34	*0.01*	0.35	*0.02*	0.35	*0.02*	0.34	*0.02*
Na_2O	2.67	*0.04*	2.78	*0.03*	2.70	*0.17*	2.76	*0.08*
TiO_2	1.81	*0.08*	1.82	*0.08*	1.84	*0.15*	1.75	*0.13*
MnO	0.17	*0.04*	0.18	*0.07*	0.14	*0.02*	0.16	*0.02*
Cl	0.02	*0.01*	0.02	*0.00*	0.03	*0.01*	0.02	*0.00*
Total	98.62		98.50		98.58		98.88	
Name	Pargasite		Pargasite		Pargasite		Pargasite	
Mg#	0.89		0.90		0.88		0.90	

Sample	**KS-12-04**		**KS-12-04**		**KS-12-04**		**KS-12-04**	
Rock Type	Gabbro		Gabbro		Gabbro		Gabbro	
grain	am3	core	am3	rim	am4	core	am4	rim
n=	4	*1-σ*	4	*1-σ*	2	*1-σ*	4	*1-σ*
SiO_2	41.69	*0.24*	41.17	*0.41*	40.54	*0.24*	41.04	*0.42*
Al_2O_3	14.07	*0.08*	13.70	*0.15*	13.98	*0.04*	14.07	*0.22*
CaO	11.87	*0.08*	11.89	*0.10*	11.89	*0.00*	11.86	*0.10*
MgO	14.66	*0.09*	14.77	*0.22*	14.89	*0.04*	14.46	*0.25*
FeO	11.72	*0.40*	11.68	*0.45*	11.73	*0.07*	11.67	*0.58*
K_2O	0.33	*0.01*	0.38	*0.02*	0.35	*0.01*	0.39	*0.01*
Na_2O	2.71	*0.04*	2.73	*0.05*	2.74	*0.06*	2.67	*0.03*
TiO_2	1.90	*0.06*	1.84	*0.06*	1.90	*0.08*	1.82	*0.05*
MnO	0.16	*0.04*	0.15	*0.03*	0.16	*0.02*	0.19	*0.03*
Cl	0.02	*0.00*	0.02	*0.01*	0.02	*0.01*	0.04	*0.01*
Total	99.14		98.34		98.20		98.21	
Name	Pargasite		Pargasite		Pargasite		Pargasite	
Mg#	0.88		0.89		0.92		0.88	

Table 7. (cont.)

Sample	**KS-12-04**		**KS-12-04**		**KS-12-31**		**KS-12-31**	
Rock Type	Gabbro		Gabbro		Gabbro		Gabbro	
grain	am5	core	am5	rim	am1	core	am1	rim
n=	6	*1-σ*	4	*1-σ*	3	*1-σ*	4	*1-σ*
SiO_2	41.04	*0.67*	41.32	*1.05*	40.27	*0.08*	40.87	*0.15*
Al_2O_3	14.13	*0.29*	13.69	*0.53*	13.85	*0.17*	13.68	*0.18*
CaO	11.94	*0.13*	11.72	*0.44*	11.79	*0.06*	11.73	*0.02*
MgO	14.88	*0.20*	14.57	*0.60*	14.34	*0.12*	14.56	*0.07*
FeO	11.52	*0.43*	12.01	*0.46*	12.13	*0.52*	12.00	*0.57*
K_2O	0.38	*0.03*	0.34	*0.06*	0.36	*0.02*	0.35	*0.02*
Na_2O	2.74	*0.07*	2.69	*0.10*	2.67	*0.04*	2.73	*0.06*
TiO_2	1.90	*0.21*	2.10	*0.35*	2.14	*0.09*	2.07	*0.08*
MnO	0.16	*0.03*	0.21	*0.02*	0.17	*0.05*	0.19	*0.04*
Cl	0.01	*0.01*	0.03	*0.02*	0.02	*0.00*	0.02	*0.01*
Total	98.70		98.69		97.73		98.19	
Name	Pargasite		Pargasite		Pargasite		Pargasite	
Mg#	0.90		0.90		0.88		0.89	

Sample	**KS-12-31**		**KS-12-31**		**KS-12-31**		**KS-12-31**	
Rock Type	Gabbro		Gabbro		Gabbro		Gabbro	
grain	am2	core	am2	rim	am3	core	am3	rim
n=	3	*1-σ*	2	*1-σ*	4	*1-σ*	3	*1-σ*
SiO_2	39.92	*0.46*	40.62	*0.06*	40.98	*0.89*	39.98	*0.59*
Al_2O_3	13.58	*0.15*	14.06	*0.22*	13.95	*0.25*	14.35	*0.12*
CaO	11.67	*0.13*	11.65	*0.03*	11.74	*0.13*	11.87	*0.03*
MgO	13.85	*0.54*	13.81	*0.15*	14.50	*0.32*	14.35	*0.30*
FeO	12.56	*0.31*	12.98	*0.17*	11.59	*0.09*	11.96	*0.26*
K_2O	0.34	*0.01*	0.35	*0.00*	0.37	*0.00*	0.37	*0.00*
Na_2O	2.66	*0.16*	2.65	*0.02*	2.66	*0.03*	2.71	*0.04*
TiO_2	2.32	*0.13*	1.91	*0.04*	2.10	*0.10*	2.24	*0.25*
MnO	0.22	*0.02*	0.23	*0.04*	0.15	*0.04*	0.16	*0.02*
Cl	0.03	*0.01*	0.03	*0.00*	0.02	*0.01*	0.02	*0.01*
Total	97.14		98.28		98.05		98.01	
Name	Pargasite		Pargasite		Pargasite		Pargasite	
Mg#	0.86		0.87		0.89		0.89	

Table 7. (cont.)

Sample	**KS-12-31**		**KS-12-31**		**KS-12-31**		**KS-12-31**	
Rock Type	Gabbro		Gabbro		Gabbro		Gabbro	
grain	am4	core	am4	rim	am5	core	am5	rim
n=	5	*1-σ*	5	*1-σ*	3	*1-σ*	4	*1-σ*
SiO_2	40.55	*0.33*	40.02	*1.00*	40.49	*0.22*	40.02	*0.88*
Al_2O_3	14.16	*0.22*	13.99	*0.37*	14.00	*0.12*	13.57	*0.52*
CaO	11.88	*0.07*	11.77	*0.05*	11.87	*0.09*	11.66	*0.08*
MgO	14.58	*0.24*	14.19	*0.96*	14.42	*0.04*	14.67	*0.51*
FeO	11.57	*0.38*	11.93	*0.25*	11.37	*0.21*	12.08	*0.21*
K_2O	0.37	*0.01*	0.38	*0.01*	0.37	*0.01*	0.35	*0.00*
Na_2O	2.69	*0.06*	2.61	*0.21*	2.70	*0.05*	2.59	*0.26*
TiO_2	2.22	*0.12*	2.15	*0.14*	2.16	*0.02*	2.00	*0.24*
MnO	0.17	*0.04*	0.15	*0.03*	0.14	*0.02*	0.16	*0.01*
Cl	0.02	*0.01*	0.03	*0.01*	0.02	*0.01*	0.02	*0.00*
Total	98.22		97.22		97.54		97.13	
Name	Pargasite		Pargasite		Pargasite			
Mg#	0.90		0.88		0.87		0.93	

Sample	**KS-12-11**		**KS-12-11**		**KS-12-11**		**KS-12-11**	
Rock Type	OL-CPX		OL-CPX		OL-CPX		OL-CPX	
grain	am1	core	am1	rim	am2	core	am2	rim
n=	3	*1-σ*	2	*1-σ*	1	*1-σ*	3	*1-σ*
SiO_2	41.33	*0.09*	41.21	*0.23*	40.55	*n/a*	41.12	*0.20*
Al_2O_3	13.89	*0.03*	13.64	*0.27*	13.56	*n/a*	13.68	*0.04*
CaO	11.71	*0.06*	11.71	*0.16*	11.63	*n/a*	11.68	*0.03*
MgO	14.36	*0.08*	14.55	*0.04*	14.07	*n/a*	14.38	*0.05*
FeO	12.25	*0.23*	12.12	*0.19*	12.49	*n/a*	11.90	*0.32*
K_2O	0.34	*0.01*	0.36	*0.00*	0.33	*n/a*	0.32	*0.01*
Na_2O	2.66	*0.02*	2.73	*0.06*	2.66	*n/a*	2.70	*0.03*
TiO_2	2.02	*0.09*	2.03	*0.01*	2.03	*n/a*	1.93	*0.07*
MnO	0.20	*0.04*	0.19	*0.01*	0.21	*n/a*	0.20	*0.02*
Cl	0.03	*0.01*	0.02	*0.00*	0.03	*n/a*	0.02	*0.00*
Total	98.78		98.56		97.56		97.93	
Name	Pargasite		Pargasite		Pargasite		Pargasite	
Mg#	0.88		0.89		0.88		0.89	

Table 7. (cont.)

Sample	**KS-12-11**		**KS-12-11**		**KS-12-11**		**KS-12-11**	
Rock Type	OL-CPX		OL-CPX		OL-CPX		OL-CPX	
grain	am3	core	am3	rim	am4	core	am4	rim
n=	3	*1-σ*	3	*1-σ*	5	*1-σ*	5	*1-σ*
SiO_2	41.89	*0.04*	41.41	*0.14*	41.87	*0.12*	41.99	*0.10*
Al_2O_3	14.97	*0.05*	14.89	*0.11*	15.04	*0.04*	15.10	*0.07*
CaO	12.25	*0.07*	12.29	*0.02*	12.26	*0.08*	12.23	*0.05*
MgO	16.60	*0.09*	16.70	*0.11*	16.51	*0.06*	16.50	*0.05*
FeO	7.49	*0.14*	8.02	*0.19*	7.37	*0.20*	7.67	*0.27*
K_2O	0.44	*0.01*	0.46	*0.02*	0.46	*0.01*	0.47	*0.01*
Na_2O	2.80	*0.01*	2.84	*0.01*	2.79	*0.02*	2.79	*0.02*
TiO_2	1.38	*0.10*	1.36	*0.11*	1.29	*0.16*	1.25	*0.11*
MnO	0.08	*0.00*	0.07	*0.07*	0.09	*0.03*	0.11	*0.01*
Cl	0.01	*0.00*	0.01	*0.00*	0.02	*0.00*	0.01	*0.01*
Total	97.91		98.06		97.70		98.12	
Name	Pargasite		Pargasite		Pargasite		Pargasite	
Mg#	0.96		0.98		0.96		0.96	

Sample	**KS-12-11**		**KS-12-11**		**KS-12-13**		**KS-12-13**	
Rock Type	OL-CPX		OL-CPX		Clinopyroxenite		Clinopyroxenite	
grain	am5	core	am5	rim	am1	core	am1	rim
n=	5	*1-σ*	5	*1-σ*	3	*1-σ*	3	*1-σ*
SiO_2	41.88	*0.43*	42.08	*0.08*	40.84	*0.57*	41.20	*0.51*
Al_2O_3	14.93	*0.10*	14.97	*0.03*	15.49	*0.21*	14.65	*0.41*
CaO	12.18	*0.07*	12.22	*0.07*	12.28	*0.09*	12.26	*0.17*
MgO	16.41	*0.07*	16.48	*0.04*	15.28	*0.02*	15.98	*0.44*
FeO	7.83	*0.24*	7.53	*0.28*	9.57	*0.21*	9.19	*0.31*
K_2O	0.44	*0.01*	0.43	*0.02*	0.43	*0.02*	0.42	*0.03*
Na_2O	2.73	*0.05*	2.78	*0.05*	2.67	*0.06*	2.75	*0.08*
TiO_2	1.27	*0.09*	1.22	*0.07*	1.29	*0.11*	1.12	*0.14*
MnO	0.10	*0.03*	0.11	*0.02*	0.08	*0.03*	0.07	*0.02*
Cl	0.01	*0.00*	0.02	*0.01*	0.02	*0.01*	0.01	*0.01*
Total	97.77		97.84		97.95		97.66	
Name	Pargasite		Pargasite		Pargasite		Pargasite	
Mg#	0.96		0.96		0.92		0.95	

Table 7. (cont.)

Sample	**KS-12-13**		**KS-12-13**		**KS-12-13**		**KS-12-13**	
Rock Type	Clinopyroxenite		Clinopyroxenite		Clinopyroxenite		Clinopyroxenite	
grain	am2	core	am2	rim	am3	core	am3	rim
n=	3	*1-σ*	3	*1-σ*	3	*1-σ*	3	*1-σ*
SiO_2	41.75	*0.17*	41.36	*0.39*	41.50	*1.00*	40.89	*0.32*
Al_2O_3	14.31	*0.15*	14.56	*0.18*	15.42	*0.60*	14.97	*0.04*
CaO	12.12	*0.04*	12.08	*0.06*	12.18	*0.02*	12.28	*0.04*
MgO	15.91	*0.09*	15.81	*0.07*	15.45	*0.50*	15.56	*0.09*
FeO	9.63	*0.39*	9.19	*0.17*	9.25	*0.19*	9.05	*0.23*
K_2O	0.40	*0.01*	0.40	*0.01*	0.45	*0.00*	0.45	*0.01*
Na_2O	2.71	*0.01*	2.68	*0.04*	2.69	*0.11*	2.71	*0.06*
TiO_2	1.35	*0.04*	1.24	*0.04*	1.21	*0.07*	1.29	*0.07*
MnO	0.11	*0.03*	0.08	*0.04*	0.11	*0.02*	0.09	*0.02*
Cl	0.01	*0.00*	0.01	*0.01*	0.01	*0.00*	0.02	*0.01*
Total	98.29		97.43		98.27		97.31	
Name	Pargasite		Pargasite		Pargasite		Pargasite	
Mg#	0.95		0.95		0.93		0.92	

Sample	**KS-12-13**		**KS-12-13**		**KS-12-13**		**KS-12-13**	
Rock Type	Clinopyroxenite		Clinopyroxenite		Clinopyroxenite		Clinopyroxenite	
grain	am4	core	am4	rim	am5	core	am5	rim
n=	5	*1-σ*	5	*1-σ*	5	*1-σ*	5	*1-σ*
SiO_2	41.72	*0.34*	40.77	*0.17*	40.96	*0.10*	40.85	*0.15*
Al_2O_3	14.21	*0.36*	15.56	*0.14*	15.24	*0.05*	15.54	*0.17*
CaO	12.11	*0.07*	12.26	*0.08*	12.27	*0.06*	12.26	*0.10*
MgO	15.79	*0.16*	15.46	*0.08*	15.43	*0.09*	15.48	*0.09*
FeO	9.70	*0.16*	9.33	*0.27*	9.45	*0.39*	9.39	*0.23*
K_2O	0.40	*0.02*	0.43	*0.01*	0.40	*0.01*	0.43	*0.02*
Na_2O	2.73	*0.02*	2.74	*0.03*	2.73	*0.03*	2.74	*0.04*
TiO_2	1.36	*0.13*	1.30	*0.10*	1.43	*0.14*	1.23	*0.12*
MnO	0.10	*0.02*	0.10	*0.04*	0.09	*0.03*	0.09	*0.03*
Cl	0.01	*0.01*	0.02	*0.01*	0.02	*0.01*	0.01	*0.01*
Total	98.14		97.97		98.01		98.02	
Name	Pargasite		Pargasite		Pargasite		Pargasite	
Mg#	0.93		0.94		0.92		0.94	

Table 7. (cont.)

Sample	**KS-12-22**		**KS-12-22**		**KS-12-22**		**KS-12-22**	
Rock Type	Wehrlite		Wehrlite		Wehrlite		Wehrlite	
grain	am1	core	am1	rim	am2	core	am2	rim
n=	4	*1-σ*	4	*1-σ*	3	*1-σ*	3	*1-σ*
SiO_2	42.97	*0.17*	43.01	*0.08*	41.70	*0.13*	41.45	*0.14*
Al_2O_3	14.23	*0.05*	14.18	*0.03*	14.59	*0.09*	14.82	*0.13*
CaO	12.15	*0.09*	12.05	*0.04*	12.11	*0.03*	12.25	*0.07*
MgO	17.05	*0.05*	17.04	*0.06*	16.87	*0.04*	16.70	*0.11*
FeO	6.81	*0.24*	6.91	*0.11*	7.05	*0.37*	6.54	*0.40*
K_2O	0.40	*0.01*	0.41	*0.01*	0.48	*0.02*	0.49	*0.00*
Na_2O	2.78	*0.06*	2.72	*0.03*	2.72	*0.06*	2.70	*0.01*
TiO_2	0.94	*0.05*	0.83	*0.03*	1.14	*0.14*	1.12	*0.12*
MnO	0.10	*0.02*	0.09	*0.02*	0.10	*0.03*	0.07	*0.03*
Cl	0.02	*0.01*	0.01	*0.00*	0.01	*0.01*	0.02	*0.00*
Total	97.45		97.25		96.77		96.15	
Name	Pargasite		Pargasite		Pargasite		Pargasite	
Mg#	0.97		0.99		0.99		0.97	

Sample	**KS-12-22**		**KS-12-22**		**KS-12-22**		**KS-12-22**	
Rock Type	Wehrlite		Wehrlite		Wehrlite		Wehrlite	
grain	am3	core	am3	rim	am4	core	am4	rim
n=	3	*1-σ*	3	*1-σ*	4	*1-σ*	4	*1-σ*
SiO_2	41.68	*0.08*	41.88	*0.11*	41.50	*0.44*	41.83	*0.15*
Al_2O_3	14.66	*0.02*	14.58	*0.04*	14.67	*0.20*	14.71	*0.04*
CaO	12.19	*0.02*	12.16	*0.07*	12.14	*0.08*	12.19	*0.05*
MgO	16.78	*0.04*	16.76	*0.01*	16.83	*0.09*	16.73	*0.05*
FeO	6.72	*0.28*	6.71	*0.16*	7.06	*0.39*	7.09	*0.21*
K_2O	0.49	*0.03*	0.48	*0.02*	0.45	*0.01*	0.45	*0.02*
Na_2O	2.73	*0.04*	2.74	*0.01*	2.78	*0.03*	2.70	*0.04*
TiO_2	1.06	*0.10*	1.05	*0.03*	1.08	*0.11*	1.12	*0.10*
MnO	0.06	*0.04*	0.07	*0.02*	0.06	*0.02*	0.04	*0.02*
Cl	0.03	*0.02*	0.02	*0.01*	0.02	*0.00*	0.02	*0.00*
Total	96.41		96.44		96.60		96.90	
Name	Pargasite		Pargasite		Pargasite		Pargasite	
Mg#	0.98		0.97		0.99		0.98	

Table 7. (cont.)

Sample	**KS-12-22**		**KS-12-22**	
Rock Type	Wehrlite		Wehrlite	
grain	am5	core	am5	rim
n=	3	*1-σ*	3	*1-σ*
SiO_2	41.84	*0.22*	41.85	*0.12*
Al_2O_3	14.44	*0.16*	14.52	*0.06*
CaO	12.18	*0.05*	12.16	*0.04*
MgO	16.85	*0.11*	16.83	*0.03*
FeO	6.95	*0.17*	6.82	*0.18*
K_2O	0.47	*0.01*	0.45	*0.01*
Na_2O	2.72	*0.05*	2.76	*0.03*
TiO_2	1.06	*0.16*	1.00	*0.01*
MnO	0.06	*0.05*	0.09	*0.02*
Cl	0.02	*0.00*	0.02	*0.01*
Total	96.58		96.48	
Name	Pargasite		Pargasite	
Mg#	0.98		0.98	

4.7.4 Clinopyroxene

A combination of WDS- and EDS-EPMA measurements indicate that all pyroxenes analyzed are the Ca- and Mg- rich end-member of clinopyroxene (Table 8). Orthopyroxene was not identified in any sample. Clinopyroxene compositions measured are from 18 grains from two olivine-clinopyroxenite samples, one clinopyroxenite, and one wehrlite sample (Table 8). The clinopyroxenes are classified based on the scheme of Morimoto (1988), using stoichiometry to recalculate the major oxide compositions (reported as wt %) of the pyroxene to atomic or elemental abundances. I plotted the relative abundances of atomic Ca (Wollastonite), Mg (Enstatite), and Fe (Ferrosilite) components, on a Wo–En–Fs ternary in the program DeltaPlot (John, 2004) and then applied that to the pyroxene quadrilateral (Fig. 17). All pyroxenes in these samples are Ca- and Mg-rich diopside (Fig. 17). For the wehrlite sample, compositions are $Wo_{47–48.5}$, $En_{44.5–45.7}$, and $Fs_{6.7–7.6}$. The two olivine-clinopyroxenite samples have slightly more Fe-rich clinopyroxenes with $Wo_{47.1–48.4}$, $En_{41.1–45.3}$, and $Fs_{7.6–10.2}$. The clinopyroxenite sample has clinopyroxene with $Wo_{46.7–47.5}$, $En_{46–48.2}$, and $Fs_{4.9–6.5}$ (Table 8). The presence of diopside in the samples is significant because diopside is usually not found in igneous rocks; in normal magmatic systems, augite is the most common clinopyroxene.

Mg# and Cr# for clinopyroxenes from the ultramafic samples form a continuous array that co-varies with SiO_2 (Fig. 18). The amount of magnesium in clinopyroxene is measured as the Mg#, which is 84–96 for clinopyroxene in all ultramafic samples analyzed (Fig. 18a; Table 8). Pyroxenes from the clinopyroxenite are at the low end of this range. The range in Cr# of clinopyroxene is far wider (Fig. 18b; Table 8). Cr# is lowest in the clinopyroxenite, at <7, whereas in the wehrlite it ranges from 7–12. In one of the olivine clinopyroxenite samples it ranges from 2–12, and in the other, Cr # is highest of all samples at 12–25.

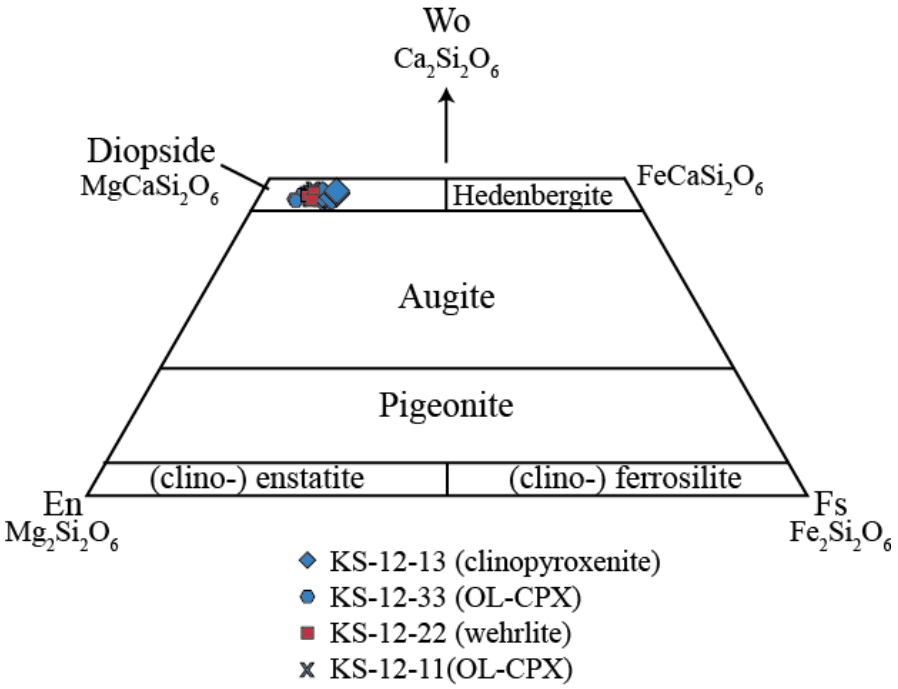

Figure 17. Pyroxene Quadrilateral
Ca, Mg, and Fe abundances of pyroxenes from four ultramafic samples indicate that these grains are diopside. The presence of diopside in the samples is significant because augite is the most common clinopyroxene found in normal igneous rocks.

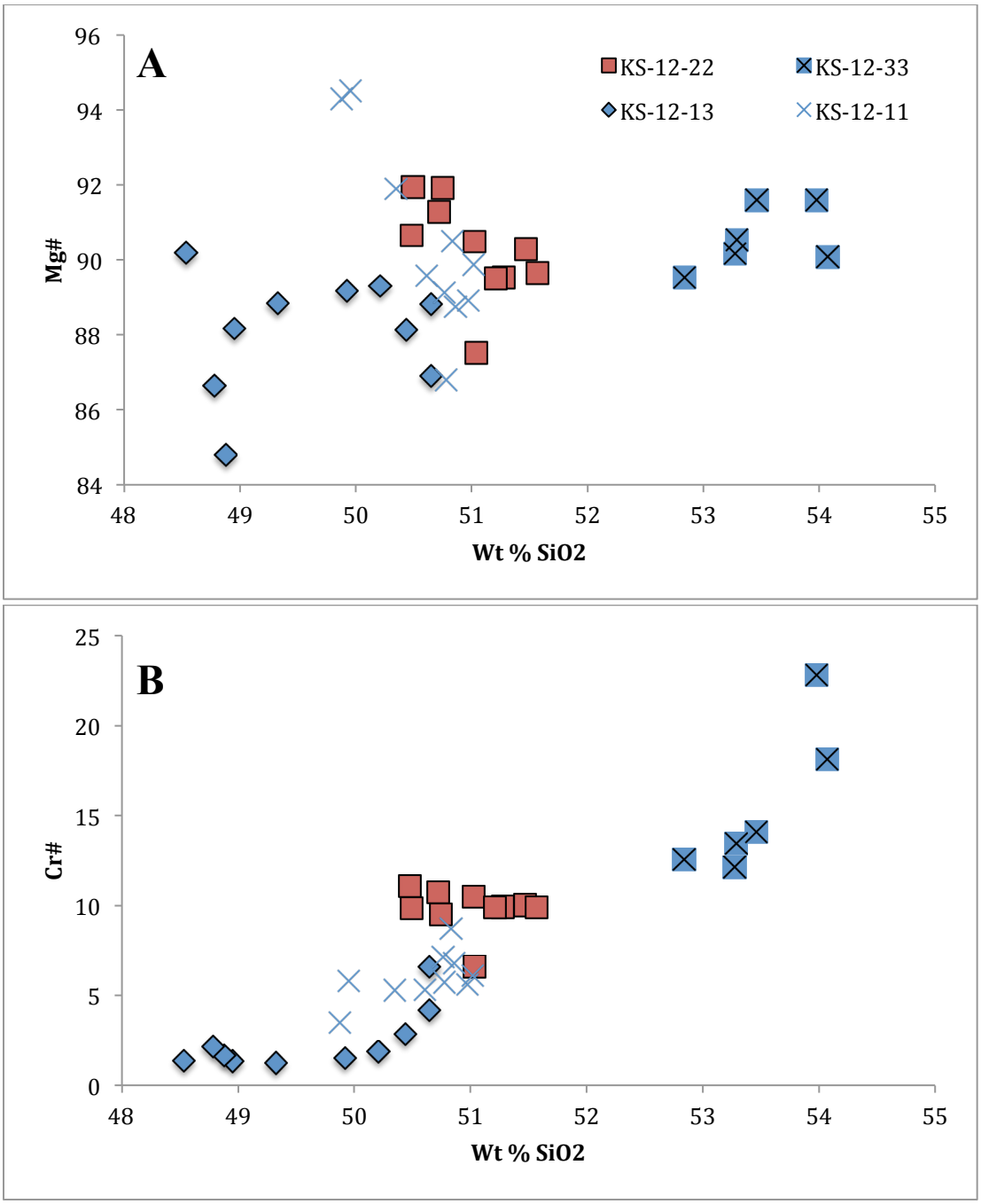

Figure 18. Mg# and Cr# in Clinopyroxene
(A) Mg# in clinopyroxene does not show much variation between enclave types. The clinopyroxenes from clinopyroxenite KS-12-13 are slightly lower in Mg# than those in the olivine-clinopyroxenites and wehrlite with Mg# 84–90. (B) Cr# in clinopyroxene appears to be more useful in distinguishing sample types. In the clinopyroxenite, Cr# is <7, whereas the wehrlite is between 7–12. For one olivine-clinopyroxenite, Cr# is higher than all samples with Cr# 12–25.

Table 8. Clinopyroxene EPMA Results

Error reported to 1-σ. n-value = number of points analyzed per grain. Mg# = atomic Mg / ($Mg + Fe^{2+}$); Wo = atomic Ca / ($Ca + Mg + Fe_t$), En = atomic Mg / ($Ca + Mg + Fe_t$), and Fs = Fe_t / ($Ca + Mg + Fe_t$); OL-CPX = olivine clinopyroxenite; Wo, En, and Fs are calculated based on Morimoto (1988) and calculations are shown in supplemental file 2.

Sample	**KS-12-11**		**KS-12-11**		**KS-12-11**		**KS-12-11**	
Rock Type	OL-CPX		OL-CPX		OL-CPX		OL-CPX	
grain	CPX1		CPX1		CPX2		CPX2	
location	core		rim		core		rim	
n=	5	*1-σ*	4	*1-σ*	4	*1-σ*	3	*1-σ*
Na_2O	0.22	*0.01*	0.24	*0.02*	0.21	*0.01*	0.22	*0.01*
MgO	15.83	*0.16*	15.64	*0.15*	15.62	*0.09*	15.56	*0.05*
Al_2O_3	4.06	*0.26*	4.60	*0.20*	4.45	*0.04*	4.44	*0.04*
SiO_2	50.83	*0.31*	50.35	*0.16*	50.97	*0.18*	50.86	*0.11*
CaO	22.89	*0.06*	23.09	*0.19*	22.96	*0.16*	22.86	*0.09*
TiO_2	0.38	*0.02*	0.44	*0.04*	0.45	*0.02*	0.42	*0.01*
FeO	4.63	*0.17*	5.05	*0.08*	5.03	*0.05*	4.82	*0.34*
MnO	0.12	*0.04*	0.12	*0.03*	0.12	*0.05*	0.12	*0.06*
Cr_2O_3	0.58	*0.07*	0.38	*0.05*	0.39	*0.11*	0.48	*0.07*
Total	99.53	*0.12*	99.91	*0.09*	100.21	*0.13*	99.78	*0.62*
Mg#	90.5		91.9		88.9		88.7	
Cr#	8.7		5.3		5.6		6.8	
Wo	47.1		47.3		47.2		47.3	
En	45.3		44.6		44.6		44.8	
Fs	7.5		8.2		8.2		7.9	

Table 8. (cont.)

Sample	**KS-12-11**		**KS-12-11**		**KS-12-11**		**KS-12-11**	
Rock Type	OL-CPX		OL-CPX		OL-CPX		OL-CPX	
grain	CPX3		CPX3		CPX4		CPX4	
location	core		rim		core		rim	
n=	3	*1-σ*	3	*1-σ*	3	*1-σ*	3	*1-σ*
Na_2O	0.21	*0.01*	0.22	*0.01*	0.21	*0.01*	0.21	*0.01*
MgO	15.64	*0.04*	15.66	*0.10*	15.47	*0.06*	15.73	*0.06*
Al_2O_3	4.44	*0.04*	4.74	*0.32*	4.56	*0.08*	4.25	*0.03*
SiO_2	49.96	*0.07*	49.88	*0.33*	50.61	*0.10*	51.02	*0.11*
CaO	23.50	*0.02*	23.31	*0.16*	23.07	*0.04*	23.05	*0.03*
TiO_2	0.50	*0.01*	0.48	*0.07*	0.46	*0.00*	0.40	*0.01*
FeO	4.83	*0.11*	5.19	*0.16*	4.65	*0.03*	4.72	*0.14*
MnO	0.11	*0.02*	0.14	*0.02*	0.09	*0.04*	0.13	*0.03*
Cr_2O_3	0.41	*0.06*	0.26	*0.04*	0.38	*0.06*	0.41	*0.05*
Total	99.59	*0.10*	99.88	*0.11*	99.52	*0.13*	99.92	*0.28*
Mg#	94.5		94.3		89.6		89.9	
Cr#	5.8		3.5		5.3		6.1	
Wo	47.9		47.4		47.8		47.4	
En	44.3		44.3		44.6		45.0	
Fs	7.8		8.3		7.6		7.7	

Table 8. (cont.)

Sample	**KS-12-11**		**KS-12-11**		**KS-12-13**		**KS-12-13**	
Rock Type	OL-CPX		OL-CPX		Clinopyroxenite		Clinopyroxenite	
grain	CPX5		CPX5		CPX1		CPX1	
location	core		rim		core		rim	
n=	3	*1-σ*	2	*1-σ*	2	*1-σ*	3	*1-σ*
Na_2O	0.22	*0.00*	0.21	*0.01*	0.20	*0.00*	0.20	*0.01*
MgO	15.53	*0.09*	15.31	*0.00*	15.15	*0.09*	14.33	*0.06*
Al_2O_3	4.45	*0.10*	4.62	*0.14*	4.17	*0.10*	6.11	*0.18*
SiO_2	50.76	*0.12*	50.78	*0.03*	50.21	*0.26*	48.54	*0.35*
CaO	23.06	*0.16*	22.78	*0.06*	23.07	*0.09*	23.08	*0.11*
TiO_2	0.56	*0.04*	0.54	*0.06*	0.43	*0.01*	0.52	*0.02*
FeO	4.76	*0.22*	4.55	*0.26*	5.90	*0.09*	6.37	*0.05*
MnO	0.08	*0.01*	0.11	*0.04*	0.17	*0.00*	0.16	*0.02*
Cr_2O_3	0.51	*0.04*	0.42	*0.01*	0.12	*0.02*	0.13	*0.04*
Total	99.93	*0.19*	99.30	*0.28*	99.42	*0.14*	99.43	*0.13*
Mg#	89.1		86.8		89.3		90.2	
Cr#	7.1		5.7		1.9		1.4	
Wo	47.6		47.8		47.3		48.0	
En	44.6		44.7		43.2		41.5	
Fs	7.8		7.6		9.6		10.5	

Table 8. (cont.)

Sample	**KS-12-13**		**KS-12-13**		**KS-12-13**		**KS-12-13**	
Rock Type	Clinopyroxenite		Clinopyroxenite		Clinopyroxenite		Clinopyroxenite	
grain	CPX2		CPX2		CPX3		CPX3	
location	core		rim		core		rim	
n=	3	*1-σ*	3	*1-σ*	3	*1-σ*	3	*1-σ*
Na_2O	0.20	*0.06*	0.21	*0.01*	0.19	*0.01*	0.19	*0.01*
MgO	15.18	*0.30*	14.34	*0.11*	15.00	*0.05*	15.10	*0.31*
Al_2O_3	4.37	*0.55*	5.79	*0.27*	5.07	*0.06*	4.41	*0.48*
SiO_2	50.65	*0.22*	48.95	*0.30*	49.92	*0.06*	50.44	*0.61*
CaO	22.82	*0.43*	22.92	*0.04*	23.17	*0.08*	23.11	*0.04*
TiO_2	0.43	*0.02*	0.57	*0.04*	0.63	*0.01*	0.48	*0.06*
FeO	5.51	*0.25*	6.50	*0.11*	5.34	*0.16*	5.58	*0.29*
MnO	0.12	*0.05*	0.15	*0.04*	0.11	*0.04*	0.13	*0.07*
Cr_2O_3	0.46	*0.12*	0.12	*0.03*	0.12	*0.03*	0.19	*0.05*
Total	99.73	*0.22*	99.55	*0.09*	99.56	*0.13*	99.63	*0.11*
Mg#	86.9		88.2		89.2		88.1	
Cr#	6.6		1.4		2.5		2.9	
Wo	47.2		47.7		48.0		47.6	
En	43.7		41.6		43.3		43.3	
Fs	9.0		10.7		8.8		9.1	

Table 8. (cont.)

Sample	**KS-12-13**		**KS-12-13**		**KS-12-13**		**KS-12-13**	
Rock Type	Clinopyroxenite		Clinopyroxenite		Clinopyroxenite		Clinopyroxenite	
grain	CPX4		CPX4		CPX5		CPX5	
location	core		rim		core		rim	
n=	3	*1-σ*	3	*1-σ*	5	*1-σ*	4	*1-σ*
Na_2O	0.19	*0.01*	0.20	*0.00*	0.19	*0.01*	0.21	*0.01*
MgO	15.30	*0.28*	14.70	*0.06*	13.95	*0.12*	14.01	*0.09*
Al_2O_3	4.31	*0.26*	5.37	*0.04*	6.31	*0.07*	6.29	*0.11*
SiO_2	50.65	*0.46*	49.32	*0.22*	48.88	*0.11*	48.78	*0.16*
CaO	23.23	*0.08*	22.95	*0.25*	22.72	*0.15*	22.96	*0.12*
TiO_2	0.50	*0.05*	0.57	*0.02*	0.58	*0.01*	0.59	*0.02*
FeO	5.29	*0.12*	6.24	*0.38*	6.28	*0.13*	6.33	*0.20*
MnO	0.12	*0.02*	0.15	*0.01*	0.11	*0.04*	0.16	*0.05*
Cr_2O_3	0.28	*0.09*	0.10	*0.03*	0.16	*0.03*	0.21	*0.03*
Total	99.86	*0.38*	99.60	*0.25*	99.17	*0.28*	99.53	*0.20*
Mg#	88.8		88.8		84.8		86.6	
Cr#	4.2		1.2		1.7		2.2	
Wo	47.7		47.5		48.2		48.4	
En	43.7		42.3		41.2		41.1	
Fs	8.6		10.2		10.5		10.5	

Table 8. (cont.)

Sample	**KS-12-33**		**KS-12-33**		**KS-12-33**		**KS-12-33**	
Rock Type	OL-CPX		OL-CPX		OL-CPX		OL-CPX	
grain	CPX1		CPX1		CPX2		CPX2	
location	core		rim		core		rim	
n=	2	*1-σ*	2	*1-σ*	2	*1-σ*	3	*1-σ*
Na_2O	0.17	*0.01*	0.17	*0.00*	0.15	*0.02*	0.13	*0.02*
MgO	17.11	*0.40*	16.78	*0.10*	17.46	*0.08*	17.35	*0.13*
Al_2O_3	2.04	*0.66*	2.42	*0.09*	1.58	*0.10*	1.57	*0.04*
SiO_2	53.46	*0.62*	53.27	*0.25*	53.98	*0.38*	54.07	*0.09*
CaO	23.68	*0.10*	23.67	*0.05*	23.58	*0.15*	23.49	*0.03*
TiO_2	0.22	*0.06*	0.29	*0.03*	0.13	*0.02*	0.16	*0.01*
FeO	3.68	*0.29*	3.61	*0.03*	3.13	*0.16*	3.36	*0.14*
MnO	0.10	*0.04*	0.08	*0.05*	0.09	*0.02*	0.05	*0.04*
Cr_2O_3	0.50	*0.02*	0.50	*0.03*	0.70	*0.05*	0.52	*0.20*
Total	100.95	*0.05*	100.79	*0.19*	100.81	*0.03*	100.71	*0.26*
Mg#	91.6		90.2		91.6		90.1	
Cr#	14.1		12.1		22.8		18.1	
Wo	47.0		47.5		46.8		46.7	
En	47.2		46.8		48.2		48.0	
Fs	5.8		5.7		4.9		5.3	

Table 8. (cont.)

Sample	**KS-12-33**		**KS-12-33**		**KS-12-22**		**KS-12-22**	
Rock Type	OL-CPX		OL-CPX		Wehrlite		Wehrlite	
grain	CPX3		CPX3		CPX1		CPX1	
location	core		rim		core		rim	
n=	3	*1-σ*	3	*1-σ*	4	*1-σ*	4	*1-σ*
Na_2O	0.20	*0.01*	0.22	*0.07*	0.18	*0.01*	0.17	*0.02*
MgO	16.41	*0.31*	16.77	*0.04*	15.80	*0.17*	15.71	*0.16*
Al_2O_3	2.83	*0.10*	2.51	*0.14*	4.11	*0.10*	4.09	*0.23*
SiO_2	52.84	*0.31*	53.29	*0.11*	50.75	*0.05*	51.03	*0.23*
CaO	23.57	*0.19*	23.70	*0.10*	23.38	*0.16*	23.40	*0.06*
TiO_2	0.30	*0.02*	0.28	*0.00*	0.42	*0.02*	0.40	*0.02*
FeO	4.06	*0.06*	3.76	*0.13*	4.44	*0.19*	4.21	*0.16*
MnO	0.09	*0.01*	0.10	*0.01*	0.08	*0.03*	0.04	*0.02*
Cr_2O_3	0.61	*0.02*	0.58	*0.07*	0.64	*0.05*	0.72	*0.11*
Total	100.90	*0.13*	101.21	*0.13*	99.81	*0.47*	99.77	*0.19*
Mg#	89.5		90.5		91.9		90.5	
Cr#	12.6		13.4		9.5		10.5	
Wo	47.5		47.4		47.8		48.2	
En	46.0		46.7		45.0		45.0	
Fs	6.5		5.9		7.2		6.9	

Table 8. (cont.)

Sample	**KS-12-22**		**KS-12-22**		**KS-12-22**		**KS-12-22**	
Rock Type	Wehrlite		Wehrlite		Wehrlite		Wehrlite	
grain	CPX2		CPX2		CPX3		CPX3	
location	core		rim		core		rim	
n=	2	*1-σ*	2	*1-σ*	4	*1-σ*	4	*1-σ*
Na_2O	0.17	*0.01*	0.17	*0.00*	0.19	*0.01*	0.22	*0.02*
MgO	15.95	*0.10*	15.90	*0.10*	15.90	*0.08*	15.70	*0.08*
Al_2O_3	3.56	*0.10*	3.57	*0.00*	3.82	*0.10*	4.38	*0.08*
SiO_2	51.47	*0.02*	51.57	*0.29*	51.28	*0.12*	50.72	*0.13*
CaO	23.34	*0.05*	23.28	*0.09*	22.94	*0.19*	23.16	*0.17*
TiO_2	0.34	*0.01*	0.33	*0.02*	0.37	*0.01*	0.40	*0.02*
FeO	4.13	*0.02*	4.13	*0.03*	4.30	*0.14*	4.63	*0.06*
MnO	0.10	*0.01*	0.10	*0.01*	0.11	*0.03*	0.11	*0.06*
Cr_2O_3	0.59	*0.06*	0.58	*0.09*	0.63	*0.08*	0.78	*0.04*
Total	99.66	*0.10*	99.65	*0.35*	99.54	*0.18*	100.10	*0.24*
Mg#	90.3		89.7		89.5		91.3	
Cr#	10.0		9.9		9.9		10.7	
Wo	47.8		47.8		47.3		47.6	
En	45.5		45.4		45.7		44.9	
Fs	6.7		6.7		7.0		7.5	

Table 8. (cont.)

Sample	**KS-12-22**		**KS-12-22**		**KS-12-22**		**KS-12-22**	
Rock Type	Wehrlite		Wehrlite		Wehrlite		Wehrlite	
grain	CPX4		CPX4		CPX5		CPX5	
location	core		rim		core		rim	
n=	3	*1-σ*	3	*1-σ*	4	*1-σ*	4	*1-σ*
Na_2O	0.18	*0.01*	0.21	*0.02*	0.21	*0.01*	0.23	*0.07*
MgO	15.43	*0.07*	15.78	*0.12*	15.90	*0.11*	15.54	*0.38*
Al_2O_3	4.58	*0.03*	4.53	*0.16*	4.10	*0.16*	4.71	*0.38*
SiO_2	50.48	*0.29*	50.49	*0.19*	51.21	*0.09*	51.04	*0.35*
CaO	23.38	*0.07*	23.06	*0.06*	22.84	*0.13*	22.68	*0.23*
TiO_2	0.45	*0.00*	0.42	*0.01*	0.38	*0.03*	0.37	*0.03*
FeO	4.30	*0.09*	4.59	*0.26*	4.55	*0.11*	4.58	*0.14*
MnO	0.08	*0.02*	0.10	*0.04*	0.14	*0.02*	0.12	*0.05*
Cr_2O_3	0.85	*0.06*	0.74	*0.06*	0.67	*0.02*	0.50	*0.03*
Total	99.73	*0.32*	99.92	*0.38*	99.99	*0.25*	99.77	*0.12*
Mg#	90.7		91.9		89.5		87.5	
Cr#	11.0		9.9		9.9		6.6	
Wo	48.5		47.4		47.0		47.3	
En	44.5		45.1		45.6		45.1	
Fs	7.1		7.5		7.4		7.6	

4.7.5 Olivine

Olivine is absent in gabbro samples, but is found in all ultramafic samples. Olivine found in previously collected gabbroic samples is discussed in Neill (2013). Olivine compositions were measured for 16 grains in two olivine-clinopyroxenite samples (Fig. 19; Table 9). Fo-content is measured using stoichiometry to calculate the elemental abundances of the olivine (calculated from wt.%) and to determine the relative amounts of Mg and Fe (Deer et al., 1992). All the samples are $Fo_{83–84}$, corresponding to the Mg-end member of olivine, forsterite.

Olivine often includes Ni in its structure under mantle conditions. The amount of Ni and the Mg# will reflect the degree of evolution of the melt, with Ni and Mg# both being higher in olivine from more mafic magma (Fig. 19). The concentration of Ni varies from 400–1600 ppm and, as with the Mg content, there is no difference between core and rim values.

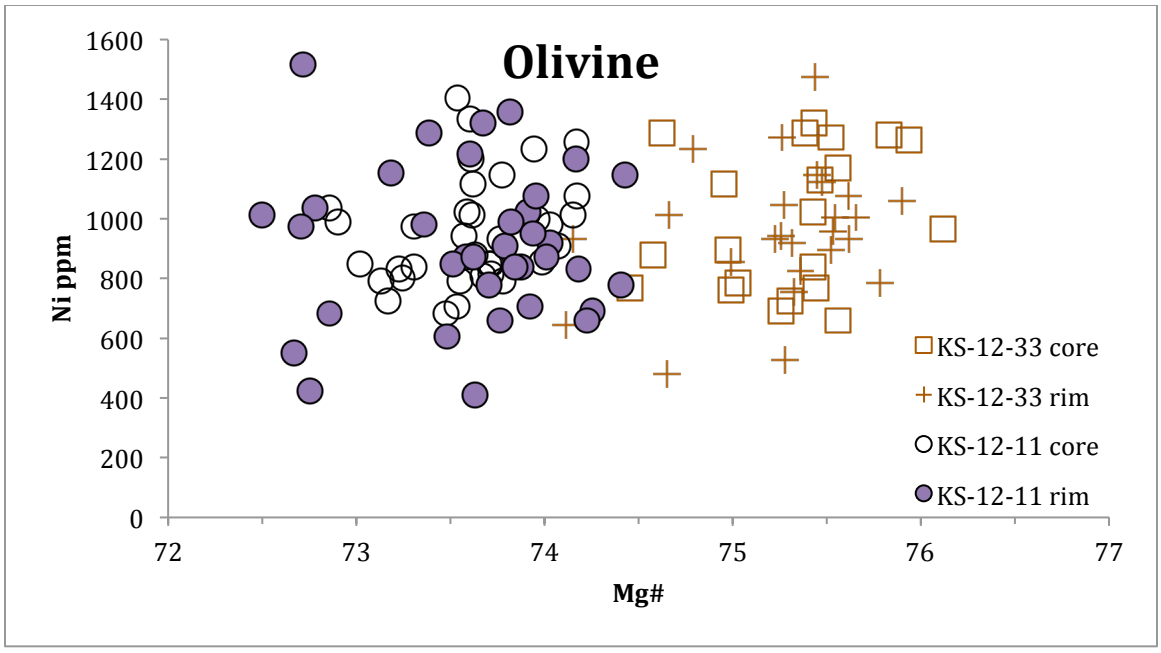

Figure 19. Ni vs. Mg# in Olivine
The olivines from two olivine-clinopyroxenite samples are between 400–1600 ppm Ni and between Mg# 72.5–76.5.

Table 9. Olivine EPMA Results

Error reported to 1-σ, n=number of points analyzed per grain; Olivine composition was calculated by % Fo = 100* (Mg / (Fe^{2+} + Mg)) (fayalite is 100 – Fo). OL-CPX = olivine clinopyroxenite

Sample	**KS-12-11**		**KS-12-11**		**KS-12-11**		**KS-12-11**	
Rock Type	OL-CPX		OL-CPX		OL-CPX		OL-CPX	
grain	OL1		OL1		OL2		OL2	
location	core		rim		core		rim	
n=	4	*1-σ*	5	*1-σ*	5	*1-σ*	5	*1-σ*
SiO_2	39.83	*0.13*	39.70	*0.08*	39.82	*0.11*	40.28	*0.20*
MgO	44.38	*0.05*	44.46	*0.07*	44.37	*0.12*	45.10	*0.18*
FeO	15.85	*0.27*	16.17	*0.31*	15.78	*0.38*	15.68	*0.06*
MnO	0.30	*0.02*	0.30	*0.04*	0.29	*0.02*	0.31	*0.02*
CaO	0.18	*0.01*	0.18	*0.01*	0.17	*0.01*	0.18	*0.00*
Cr_2O_3	0.01	-	0.04	*0.01*	0.02	*0.01*	0.03	*0.03*
NiO	0.12	*0.02*	0.15	*0.03*	0.12	*0.02*	0.11	*0.02*
Total	100.65		100.97		100.56		101.67	
%Fo	83.30		83.05		83.37		83.68	

Sample	**KS-12-11**		**KS-12-11**		**KS-12-11**		**KS-12-11**	
Rock Type	OL-CPX		OL-CPX		OL-CPX		OL-CPX	
grain	OL3		OL3		OL4		OL4	
location	core		rim		core		rim	
n=	5	*1-σ*	5	*1-σ*	3	*1-σ*	3	*1-σ*
SiO_2	39.69	*0.10*	39.63	*0.05*	39.83	*0.01*	39.91	*0.19*
MgO	44.36	*0.15*	44.28	*0.09*	44.38	*0.17*	44.66	*0.10*
FeO	16.19	*0.31*	15.72	*0.17*	15.66	*0.32*	16.28	*0.69*
MnO	0.30	*0.01*	0.33	*0.03*	0.31	*0.01*	0.31	*0.01*
CaO	0.17	*0.00*	0.17	*0.01*	0.17	*0.00*	0.18	*0.01*
Cr_2O_3	0.01	*0.01*	0.02	*0.00*	0.01	-	0.02	*0.01*
NiO	0.12	*0.01*	0.11	*0.02*	0.11	*0.02*	0.10	*0.03*
Total	100.84		100.24		100.47		101.45	
%Fo	83.01		83.39		83.48		83.02	

Table 9. (cont.)

Sample	**KS-12-11**		**KS-12-11**		**KS-12-11**		**KS-12-11**	
Rock Type	OL-CPX		OL-CPX		OL-CPX		OL-CPX	
grain	OL5		OL5		OL6		OL6	
location	core		rim		core		rim	
n=	3	*1-σ*	3	*1-σ*	3	*1-σ*	3	*1-σ*
SiO_2	39.63	*0.09*	39.50	*0.07*	39.57	*0.08*	39.33	*0.04*
MgO	44.30	*0.08*	44.01	*0.22*	44.17	*0.04*	43.85	*0.19*
FeO	16.02	*0.21*	15.70	*0.21*	15.69	*0.19*	15.58	*0.14*
MnO	0.29	*0.02*	0.30	*0.01*	0.29	*0.05*	0.28	*0.03*
CaO	0.18	*0.00*	0.18	*0.01*	0.16	*0.00*	0.17	*0.01*
Cr_2O_3	-	-	0.02	*0.02*	0.02	*0.01*	0.03	*0.02*
NiO	0.12	*0.03*	0.09	*0.01*	0.13	*0.02*	0.15	*0.04*
Total	100.53		99.80		100.03		99.37	
%Fo	83.14		83.32		83.38		83.38	

Sample	**KS-12-11**		**KS-12-11**		**KS-12-11**		**KS-12-11**	
Rock Type	OL-CPX		OL-CPX		OL-CPX		OL-CPX	
grain	OL7		OL7		OL8		OL8	
location	core		rim		core		rim	
n=	3	*1-σ*	3	*1-σ*	3	*1-σ*	3	*1-σ*
SiO_2	39.59	*0.11*	39.61	*0.09*	39.68	*0.14*	39.66	*0.12*
MgO	44.22	*0.06*	44.23	*0.12*	44.29	*0.12*	44.27	*0.20*
FeO	15.81	*0.07*	16.29	*0.56*	16.02	*0.47*	15.56	*0.39*
MnO	0.29	*0.01*	0.29	*0.03*	0.29	*0.01*	0.29	*0.01*
CaO	0.17	*0.01*	0.18	*0.02*	0.16	*0.01*	0.18	*0.01*
Cr_2O_3	0.03	*0.01*	0.02	*0.01*	0.03	-	0.01	*0.01*
NiO	0.13	*0.03*	0.10	*0.04*	0.12	*0.04*	0.11	*0.05*
Total	100.22		100.73		100.59		100.07	
%Fo	83.29		82.88		83.13		83.53	

Table 9. (cont.)

Sample	**KS-12-11**		**KS-12-11**		**KS-12-11**		**KS-12-11**	
Rock Type	OL-CPX		OL-CPX		OL-CPX		OL-CPX	
grain	OL9		OL9		OL10		OL10	
location	core		rim		core		rim	
n=	3	*1-σ*	3	*1-σ*	3	*1-σ*	3	*1-σ*
SiO_2	39.56	*0.10*	39.34	*0.00*	39.65	*0.04*	39.64	*0.01*
MgO	44.13	*0.19*	44.01	*0.07*	44.24	*0.17*	44.03	*0.06*
FeO	15.85	*0.36*	16.46	*0.29*	15.90	*0.15*	15.63	*0.15*
MnO	0.29	*0.02*	0.30	*0.01*	0.30	*0.02*	0.32	*0.02*
CaO	0.17	*0.00*	0.18	*0.01*	0.17	*0.01*	0.16	*0.00*
Cr_2O_3	0.01	*0.00*	0.01	*0.01*	0.01	-	0.02	*0.01*
NiO	0.14	*0.04*	0.12	*0.04*	0.11	*0.01*	0.12	*0.02*
Total	100.15		100.40		100.36		99.91	
%Fo	83.23		82.66		83.22		83.40	

Sample	**KS-12-33**		**KS-12-33**		**KS-12-33**		**KS-12-33**	
Rock Type	OL-CPX		OL-CPX		OL-CPX		OL-CPX	
grain	OL1		OL1		OL2		OL2	
location	core		rim		core		rim	
n=	4	*1-σ*	4	*1-σ*	2	*1-σ*	4	*1-σ*
SiO_2	40.25	*0.08*	40.24	*0.39*	40.36	*0.08*	40.47	*0.12*
MgO	45.72	*0.04*	45.62	*0.31*	46.02	*0.06*	46.12	*0.09*
FeO	14.71	*0.23*	15.32	*0.56*	15.34	*0.66*	15.09	*0.11*
MnO	0.28	*0.02*	0.29	*0.04*	0.29	*0.01*	0.25	*0.02*
CaO	0.15	*0.02*	0.15	*0.00*	0.18	*0.06*	0.15	*0.01*
Cr_2O_3	0.02	*0.00*	0.02	*0.01*	0.03	*0.00*	0.03	-
NiO	0.13	*0.04*	0.11	*0.04*	0.12	*0.04*	0.11	*0.01*
Total	101.26		101.73		102.35		102.19	
%Fo	84.71		84.15		84.25		84.50	

Table 9. (cont.)

Sample	**KS-12-33**		**KS-12-33**		**KS-12-33**		**KS-12-33**	
Rock Type	OL-CPX		OL-CPX		OL-CPX		OL-CPX	
grain	OL3		OL3		OL4		OL4	
location	core		rim		core		rim	
n=	4	*1-σ*	4	*1-σ*	4	*1-σ*	4	*1-σ*
SiO_2	40.39	*0.12*	40.29	*0.13*	40.44	*0.13*	40.44	*0.06*
MgO	45.85	*0.04*	45.82	*0.09*	46.04	*0.20*	45.99	*0.10*
FeO	14.80	*0.28*	14.91	*0.12*	15.44	*0.38*	14.95	*0.23*
MnO	0.27	*0.02*	0.28	*0.02*	0.28	*0.03*	0.28	*0.02*
CaO	0.17	*0.00*	0.16	*0.01*	0.16	*0.02*	0.14	*0.01*
Cr_2O_3	0.01	*0.01*	0.00	*0.01*	0.01	*0.01*	0.01	*0.01*
NiO	0.13	*0.03*	0.15	*0.03*	0.13	*0.03*	0.12	*0.02*
Total	101.60		101.60		102.49		101.92	
%Fo	84.67		84.56		84.17		84.58	

Sample	**KS-12-33**		**KS-12-33**		**KS-12-33**		**KS-12-33**	
Rock Type	OL-CPX		OL-CPX		OL-CPX		OL-CPX	
grain	OL5		OL5		OL6		OL6	
location	core		rim		core		rim	
n=	4	*1-σ*	4	*1-σ*	3	*1-σ*	5	*1-σ*
SiO_2	40.39	*0.04*	40.54	*0.16*	40.33	*0.19*	40.41	*0.24*
MgO	45.98	*0.07*	46.03	*0.17*	45.78	*0.09*	45.82	*0.22*
FeO	15.22	*0.20*	15.42	*0.54*	14.96	*0.11*	14.95	*0.20*
MnO	0.30	*0.02*	0.27	*0.02*	0.28	*0.03*	0.27	*0.02*
CaO	0.15	*0.01*	0.15	*0.01*	0.16	*0.01*	0.16	*0.00*
Cr_2O_3	0.02	*0.01*	0.02	*0.01*	0.02	*0.02*	0.01	*0.01*
NiO	0.12	*0.03*	0.12	*0.02*	0.13	*0.04*	0.11	*0.03*
Total	102.17		102.54		101.64		101.72	
%Fo	84.34		84.18		84.51		84.53	

4.7.6 Oxides

There are two different types of oxides present in the Kasatochi enclaves. The oxide phase in the gabbros is magnetite, as discussed in Neill (2013). The oxides from the ultramafic samples analyzed are spinel, based on chromium-number (Cr# = atomic Cr / (Cr + Al)) and magnesium number (Mg# = atomic Mg/ (Mg + Fe^{2+})) in the classification scheme of Stormer (1983) (Table 10; Fig. 20). Before calculating Mg# and Cr#, I recalculated spinel compositions for Fe^{2+} and Fe^{3+} using stoichiometry (three cations per four oxygens) and the methods of Stormer (1983) and Carmichael (1967). Total Fe in wehrlite spinels is between 28–33 wt.% and is ~32.5 wt.% in olivine-clinopyroxenite (Table 10). The ratio of Fe^{2+}/Fe^{3+} is ~0.55 for all samples (Supplemental File 2). Al_2O_3 in wehrlite is between 26–34 wt.% in wehrlite and is ~24.6 wt.% in olivine-clinopyroxenite. In the wehrlite, there is less Cr than Al in all but one sample (21–27 wt.% Cr_2O_3). However, spinel in the olivine-clinopyroxenite is more enriched in Cr than Al (~29.1 wt.% Cr_2O_3). The compositions for spinel crystals from olivine-clinopyroxenite plot closest to the Cr-spinel field, which is Cr# > 50 (Fig. 20). The results of recalculations yield Cr# 29–41 in wehrlite and ~44 in olivine clinopyroxenite (Fig. 20). For the samples to be within the Cr-spinel field, the Cr# must be >50.

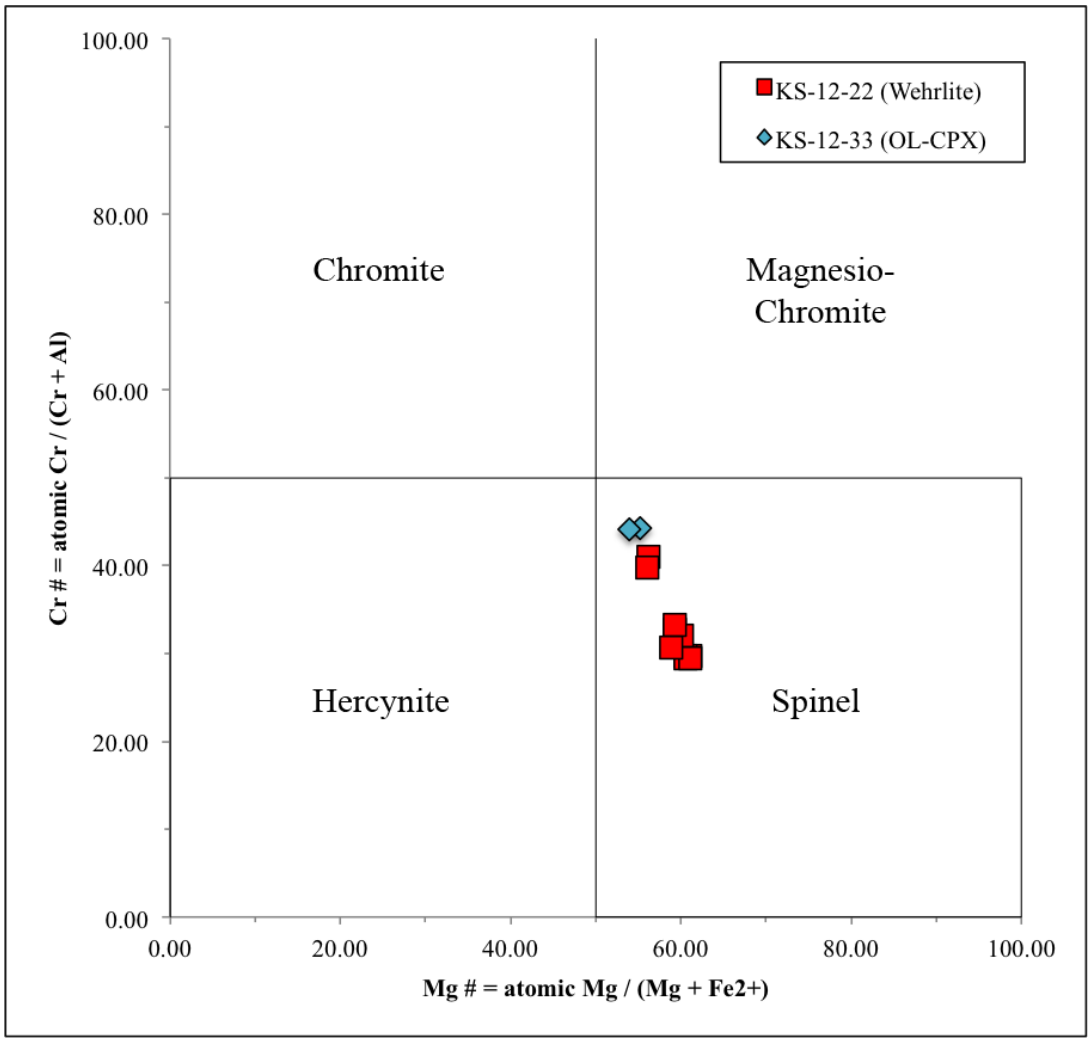

Figure 20. Spinel Classification Diagram
Mg# plotted against Cr# indicate that all oxide phases from ultramafic enclaves analyzed are spinel, with fairly uniform compositions. (Modified after Irvine, 1965). OL-CPX=olivine clinopyroxenite

Table 10. Spinel EPMA Results
Error reported to 1-σ. n-value = number of points analyzed per grain. The Fe recalculation is based on three cations in the mineral structure for every four oxygens. Cr# = atomic Cr / (Cr+Al) and Mg# = atomic Mg / (Mg+Fe^{2+})

Sample	**KS-12-22**		**KS-12-22**		**KS-12-22**		**KS-12-22**		**KS-12-22**	
Rock Type	Wehrlite		Wehrlite		Wehrlite		Wehrlite		Wehrlite	
grain	CR1		CR1		CR2		CR2		CR3	
location	core		rim		core		rim		core	
n=	4	*1-σ*	3	*1-σ*	3	*1-σ*	2	*1-σ*	4	*1-σ*
MnO	0.23	*0.01*	0.24	*0.05*	0.25	*0.05*	0.22	*0.07*	0.22	*0.03*
FeO_t	30.84	*0.12*	30.86	*0.08*	28.94	*0.14*	28.84	*0.08*	29.37	*0.12*
MgO	12.55	*0.08*	12.58	*0.02*	14.20	*0.02*	14.06	*0.03*	13.59	*0.09*
Al_2O_3	26.97	*0.20*	27.65	*0.40*	33.95	*0.02*	34.03	*0.09*	32.05	*0.15*
TiO_2	0.53	*0.06*	0.56	*0.05*	0.50	*0.02*	0.57	*0.04*	0.51	*0.06*
Cr_2O_3	27.89	*0.27*	27.22	*0.07*	21.47	*0.17*	21.46	*0.47*	23.30	*0.28*
Total	98.92		99.02		99.25		99.14		98.94	
FeO	17.18		17.28		15.86		16.06		16.39	
Fe_2O_3	15.18		15.09		14.53		14.19		14.42	
SUM	100.53		100.62		100.75		100.61		100.46	
Cr#	40.96		39.77		29.79		29.73		32.78	
Mg#	56.22		56.13		61.14		60.61		59.30	

Sample	**KS-12-22**		**KS-12-22**		**KS-12-22**		**KS-12-22**		**KS-12-22**	
Rock Type	Wehrlite		Wehrlite		Wehrlite		Wehrlite		Wehrlite	
grain	CR3		CR4		CR4		CR5		CR5	
location	rim		core		rim		core		rim	
n=	4	*1-σ*	3	*1-σ*	3	*1-σ*	5	*1-σ*	5	*1-σ*
MnO	0.21	*0.02*	0.25	*0.01*	0.21	*0.02*	0.21	*0.02*	0.21	*0.03*
FeO_t	29.23	*0.13*	28.83	*0.32*	28.98	*0.37*	29.73	*0.22*	32.44	*0.13*
MgO	13.81	*0.03*	14.00	*0.13*	14.09	*0.16*	13.55	*0.18*	13.89	*0.12*
Al_2O_3	32.43	*0.19*	34.09	*0.16*	34.00	*0.08*	31.60	*0.25*	32.97	*0.33*
TiO_2	0.48	*0.06*	0.49	*0.04*	0.43	*0.10*	0.50	*0.10*	0.49	*0.12*
Cr_2O_3	22.80	*0.52*	21.22	*0.38*	21.16	*0.76*	23.50	*0.17*	21.78	*0.50*
Total	98.89		98.83		98.85		99.05		101.71	
FeO	16.07		16.03		15.79		16.38		17.03	
Fe_2O_3	14.61		14.22		14.65		14.83		17.12	
SUM	100.41		100.29		100.33		100.57		103.49	
Cr#	32.04		29.46		29.45		33.29		30.71	
Mg#	60.16		60.55		61.07		59.25		58.90	

Table 10. (cont.)

Sample	**KS-12-33**		**KS-12-33**	
Rock Type	Olivine Clinopyroxenite		Olivine Clinopyroxenite	
grain	CR1		CR1	
location	core		rim	
n=	7	*1-σ*	4	*1-σ*
MnO	0.26	*0.04*	0.26	*0.03*
FeO_t	32.69	*0.20*	32.53	*0.60*
MgO	12.37	*0.17*	12.01	*0.66*
Al_2O_3	24.62	*0.18*	24.66	*0.52*
TiO_2	0.80	*0.06*	0.81	*0.08*
Cr_2O_3	29.17	*0.23*	29.08	*0.80*
Total	99.82		99.26	
FeO	17.65		18.02	
Fe_2O_3	16.71		16.12	
SUM	101.57		100.96	
Cr#	44.28		44.18	
Mg#	55.20		53.94	

5. Discussion of Results

This project is the first undertaking of a comprehensive analysis of the Kasatochi enclaves and offers initial constraints on their origins. Because gabbroic enclaves of Kasatochi's 2008 and pre-2008 eruptive sequences have been analyzed to a limited degree (Waythomas et al., 2010; Neill, 2013), some references will be made here to Neill's (2013) analyses of gabbroic enclaves. In addition, comparisons to host-lava chemistry rely on the work of Neill (2013), who thoroughly examined the chemistry of the host lavas. This is the first report of ultramafic enclaves from Kasatochi.

The gabbroic enclaves are texturally and mineralogically distinct from the ultramafic enclaves, and the origin of each will be treated separately. I will begin by examining the idea that the gabbroic enclaves are cumulates of the basaltic andesite erupted in 2008 at Kasatochi. I will then compare the ultramafic enclaves to mantle xenoliths and the gabbroic enclaves. Finally, I will compare the Kasatochi enclaves to volcanic inclusions from the neighboring volcanoes (Fig. 1) Adagdak (Adak Island), Moffett (Adak Island), and Kanaga to look at regional continuity in igneous processes in the Aleutian subduction zone.

5.1 Analysis of Gabbroic Enclaves

Texturally and compositionally, the hornblende gabbro enclaves from Kasatochi are similar to cumulate inclusions from other volcanoes of the Central Aleutian arc. In the Central Aleutians, inclusions found on other volcanic islands include cumulates that formed from a contemporaneous host magma, and cognate xenoliths with crystals both related (cumulate) and unrelated (relict mineral phases with disequilibrium textures) to the host lava (Conrad et al., 1983). In most arcs, cumulates are further divided based on mineral abundance as: (1) olivine-bearing gabbro and clinopyroxenites, (2) olivine-rich ultramafic rocks and gabbronorite, and (3) rocks with cumulus amphibole (Beard, 1986). Based on the presence of (1) up to 20 vol.% pore space and interstitial glass, (2) textural and modal layering, (3) euhedral and acicular mineral textures, and (3) unzoned minerals,

the hornblende gabbro enclaves from Kasatochi are interpreted as cumulates from a host magma that is co-evolving with and genetically related to.

Texturally, the gabbro enclaves are not uniform; they are found as layered and un-layered, fine-grained to pegmatitic, and can contain both prismatic and acicular mineral habits. However, all gabbroic samples examined here are chemically and mineralogically related to each other. They are composed of the same minerals: plagioclase ($An_{91–93}$), diopside, pargasitic amphibole, and accessory magnetite. Whole-rock compositions for major element oxides fall within a 3 wt.% range (e.g., 40–43 wt.% SiO_2; Table 5). Mineral compositions are also uniform, with no zoning in either plagioclase or amphibole, even for crystals that are >1 cm (section 4.7).

The gabbro textures reveal important clues to the early crystallization of crystals in the magma chamber. Firstly, the interstitial glass, which makes up to 25% of the total volume of all of the Kasatochi gabbro enclaves, is somewhat common in igneous inclusions (e.g., Hermes and Cornell, 1981; Wager, 1962; Bacon, 1986; and Eichelberger and Gooley, 1977) including Adagdak and Moffett volcanoes on Adak Island (DeBari et al., 1987; Conrad et al., 1983). Its presence indicates that the rocks did not completely crystallize before they were erupted and that the enclave was rapidly cooled during eruption (e.g., Conrad et al., 1983). Secondly, the presence of euhedral crystals growing into open voids further suggests equilibrium with a hydrous magma or vapor phase prior to eruption.

The modal and textural layering in many of the hornblende gabbro enclaves is also common in cumulate rocks. Layering forms either as crystals (1) grow off magma chamber walls, (2) accumulate along walls by magma convection, or (3) accumulate by crystal settling/floating (e.g., Wager et al., 1960). Large (>1cm), aligned minerals, dominantly acicular or prismatic hornblende, in a finer-grained isotropic groundmass of plagioclase, hornblende, and clinopyroxene, often define the layering in the Kasatochi enclaves (Fig. 5A, B). In many samples acicular amphiboles grew in the same general direction (Fig. 4A). Because the layering often includes radiating, acicular amphibole it seems most likely that the crystals grew in place and formed by growing outward from

magma chamber walls (Fig. 21). The net result is compositional layering that would have been parallel to chamber walls and acicular crystals that would have been perpendicular to chamber walls (Fig. 21). The bulk of the samples have unaligned textures suggesting that the rocks were not formed by convection or crystal settling, where a pervasive alignment of crystal grains is expected.

Based on the presence of unzoned, euhedral minerals surrounded by anhedral crystals and melt (Fig. 6), the Kasatochi enclaves can be further classified as orthocumulates (Wager et al., 1960). Orthocumulates are a type of cumulate with more than one cumulus mineral and intercumulus liquid or crystal phases in equilibrium with a contemporaneous magma (Wager et al., 1960). The lack of zonation in plagioclase and amphibole, in addition to the presence of elongate, acicular amphibole, suggests rapid growth under unchanging P/T conditions in a hydrous, chemically stable magma. There are no alteration rims on minerals in contact with interstitial melt, and exsolution is rare, only present in some clinopyroxene, suggesting equilibrium conditions between the melt and the crystallizing minerals. If the gabbros are true orthocumulates, then the melt should be in equilibrium with, and related to, the host lava.

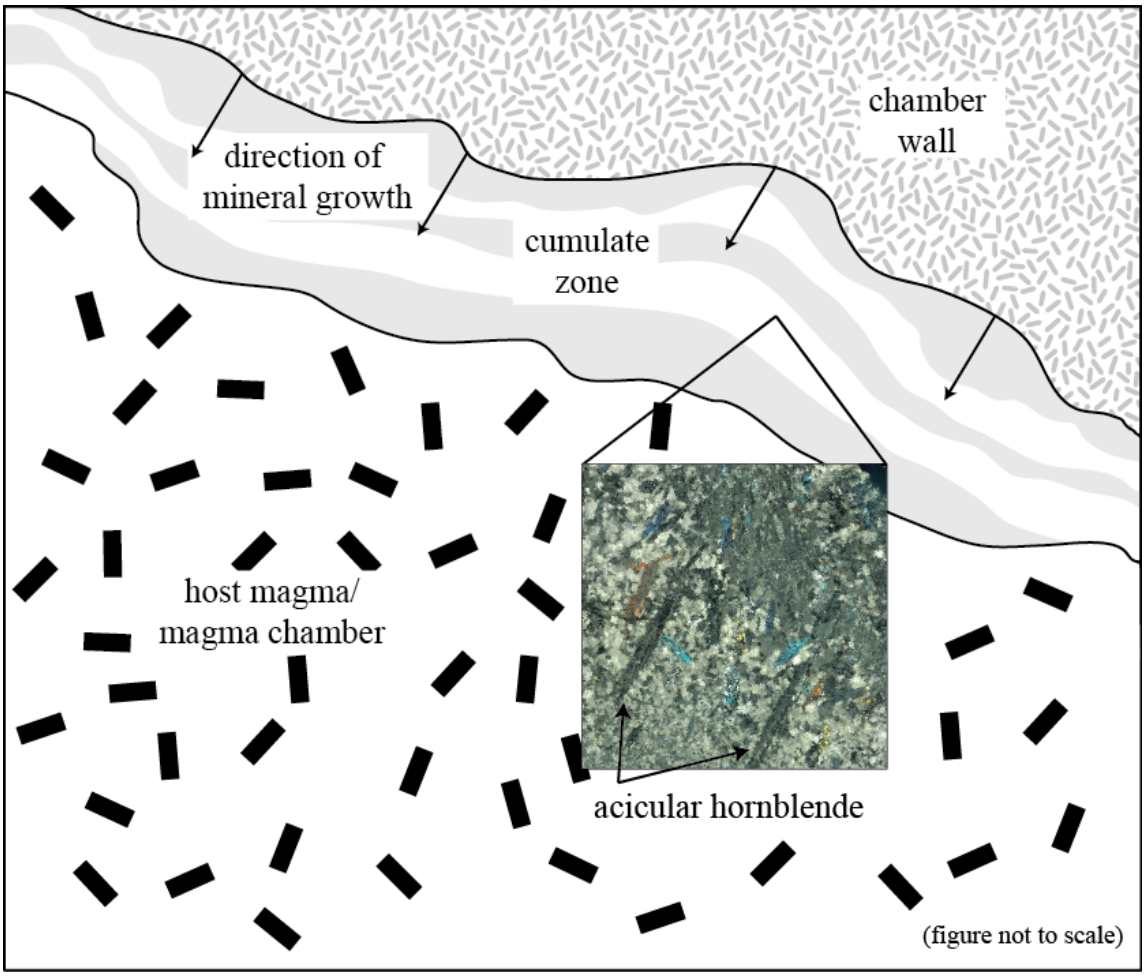

Figure 21. Cumulate Formation in Magma Chambers
This schematic diagram of cumulate formation within a magma chamber shows that acicular crystals (primarily hornblende) would grow perpendicular to the chamber walls towards the middle of the chamber and layering would form parallel to chamber walls.

5.2 Relationship Between Host Lava and Gabbroic Enclaves

If the gabbroic enclaves from Kasatochi are indeed cumulates as suggested by their textures and compositions, they should be chemically related to the lavas in which they are found. In order to examine their relationship, I rely on chemical analyses of the 2008 eruptive products by Neill (2013). Based on chemical heterogeneity in the 2008 eruptive products, there are two distinct systems: basaltic andesite and andesite (Neill, 2013). Blocks of gabbro are found in place exclusively within the 2008 basaltic andesite (Waythomas et al., 2010). Based on their whole-rock compositions, they could be fractionated from either the basaltic andesite or a parental magma related to both the basaltic andesite and the andesite. To investigate these two possibilities further, I will also show compositions of interstitial glass that were analyzed by C. Nye (written communication).

The glass and host lavas are compositionally more fractionated than the gabbros, but all samples fall along well-defined trend-lines in major oxides vs. SiO_2 compositions (Figs. 22 & 23), suggesting that they are related genetically and compositionally. The SiO_2 content of the gabbroic enclaves is lower than the basaltic andesite and andesite by 15–20 wt.% and is lower than the interstitial glass by 10 wt.% (Figs. 22 & 23), suggesting that the glass and the host lavas are more chemically evolved than the gabbros. This is supported by the greater abundance of compatible elements (except Ni and Cr) and lesser abundance of incompatible elements in the gabbros than in the host lavas. For example, the gabbros contain ~4 wt.% more MgO than either the host lavas or the glass (Fig. 22A). This is because they contain up to 20% Mg-rich clinopyroxene. The higher Ca-content (~4 wt.%; Fig. 22B) in the gabbros is a reflection of Ca-rich clinopyroxene and calcic plagioclase ($An_{>90}$) in contrast to the basaltic andesite, which contains less clinopyroxene and less-calcic plagioclase ($An_{70–90}$; Neill, 2013). The basaltic andesite and andesite are compositionally more evolved than the gabbro because they contain more alkalis and less Ca and Mg (Figs. 22 and 23). The glass is also more evolved than the gabbro because it has ~3 wt.% alkalis as opposed to ~1 wt.% for the gabbros (Fig. 23).

An AFM plot, which categorizes rocks based on trends formed by fractional crystallization of a parental magma (Irving and Baragar, 1971), shows that the gabbros fall along a tholeiitic trend, whereas the host lavas follow a calc-alkaline fractionation trend. In theory, tholeiitic and calc-alkaline series are petrologically distinct and should follow different fractionation trends—the tholeiitic series above the dashed line and the calc-alkaline series below (Fig. 24). The fact that the gabbros, their interstitial fluid and the host lavas all fall along trends in major element concentrations that can be explained by fractionation, suggests that the relationship between tholeiitic basalts (the gabbro) and calc-alkaline lavas (the glass and the host lavas) is more complicated. This is supported by two recent studies in the Izu-Bonin and Aleutian arcs, which propose that long magma residence times (on the order of several thousand years), crystal fractionation, wall-rock assimilation, and magma mixing between basaltic and more felsic material all affect and complicate the evolution of tholeiitic and calc-alkaline magmas at subduction zones (Tatsumi and Suzuki, 2009; George et al., 2004).

The basaltic glass filling the interstitial pore space in the gabbros is ~50 wt.% SiO_2, which is closer to the basaltic andesite host lava (52–57 wt.% SiO_2) than to the gabbros (40–45 wt.% SiO_2). In addition, the concentration of CaO, MgO, and alkalis is within 2 wt.% for the basaltic andesite and the interstitial glass (Fig. 22 & 23). In contrast, the total amount of alkalis in the gabbroic enclaves reach 1.5 wt.% lower (Fig. 23) and CaO is up to 4 wt.% higher (Fig. 22B) than in the interstitial glass. Concentrations of Ni and Cr are higher in the interstitial glass than in the gabbros (Fig. 25), which could mean that both the gabbros and the basaltic andesite are products of fractionation from a parental magma similar in composition to the glass preserved in the gabbros. In this model, the gabbros formed by the extraction and accumulation of plagioclase, hornblende and clinopyroxene from the basaltic parental magma and the basaltic andesite is a more silicic magma that remained after crystal removal. A second possibility is that all three (glass, gabbro, and basaltic andesite) are the result of fractionation of a magma more mafic than the gabbro and that the interstitial glass is melt that was trapped within the gabbro midway to “evolving” to more silicic basaltic

andesite. Based on the trends and similarities in major element composition, it seems likely that the interstitial glass, gabbro, and basaltic andesite are indeed related. The high amounts of Ni and Cr in the interstitial glass suggest that the glass is the least evolved of the three rock types and is representative of the magma that was parental to both the gabbro and basaltic andesite.

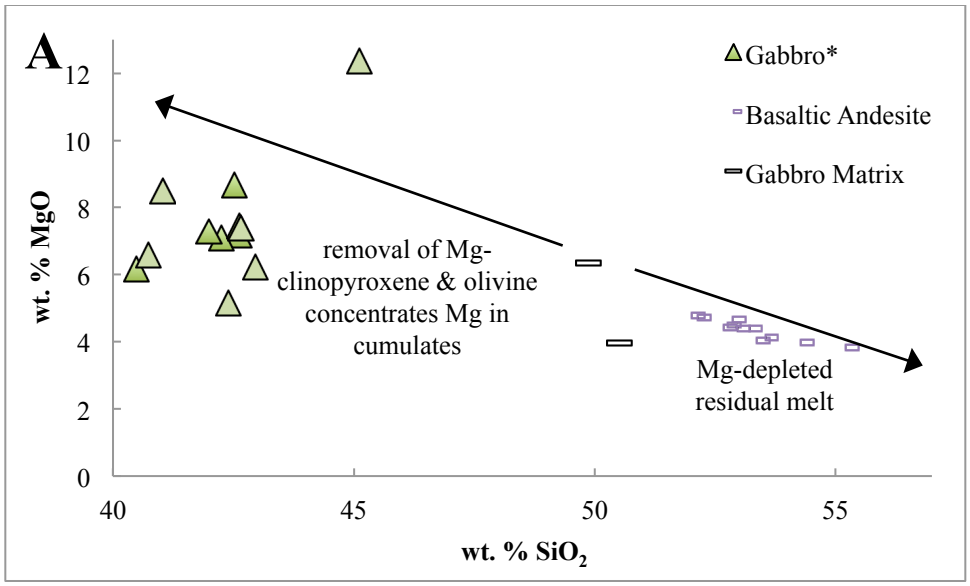

Figure 22. Host Lava and Gabbro Whole-Rock Compositions
Comparison between whole-rock major elements in gabbros, interstitial glass (Gabbro Matrix), and host basaltic andesite shows that (A) MgO is higher in the gabbros, which have less SiO_2 than the host rocks and the interstitial glass; and (B) wt.% CaO is higher for the gabbro samples than the glass and the basaltic andesite. These samples fall along trend lines that reflect fractionation: as SiO_2 increases (as the melt evolves) the amount of MgO and CaO systematically decrease along a linear trend. (Additional gabbro, basaltic andesite, and glass analyses are from Neill (2013)).

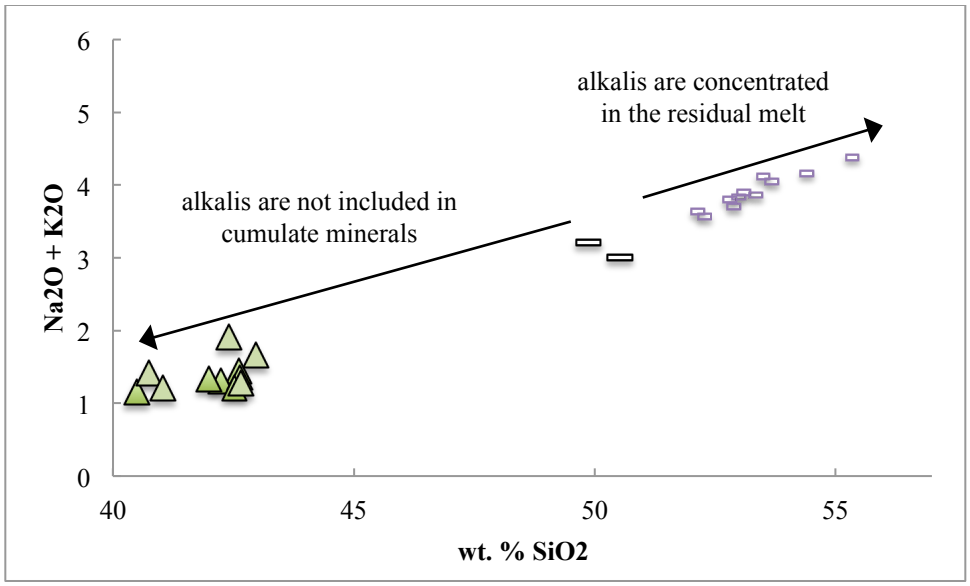

Figure 23. SiO_2 vs. Total Alkalis in Host Lava and Gabbro
The total alkali content of the gabbros lies along a trend line that connects them compositionally to the interstitial glass and the 2008 basaltic andesite. The symbols are the same as in Fig. 22 (additional gabbro, basaltic andesite, and glass analyses are from Neill, 2013).

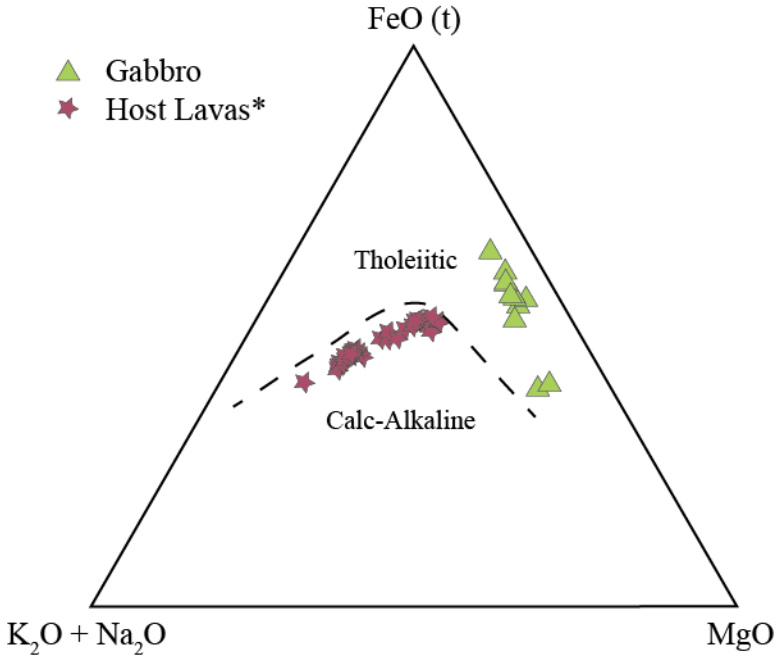

Figure 24. AFM Diagram
The basaltic andesite and andesite (*plotted as Host Lavas) follow a calc-alkaline trend whereas the enclaves are all follow a tholeiitic trend. Diagram and dashed line based on Irving and Baragar (1971). Compositions for host lava are from Neill (2013).

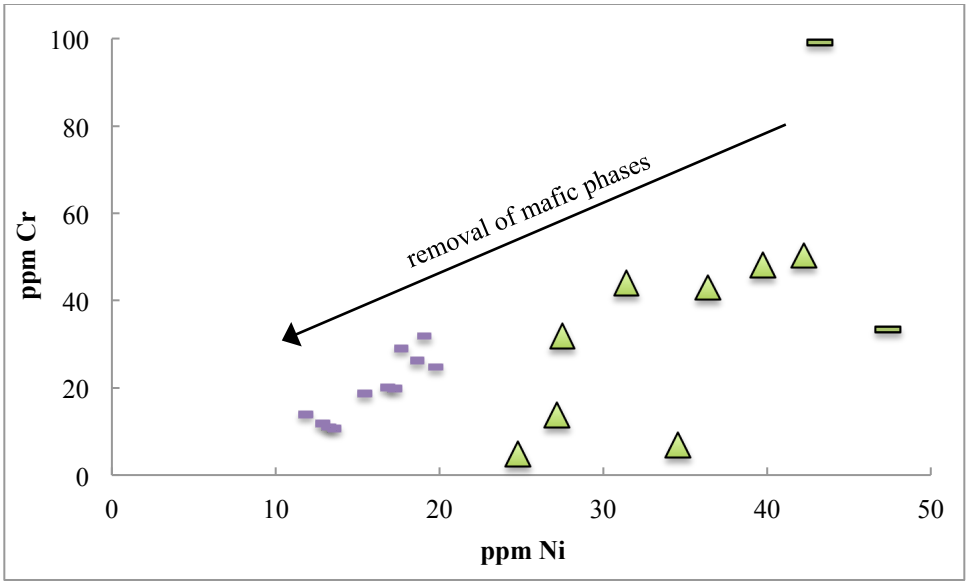

Figure 25. Ni vs. Cr in Host Lava and Gabbro
Ni and Cr are higher in the gabbros than in the basaltic andesite and even higher in the interstitial glass (symbols are the same as Fig. 22A). The high Ni and Cr values support the argusment that the interstitial glass is the remainder of melt that is parental to the gabbro and basaltic andesite.

5.3 Analysis of Ultramafic Enclaves

Based on mineralogy alone, it is tempting to seek a mantle origin for the ultramafic enclaves. To examine this relationship, I compare the Kasatochi ultramafic enclaves to xenoliths interpreted as being of mantle origin. I chose to use xenoliths from Shiveluch and Avacha, subduction-zone volcanoes that are located in Kamchatka, Russia (Bryant et al., 2007; Ionov, 2010).

The presence of (1) minor exsolution in clinopyroxene, (2) clinopyroxene replacing olivine, and (3) interstitial hornblende (replacing both olivine and clinopyroxene) that is the same composition as the amphibole in the hornblende gabbro, suggests that the enclaves are xenoliths that were hosted in a hydrous melt where they were unstable. If the ultramafic enclaves were unstable in the host melt, then they could have formed within the mantle and it would follow that the minerals in the ultramafic enclaves should have mantle compositions.

Olivine and spinel, both present in all ultramafic samples, are two minerals commonly used to characterize mantle-derived rocks (Bryant et al., 2007; Arai, 1994). The olivine-spinel mantle array (OSMA), (Arai, 1987; 1990; and 1994) is a field of positively correlated Fo-content in olivine and Cr# in spinel that defines mantle compositions for these minerals. I plotted olivine and spinel compositions for one Kasatochi sample, as well as the values for Shiveluch xenoliths and dunite cumulates from Adak (DeBari et al., 1987), on the OSMA diagram (Fig. 26). The minerals from the Kasatochi olivine-clinopyroxenite are distinct from and do not fall within the OSMA and are more closely related to samples from Adak Island. Spinel from mantle xenoliths is enriched in Cr in relation to Mg and Al (e.g., Arai, 1987). I find that while Kasatochi spinel Mg# overlaps that of mantle-derived spinel, the Cr# is much lower (Fig. 27). Additionally, the atomic amount of Cr (compared to Al and Fe^{3+}) is higher for the mantle peridotites than for the Kasatochi enclaves (Fig. 28).

Olivine chemistry is also a useful indicator of mantle origin (Bryant et al., 2007; Ionov, 2010). Ni can substitute for Fe^{2+} in olivine under mantle conditions and it follows that there is more Ni in mantle olivines than in olivines formed in non-mantle igneous

environments. The Fo-content of olivine from Avacha and Shiveluch mantle xenoliths ($Fo_{81–87}$) overlaps the composition of olivines from Kasatochi wehrlite and olivine-clinopyroxenite enclaves ($Fo_{82–86}$). However, wt.% NiO is >0.15 in the mantle olivines and <0.15 wt.% in the Kasatochi olivines (Fig. 29). The amount of NiO is therefore too low to support a mantle source.

Whole-rock and mineral compositions further indicate that these enclaves are not mantle-derived (Fig. 30). Values of compatible elements like Ni, Cr, and, Mg, which are elevated in the mantle are low in the ultramafic samples, whereas Ti, an incompatible element, is high. Whole-rock compositions for Kasatochi ultramafic enclaves do not overlap with the fields for the mantle xenoliths. In fact, Kasatochi enclaves, although similar in wt.% SiO_2 to the mantle xenoliths, exhibit compositions of more fractionated rocks by having lower wt.% MgO, Ni and Cr (ppm), and higher wt.% TiO_2. The combination of the mineral and whole-rock compositions for the ultramafic enclaves strongly suggests that the Kasatochi enclaves do not originate in the mantle.

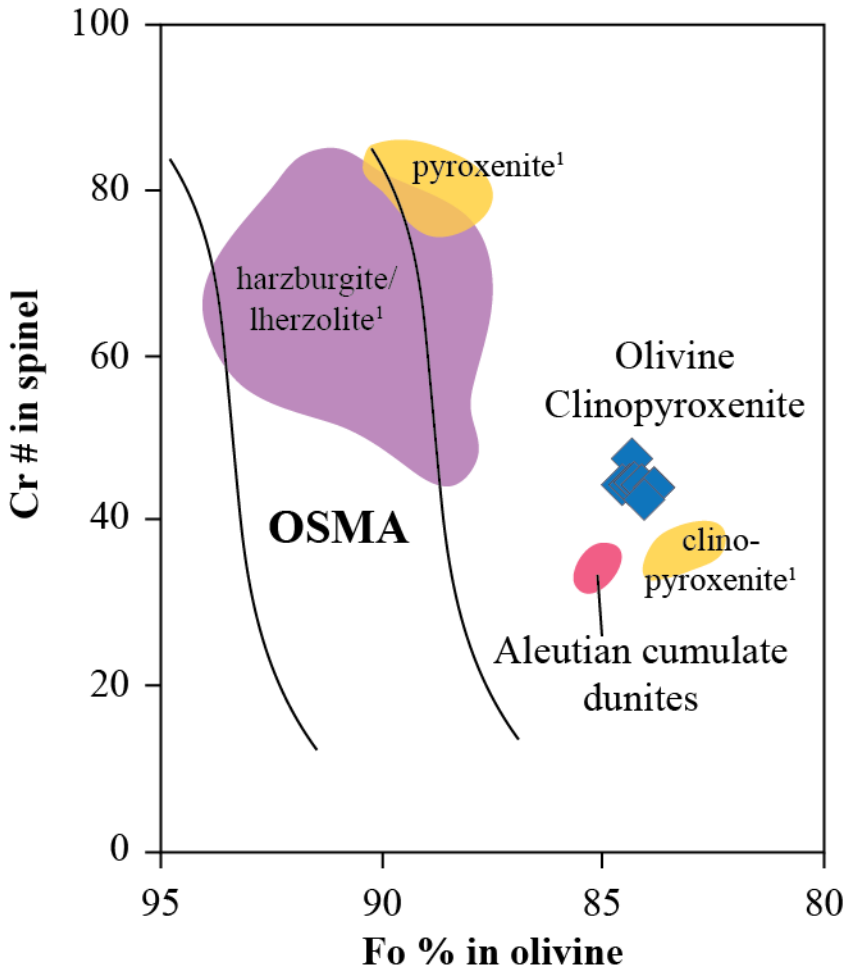

Figure 26. OSMA Diagram
The OSMA is a compositional zone defined by Arai (1994) that includes compositions for olivine and spinel that define a field for mantle-derived rocks. The Kasatochi sample is a clinopyroxenite (blue squares) compositionally more similar to Aleutian cumulate dunites (Aleutian data from DeBari et al., 1987).
[1]Bryant et al., 2007

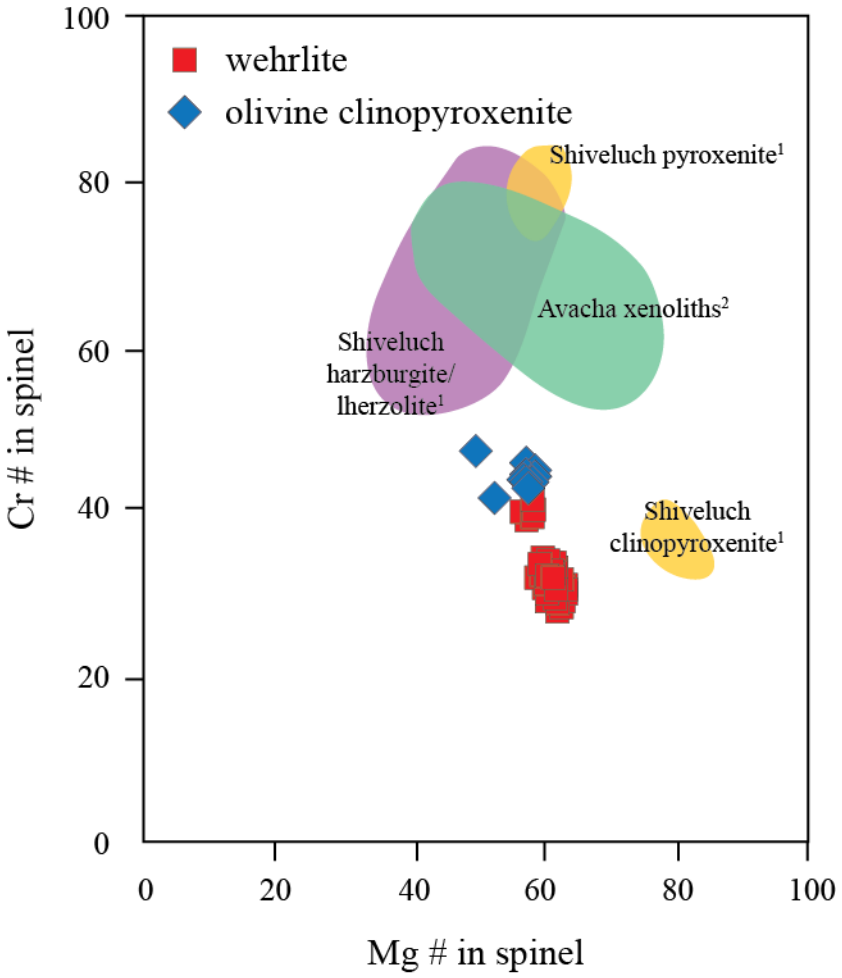

Figure 27. Mg# in Ultramafic Enclave Spinel Compared to Mantle Spinel
A comparison between the xenoliths from two Kamchatka andesitic volcanoes, Avacha and Shiveluch, and the spinel from peridotite and pyroxenite enclaves at Kasatochi suggest a different heritage. The Mg# is comparable, but the Cr# for the Kasatochi enclaves is significantly lower (except for the clinopyroxenite). Cr# = atomic Cr/ (Cr+Al) and Mg# = atomic Mg/ (Mg+Fe^{2+}) [1]Bryant et al., 2007, [2]Ionov, 2010

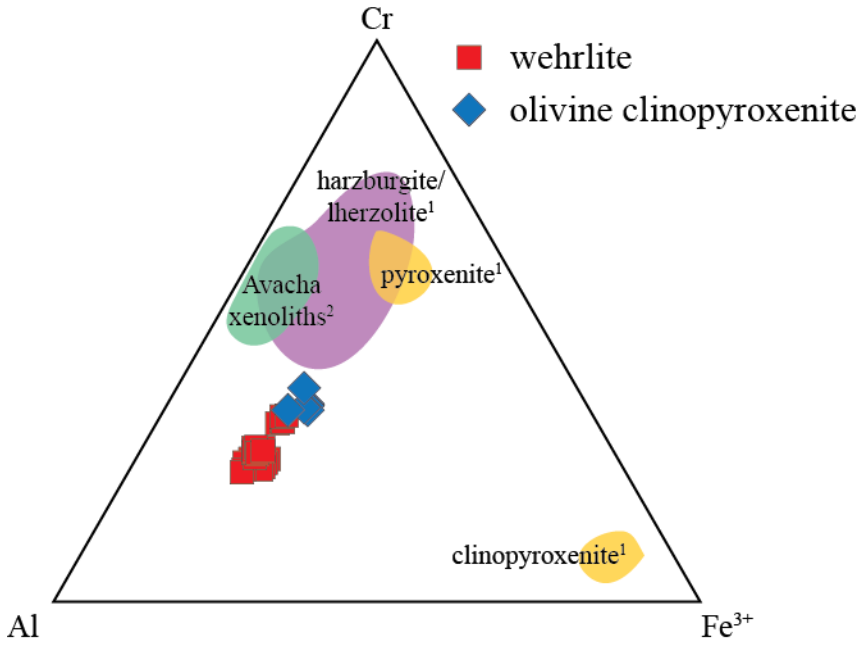

Figure 28. Spinel Ternary
The Cr-Al-Fe^{3+} ternary is another means of assessing the compositional diversity and origin of spinel. The enclaves from Kasatochi do not overlap with the fields for the Kamchatka mantle xenoliths. [1]Bryant et al., 2007, [2]Ionov, 2010

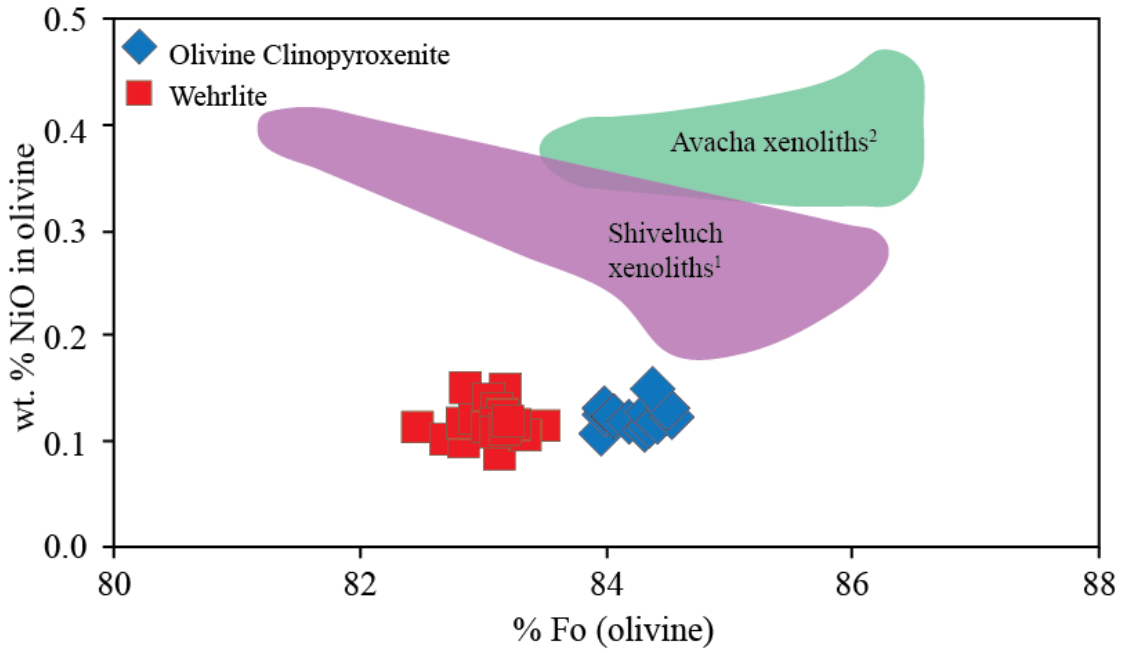

Figure 29. %Fo vs. wt.% NiO in Olivine Compared to Mantle Olivines
Another means of comparing mantle to cumulate compositions is using the Fo-content and wt.% NiO in olivine. In mantle rocks, the amount of Mg (Fo-content) as well as the amount of Ni is elevated, which is reflected in the olivine compositions (the dominant mineral in peridotites). Based on the Kamchatka xenoliths, the Kasatochi olivines have less NiO than they would if they were mantle-derived. [1]Bryant et al., 2007, [2]Ionov, 2010

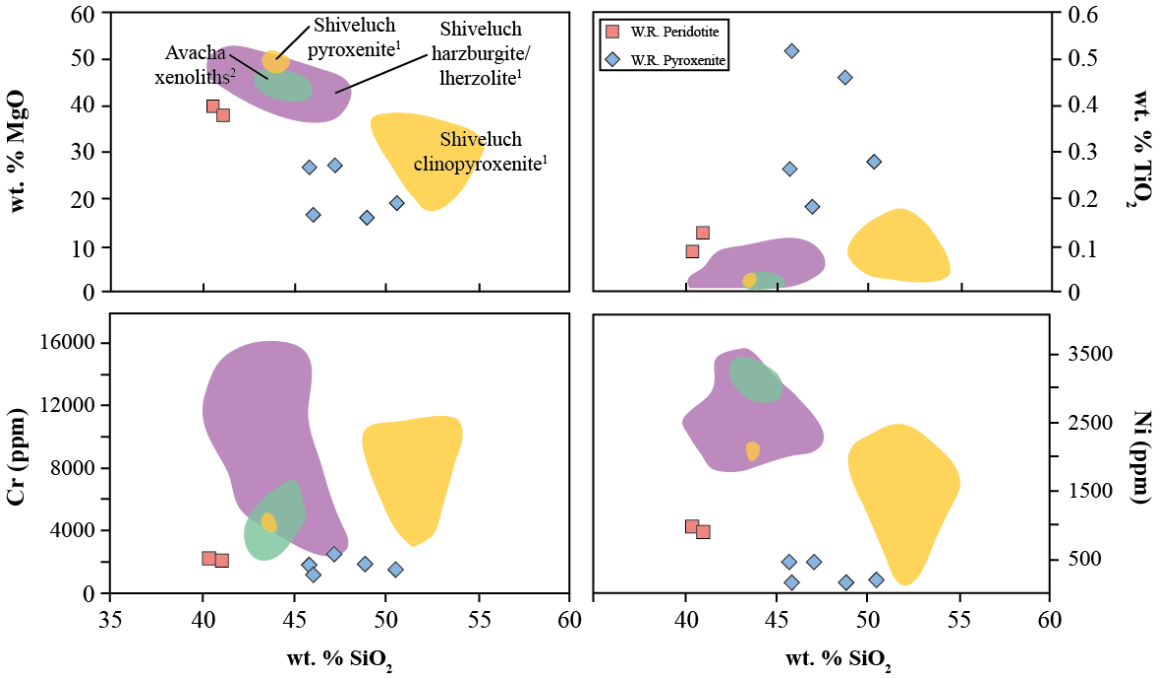

Figure 30. Whole-Rock Compositions Compared to Mantle Xenoliths
Whole-rock compositions for the ultramafic samples are not comparable to mantle compositions. The SiO_2 compositions are within the correct range, but compatible elements are mildly depleted and the incompatible element, TiO_2, is too high, especially for the pyroxenite. [1]Bryant et al., 2007, [2]Ionov, 2010

5.4 Relationship Between Ultramafic and Gabbroic Enclaves and the Host Lava

It is not uncommon for mafic and ultramafic enclaves to be included together in a single eruption (e.g. Aoki, 1971). If the mafic and ultramafic enclaves from Kasatochi are related, their whole-rock major- and trace- element compositions should fall along the same linear trend-line that connects the gabbroic enclaves to the interstitial glass and the basaltic andesite. The ultramafic enclaves are not related to the gabbros or basaltic andesite by compositional fractionation. Instead, the major element composition of the pyroxenites is wildly variable and the peridotites and pyroxenites both are compositionally distinct from the gabbroic enclaves, the interstitial glass within the gabbroic enclaves, and the basaltic andesite.

While the compositions of the ultramafic samples are more primitive than the basaltic andesite and the interstitial glass, they do not fall on an obvious fractionation trend-line. MgO is higher in samples with lower wt.% SiO_2, which reflects the abundance of Mg-rich minerals such as diopside and forsterite olivine in silica-poor rocks such as the ultramafic enclaves. However, the amount of MgO in the gabbroic enclaves is nearly as high as in the ultramafic enclaves (Fig. 31A), despite having the same, or lower, wt.% SiO_2. In comparison, CaO is scattered and varies by up to 8 wt.% in the pyroxenite samples (Fig. 31B). Interestingly, the pyroxenite enclaves fall along a trend-line between the basaltic andesite and the gabbroic enclaves, but the peridotites (wehrlites) have very low CaO compared to their wt.% SiO_2.

There is also a distinction between Ni and Cr compositions in the ultramafic samples and the gabbroic enclaves, interstitial glass, and basaltic andesite (Fig. 32). There is >150 ppm more Ni in the pyroxenites, and >900 ppm more Ni in the peridotites, than in the three other rock types. There is an even greater difference in Cr-content, with >900 ppm more Cr in the pyroxenites and >1900 ppm more Cr in the peridotites than in the gabbros, interstitial glass, or basaltic andesite. The large difference in Ni and Cr reflects the mineralogy of the samples: the olivine from the ultramafic enclaves is ~10% more forsteritic and contains up to 1.5 wt.% more NiO than olivine from the gabbros (Neill,

2013) (Fig. 33). Additionally, the oxide phase in the ultramafic enclaves is spinel, which contains 20–30 wt.% Cr_2O_3, while the oxide phase in the gabbros and basaltic andesite is magnetite, which contains <0.32 wt.% Cr_2O_3 (Neill, 2013).

Based on the lack of fractionation-based trends, it seems unlikely that the ultramafic enclaves were crystallized from the same system as the gabbro and basaltic andesite.

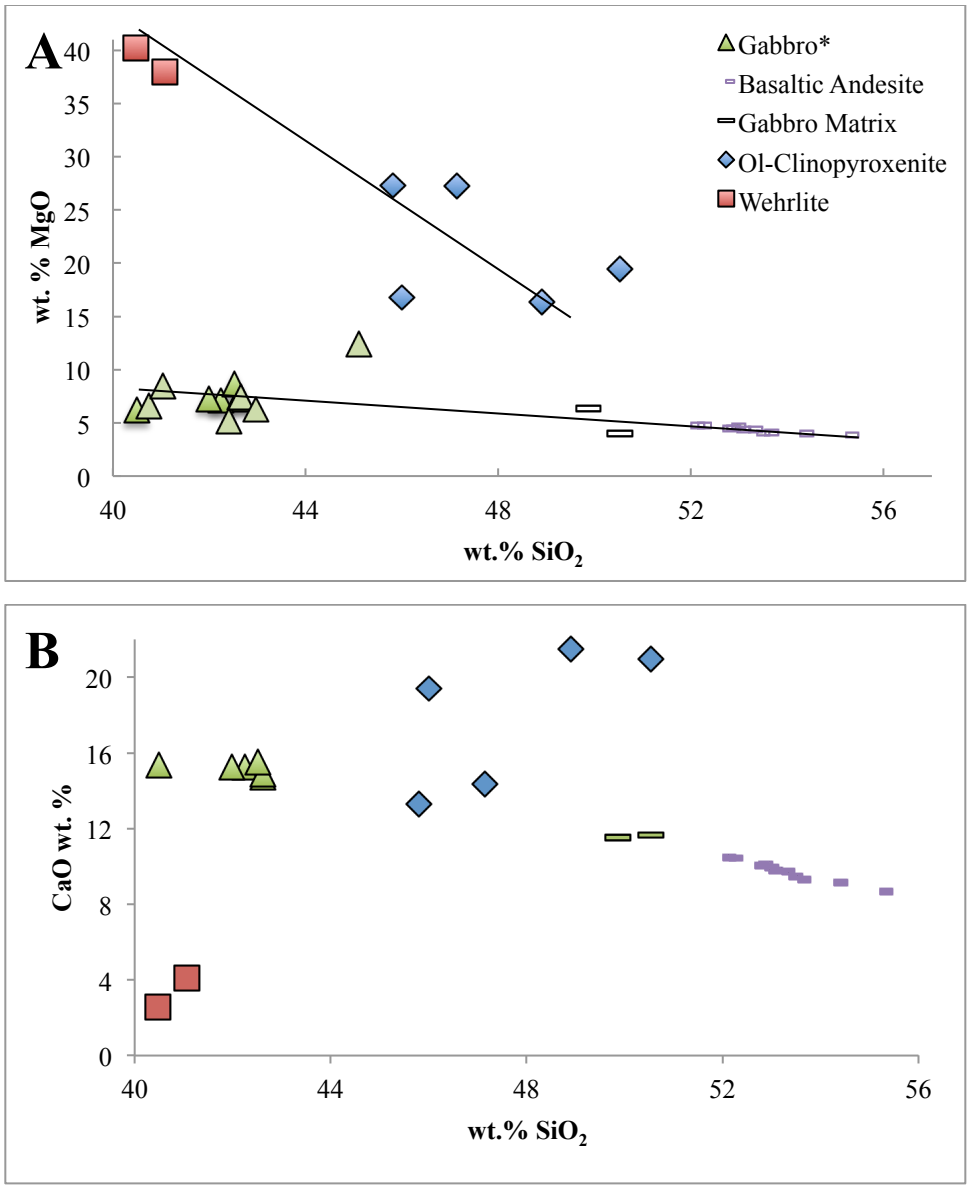

Figure 31. CaO and MgO in Ultramafic and Mafic Enclaves Compared to Host Lava
Whole-rock compositions of the wehrlite and olivine-clinopyroxenites compared to the gabbroic enclaves, interstitial glass, and basaltic andesite: (A) The amount of MgO is higher than the gabbros, glass, and basaltic andesite by 10 wt.% for the olivine-clinopyroxenite and by 35 wt.% for the wehrlite. These samples fall along a separate trend-line from the one relating the gabbro and basaltic andesite. (B) There is no apparent trend that forms between the ultramafic samples and the gabbros or the basaltic andesite. The SiO_2 content of the olivine-clinopyroxenite samples falls between the gabbro and the interstitial glass, but there is scatter in both the amount of SiO_2 and the amount of CaO. The wehrlite samples plot far from the trend-line between gabbros and host rock.

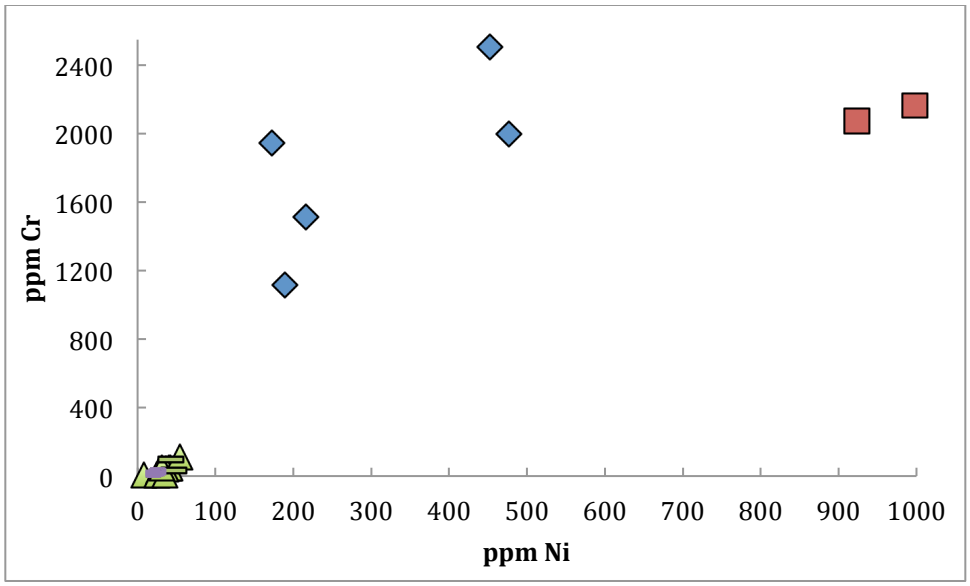

Figure 32. Ni and Cr in Ultramafic and Mafic Enclaves Compared to Host Lava
Both Ni and Cr are significantly more concentrated in the ultramafic samples than the gabbros, host rock, or the basaltic glass. All the values for gabbro, host rock, and glass are <50 ppm Ni and <100 ppm Cr. For comparison, the olivine-clinopyroxenites have 200–500 ppm Ni and 1000–2500 ppm Cr and the wehrlite samples have ~1000 ppm Ni and ~2000 ppm Cr. Symbols are the same as Fig. 31.

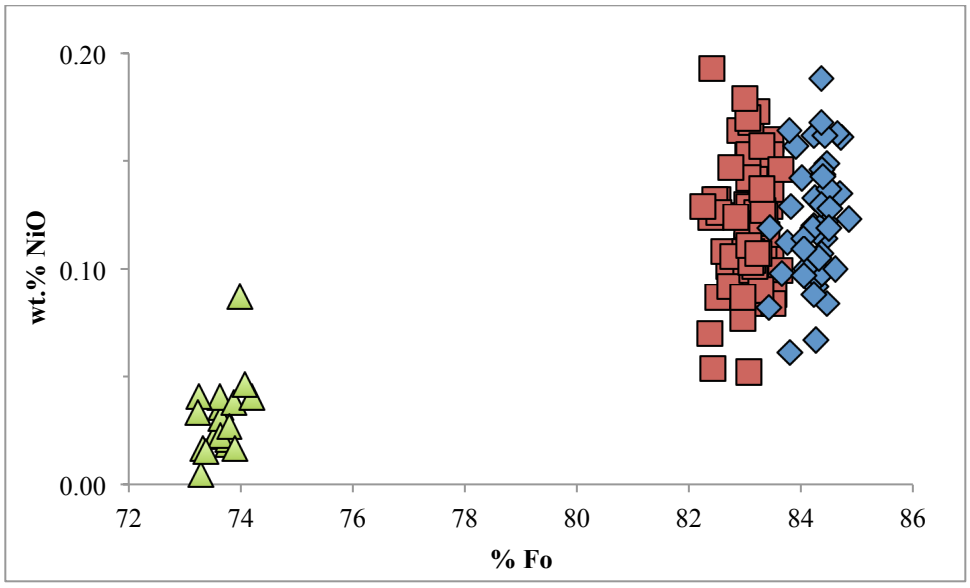

Figure 33. %Fo vs. wt.% NiO in Ultramafic and Mafic Olivines
A comparison between Fo-content and wt.% NiO in olivine within gabbroic and ultramafic enclaves shows that ultramafic samples contain more Ni (0.5–0.2 wt.%) and contain olivines that are more Fo-rich (Fo_{73} in gabbro and $Fo_{82–85}$). Symbols are the same as Fig. 31. The gabbro olivine analysis is from Neill (2013).

5.5 Regional Comparison to Inclusions from Adak Island Lavas

Inclusions from Adak Island lavas (Fig. 1) fall into three texturally distinct categories (Conrad et al., 1983), the cumulate and composite are comparable to the Kasatochi enclaves. The cumulate inclusions are compositionally related to the host rock (Conrad et al., 1983 and references therein), just as the Kasatochi gabbros are interpreted here as cumulates related to the basaltic andesite in which they are hosted. On the other hand, the Kasatochi peridotites and pyroxenites are distinct from the 2008 lavas and may therefore be compared to the Adak composite xenoliths, which are thought to originate in the lower crust and upper mantle (DeBari et al., 1987). It is possible that the ultramafic enclaves from Kasatochi share a similar origin to the Adak inclusions. This comparison contributes to a regional distribution of enclaves that will help lead to a better understanding of variation in igneous processes along the strike of the arc and of the crustal structure below the surface of the arc.

The same minerals (amphibole, plagioclase, clinopyroxene, magnetite, and olivine) with similar compositions are found in the hornblende gabbro inclusions from both Kasatochi and Adak (Neill, 2013; Conrad et al., 1983). Plagioclase in the Adak inclusions is Ca-rich anorthite up to An_{95} (Conrad et al., 1983) and overlaps with the plagioclase in the Kasatochi gabbros, which are $An_{91–95}$. Recalculated amphibole compositions from both Kasatochi and Adak inclusions have Ca >1.5 pfu, (Na+K) > 0.5, and $Fe^{3+}<^{iv}Al$ and plot as pargasite (Fig. 34). Clinopyroxene in the gabbros is diopside in both the Adak inclusions and the Kasatochi enclaves (Conrad et al., 1983).

Similarly, the ultramafic sample suite from Kasatochi overlaps mineralogically and compositionally with the Adak composite xenoliths of Adak. The same rock types, wehrlite, olivine-clinopyroxenite, and clinopyroxenite, are found at Kasatochi and Adak volcanic centers and the minerals from these rocks are compositionally similar (DeBari et al., 1987). Olivines from Kasatochi ultramafic enclaves are Mg-rich, with $Fo_{83–87}$, and Ni (ppm) up 1900 (ppm) (DeBari et al., 1987). Clinopyroxene from Kasatochi is also compositionally similar to that of Adak inclusions, with 0.2–0.5 FeO_t/MgO and 0.1–0.9 wt.% Cr_2O_3 for both (Fig. 35; Pope, 1983; Conrad et al., 1983; DeBari et al., 1987). The

amount of Cr in the Kasatochi enclaves is slightly higher than the Adak inclusions with Cr# 30–40 for the Kasatochi enclaves compared to 22–35 in the Adak inclusions (Figs. 26, 27). Finally, ultramafic enclaves from both localities contain interstitial pargasite (Fig. 34) suggesting both were altered post-crystallization in a hydrous magmatic environment.

The similarities between the mineral compositions in the Kasatochi and Adak ultramafic inclusions suggest that the two formed by similar processes. Adak ultramafic inclusions were interpreted as forming via fractionation of water-undersaturated spinel lherzolite (DeBari et al., 1987). Although I do not conclude that the Adak and Kasatochi enclaves share the same parent magma, it is possible that the ultramafic enclaves from Kasatochi are also derived from water-undersaturated spinel lherzolite. Furthermore, it is probable, based on the presence of interstitial amphibole, that ultramafic enclaves from Kasatochi and Adak were altered in the presence of a fluid or hydrous phase.

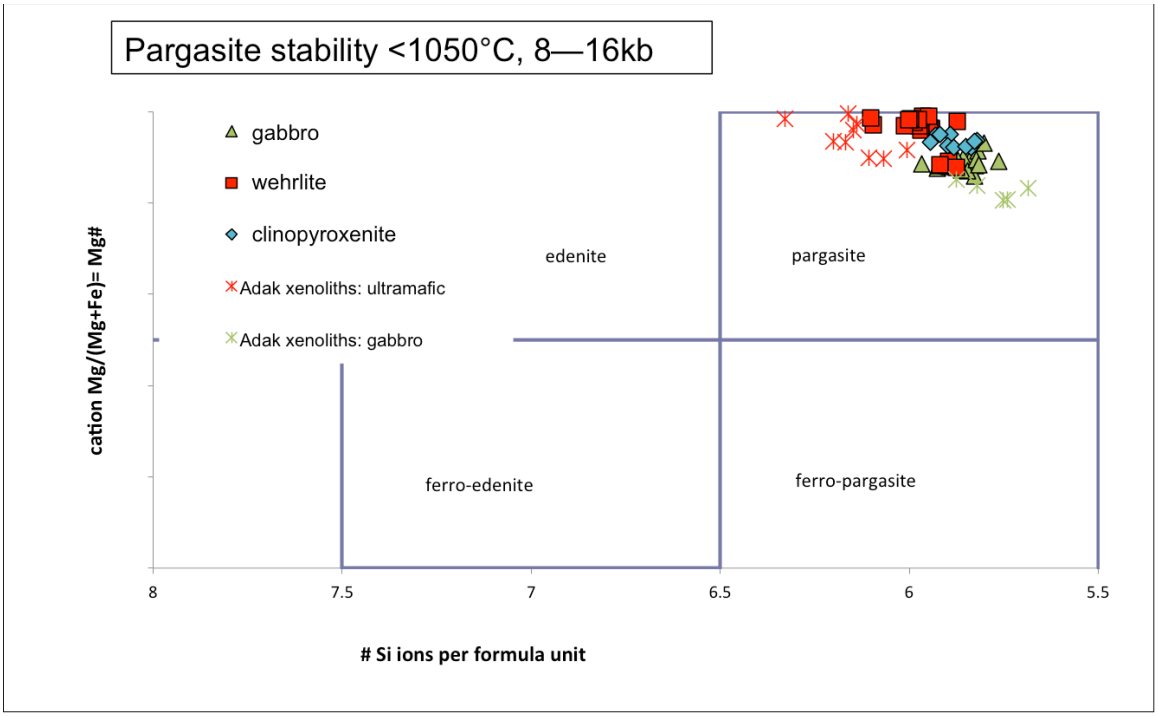

Amphibole Compositions

Figure 34. Kasatochi Amphibole Compositions Compared to Adak Inclusions
The amphiboles from Adak inclusions are pargasitic like both ultramafic and mafic Kasatochi enclaves. The presence of amphibole suggests a hydrous magmatic environment for the formation of the gabbroic enclaves. It also suggests that the ultramafic enclaves were altered in the presence of a fluid phase. Data for Adak inclusions are from Conrad and Kay, 1984.

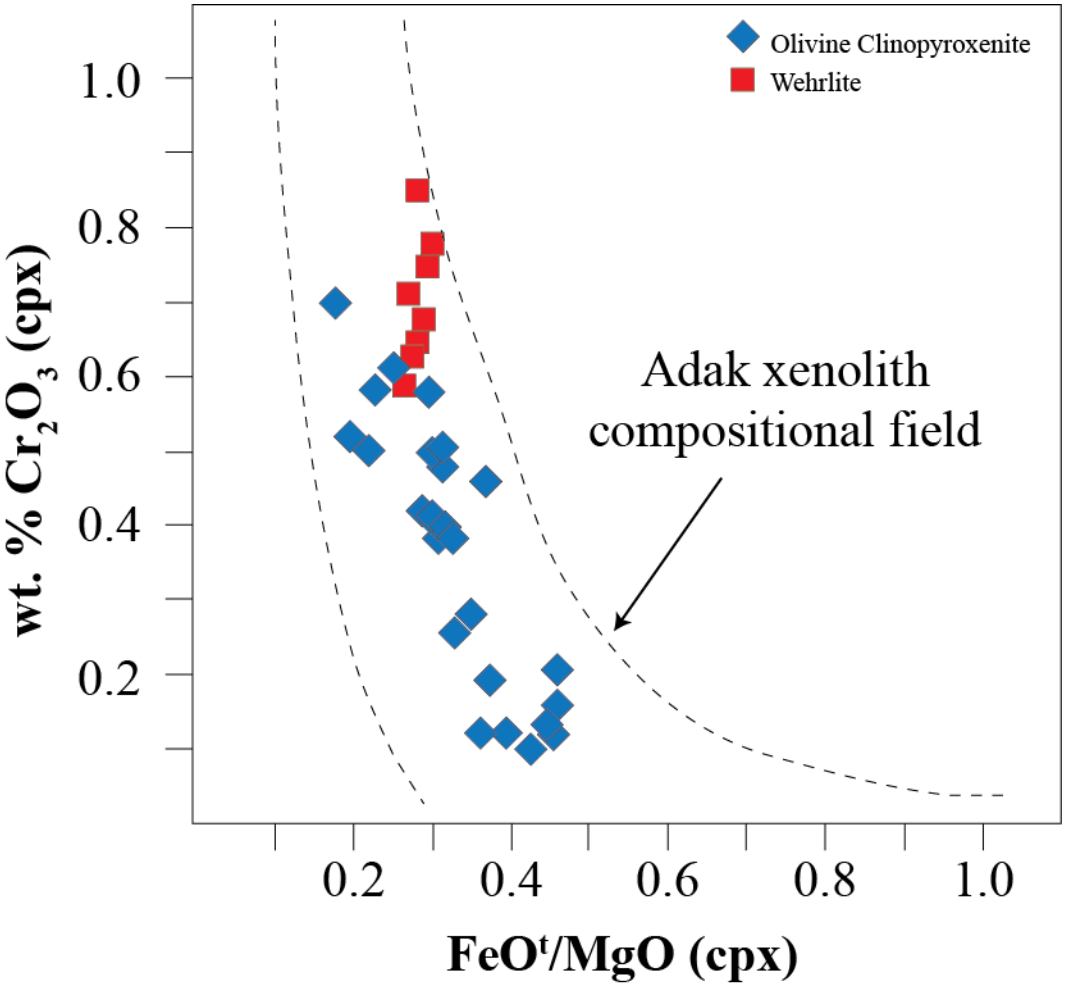

Figure 35. Kasatochi Clinopyroxene Compositions Compared to Adak Inclusions
Clinopyroxene compositions from ultramafic enclaves at Kasatochi are compared to the field for inclusions from Adagdak and Moffett (Adak volcanic centers). The data field is from DeBari and others (1987), Conrad and Kay (1984), and Pope (1983).

6. Conclusion

Hornblende gabbro, clinopyroxenite, olivine-clinopyroxenite, and wehrlite enclaves found on Kasatochi after the 2008 eruption are directly comparable to enclaves found elsewhere in the Central Aleutians (e.g. Adak Island). The enclave suites are divided into (a) a mafic suite characterized by modal layering, fine to pegmatitic grain size and acicular hornblende up to 6 cm long and (2) an ultramafic suite with granular textures that are quite different from the aligned layering found in the mafic suite. Interstitial melt is preserved within the mafic enclaves is likely the remainder of the melt that was crystallizing to form the mafic enclaves and the basaltic andesite erupted in 2008.

The mafic enclaves are orthocumulate hornblende gabbros that contain pargasitic amphibole, diopside, anorthite-rich plagioclase, and magnetite. The gabbros are compositionally related to the basaltic andesite as suggested by fractionation trends in whole-rock major- and trace-element abundances. Based on these trends and high concentrations of Ni and Cr, the interstitial glass is interpreted as the remnant of the parental magma that fractionated to form both the basaltic andesite and the gabbro.

The ultramafic enclaves are wehrlites, olivine-clinopyroxenites, and clinopyroxenite that include Ni-rich forsteritic olivine, diopside, spinel, and interstitial pargasite with compositions distinct from mantle xenoliths. Additionally, there is no apparent chemical relationship between the ultramafic enclaves and the 2008 basaltic andesite. Based on compositional similarities to ultramafic xenoliths from Adak Island, the ultramafic suite could have formed by the fractionation of spinel-lherzolite in the upper mantle.

The similarities between crystalline enclaves from Adak Island and Kasatochi begin to build a regional distribution of crustal fragments in the Central Aleutian arc. These inclusions are sampled directly from different depths, allowing us to look at the composition of crust that is otherwise only studied using geophysical methods. Furthermore, the hornblende gabbro samples are only partially crystallized, which

suggests that these are pieces of new crust currently forming within the magma system under Kasatochi. Understanding the Kasatochi enclaves is the first step towards building a regional database for crustal rocks from the Central Aleutian arc. Such a database will shed light on the structure and composition of the sub-arc crust and also on the processes that form new crust at intra-oceanic arcs.

7. References

Aoki, K.I. (1971) Petrology of ultramafic inclusions from Intino-megata, Japan. *Contributions to Mineralogy and Petrology*, **30(4)**, 314-331.

Arai, S., (1987) An estimation of the least depleted spinel peridotite on the basis of the olivine-spinel mantle array. *Neues Jahrb. Mineral. Monatsh*, 347-354.

Arai, S., (1990) What kind of magmas could be equilibrated with ophiolitic peridotites? *in* Ophiolites, Oceanic Crustal Analogue. Proc. Symp. "Troodos 1987" (editors: J. Malpas, E. Moores, A. Panayiotou and C. Xenophontos). *Geological Survey Dept., Min. Agric. Natural Resources, Nicosia*, 557-565 p.

Arai, S. (1994), Characterization of spinel peridotites by olivine-spinel compositional relationships: Review and interpretation. *Chemical Geology* **113**, 191–204.

Arculus, R.J. (1994) Aspects of magma genesis in arcs. *Lithos* **33(1–3)**, 189–208.

Bacon, C.R. (1986) Magmatic Inclusions in silicic and intermediate volcanic rock. *Journal of Geophysical Research* **9**, 6091–6112.

Beard, J.S. (1986) Characteristic mineralogy of arc-related cumulate gabbros: Implications for the tectonic setting of gabbroic plutons and for andesite genesis. *Geology* **14**, p. 848-851.

Bryant, J.A., Yogodzinski, G.M., and Churikova, T.G. (2007) Melt-mantle interactions beneath the Kamchatka arc: Evidence from ultramafic xenoliths from Shiveluch volcano. *Geochemistry Geophysics Geosystems* **8(4)**, 24 p. doi: 10.1029/2006GC001443.

Carmichael, I.S.E. (1967) The iron-titanium oxides of salic volcanic rocks and their associated ferromagnesian silicates. *Contributions to Mineralogy and Petrology* **14**, 36–64.

Conrad, W.K., Kay, S.M., and Kay, R.W. (1983) Magma mixing in the Aleutian arc: Evidence from cognate inclusions and composite xenoliths. *Journal of Volcanology and Geothermal Research* **18**, 279-295.

Conrad, W.K., and Kay, R.W. (1984) Ultramafic and Mafic Inclusions from Adak Island: Crystallization History, and Implications for the Nature of Primary Magmas and Crustal Evolution of the Aleutian Arc. *Journal of Petrology* **25(1)**, 88-125.

DeBari, S., Kay, S.M., and Kay, R.W. (1987) Ultramafic xenoliths from Adagdak volcano, Adak, Aleutian islands, Alaska: Deformed igneous cumulates from the MOHO of and island arc. *Journal of Geology* **95**, 329–341.

Deer, W.A., Howie, R.A., and Zussman, J. (1992) *Rock Forming Minerals*. London: Longman, 696 p.

Donovan, J.J., and Tingle, T.N. (1996) An Improved Mean Atomic Number Background Correction for Quantitative Microanalysis. *Journal of Microscopy and Microanalysis* **2(1)**, 1–7.

Eichelberger, J.C., and Gooley, R. (1977) Evolution of silicic magma chambers and their relationships to basaltic volcanism *in* The Earth's Crust (editors: J. G. Heacock, G. V. Keller, J. E. Oliver and G. Simmons). *American Geophysical Union, Washington, D. C.* p. 57–77. doi: 10.1029/GM020p0057

Fliedner, M. M., and Klemperer, S. L. (2000) Crustal structure transitions from oceanic arc to continental arc, eastern Aleutian Islands and Alaska Peninsula. *Earth and Planetary Science Letters* **179**, 567–579.

Fournelle, J. H., Marsh, B. D., and Myers, J. D. (1994) Age, character, and significance of Aleutian arc volcanism *in* The geology of Alaska (editors: Plafker, G., and Berg, H. C.). *Boulder, Colorado, Geological Society of America*, **G-1**, 723–757.

Gast, P.W. (1968) Trace element fractionation and the origin of tholeiitic and alkaline magma types. *Geochimica et Cosmochimica Acta* **32**, 1057–1086.

Geist, E. L., Childs, J. R., and Scholl, D. W., (1988) The origin of summit basins of the Aleutian Ridge: Implications for block rotation of an arc massif: Tectonics **7**, 327–342.

George, R., Turner, S., Hawkesworth, C., Bacon, C.R. Nye, C., Stelling, P., and Dreher, S. (2004) Chemical Versus Temporal Controls on the Evolution of Tholeiitic and Calc-Alkaline Magmas at two Volcanoes in the Alaska-Aleutian Arc. *Journal of Petrology*, **45(1)**, 203–219.

Green, T.H. (1980) Island arc and continent-building magmatism – a review of petrogenetic models based on experimental petrology and geochemistry. *Tectonophysics* **63**, 367–385.

Hawkins, J.W., Bloomer, S.H., Evans, C.A., and Melchior, J.T. (1984) Evolution of Intra-Oceanic Arc-Trench Systems. *Tectonophysics* **102(104)**, 175–205.

Hermes, O.D., and Cornell, W.C. (1981) Quenched Crystal Mush and Associated Magma Compositions as Indicated by Intercumulus Glasses from Mt. Vesuvius, Italy. *Journal of Volcanology and Geothermal Research* **9**, 133–149.

Holbrook, W.S., Lizarralde, D., McGeary, S., Bangs, N., and Diebold, J. (1999) Structure and composition of the Aleutian island arc and implications for continental crustal growth.*Geology* **27(1)**, 31-34.

Ionov, D.A. (2010) Petrology of Mantle Wedge Lithosphere: New Data on Supra-Subduction Zone Peridotite Xenoliths from the Andesitic AvachaVolcano, Kamchatka: Journal of Petrology **51(1&2)**, 327-361.

Irvine, T.N., (1965) Chromian Spinel as a Petrogenetic Indicator: Part1. Theory. *Canadian Journal of Earth Sciences* **2**, 648–672.

Irving, T. N., and Baragar, W.R.A. (1971) A guide to the chemical classification of the common volcanic rocks. *Canadian Journal of Earth Science* **8**, 523-548.

Jana, D. (2006) Sample Preparation Techniques in Petrographic Examination of Construction Materials: A State-of-the-Art Review. *Proceedings of the Twenty-Eighth Conference on Cement Microscopy, Denver, Colorado, U.S.A. April 30–May 4*, 2006, 23-34.

Jarosewich, E., Nelen, J.A. and Norber, J. A. (1980), Reference Samples for Electron Microprobe Analysis. *Geostandards Newsletter* **4**, 43–47. doi: 10.1111/j.1751-908X.1980.tb00273.x

Jicha, B.R., Scholl, D.W., Singer, B.S., Yogodzinski, G.M., and Kay, S.M. (2006) Revised age of Aleutian Island Arc formation implies high rate of magma production. *Geology* **34(8)**, 661–664.

Jicha, B.R., Singer, B.S., Brophy, J.G., Fournelle, J.H., Johnson, C.M., Beard, B.L., Lapen, T.J., and N.J. Mahlen (2004) Variable Impact of the Subducted Slab on Aleutian Island Arc Magma Sources: Evidence from Sr, Nd, Pb, and Hf Isotopes and Trace Element Abundances. *Journal of Petrology* **45(9)**, 1845–1875.

John, C.M., (2004) Plotting and Analyzing Data Trends in Ternary Diagrams Made Easy. *EOS*, **85(16)**, 158 p.

Kay, S. M., Kay, R. W., and Citron, G. P. (1982) Tectonic controls on tholeiitic and calc-alkaline magmatism in the Aleutian arc. *Journal of Geophysical Research* **87**, 4051–4072.

Kay, S.M., and Kay, R.W. (1994) Aleutian magmas in space and time, *in* The geology of Alaska (editors: Plafker, G., and Berg, H. C.). *Boulder, Colorado, Geological Society of America*, **G-1**, 687–722.

Kelemen, P.B., Yogodzinski, G.M., and Scholl, D.W. (2003) Along-strike Variation in Lavas of the Aleutian Island Arc: Implications for the Genesis of High Mg# Andesite and the Continental Crust. *Geophysical Monograph Series* **138**, 223-276.

Kentner, A.E., Nadin, E.S., Izbekov, P.E., Nye, C.J., and Neill, O.K. (2012) Gabbroic and Peridotitic Enclaves from the 2008 Kasatochi Eruption, Aleutian Islands, Alaska. *American Geophysical Union, Fall Meeting 2012*. Abstract #V31A-2759, San Francisco.

Kristiansen, N. I., Stohl, A., Prata, A.J., Richter, A., Ekhardt, S., Seibert, P., Hoffmann, A., Ritter, C., Bitar, L., Duck, T.J., and Stebel, K. (2010), Remote sensing and inverse transport modeling of the Kasatochi eruption sulfur dioxide cloud. *Journal of Geophysical Research* **115**, D00L16. doi:10.1029/2009JD013286.

Leake, B.E., Woolley, A.R., Arps, C.E.S., Birch, W.D., Gilbert, M.C., Grice, J.D., Hawthorne, F.C., Kato, A., Kisch, H.J., Krivovichev, V.G., Linthout, K., Laird, J., Mandarino, J.A., Maresch, W.V., Nickel, E.H., Rock, N.M.S., Schumacher, J.C., Smith, D.C., Stephenson, C.N., Ungaretti, L., Whittaker, E.J.W., & Youzhi, G. (1997) Nomenclature of amphiboles: report of the Subcommittee of Amphiboles of the International Mineralogical Association, commission on new minerals and minerals' names. *American Mineralogist* **82**, 1019-1037.

Lizarralde, D., Holbrook, W.S., McGeary, S., Bangs, N., and Diebold, J., (2002) Crustal construction of a volcanic arc, wide-angle seismic results from the western Alaska Peninsula. *Journal of Geophysical Research* **107**, 2164. doi: 10.1029/2001JB000230.

Morimoto, N. (1988) Nomenclature of pyroxenes. *Mineralogy and Petrology* **39**, 55-76.

Neill, O.K., (2013) Petrologic and geochemical tracers of magmatic movement in volcanic arc systems: case studies from the Aleutian Islands and Kamchatka, Russia: *Ph.D. thesis, University of Alaska Fairbanks, Fairbanks, AK*, 189 p.

Nielsen, C.H., and Sigurdsson, H. (1981) Quantitative methods for electron microprobe analysis of sodium in natural and synthetic glass. *American Mineralogist* **66**, 547–552.

Pope, R.R. (1983) The petrology of ultramafic and mafic xenoliths from Kanaga Island, the central Aleutians: *M.S. thesis, Cornell University, Ithaca, NY*, 121 p.

Potts, P.J. (1987) A Handbook of Silicate Rock Analysis. *Blackie, New York, Chapman and Hall*, 622p.

Ryan, W. B. F., Carbotte, S.M., Coplan, J.O., O'Hara, S., Melkonian, A., Arko, R., Weissel, R.A., Ferrini, V., Goodwillie, F., Nitsche, F., Bonczkowsi, J., and Zemsky, R. (2009), Global Multi-Resolution Topography synthesis. *Geochemistry Geophysics Geosystems* **10**, Q03014, doi:10.1029/2008GC002332.

Scott, W.E., Nye, C.J., Waythomas, C.F., Neal, C.A. (2010) August 2008 eruption of Kasatochi volcano - resetting an island landscape. *Artic, Antartic, and Alpine Research* **42(3)**, 250–259.

Shillington, D.J., Van Avendonk, H.J.A., Holbrook, W.S., Kelemen, P.B., and Hornbach, M.J. (2004) Composition and structure of the central Aleutian island arc from arc-parallel wide-angle seismic data. *Geochemistry Geophysics Geosystems* **5(10)**, 32 p. doi: 10.1029/2004GC000715.

Śliwiński, M.G. (2012) Geochemistry of the Late Devonian 'Punctuata' Event in the Western Canada Sedimentary Basin. *Ph.D. thesis, University of Alaska Fairbanks, Fairbanks, AK*.

Stern, R.J. (2002) Subduction Zones. *Reviews of Geophysics* **40(4)**, 13 p.

Stormer, J.C. (1983) The effects of recalculation on temperature and oxygen fugacity from analyses of multicomponent iron-titanium oxides. *American Mineralogist* **68(5-6),** 586-594.

Streckeisen, A. (1974) Classification and nomenclature of plutonic rocks recommendations of the IUGS subcommission on the systematics of Igneous Rocks. *Geologische Rundschau* **63** (2), 773–786.

Takahashi, N., Kodaira, S., Klemperer, S.L., Tatsumi, Y., Kaneda, Y., and Suyehiro, K. (2006) Crustal Structure and Evolution of the Mariana Intra-Oceanic Island Arc. *Geology* **35(3)**, 203–206.

Tatsumi, Y. and Suzuki, T. (2009) Tholeiitic vs. Calc-Alkaline Differentiation and Evolution of Arc Crust: Constraints from Melting Experiments on a Basalt from the Izu—Bonin—Mariana Arc. *Journal of Petrology* **50(8)**, 1575–1603.

Wager, L.R., Brown, G.M., and Wadsworth, W.J. (1960) Types of Igneous Cumulates. *Journal of Petrology* **1(1)**, 73–85.

Wager, L.R. (1962) Igneous cumulates from the 1902 eruption of Soufrière, St. Vincent. *Bulletin Volcanologique* **24**, 93–99.

Waythomas, C.F., Scott, W.E., Prejean, S.G., Schneider, D.J., Izbekov, P., and Nye, C.J. (2010) The 7-8 August 2008 eruption of Kasatochi Volcano, central Aleutian Islands, Alaska. *Journal of Geophysical Research* **115**, 23p. doi: 10.1029/2010JB007437.

Yogodzinski, G.M., and Kelemen P.B. (2007) Trace elements in clinopyroxenes from Aleutian xenoliths: Implications for primitive subduction magmatism in an island arc. *Earth and Planetary Science Letters* **256(3–4)**, 617–632.

Yogodzinski, G.M. and Kelemen, P.B. (1998) Slab melting in the Aleutians: implications of an ion probe study of clinopyroxene in primitive adakite and basalt. *Earth and Planetary Science Letters* **158**, 53–65.

Appendix

Appendix 1: Rock Slab Images

The images included in Appendix 1 were taken using a flatbed scanner. Before scanning, the samples were cut with a diamond blade rock saw, polished down to 1000μm, and cleaned. Important features of each sample are annotated in the included images.

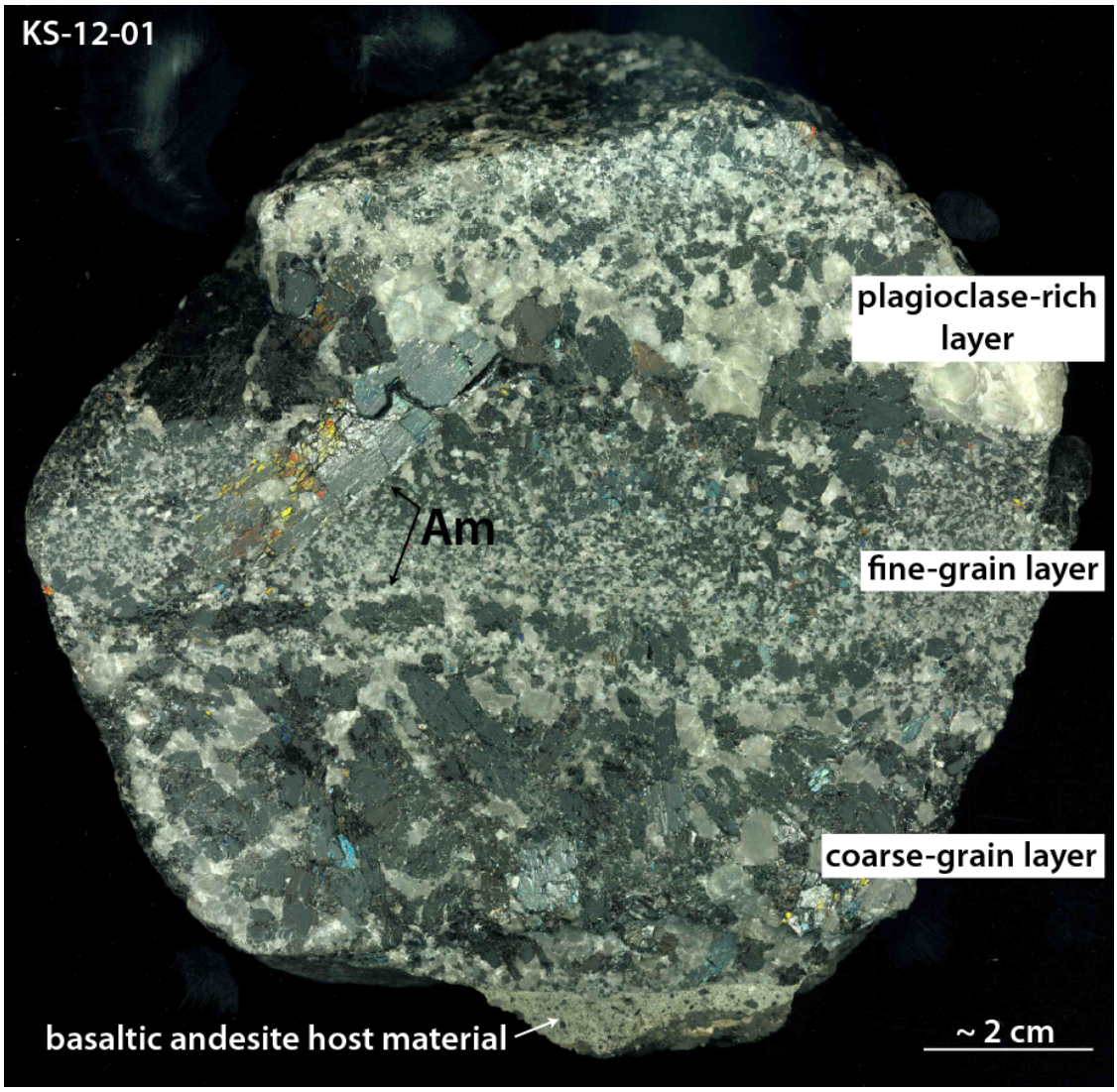

Figure A1. Slab of Layered Gabbro KS-12-01

The sample above shows typical, arrhythmic layering in hornblende gabbro from Kasatochi. This sample is an example of the variation in layering based on grain size changes and modal abundance.

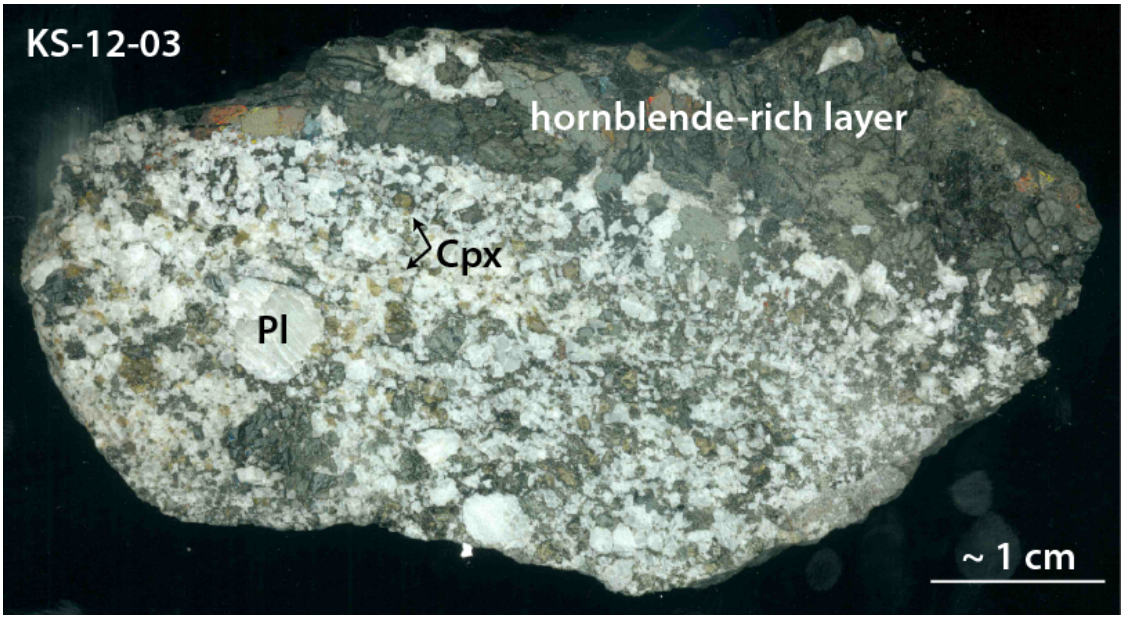

Figure A2. Slab of Gabbro KS-12-03
This inequigranular gabbro has a higher abundance of brown-green clinopyroxene (Cpx), large plagioclase (Pl), and a layer made up of ~99% hornblende (top).

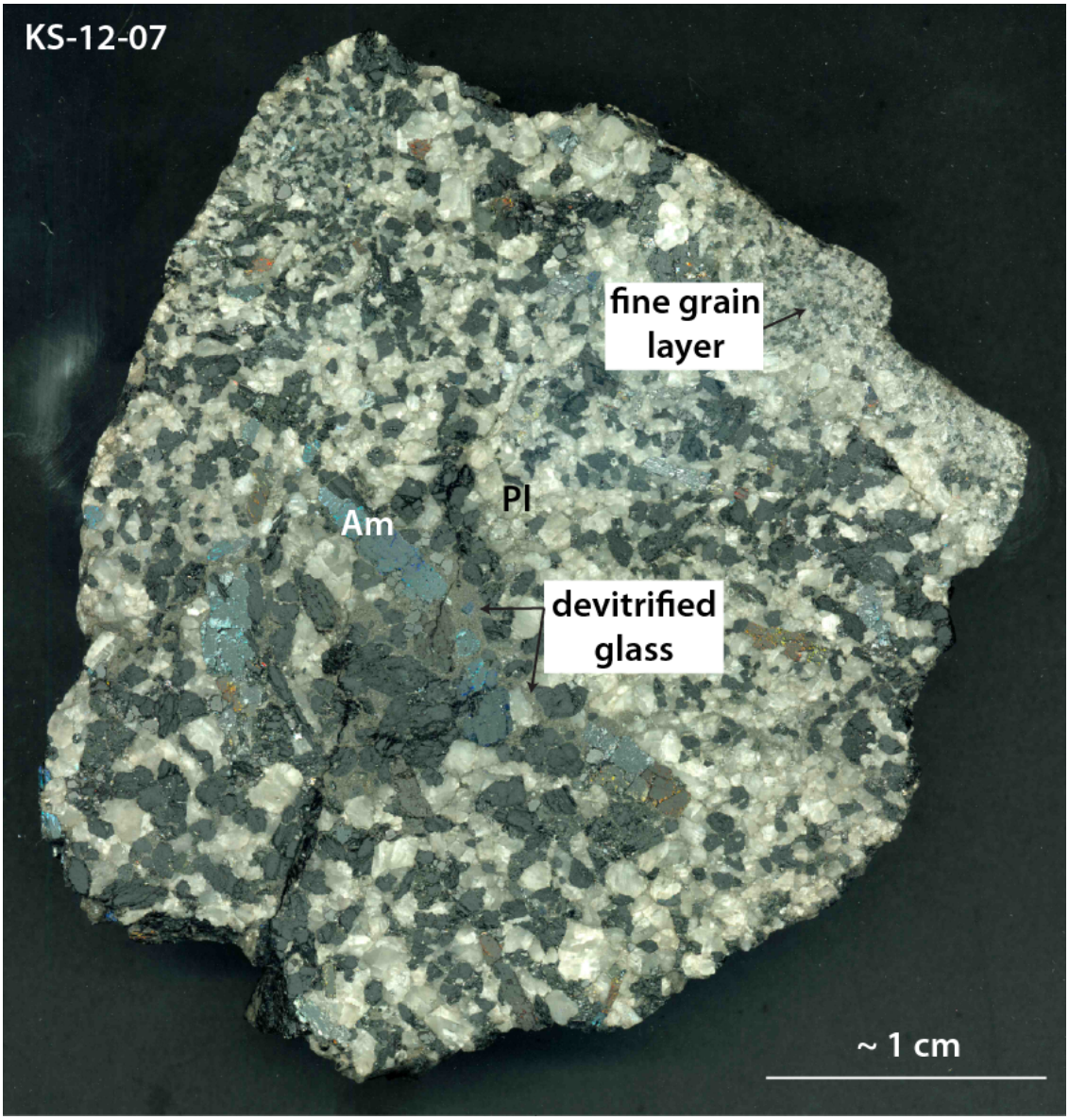

Figure A3. Slab of Gabbro KS-12-07
The glass in the sample layered as devitrified is cryptocrystalline, containing small crystals that can be seen in BSE imagery. In this sample, the glass is concentrated with larger euhedral hornblende.

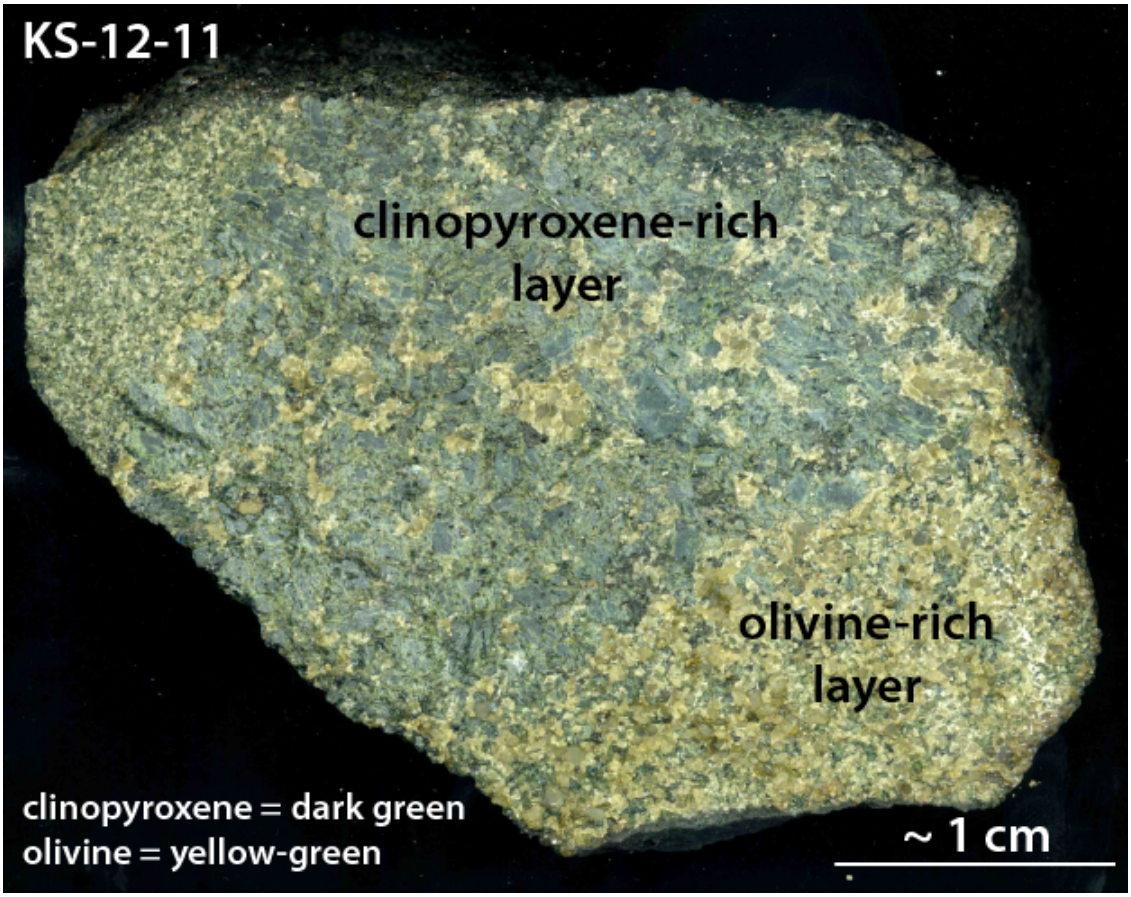

Figure A4. Slab of Peridotite KS-12-11
The layering in this peridotite is atypical and was only seen in this sample. The layering is defined by the relative abundance of clinopyroxene and olivine.

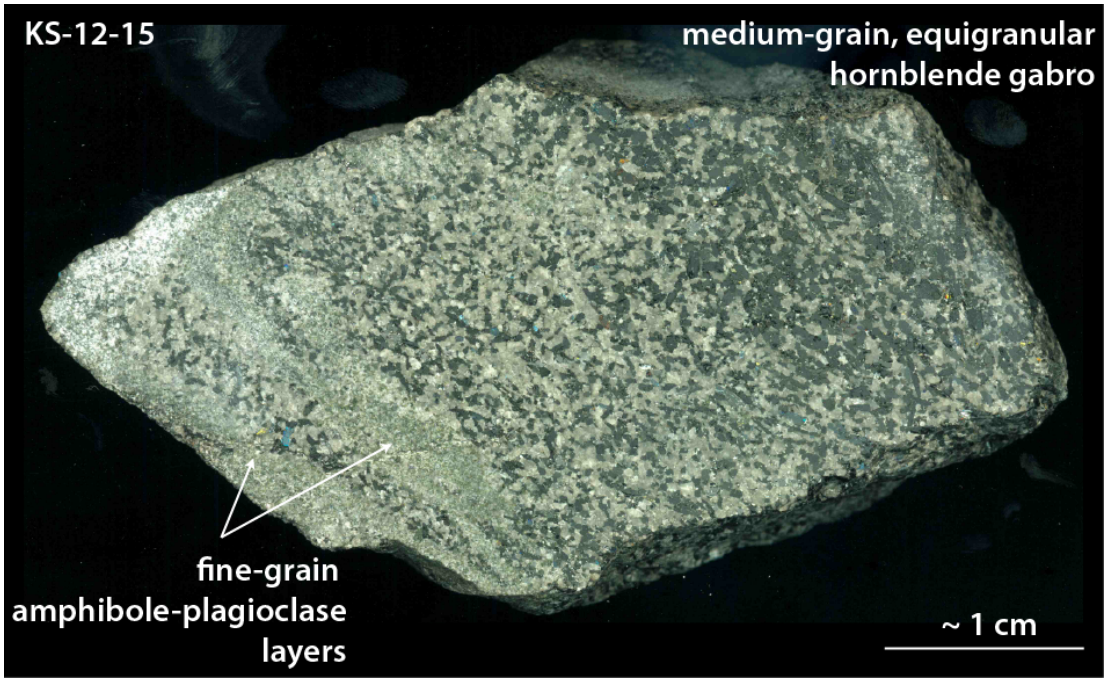

Figure A5. Slab of Gabbro KS-12-05
The gabbro shown above is a fine grain, equigranular hornblende gabbro with discontinuous "blebs" of very fine-grained material (shown in the bottom left of the sample).

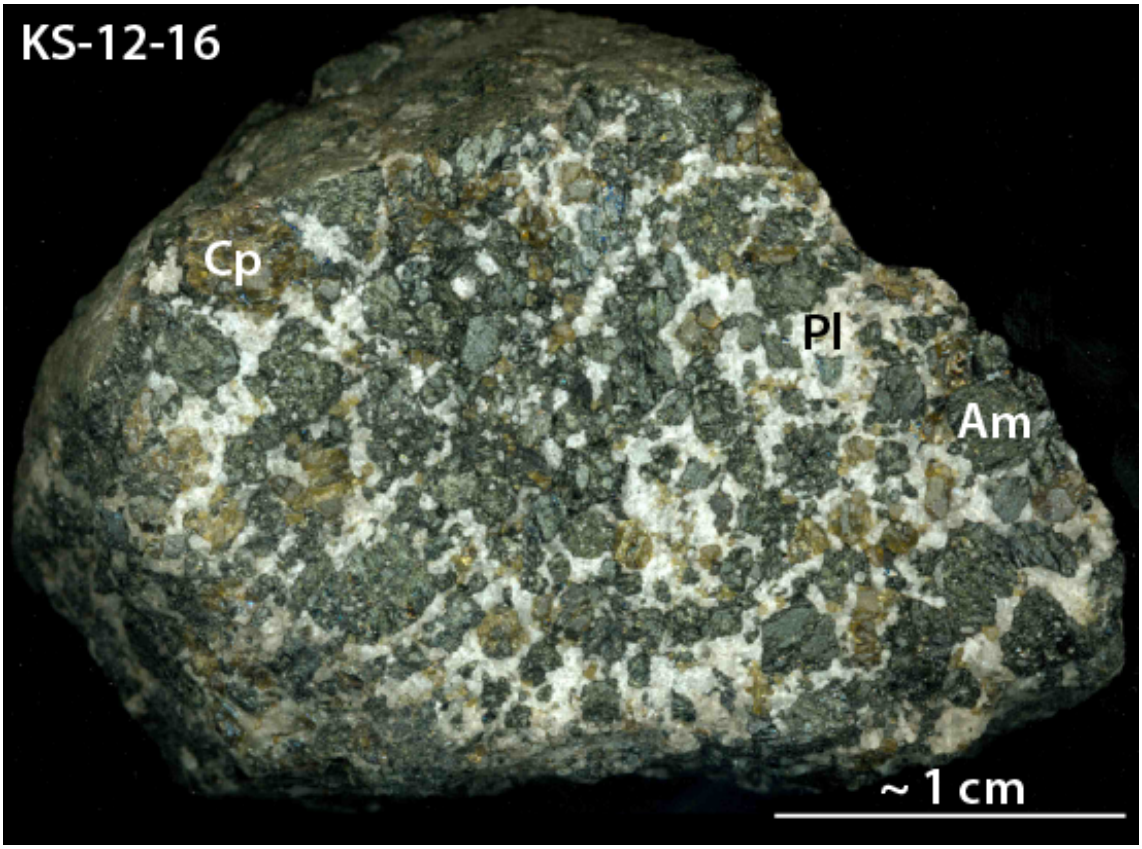

Figure A6. Slab of Gabbro KS-12-16
The gabbro above is an example of an equigranular gabbro with brown-green clinopyroxene (Cp) and black hornblende (Am) surrounded by white plagioclase (Pl).

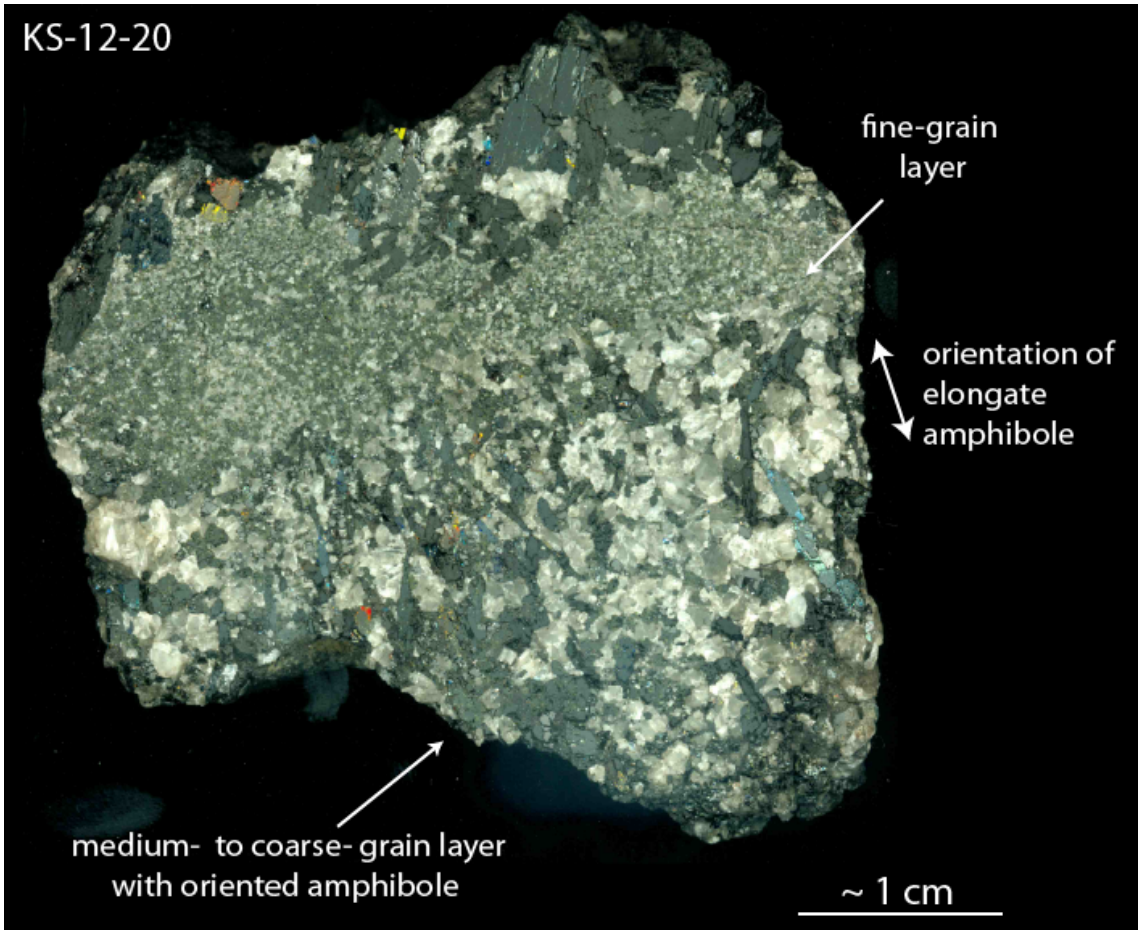

Figure A7. Slab of Layered Gabbro KS-12-20
The layered gabbro above includes a layer of fine-grain gabbro sandwiched between two layeres of coarse-grain gabbro. Acicular hornblende within the coarse layers are oriented roughly perpendicular to the plane defined by layering.

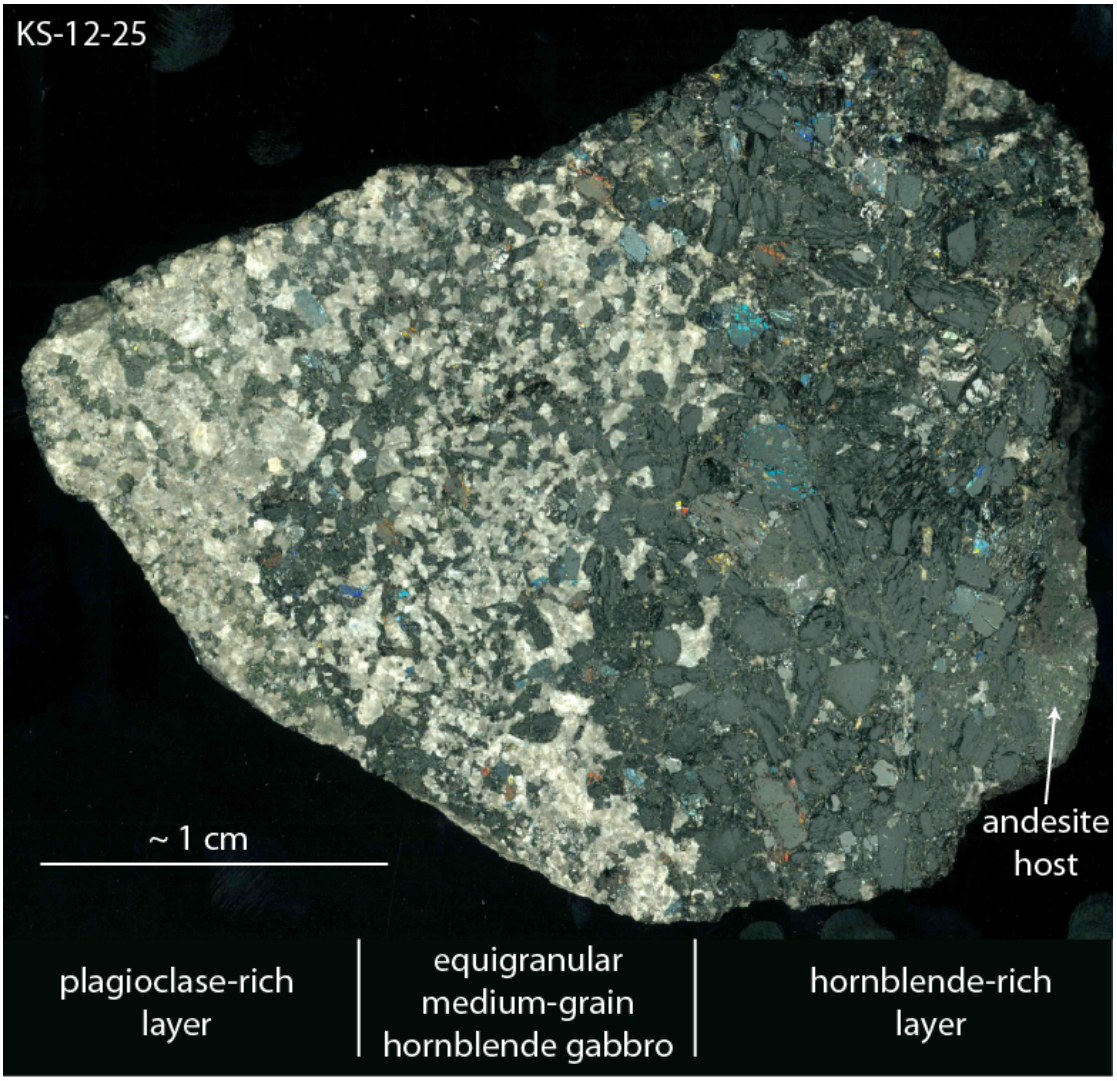

Figure A8. Slab of Layered Gabbro KS-12-25
In this layered gabbro, the layering is defined by both grain size and modal abundance.

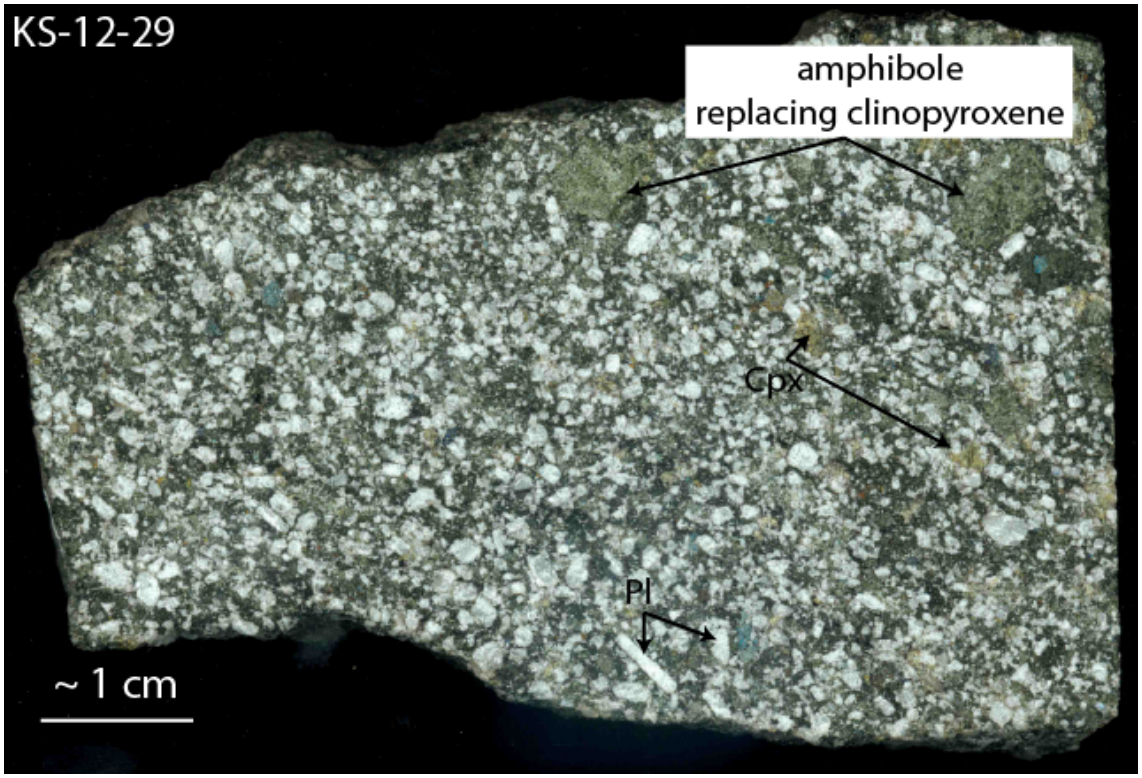

Figure A9. Slab of Gabbro KS-12-29
This gabbro is inequigranular and contains large clinopyroxene phenocrysts with hornblende rims.

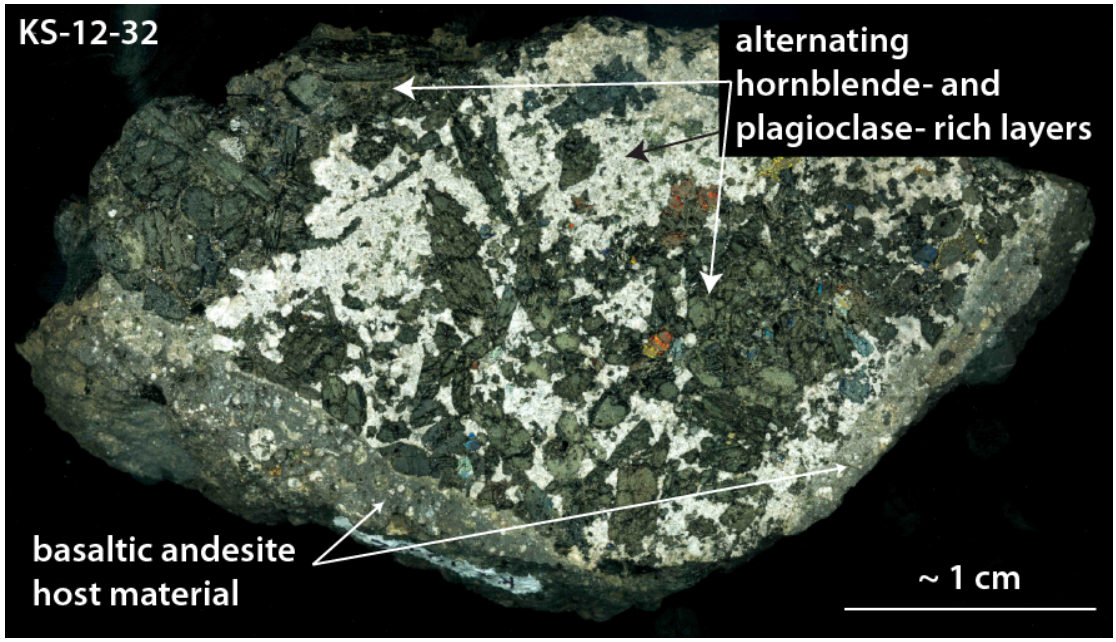

Figure A10. Slab of Gabbro KS-12-32
This smaller sample is a gabbro with euhedral amphibole in layers or clumps surrounded by more plagioclase-rich material.

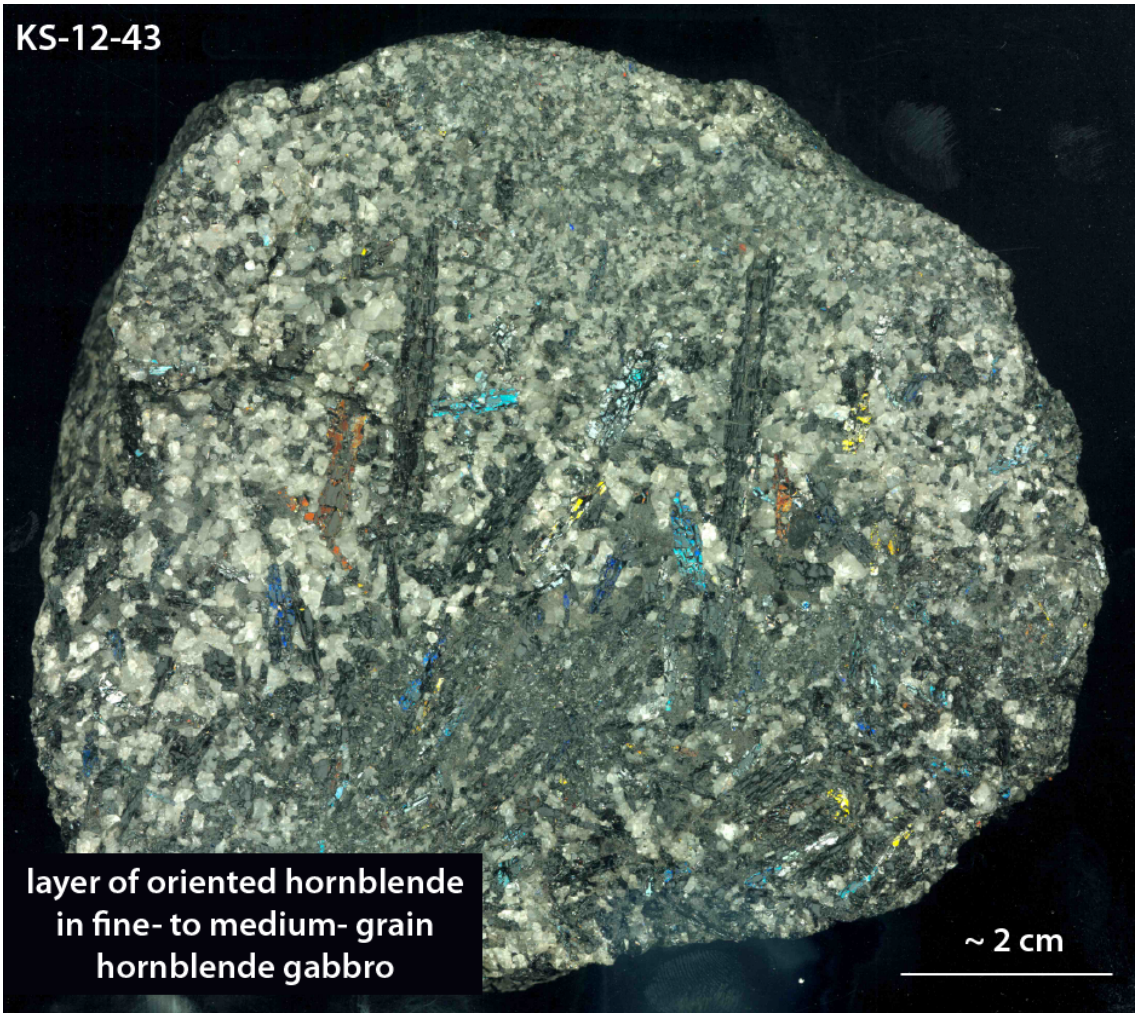

Figure A11. Slab of Gabbro KS-12-43
In this sample, hornblende is acicular and radiating towards the top of the image. The surrounding gabbroic material is equigranular and medium grain size.

Appendix 2: Thin Section Preparation

I prepared these directions for thin section preparation for undergraduate students that assisted me with the Kasatochi slides. These directions apply to the multi-user facilities within AIL at UAF, but can easily be modified for use at other laboratories. The process below does not include epoxy impregnation.

Step 1: Cut the billets

Cutting billet is very easy, but the better you do here, the easier the following steps will be. You should budget about 5 minutes of time per rock sample.

1. Decide where to cut the rock. If there is any fabric, cut the slab *perpendicular* to the direction of the fabric. Make sure that the slab includes any important features such as melt inclusions, interesting or unusual mineral, veins of different composition from the rest of the rock, textural variations. If the textural differences in the rock are too great, cut multiple thin sections and amend a letter to the sample number. Keep track of this for later.
2. The slab cut will be a ½ inch thick section of the rock sample. Basically, use the diamond saw to cut a ½-1 inch thick section of the rock that you decide to make into a thin section. If the end is important, one side of the slab can be uneven (I.E. not cut).
3. Cut the billet out of the slab. This is .9 X 1.8 inch rectangle. Any larger and the billet will not fit on the slide. If the billet splits in half at this stage, it can be fixed when adhered to the glass slide. If the billet crumbles, set the sample aside for the epoxy impregnation method.
4. Once the billet is cut, wash it off under water and clean up any remaining dirt on it and the hand sample. Place on paper towels to dry. Label the paper towels with the sample number.
5. When the sample is dry, label every piece of rock with the sample number. Separate the billets from the hand samples so that the billets can be made into thin sections and the hand samples stored. You are now ready to make a thin section!

Step 2: Making the slide

Follow these steps to make a "probe-quality" thin section with a highly polished surface and no cover slip. Pavel Izbekov and Sarah Henton can both be credited with teaching me this process. That said, many processes are possible: find the one that works best for you.

1. Turn on the hot plate to 75 - 80°C (this is marked by an arrow on the thermometer). Make sure there is a surface thermometer on the plate to keep track of the temperature. Before the plate heats up, place a fresh piece of foil on the surface. This will protect your slides as well as the plate.
2. Polish the specimen using the grinding wheel (Ameritool). The grit that you use will vary, but the finer the grit, the easier the next step will be. Press firmly and evenly. You are done when the surface is shiny when dry and the surface is "true" or completely flat and level (use a razor blade or glass slide to check).
3. Clean the slide using the ultrasonic cleaner (polished side up) and soap and water.
4. Polish the specimen further by using the polishing powders and the appropriate glass plate. At this stage, 1000 grit will work. Hand polish for 1-2 minutes.
5. Clean samples once more in the ultrasonic bath. While the specimens are being cleaned, prepare the glass slides by rounding edges and engraving sample numbers on to the glass. Clean the slides with isopropyl alcohol or windex.
6. Remove the slides from the ultrasonic bath and place on the hot plate, polished side up. Clean the polished side with isopropyl alcohol. If there is canned air available, clean any dust off the polished specimens and glass slides.
7. Mix epoxy: Follow manufacturer's directions. If available, use Petropoxy 154. Petropoxy154 is a 10 ml to 1 ml (or 1 cc mix). Petropoxy 154 can be found in the glass cabinet on the far left above the hot plate. Find a small cup, wood mixing stick, syringe, resin, and curing agent. Squeeze 10 ml of resin into the cup. Add 1 cc of curing agent using the syringe (if either is running low, see Ken or Karen). Mix well using the stick. Epoxy will be good for up to 5 days. If doing a small amount of slides, mix 5 ml resin with 0.5 ml curing agent.

8. Place specimens next to their glass slide on the hot plate to dry. The epoxy cures within 10 minutes if the samples are placed on a hot plate between 135 and 140 °C. Go ahead and heat the plate up to this temperature now.
9. Allow samples to cool off the plate so that you can handle them easier. You will affix the billet to the slide using epoxy. Spread a small amount of epoxy on the polished side of the billet and press the billet down on to the glass slide (the side cleared of dust!). Press firmly and in a circular motion to remove as money bubbles as possible. When you are happy with the product, place the slide and rock on the hot plate. Remove from plate when you can poke the epoxy with the sharp end of a wooden stick, pen, or pencil without leaving an indentation.

Step 3: Cutting and polishing to 30μm:

1. You will use the yellow machine across from the hotplate to cut the bulk of the billet off of the thin section and begin the polishing process. There are "rotators" in this machine, a saw and a grinding wheel. There is also an arm with a vacuum that holds your slide. The idea is that this is a precise tool that can help you get your slide close to 30μm with little effort. However, this is more of an art than a science given the condition of the tool. Wipe the suction area clear of any debris. Turn on the water (at the faucet and on the face of the tool). You might need to put down a towel or cup to collect dripping water. Turn on the vacuum and test the suction. If everything is ready to go, put a little water on your slide and put on the suction.
2. Cut the section! This should be about 2 mm thick. Cut a small knick in the billet to make sure you that you will not cut too close to the slide. Be gentle as forcing the rock through can break your slide.
3. Polish: The first polish step will be using the grinder on the wheel. Be careful when you start that the rock is far away from the grinder – the slide can be broken if you try to grind partway through the billet. Use an up and down motion on the grinder. Check frequently: (1) quality of suction to the slide and (2) thickness of the slide. Once the slide starts getting thin enough to pass light through, check it

under the cross polarizer. You are done when you start to see some birefringence coming through.

4. Polish: Go back to the glass plate and 1000 grit. You will want clean grit to prevent scratching your slide. If at any point you feel debris in the grit while polishing, stop immediately, clean the plate, and use new grit. You are going to spend the most time and patience on this step. The goal here is to get the slide close to 35–30μm. If you go all the way to 30μm you risk losing your slide while putting on the probe polish. The goals are (1) no saw-marks visible under reflected light and (2) high first order birefringence for feldspar, quartz, and some orthopyroxene (it is more guesswork when working with ultramafic samples).
5. When you are satisfied with the thickness of the slide, get a new glass plate and the white polishing powder. Make sure everything is clean before you begin. Add water to the polish and polish the slide for 2-3 minutes (depends on how hard you press). This step makes the probe polish very easy to attain.
6. The final step is putting on the probe polish. The wheel that you use is next to the whiteboard. Remove the black cover and get a polish from the top drawer below the wheel. Any of the options will do, best to choose the one that is in the best condition. Set up and turn everything on. You will turn the speed up to around 100-150. Get out a plastic slide holder and clean thoroughly to prevent scratching your slide. Also make sure that your slide is clean by washing it with soap and water and giving it another ultrasonic bath. Remove from the bath and allow to dry. Place the slide in the slide holder, glass side to plastic. You need to create cohesion between the slide and the slide holder – use the purple oil and apply one drop to the holder. Make sure that your slide is rock side out or risk frosting your slide! Press “run” and polish the slide for 3-4 minutes pressing firmly. Switch the direction you hold the slide half way through to prevent preferentially polishing one side. This step is done when your slide is reflective and the minerals “pop” when the slide is viewed under reflected light.

Appendix 3: EPMA Locations for Selected Minerals

The images included in Appendix 3 were taken using a transmitted light petrographic microscope. Locations for amphibole and plagioclase analyses are shown in the selected slides. The images were taken using both plane-polarized (PPL) and cross-polarized (XPL) light as indicated in the captions.

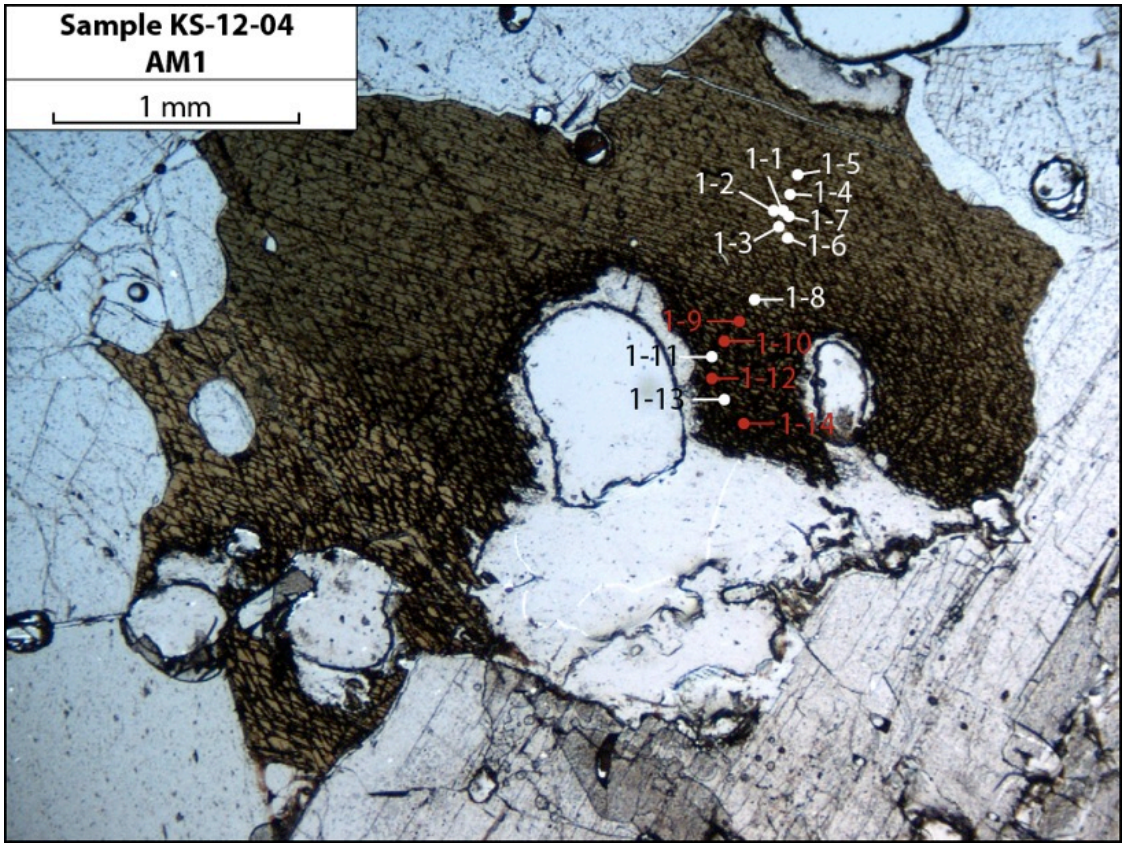

Figure A12. AM1 in Gabbro KS-12-04 (PPL)

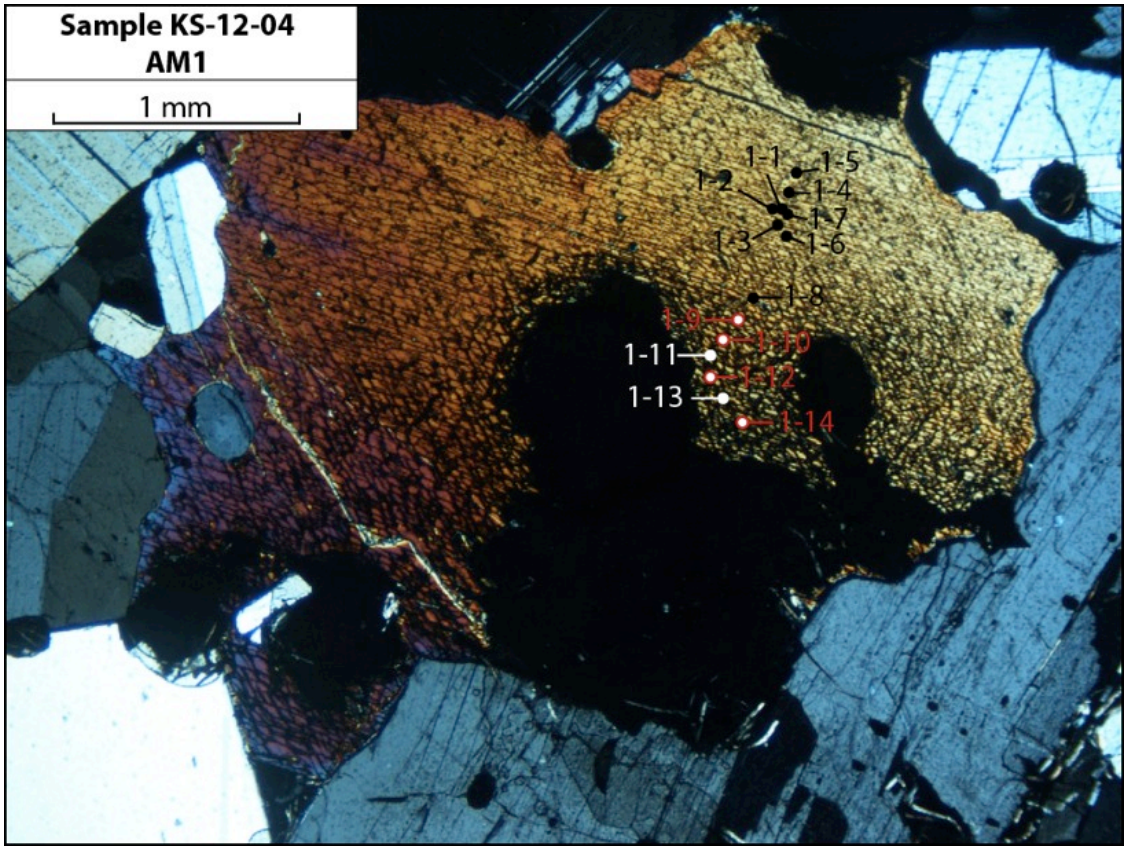

Figure A13. AM1 in Gabbro KS-12-04 (XPL)

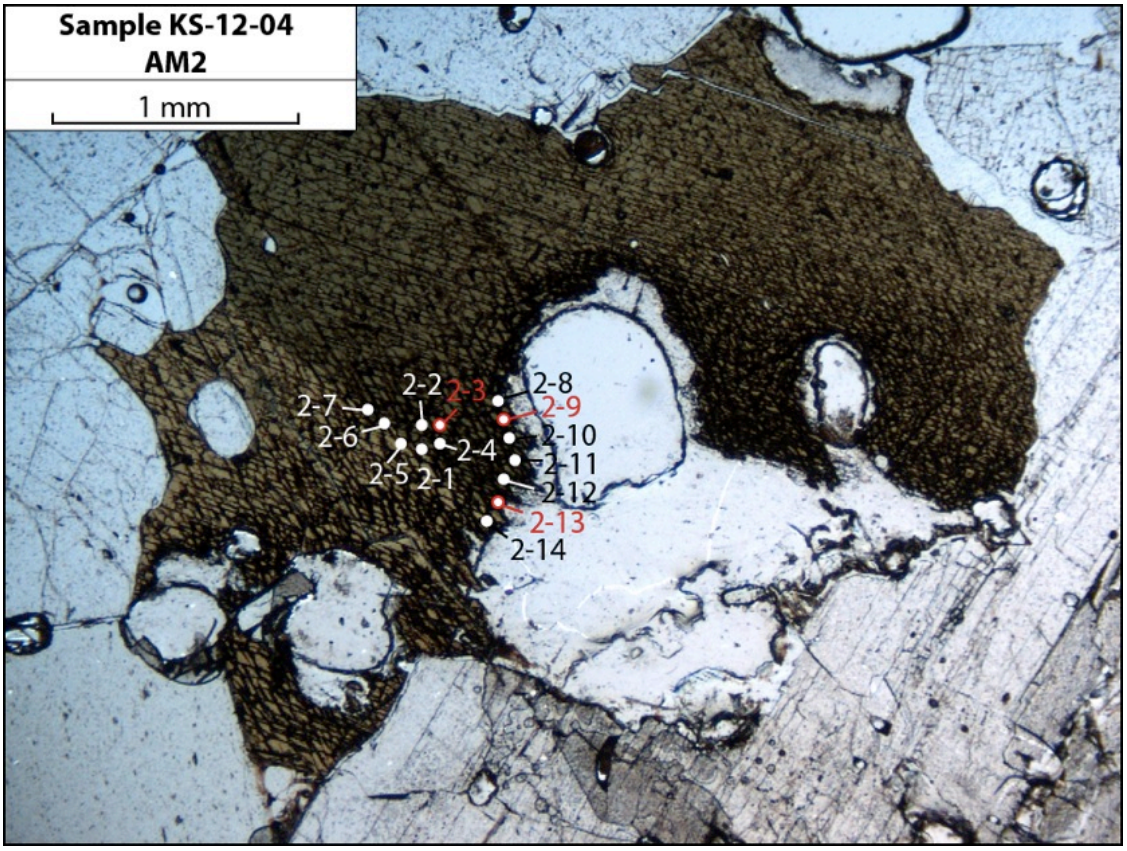

Figure A14. AM2 in Gabbro KS-12-04 (PPL)

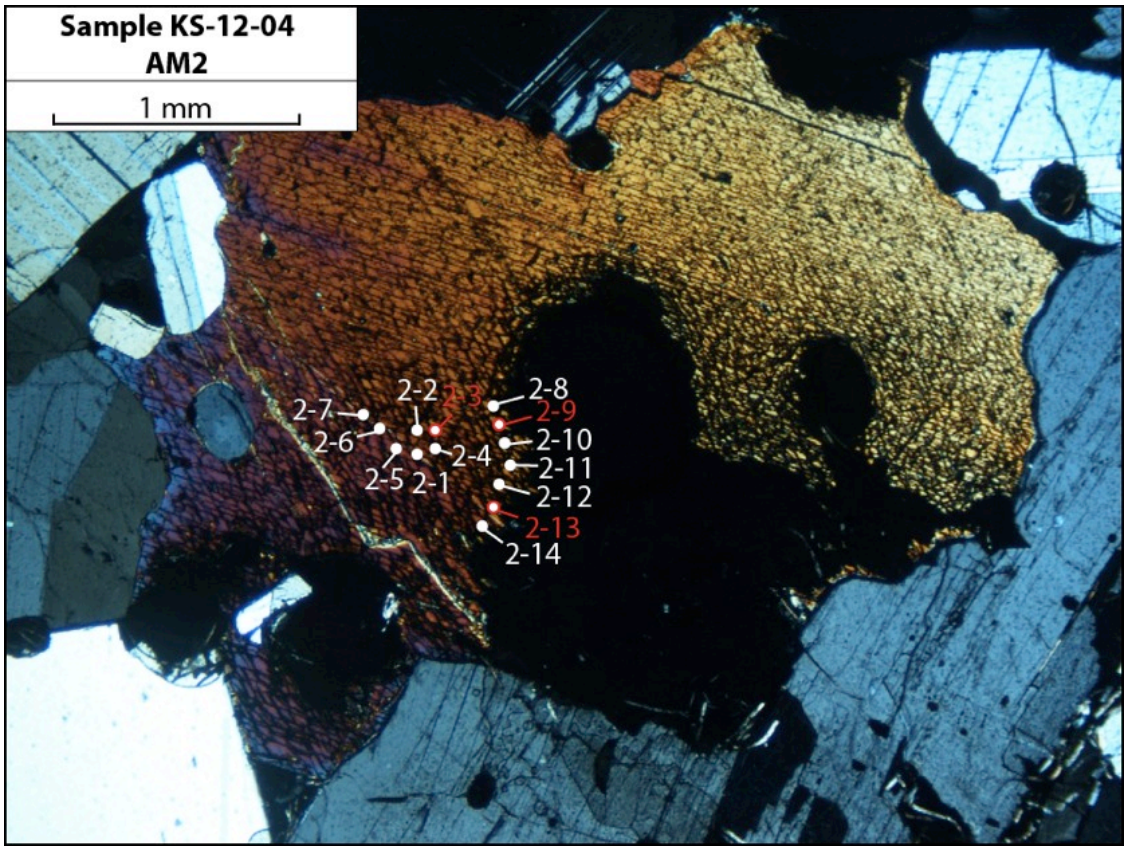

Figure A15. AM2 in Gabbro KS-12-04 (XPL)

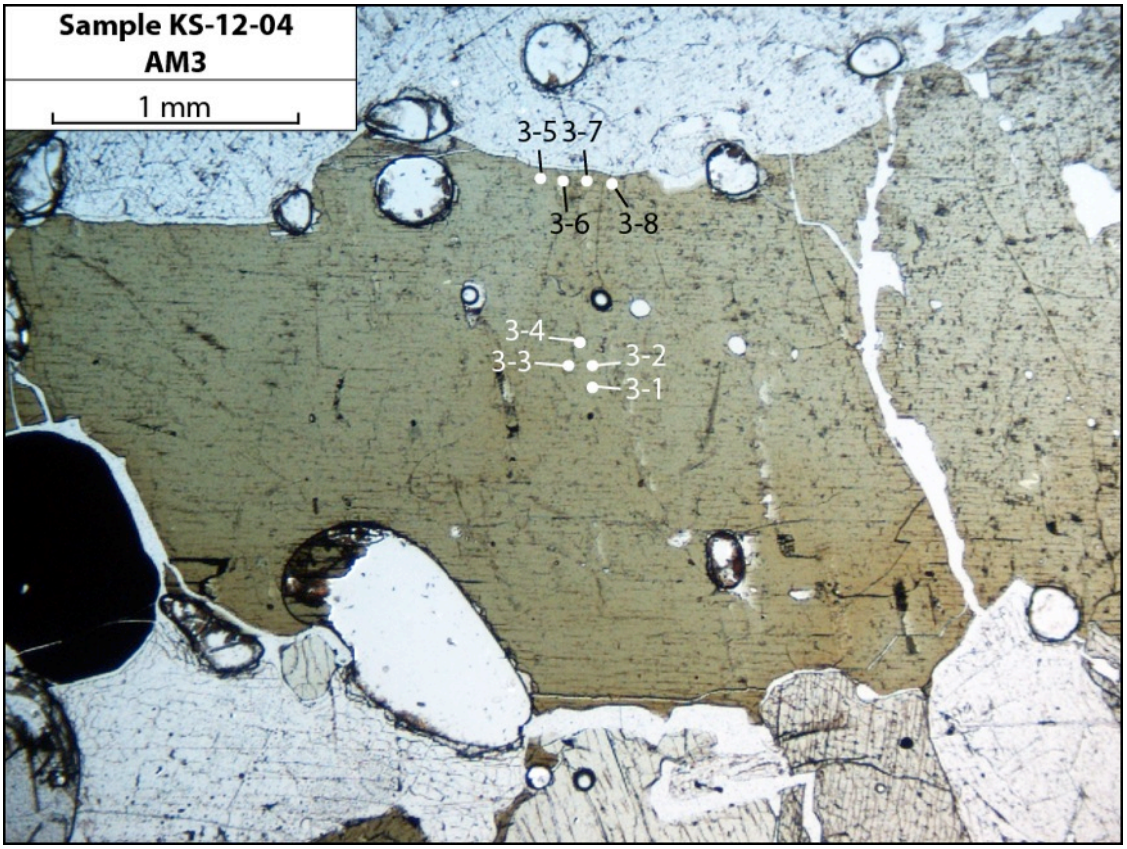

Figure A16. AM3 in Gabbro KS-12-04 (PPL)

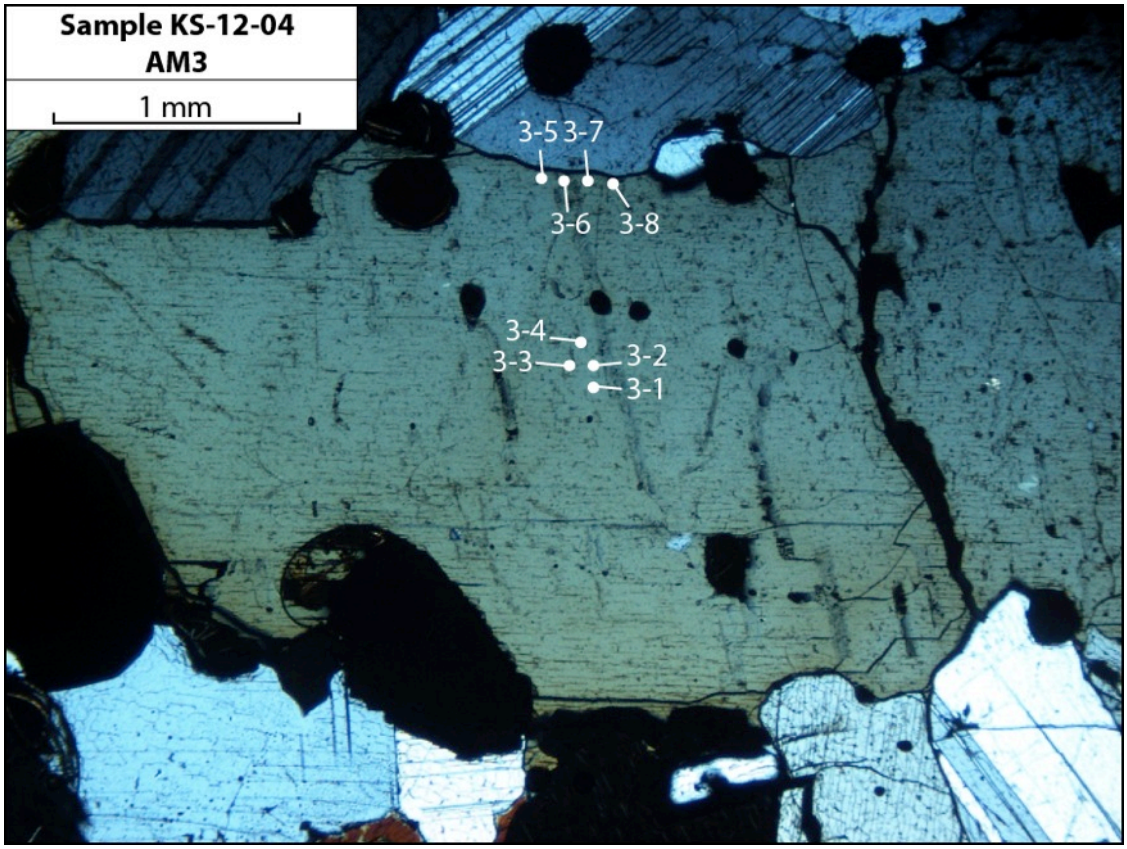

Figure A17. AM3 in Gabbro KS-12-04 (XPL)

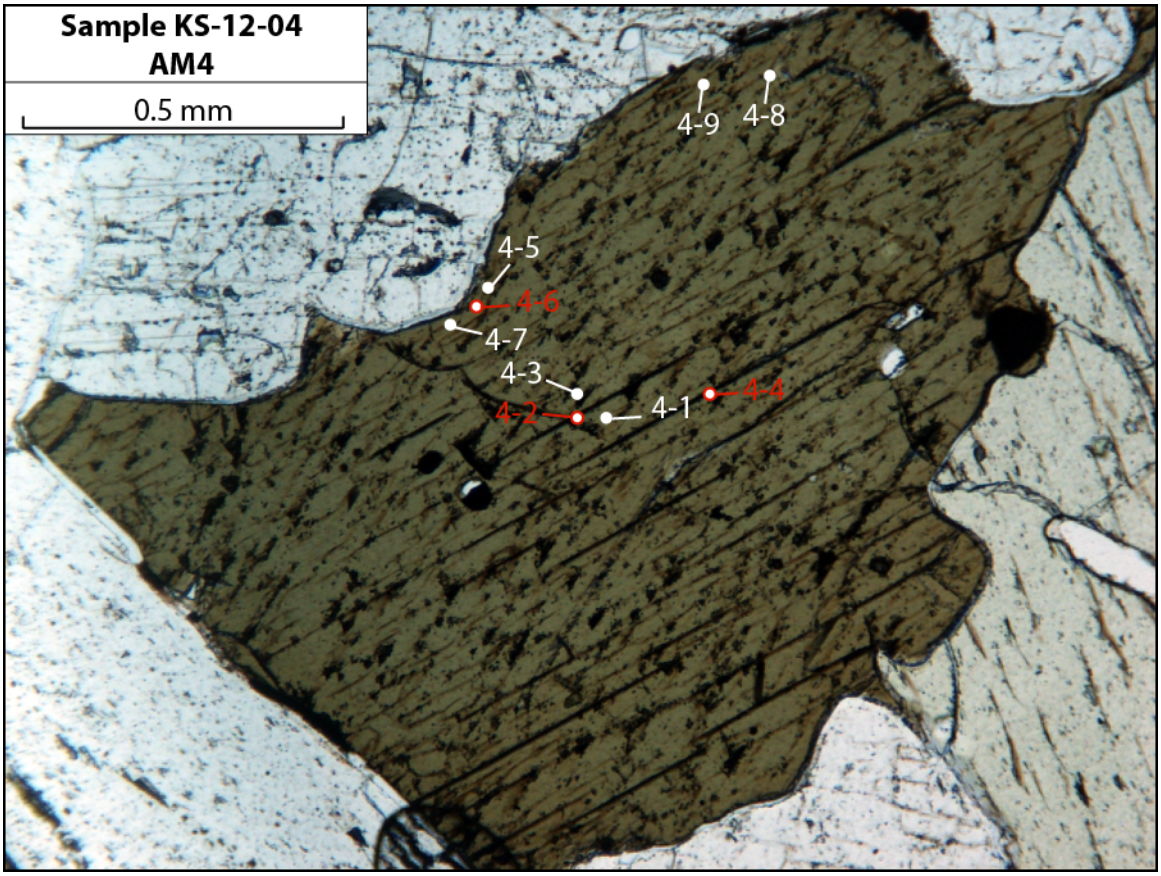

Figure A18. AM4 in Gabbro KS-12-04 (PPL)

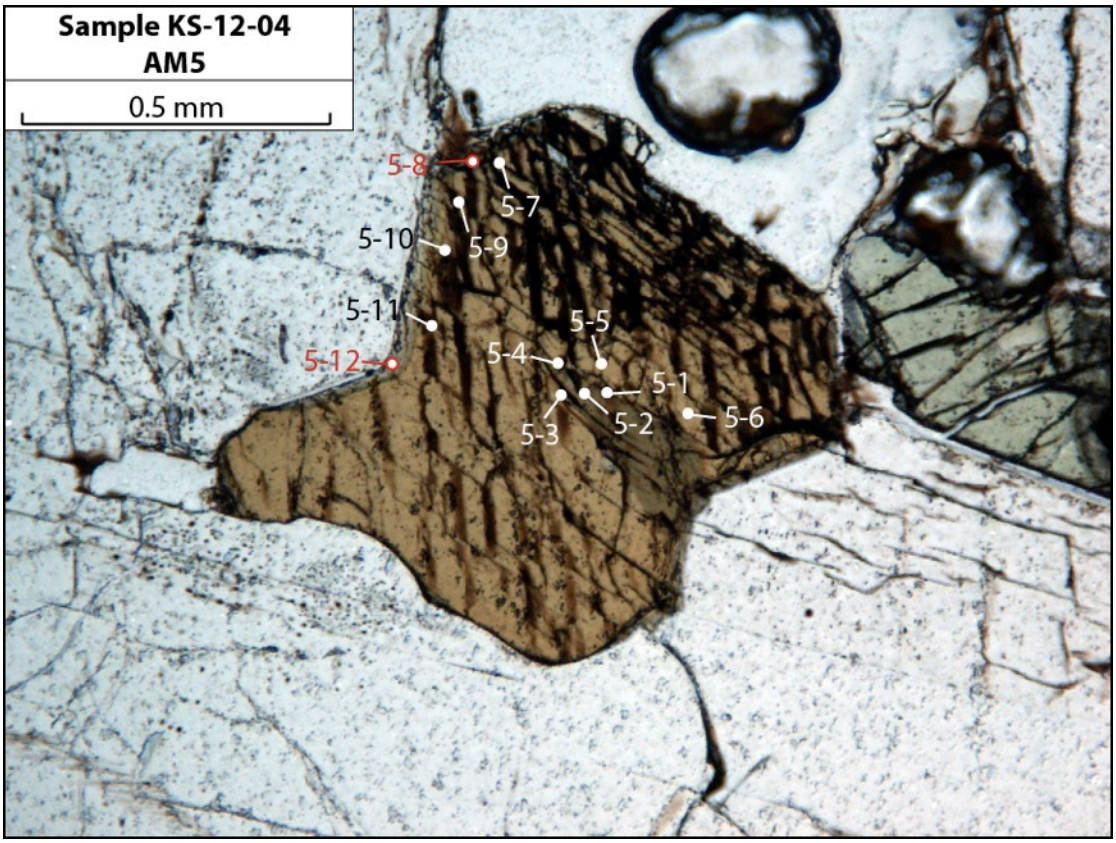

Figure A19. AM5 in Gabbro KS-12-04 (PPL)

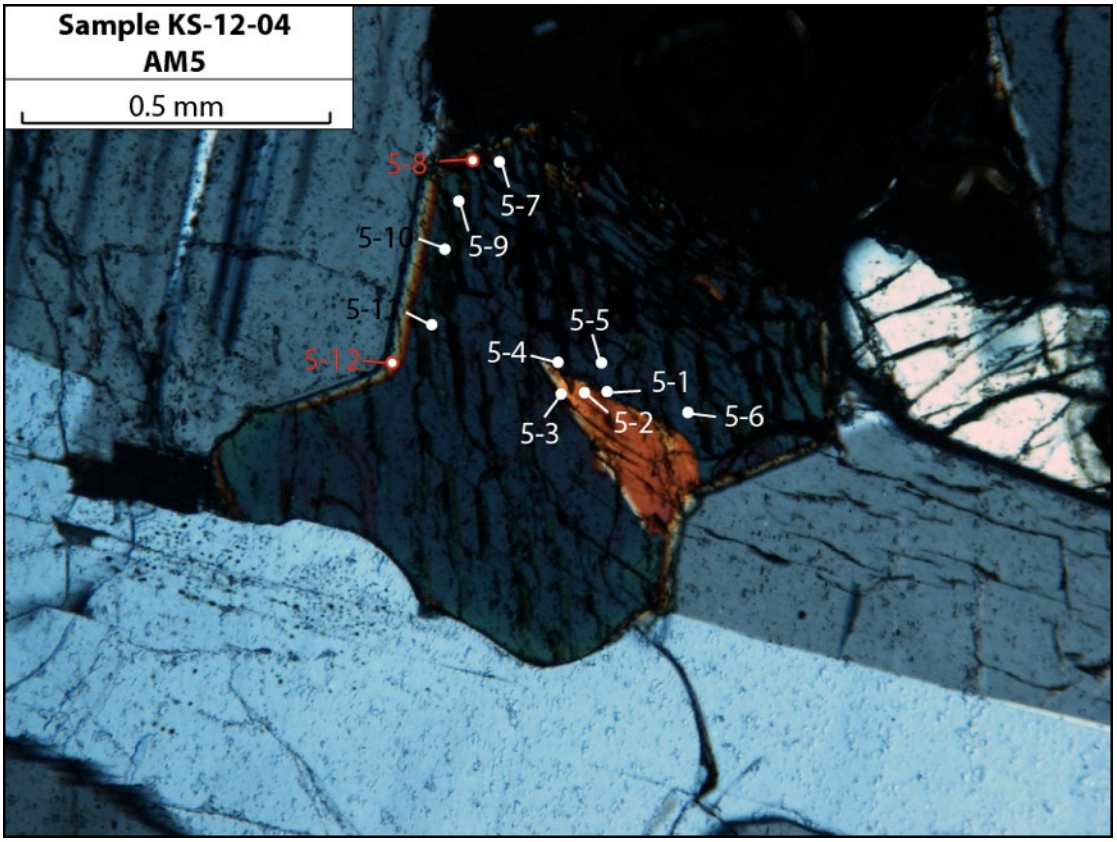

Figure A20. AM5 in Gabbro KS-12-04 (XPL)

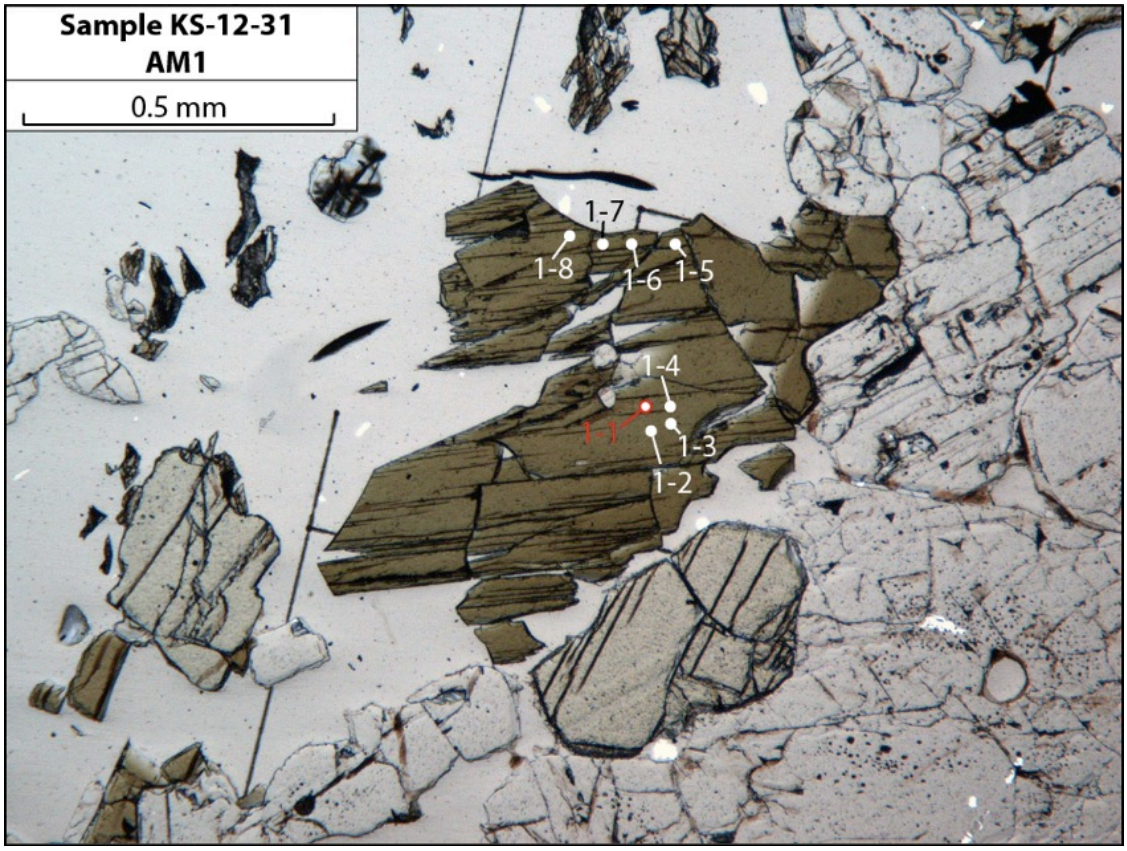

Figure A21. AM1 in Gabbro KS-12-31 (PPL)

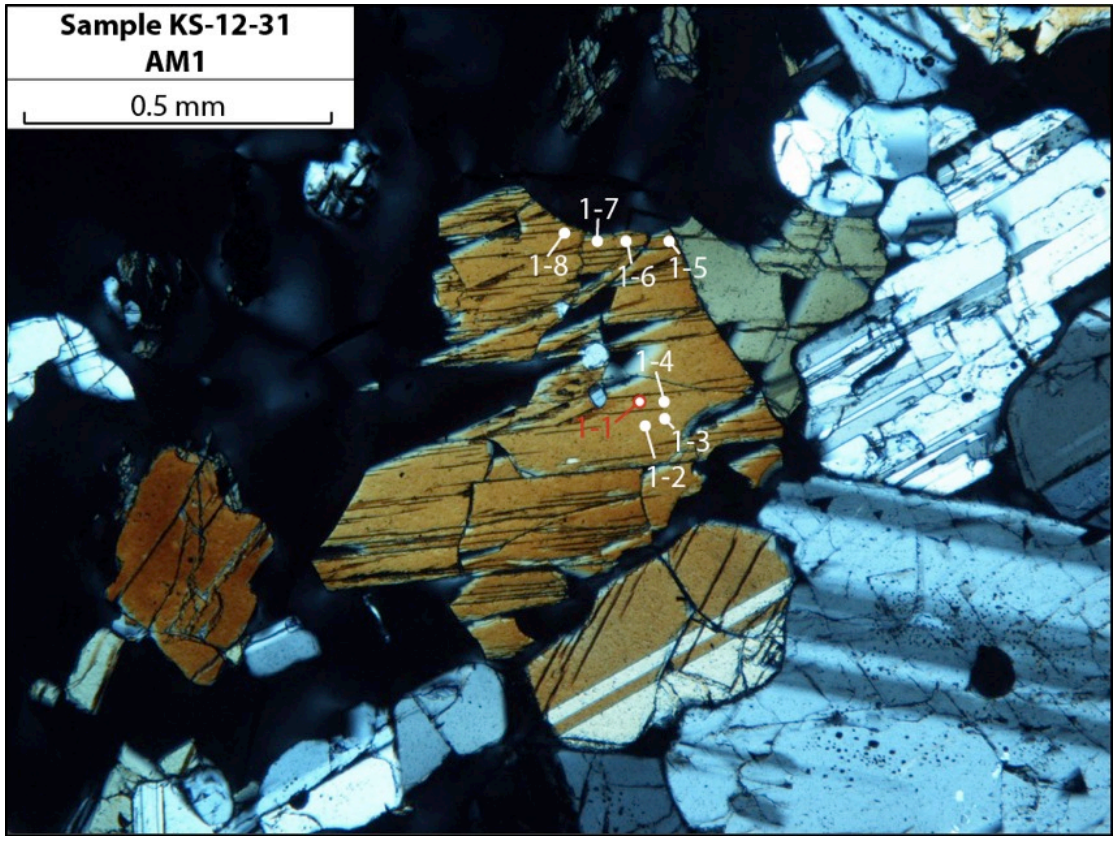

Figure A22. AM1 in Gabbro KS-12-31 (XPL)

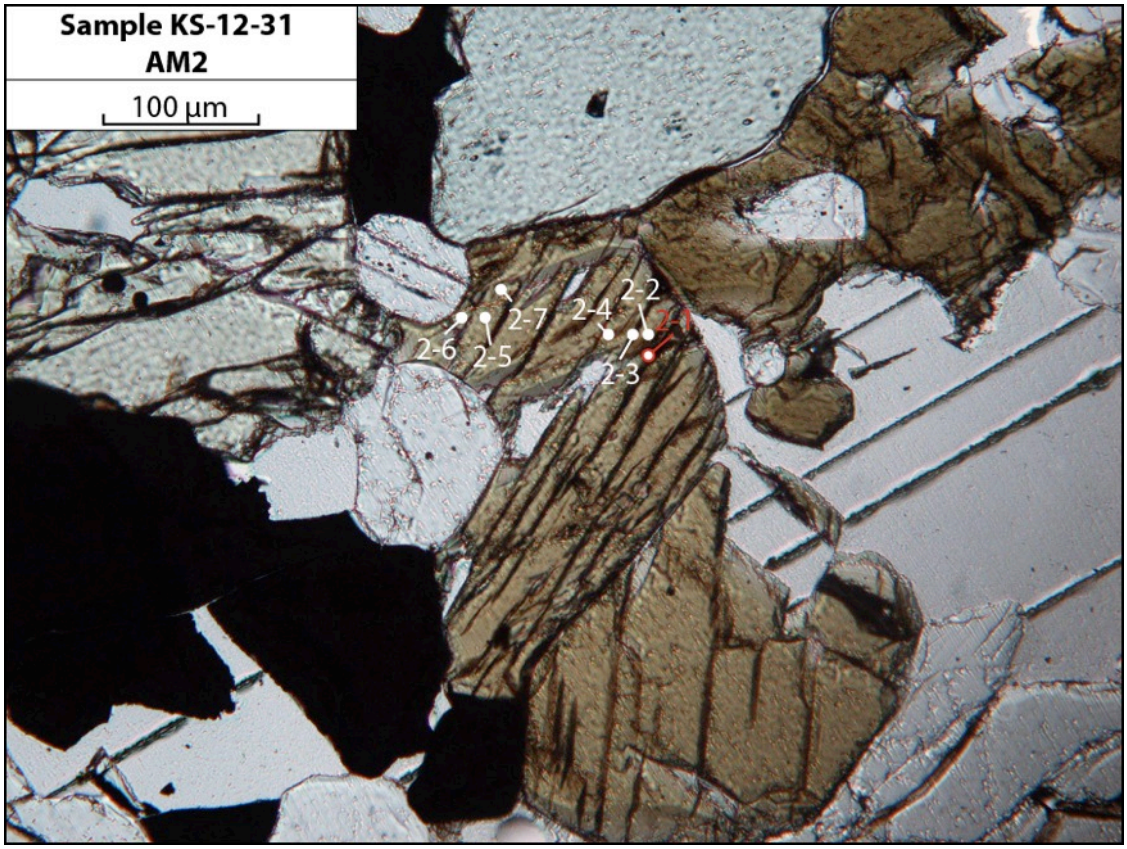

Figure A23. AM2 in Gabbro KS-12-31 (PPL)

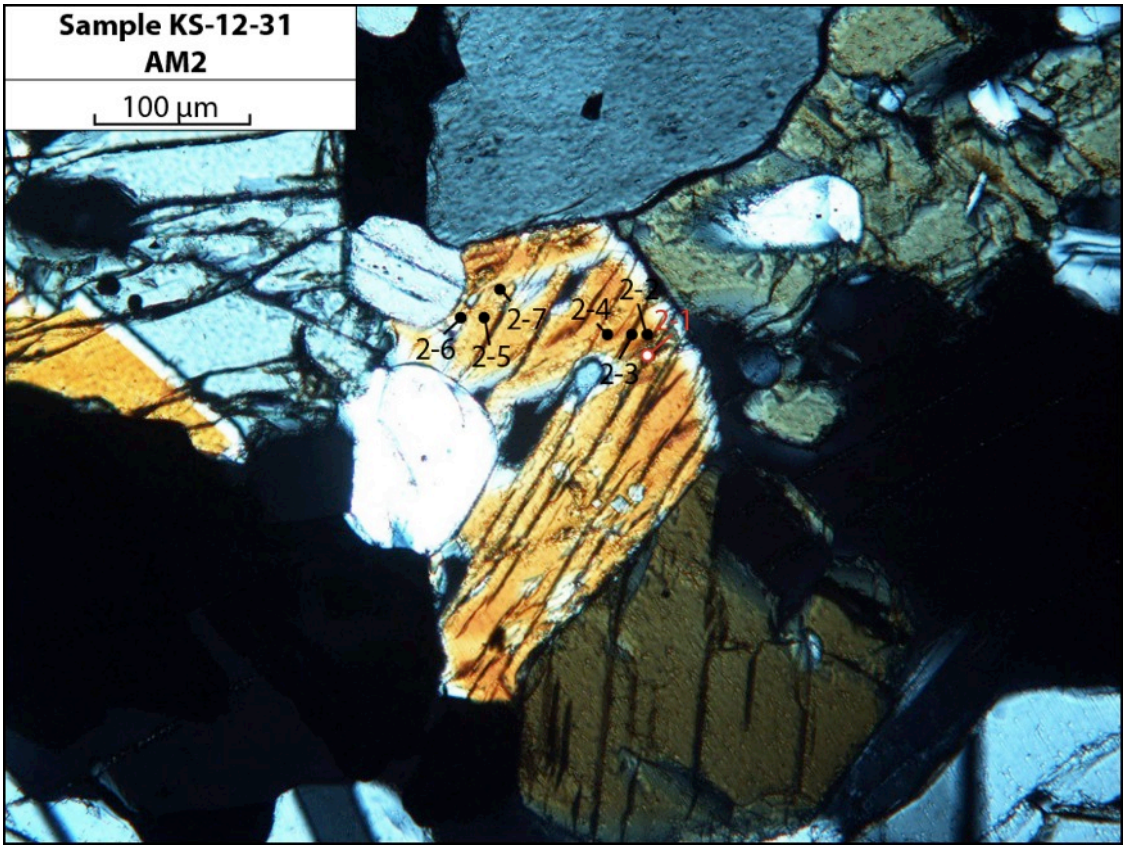

Figure A24. AM2 in Gabbro KS-12-31 (XPL)

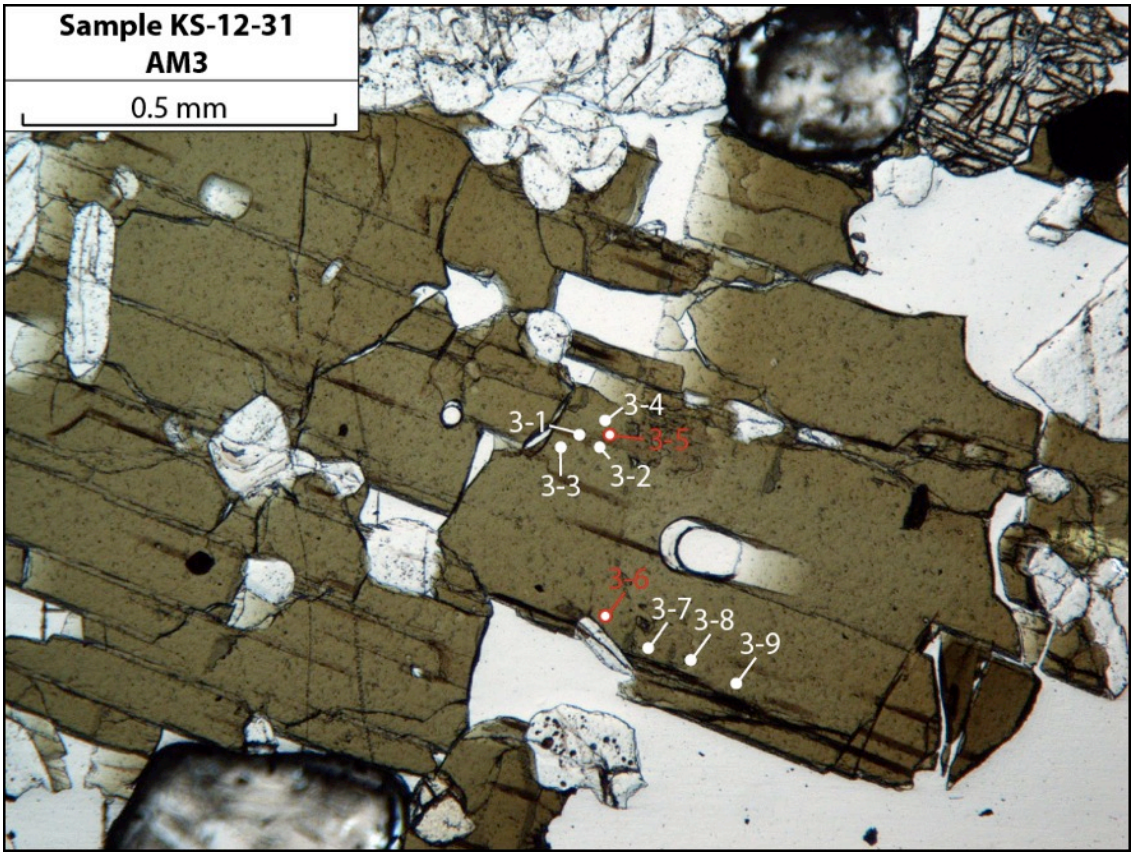

Figure A25. AM3 in Gabbro KS-12-31 (PPL)

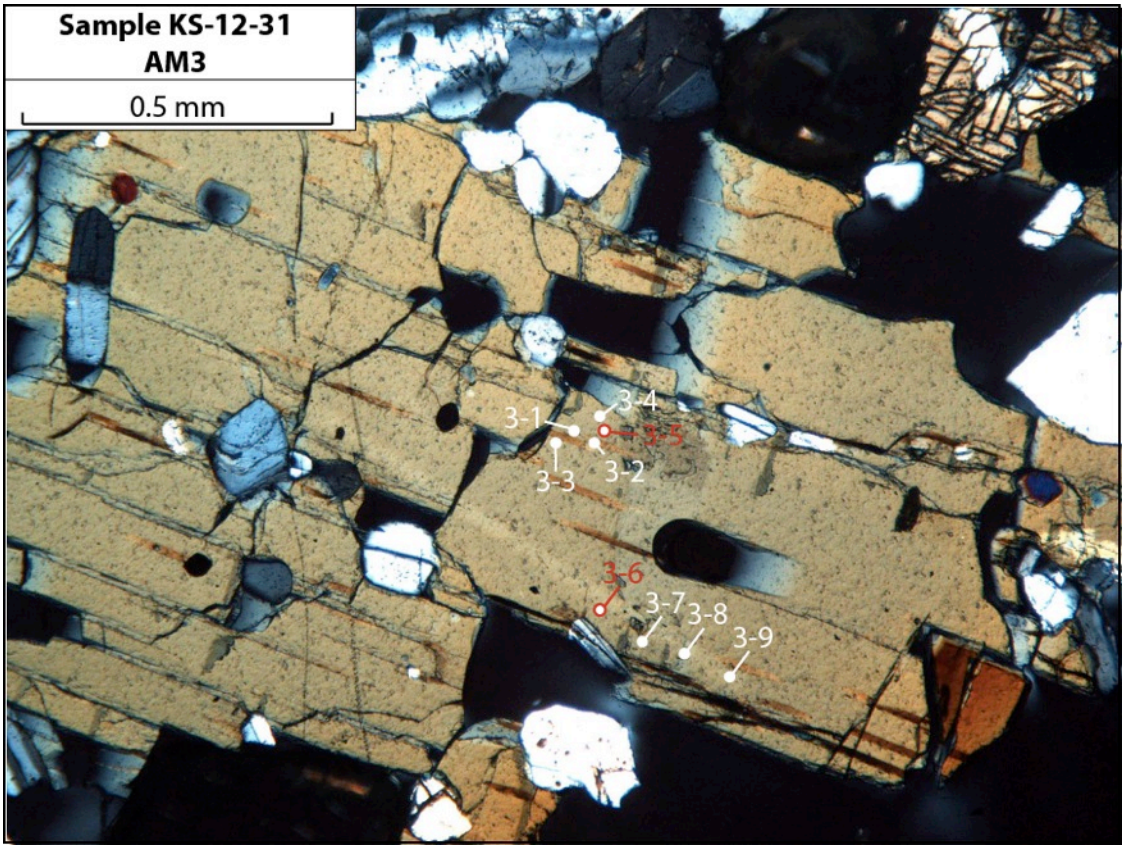

Figure A26. AM3 in Gabbro KS-12-31 (XPL)

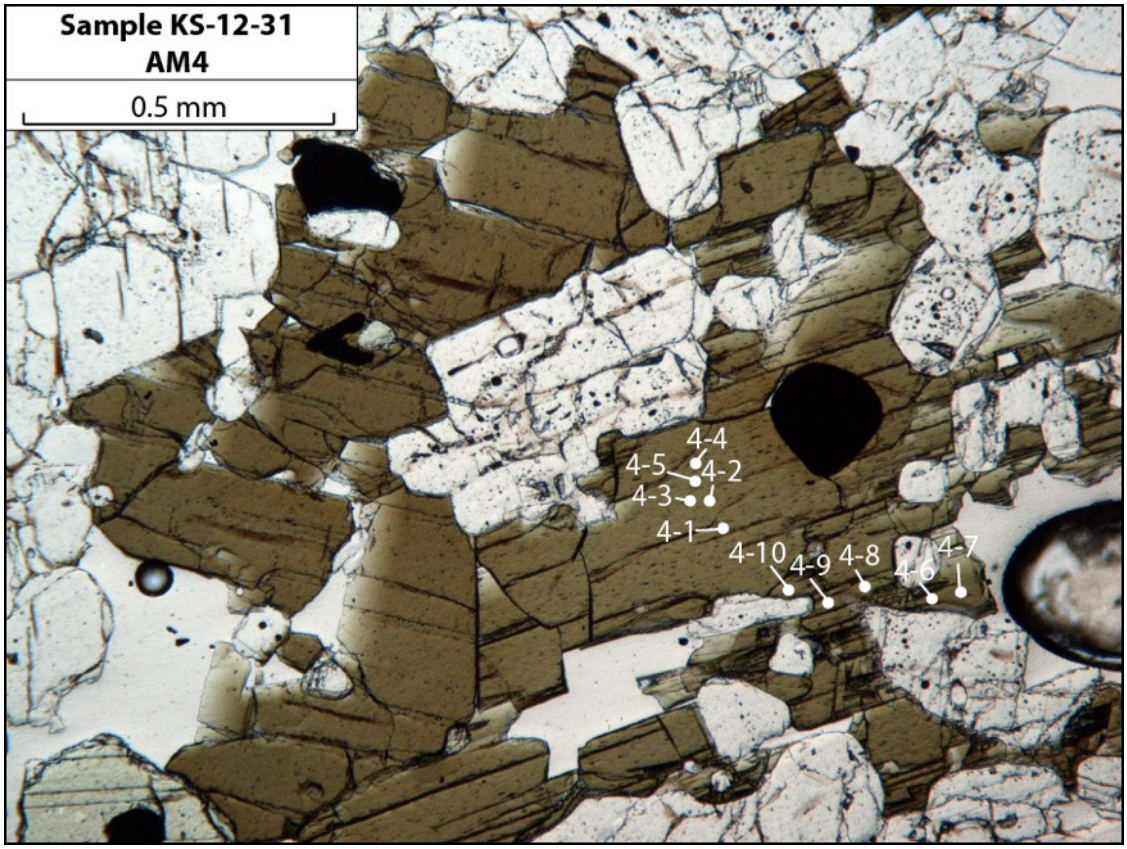

Figure A27. AM4 in Gabbro KS-12-31 (PPL)

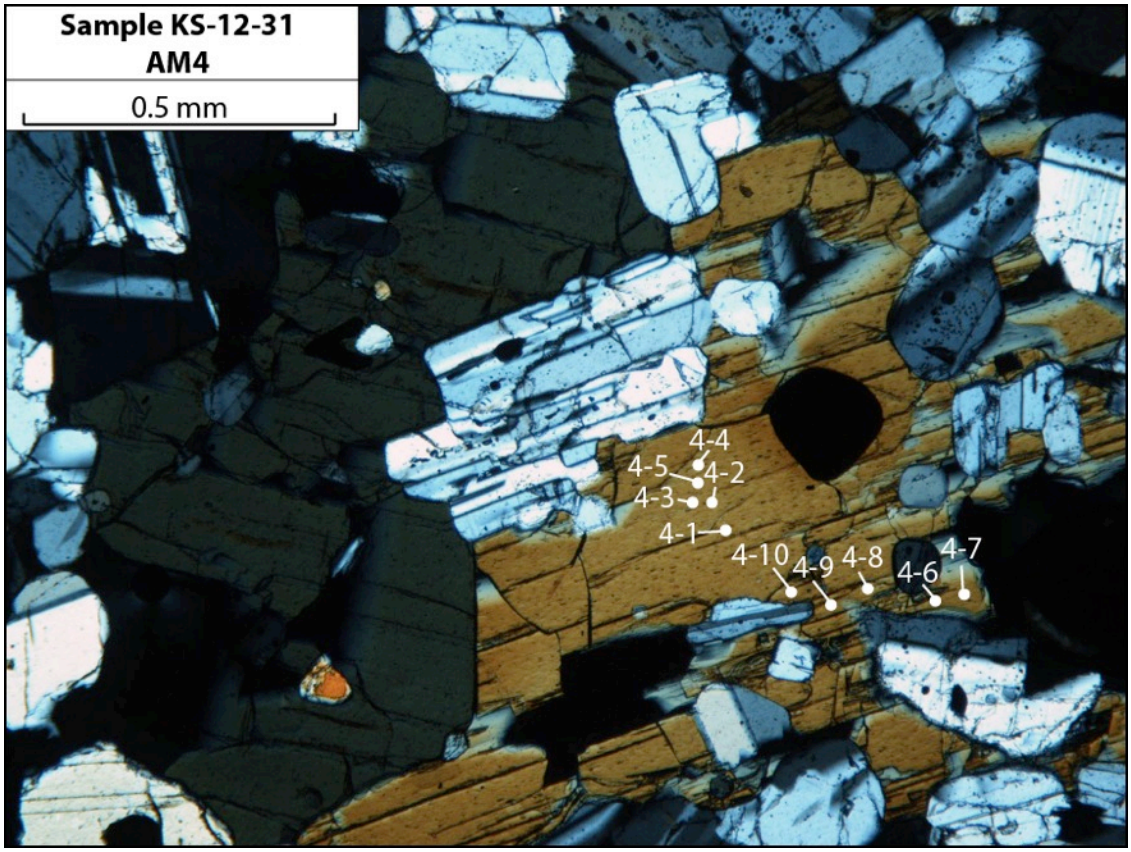

Figure A28. AM4 in Gabbro KS-12-31 (XPL)

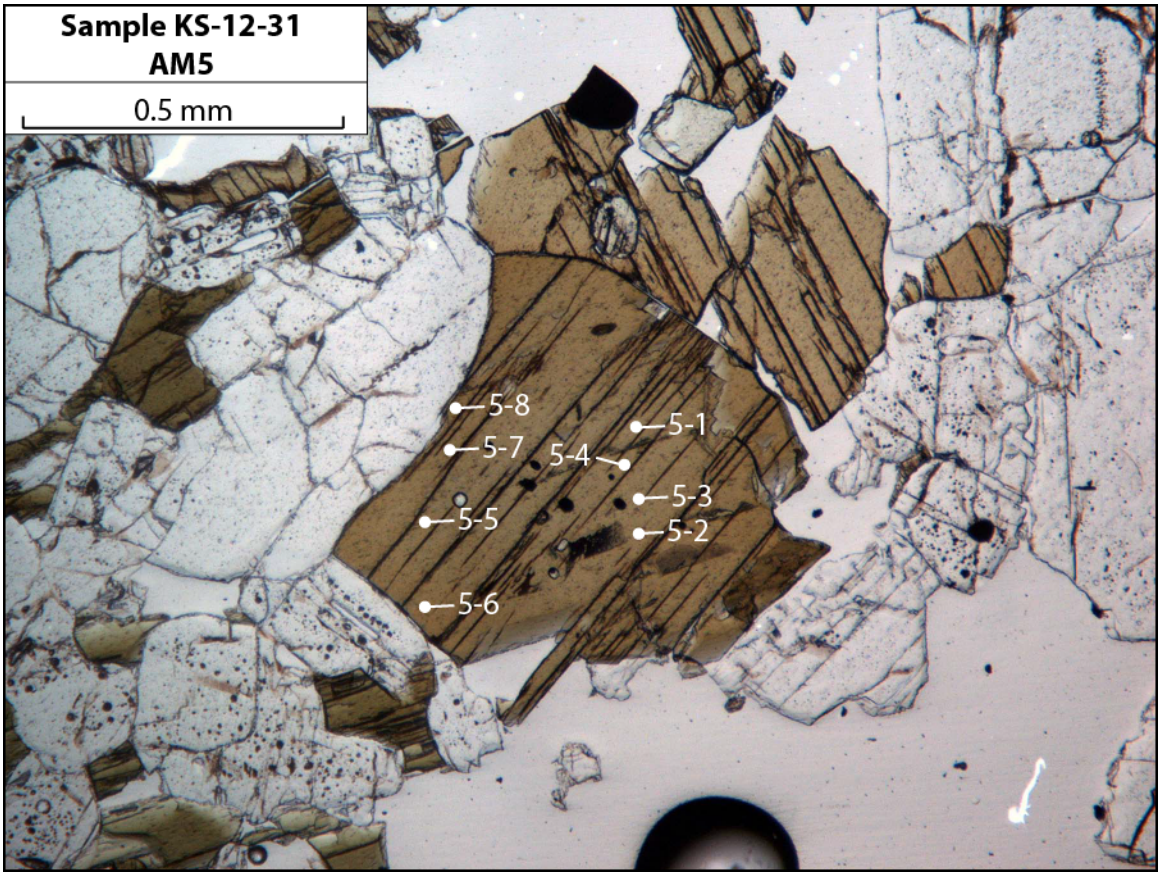

Figure A29. AM5 in Gabbro KS-12-31 (PPL)

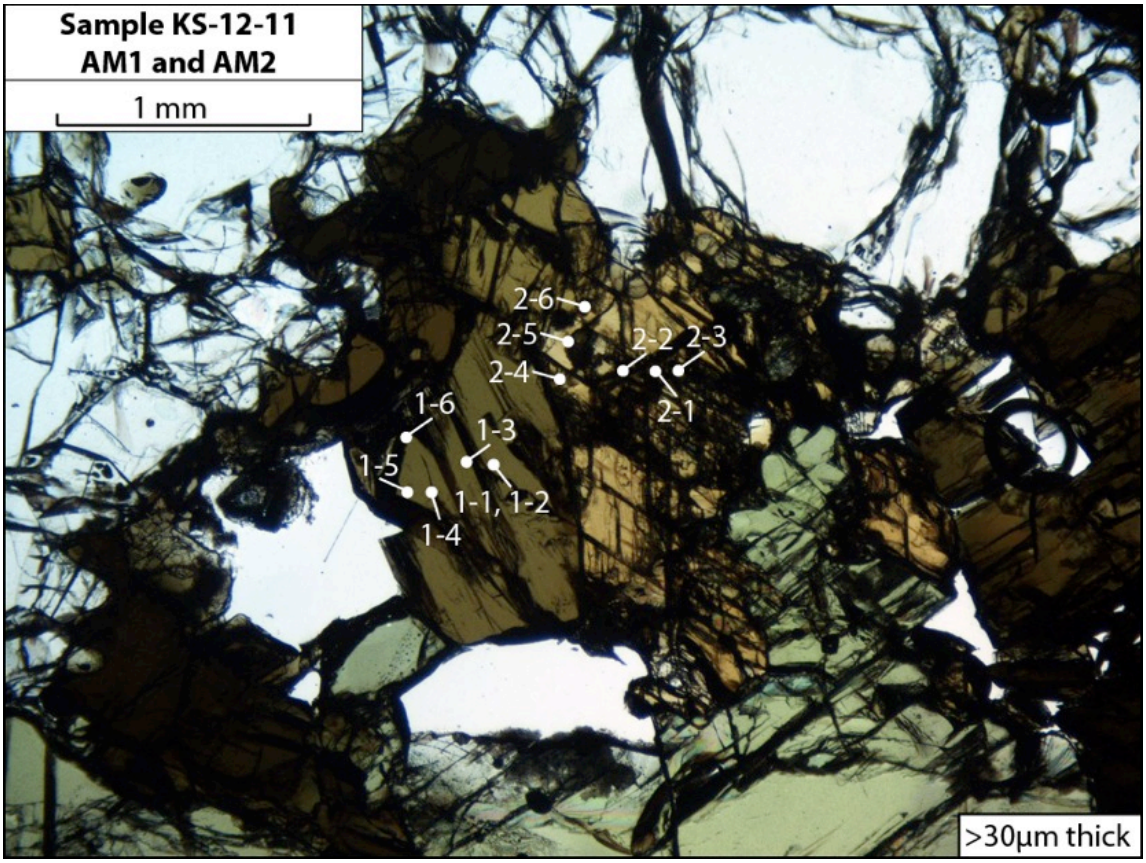

Figure A30. AM1 and AM2 in Pyroxenite KS-12-11 (PPL)

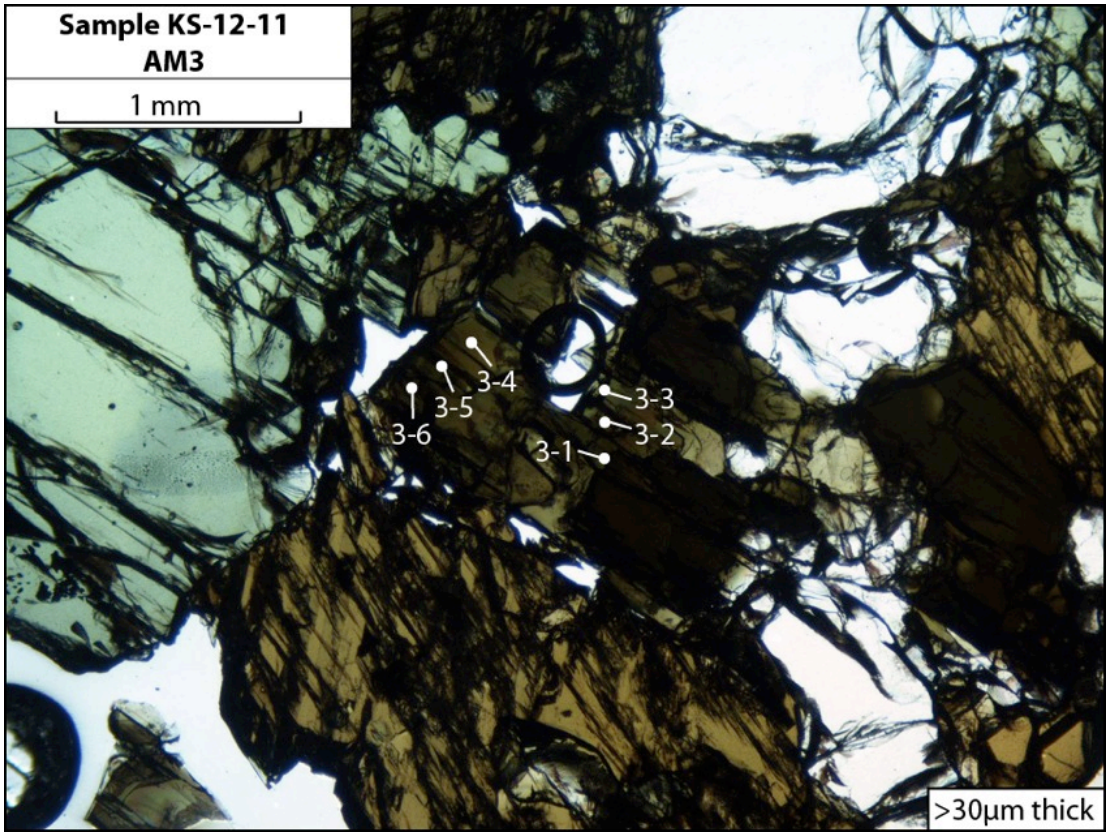

Figure A31. AM3 in Pyroxenite KS-12-11 (PPL)

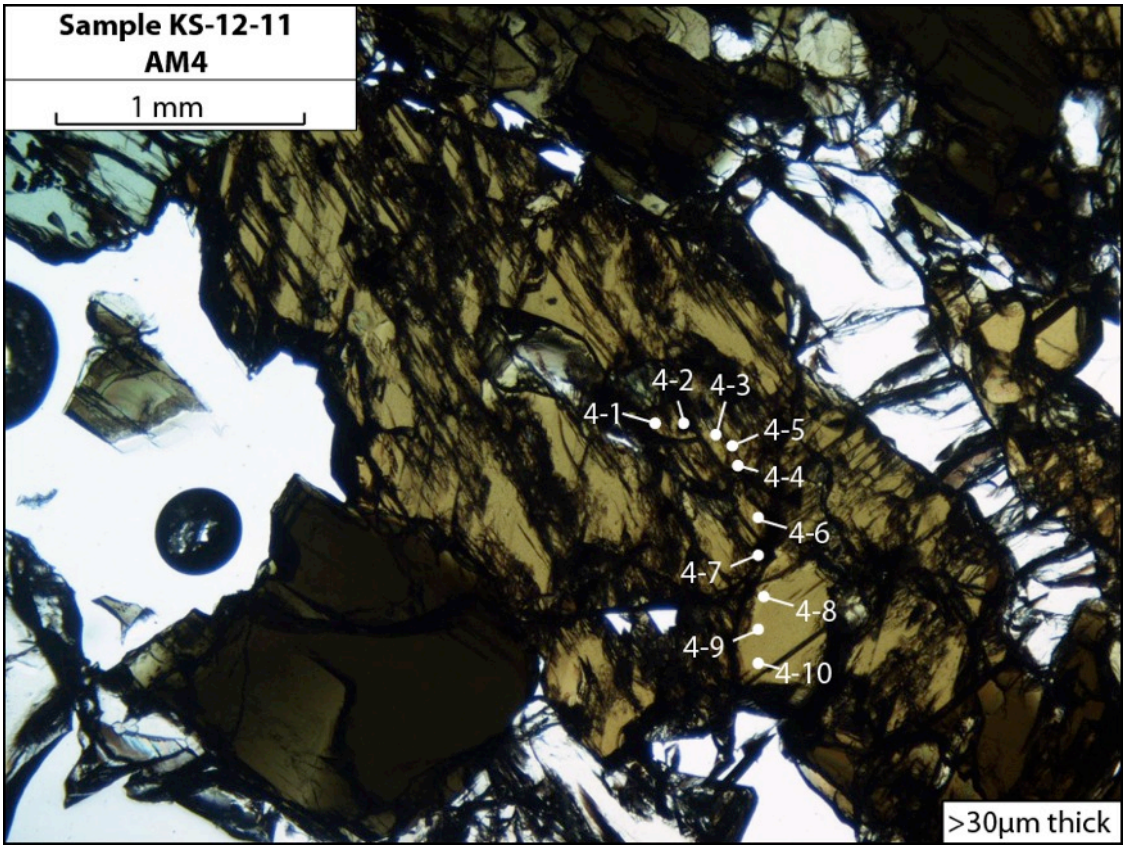

Figure A32. AM4 in Pyroxenite KS-12-11 (PPL)

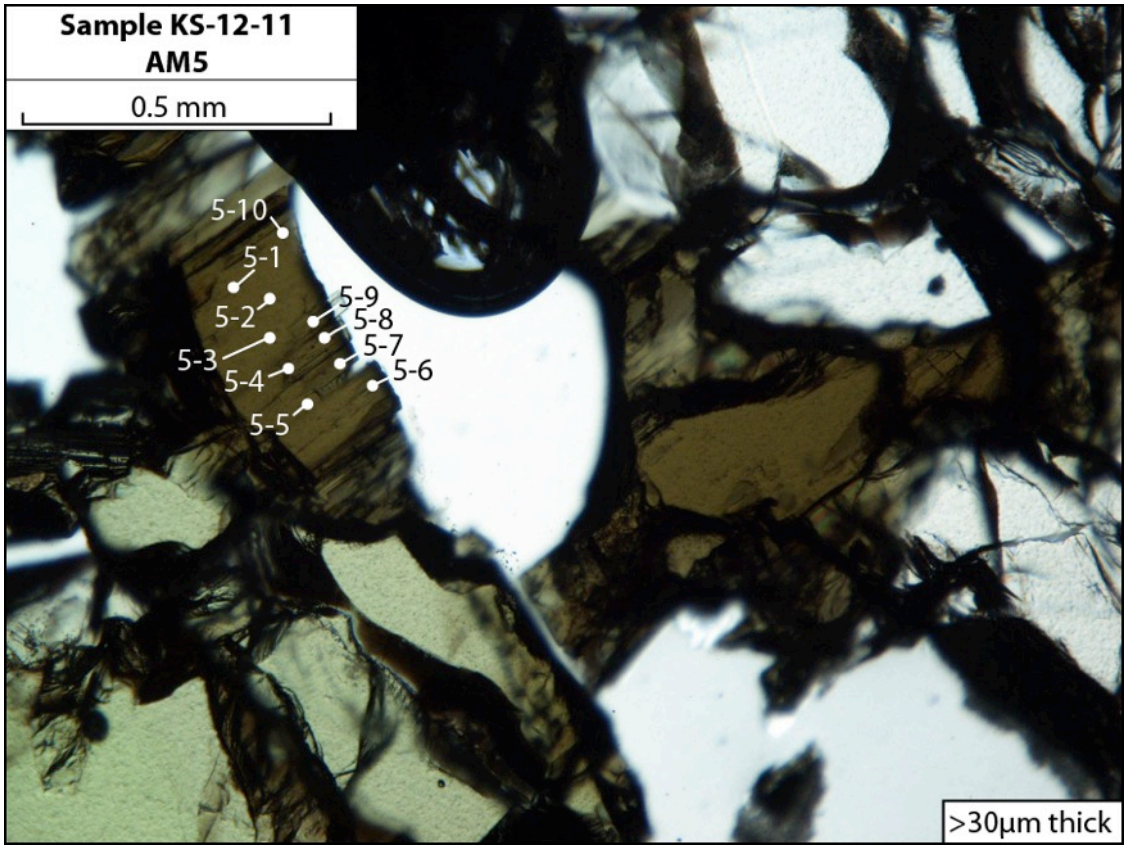

Figure A33. AM5 in Pyroxenite KS-12-11 (PPL)

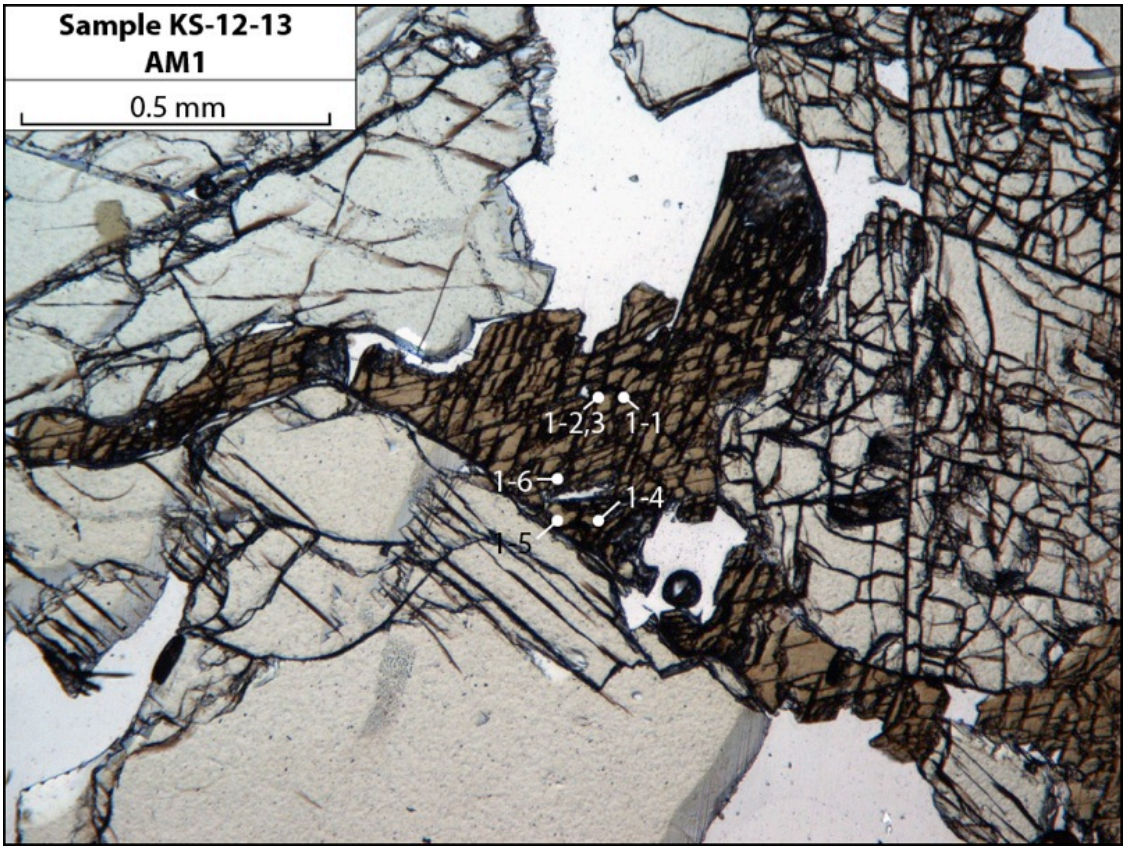

Figure A34. AM1 in Clinopyroxenite KS-12-13 (PPL)

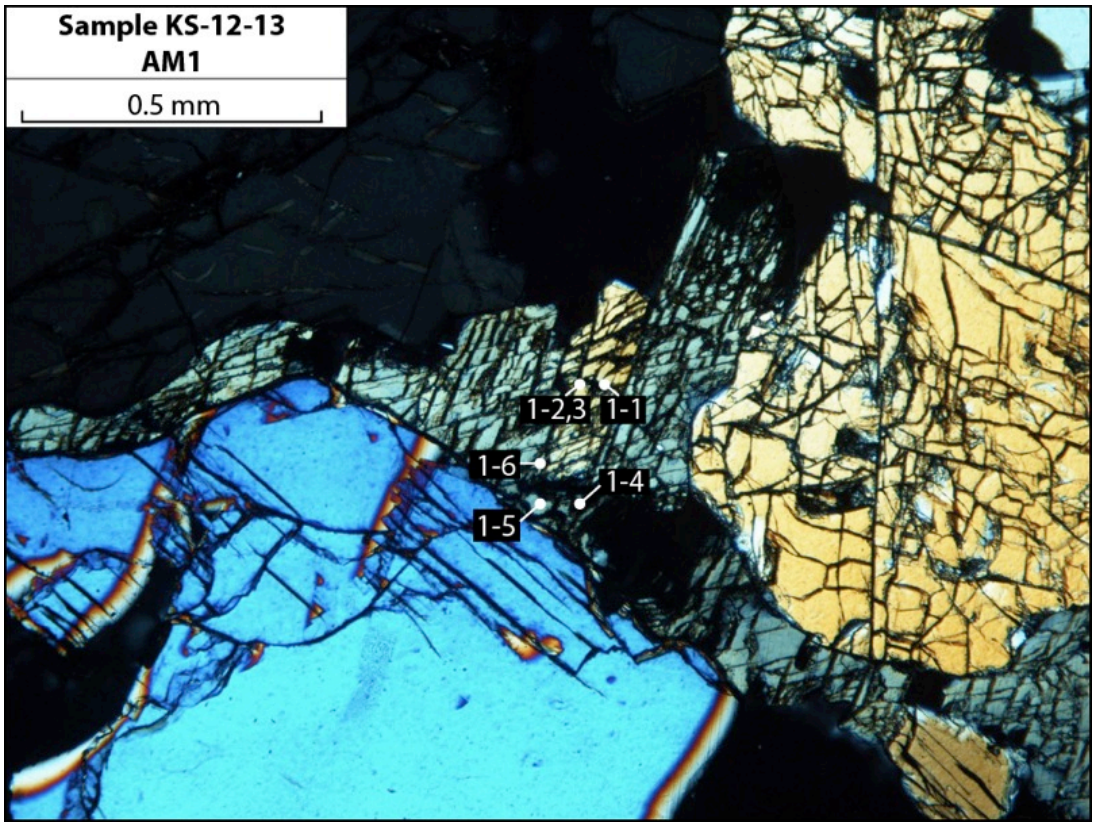

Figure A35. AM1 in Clinopyroxenite KS-12-13 (XPL)

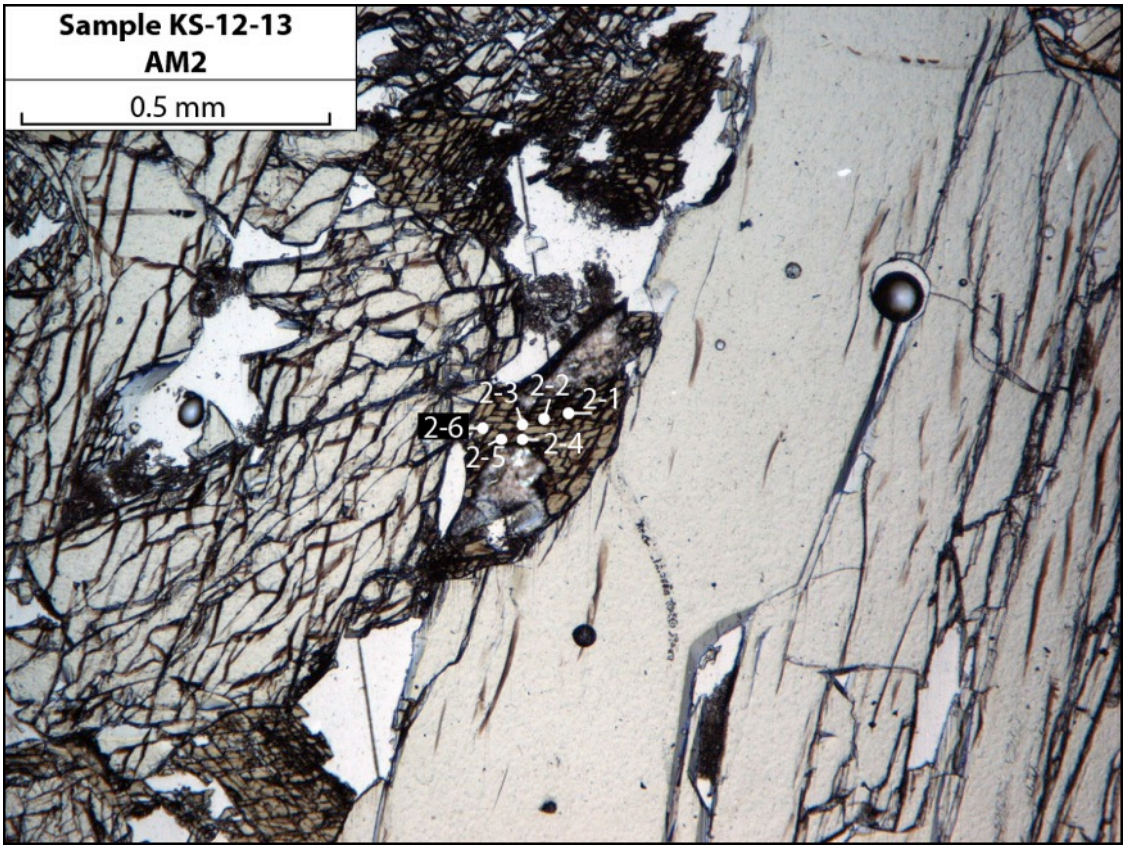

Figure A36. AM2 in Clinopyroxenite KS-12-13 (PPL)

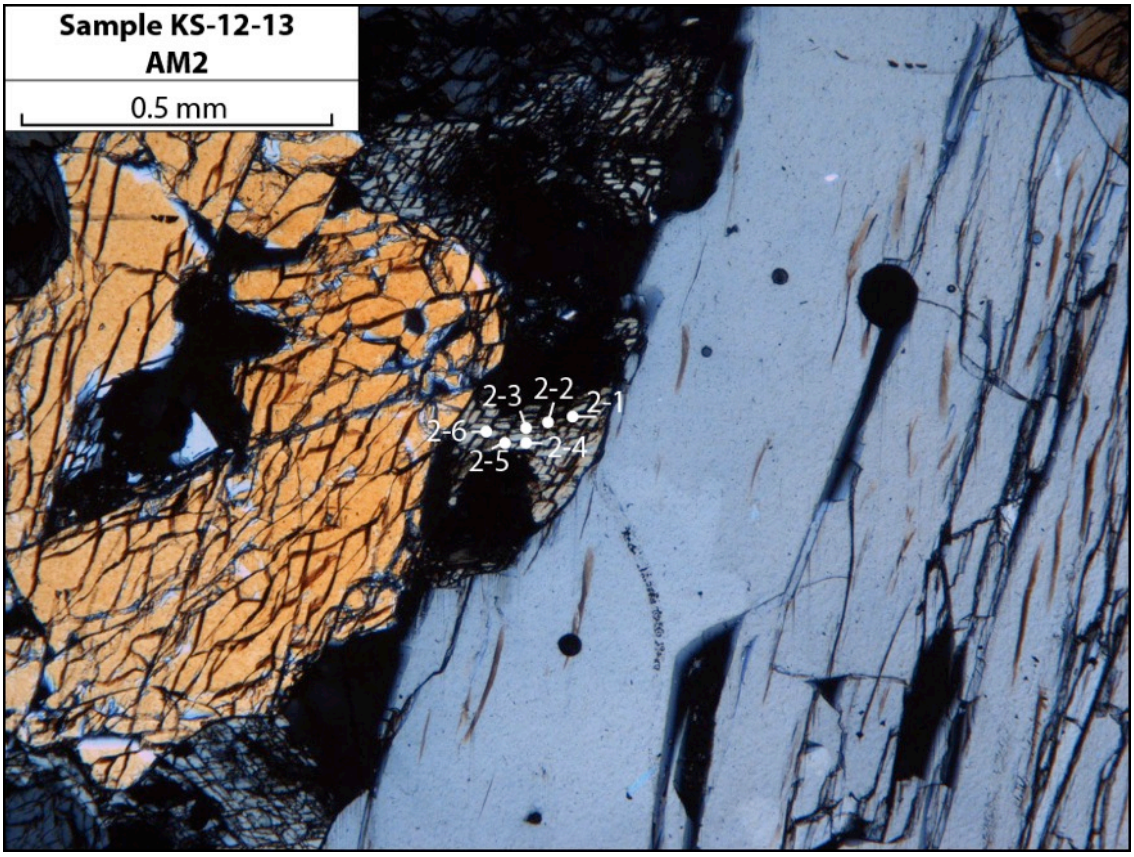

Figure A37. AM2 in Clinopyroxenite KS-12-13 (XPL)

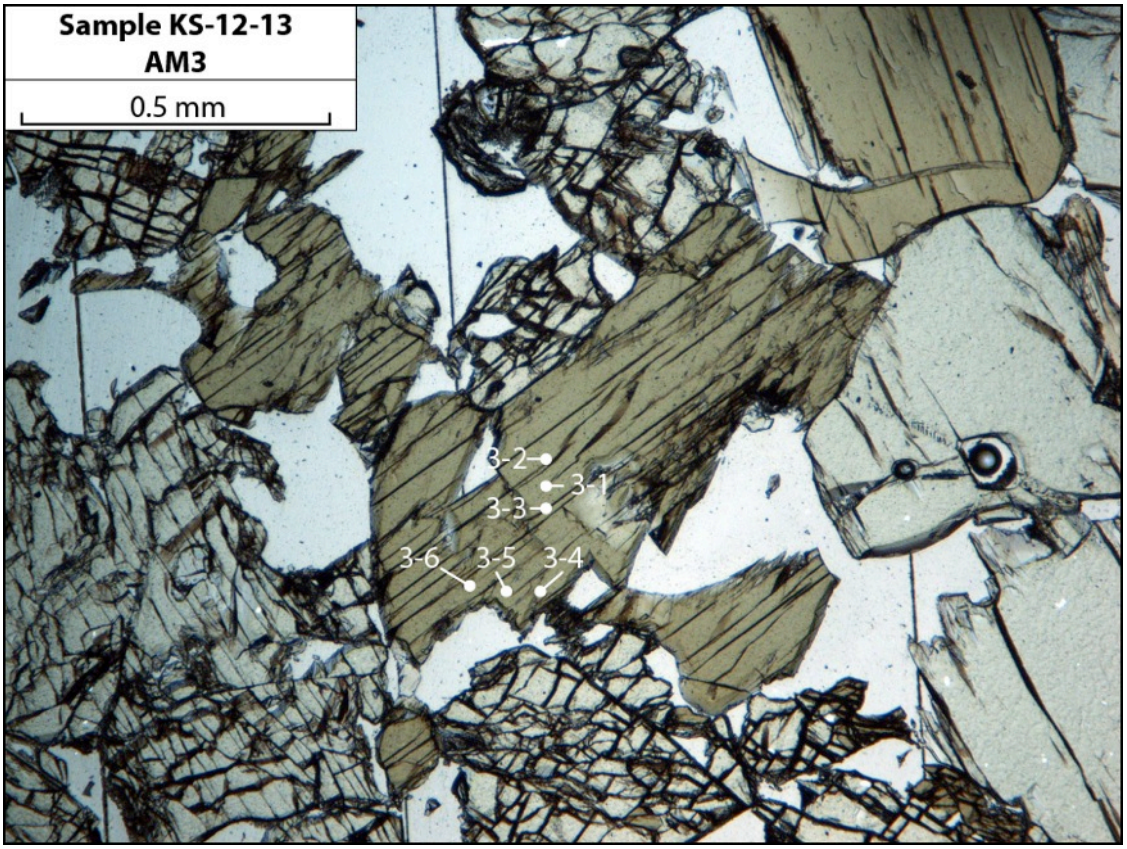

Figure A38. AM3 in Clinopyroxenite KS-12-13 (PPL)

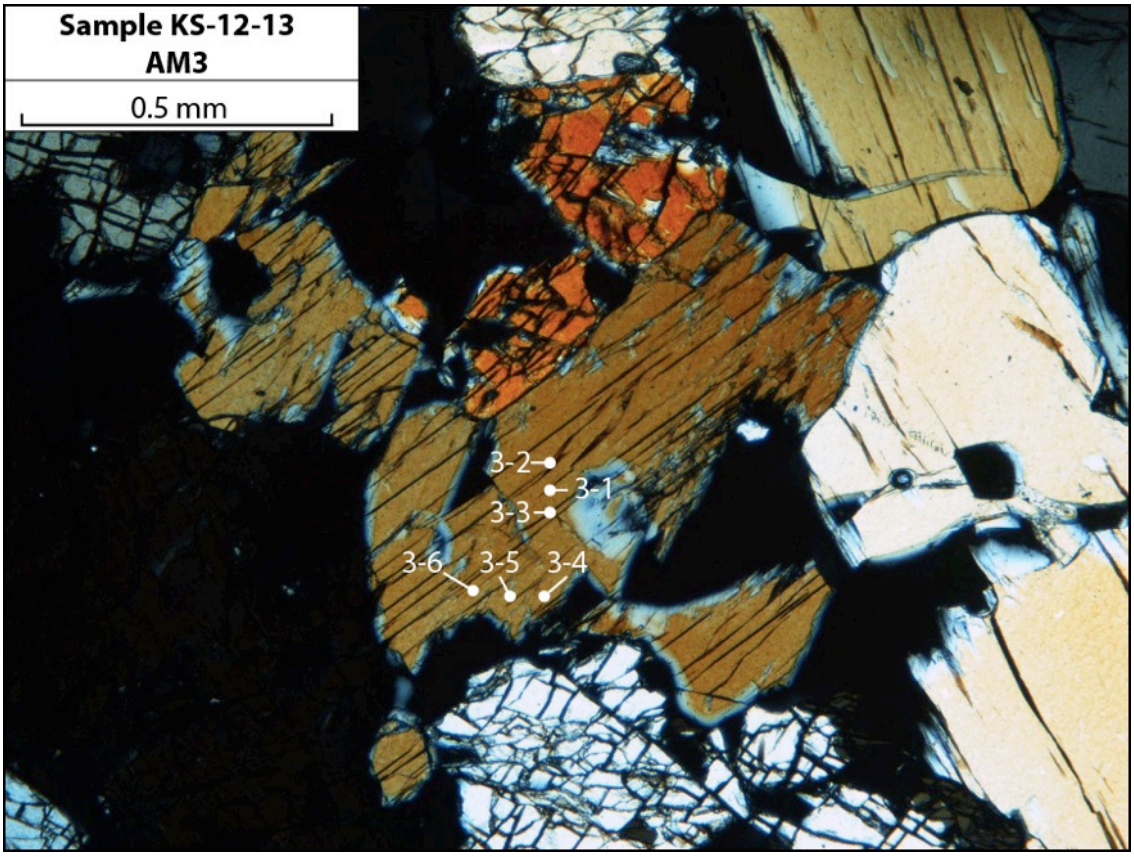

Figure A39. AM3 in Clinopyroxenite KS-12-13 (XPL)

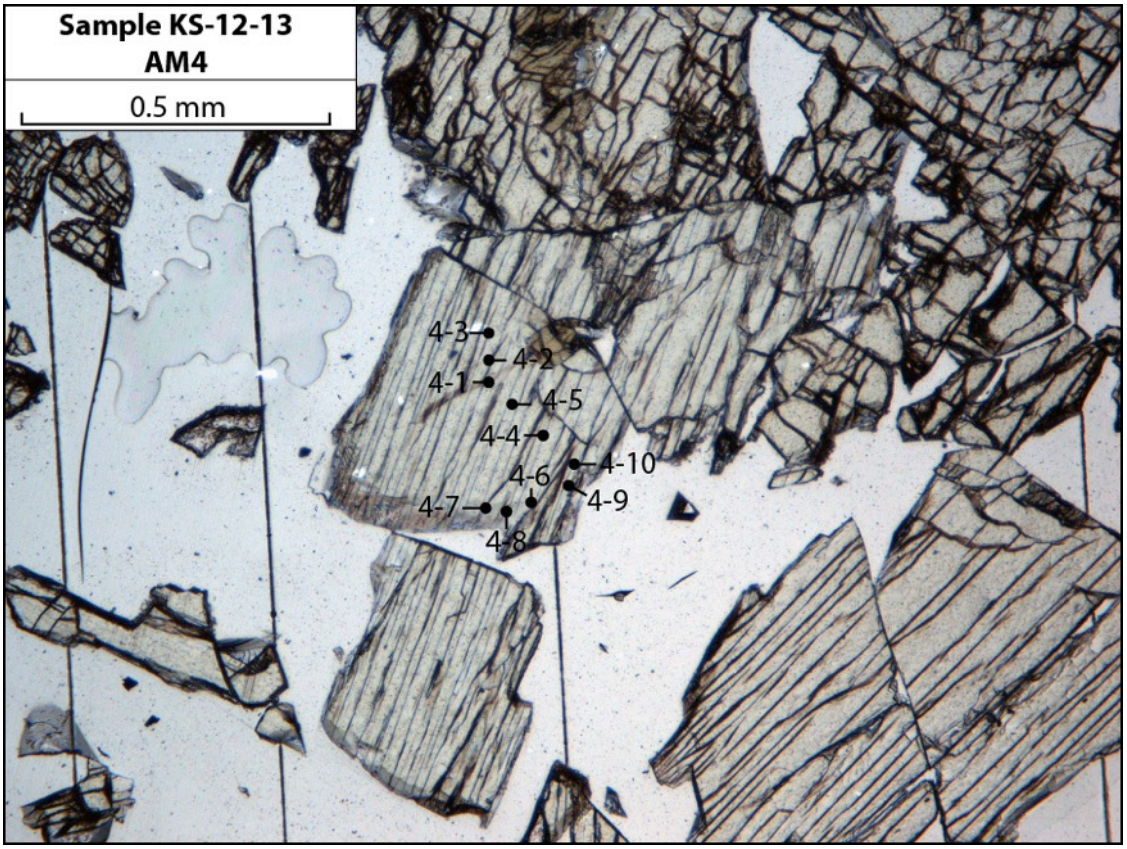

Figure A40. AM4 in Clinopyroxenite KS-12-13 (PPL)

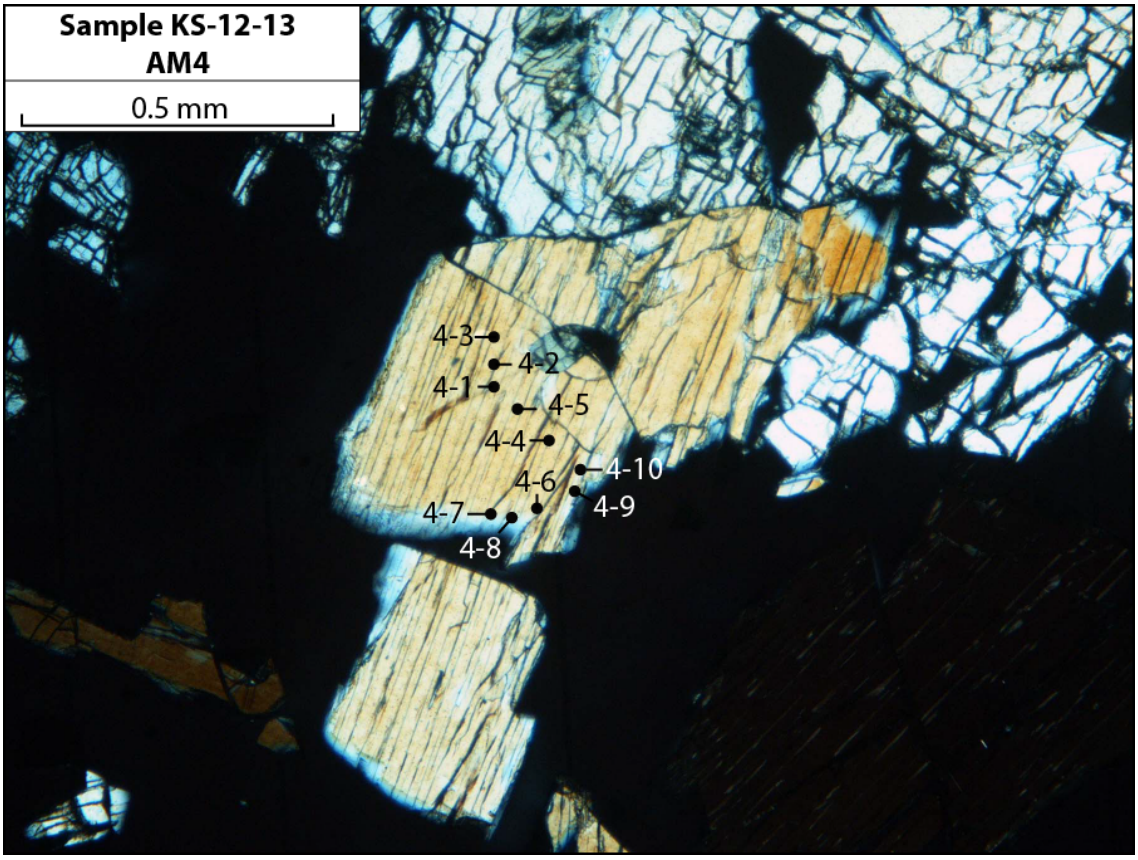

Figure A41. AM4 in Clinopyroxenite KS-12-13 (XPL)

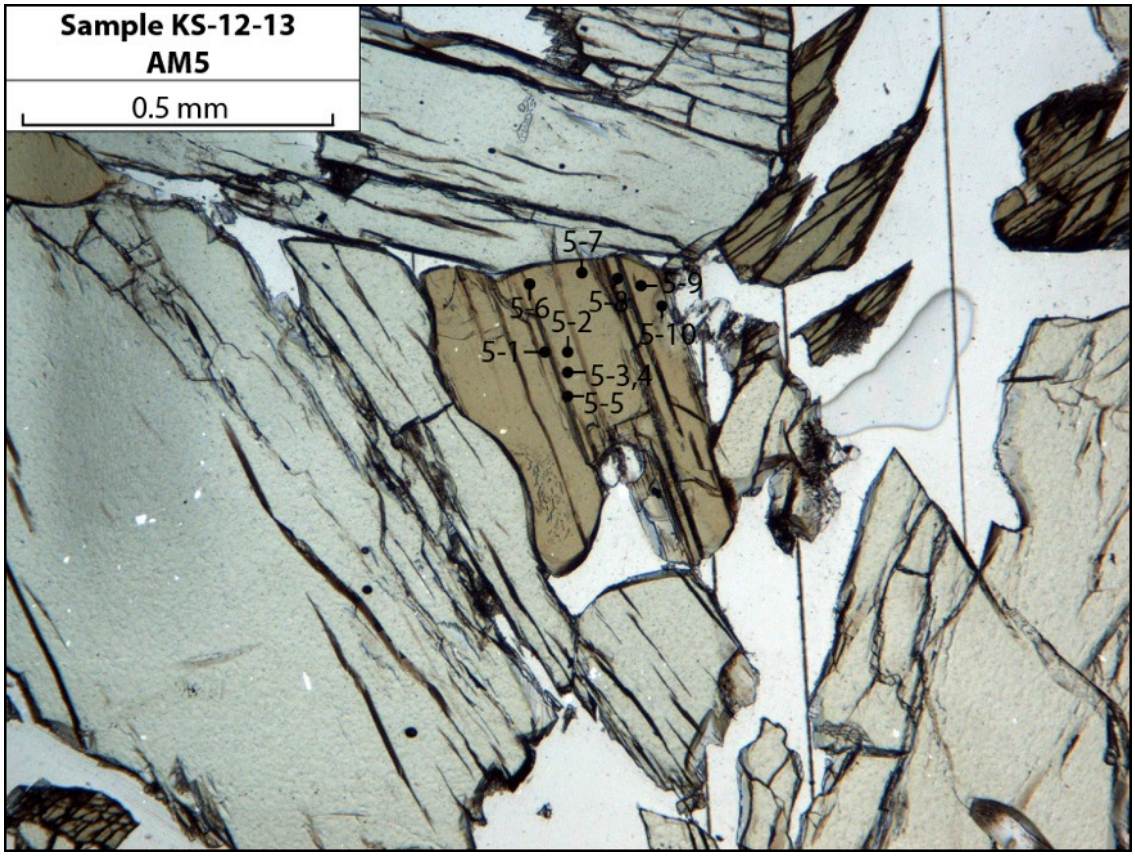

Figure A42. AM5 in Clinopyroxenite KS-12-13 (PPL)

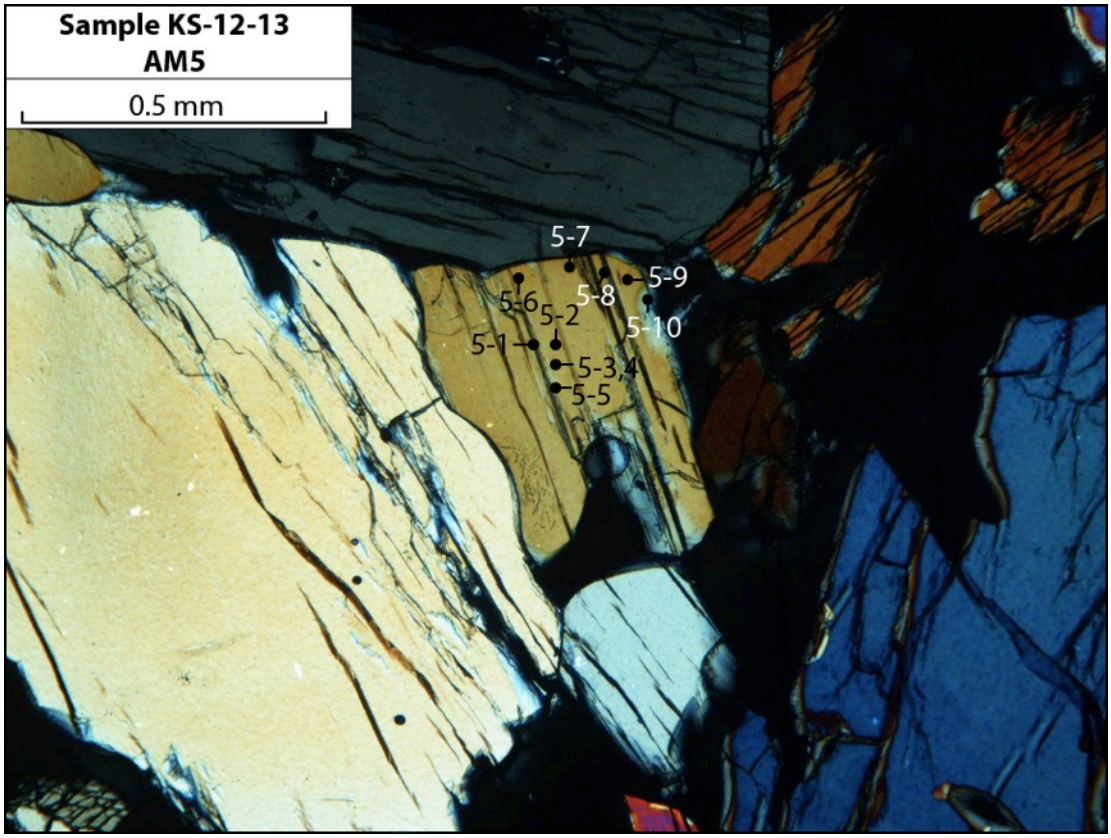

Figure A43. AM5 in Clinopyroxenite KS-12-13 (XPL)

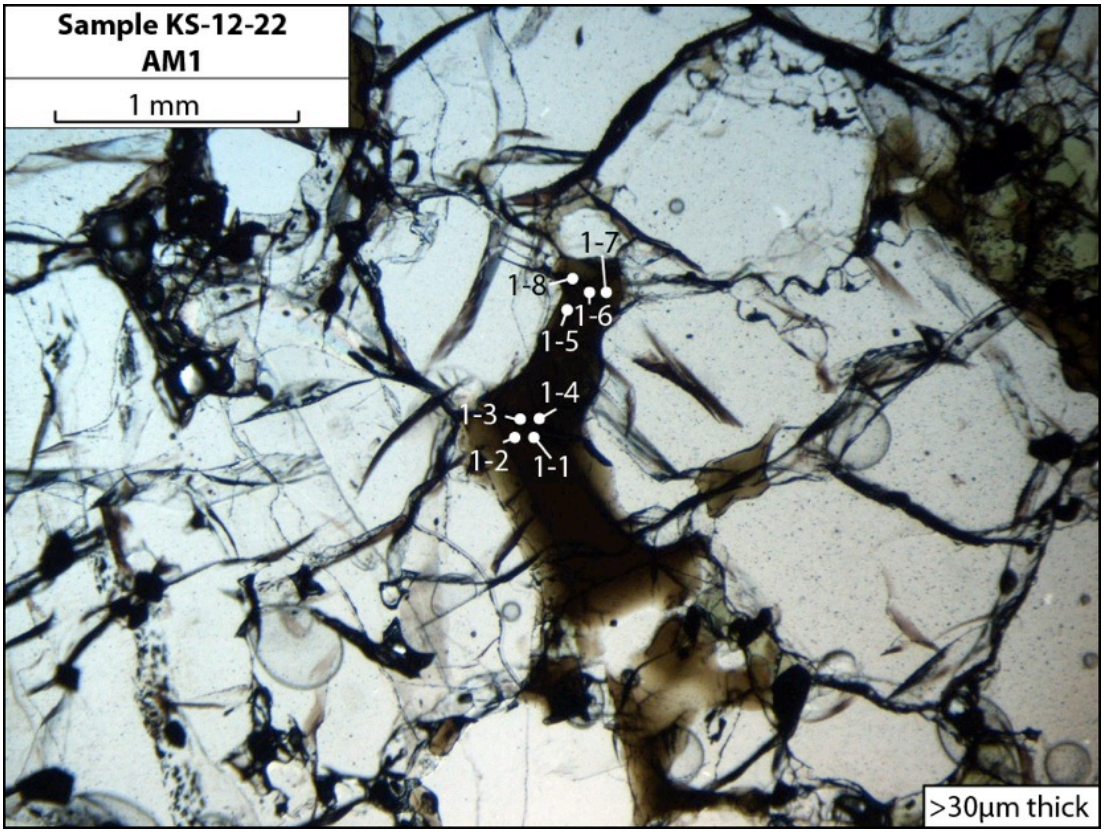

Figure A44. AM1 in Wehrlite KS-12-22 (PPL)

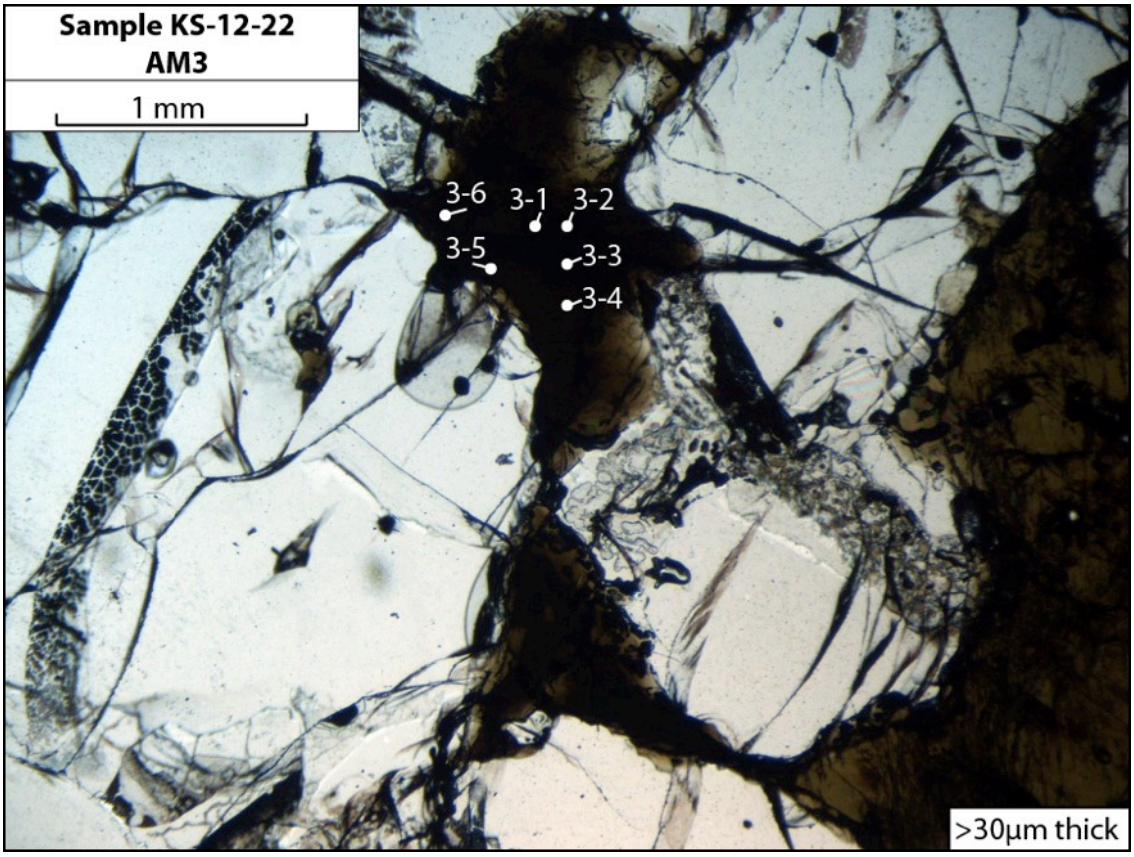

Figure A45. AM3 in Wehrlite KS-12-22 (PPL)

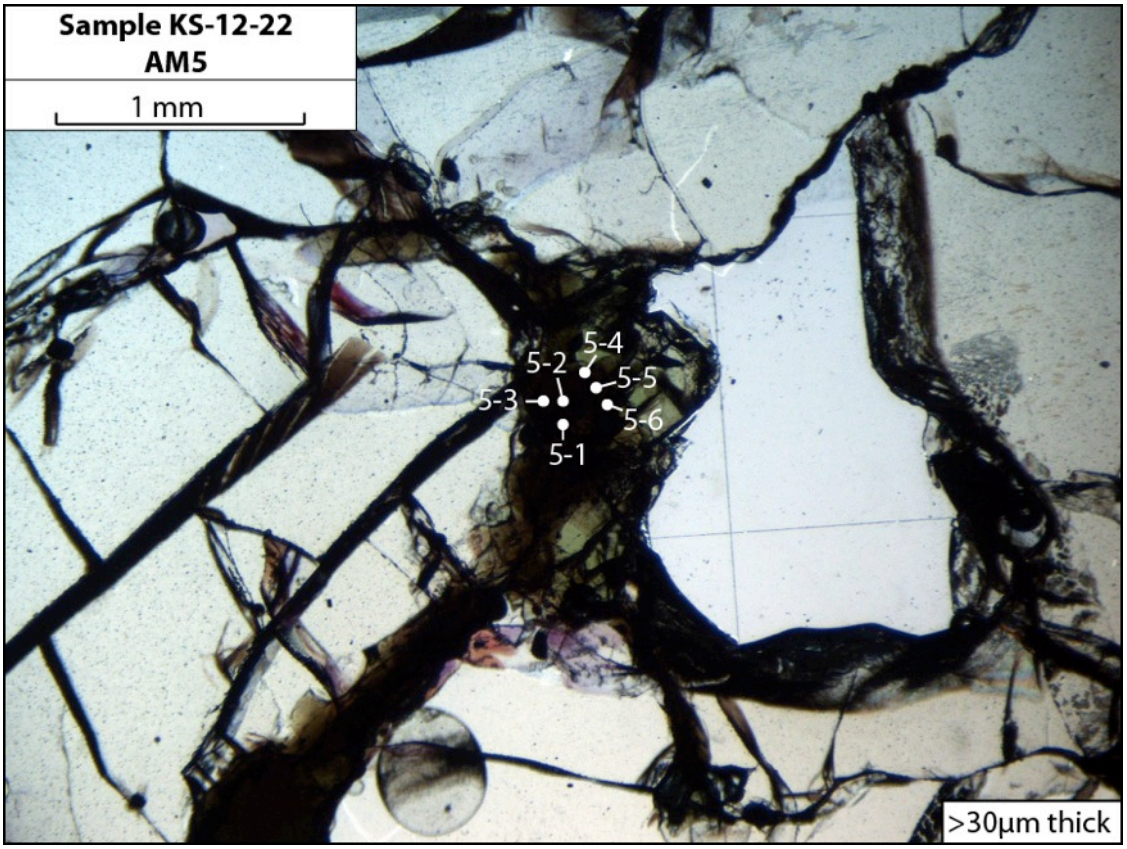

Figure A46. AM5 in Wehrlite KS-12-22 (PPL)

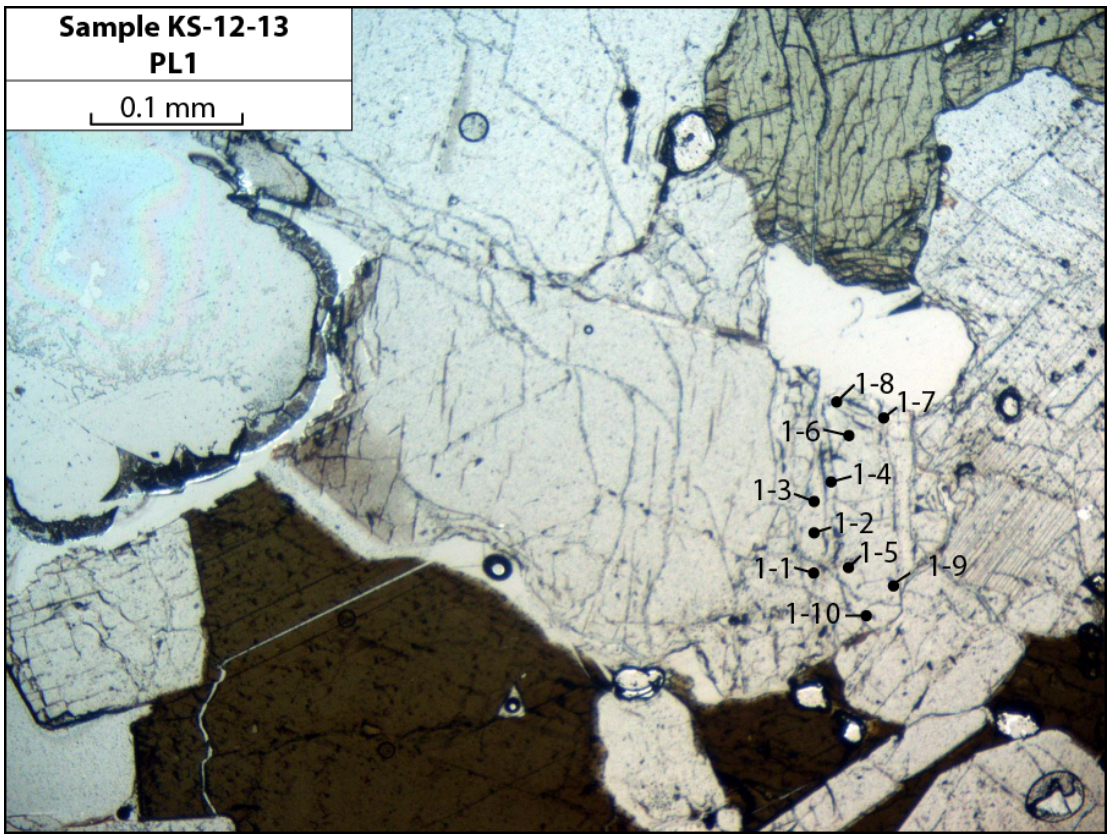

Figure A47. PL1 in Clinopyroxenite KS-12-13 (PPL)

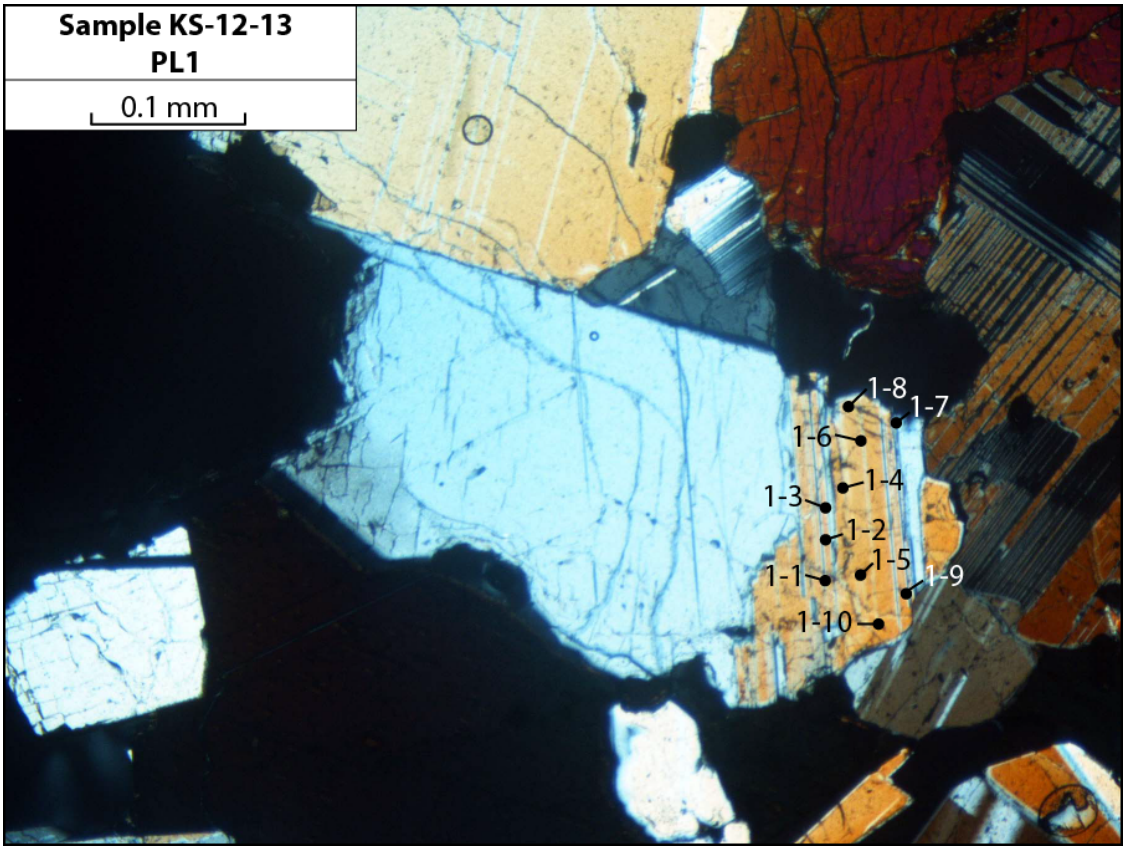

Figure A48. PL1 in Clinopyroxenite KS-12-13 (XPL)

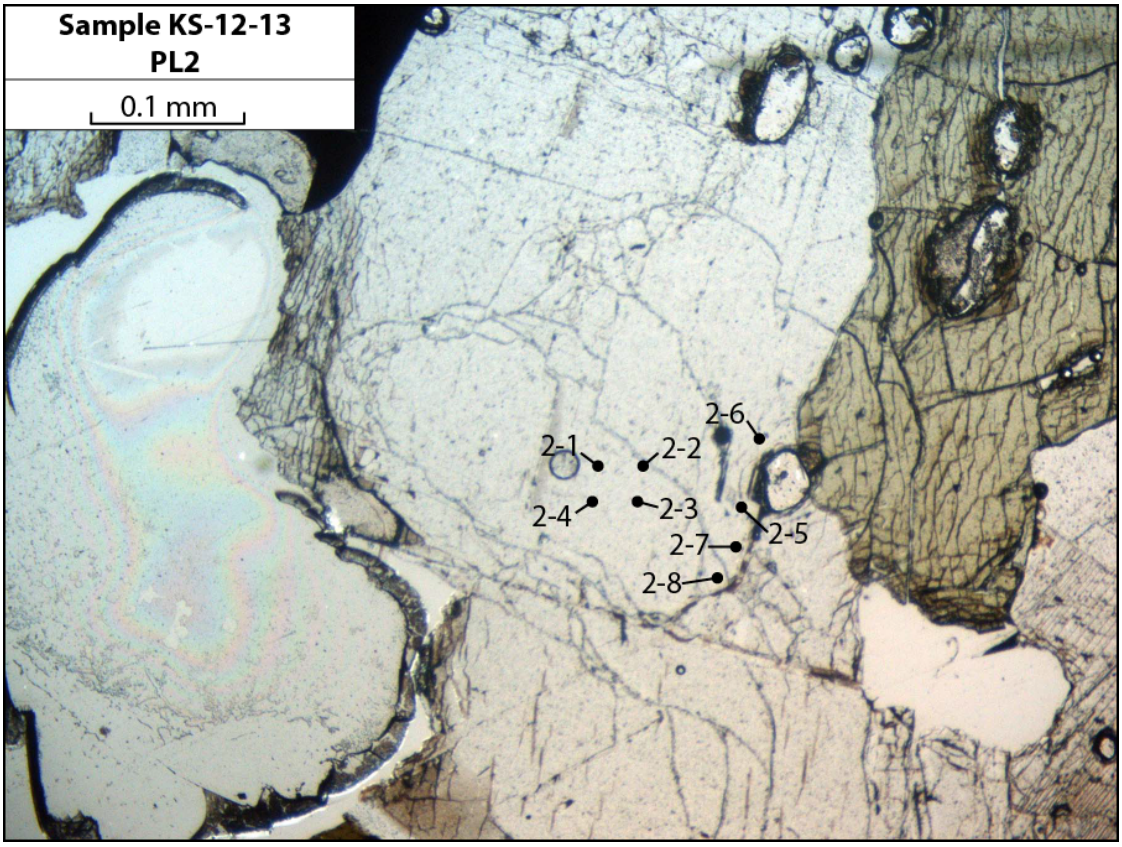

Figure A49. PL2 in Clinopyroxenite KS-12-13 (PPL)

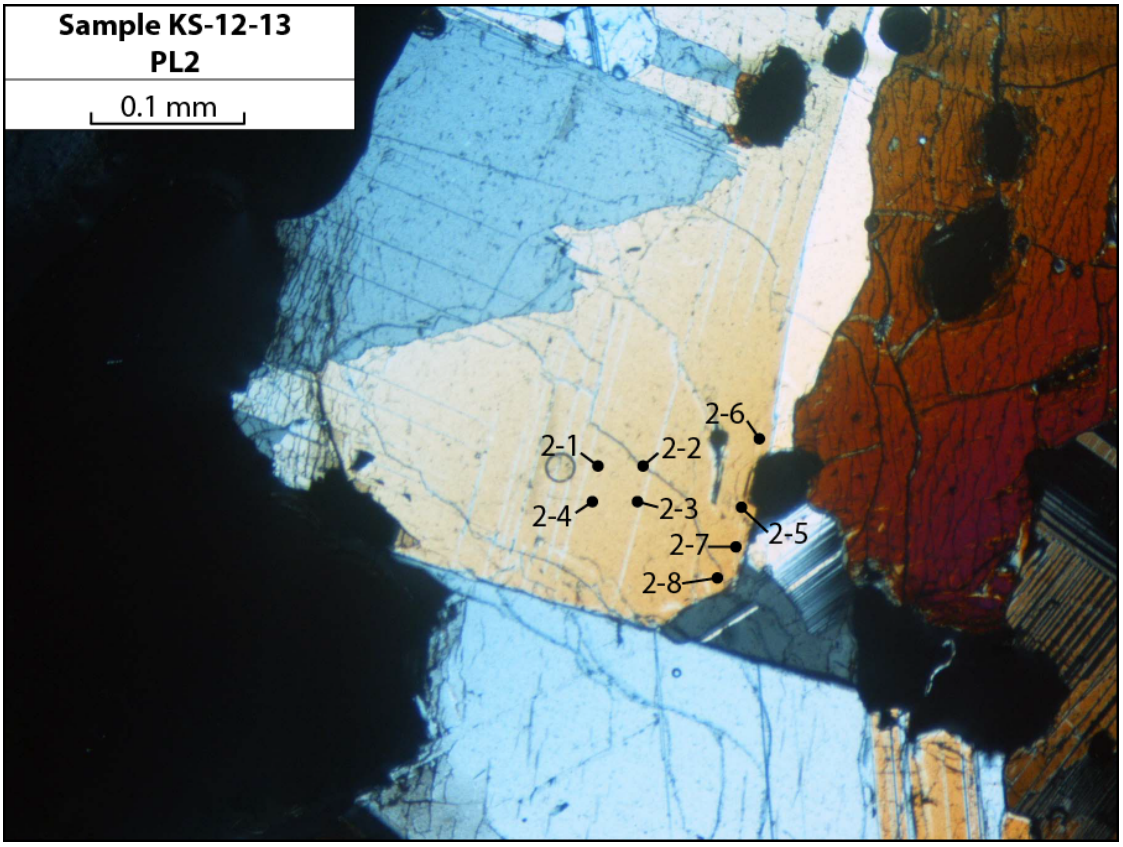

Figure A50. PL2 in Clinopyroxenite KS-12-13 (XPL)